SUPERCRITICAL GAS COOLING AND CONDENSATION OF REFRIGERANT R410A AT NEAR-CRITICAL PRESSURES

A Thesis
Presented to
The Academic Faculty

by

Biswajit Mitra

In Partial Fulfillment
of the Requirements for the Degree
Doctor of Philosophy in
Mechanical Engineering

Georgia Institute of Technology
August 2005

SUPERCRITICAL GAS COOLING AND CONDENSATION OF REFRIGERANT R410A AT NEAR-CRITICAL PRESSURES

Approved by:

Dr. Srinivas Garimella, Advisor
Woodruff School of Mechanical Engineering
Georgia Institute of Technology

Dr. Tom Fuller
School of Chemical and Biomolecular Engineering
Georgia Institute of Technology

Dr. S. Mostafa Ghiaasiaan
Woodruff School of Mechanical Engineering
Georgia Institute of Technology

Dr. Victor Breedveld
School of Chemical and Biomolecular Engineering
Georgia Institute of Technology

Dr. Samuel Graham
Woodruff School of Mechanical Engineering
Georgia Institute of Technology

Date Approved: June 14, 2005

To my parents --- after all, they bore me, raised me, supported me, taught me, loved me and continue to do so…

ACKNOWLEGDGEMENTS

I would like to take this opportunity to deeply thank the various people who, over the last few years, have helped me immensely in completing this work. First, I would like to thank my advisor, Dr. Srinivas Garimella. This thesis wouldn't have been possible without his kind support, trenchant critiques, probing questions, and remarkable patience. I am grateful to my committee members --- Drs. S. Mostafa Ghiaasiaan, Samuel Graham, Tom Fuller and Victor Breedveld for their patience while I finished writing my thesis. I would also like to thank the Air Conditioning and Refrigeration Technology Institute and American Society of Heating, Refrigerating and Air-Conditioning Engineers for funding this project.

Special thanks are due to Dr. Yirong Jiang, Matthew D. Determan and Tim Ernst for helping me understand and perform experiments on the test facility. They also provided me a helping hand whenever I was in need. Thanks are also in order for Akhil Agarwal and Lalit Kr. Bohra for accompanying me during experiments when no one was around, Vishwanath Subramaniam for helping me during the most strenuous hours and Jesse Killion for showing me around and helping me get acclimated to this country.

TABLE OF CONTENTS

LIST OF TABLES

LIST OF FIGURES

LIST OF SYMBOLS

Symbols

A	area
Cp	specific heat (kJ/kg-K)
$\overline{Cp}$	mean specific heat ($(h_w - h_b)/(T_w - T_b)$) (kJ/kg-K)
d	derivative operator
d, D	diameter (m)
D^+	non-dimensional tube diameter
DP	differential pressure drop
E	specific work of thermal contraction/expansion
f	friction factor
F	ratio of axial shear force to gravitational body force Jaster and Kosky (1976)
$F_2(Re_l, Pr)$	dimensionless heat transfer resistance
Fr	Froude number
g	gravitational constant 9.81 m/s^2
G	mass flux (kg/m^2-s)
Ga	Galileo number
Gr	Grashoff Number
h	enthalpy (kJ/kg), condensation heat transfer coefficient (W/m^2-K), height (m)
$\bar{h}$	average heat transfer coefficient (W/m^2-K)
I.D.	tube inner diameter (m)

J, j	superficial velocity (m/s)
Ja	Jakob number = $Cp_l\left(T_{sat} - T_w\right)/h_{lv}$
k	thermal conductivity (W/m-K)
L	length
LMTD	log-mean temperature difference (K)
$\dot{m}$, $\dot{m}'$	mass flow rate (kg/s)
N	number
Nu	Nusselt number
O.D.	tube outer diameter (m)
P,p	pressure (kPa), wetted perimeter (m)
Pr	Prandtl number
Q	heat duty (W)
r	radial direction
r^*	tube to annulus diameter ratio
R	heat transfer resistance (K/W)
Ra	Rayleigh number $\left(g\beta\Delta TD^3\,\mathrm{Pr}_l\right)/\left(\upsilon_l^2\right)$, $\left(g\left(\rho_l-\rho_v\right)D^3\,\mathrm{Pr}_l\right)/\left(\rho_l\upsilon_l^2\right)$
Re	Reynolds number
T	temperature (ºC, K)
U	absolute uncertainty
UA	overall heat transfer conductance (W/K)
V, v	velocity (m/s)
Vol	volumetric flow rate (m^3/s)
w	width, thickness (m), water

W	power (W)
We	Weber number
x	quality
X	Martinelli parameter
Y	Chisholm Y coefficient (Chisholm 1973)
α	void fraction
β	coefficient of thermal expansion (1/K)
∂	partial derivative operator
δ	film thickness
Δ	change, difference
ε	tube roughness (m),
ξ	friction factor
η	efficiency
ϕ	two-phase multiplier
λ	ratio of interface and film velocities
μ	dynamic viscosity (kg/m-s)
ν	kinematic viscosity (m^2-s)
ρ	density (kg/m^3)
σ	surface tension (N/m)
θ	angle subtended from the top of the tube to the liquid pool level in stratified wavy flow (rad)
Ω	angle subtended from the top of the tube to the liquid pool level to the differential element in stratified wavy flow (rad)

τ	torque (N-m), shear stress (kPa)
ω	angular speed (rad/s)

Subscripts and Superscripts

+	dimensionless turbulent parameter
∞	ambient, infinity
actual	actual diameter in present study
air	ambient property
ambient	ambient
annular	annular flow
annulus	annulus-side
avg	average
b	bulk
conf	confinement
conv	convection
crit	critical
DB	Dittus-Boelter
eff	effective
equivalent	equivalent length
f	friction, force
fg	latent heat
fluid	fluid temperature
forced	forced convection
G	gas phase

GO	vapor only phase
h	hydraulic
i, in	inlet
l	liquid phase
lp	liquid pool
L	tube length, liquid phase, left side
Liquid	liquid pool
LO	liquid only phase
M	middle
nc	natural convection
o,out	outlet
pre	pre-condenser/cooler
prim	primary loop
post	post-condenser/cooler
pump	pump
R	right side,
r	reduced
rad	radiation
refg	refrigerant
sat	saturation
sec	secondary loop
shaft	pump shaft input
shell	shell side of the shell-and-tube heat exchanger

so	Soliman modified (Soliman 1982)
test	test section
top	laminar film condensation region in stratified flow
tp	two phase
tt	turbulent-turbulent
turb	turbulent
v	vapor phase
w, water	water-side
wall	at the wall, wall
wavy	wavy flow

SUMMARY

A comprehensive study of heat transfer and pressure drop of refrigerant R410A during condensation and supercritical cooling at near-critical pressures was conducted. Investigations were carried out at five nominal pressures: 0.8, 0.9, 1.0, 1.1 and $1.2 \times p_{crit}$. The refrigerant was tested in commercially available horizontal smooth tubes of 6.2 and 9.4 mm I.D. Heat transfer coefficients were measured using a thermal amplification technique that measures heat duty accurately while also providing refrigerant heat transfer coefficients with low uncertainties. For condensation tests, local heat transfer coefficients and pressure drops were measured for the mass flux range $200 < G < 800 kg/m^2\text{-}s$ in small quality increments over entire vapor-liquid region. For supercritical tests, local heat transfer coefficients and pressure drops were measured for the same mass flux range as in the condensation tests for temperatures ranging from 30 – 110°C. The heat transfer coefficients uncertainties in this study varied between 7.7 to 14%, whereas the pressure drop uncertainties were 1.9%, except at extremely low mass fluxes ($G = 200 kg/m^2\text{-}s$). For both phase-change condensation and supercritical cooling, frictional pressure gradients were calculated by separating the deceleration component due to momentum change from the measured pressure gradients.

Condensation heat transfer coefficients and pressure drops increased with quality and mass flux. The effect of reduced pressure on heat transfer is not very significant, while this effect is more pronounced on the pressure gradient. The flow regime transition criteria of Coleman and Garimella (2003) were used to initially designate the prevailing flow regimes for a given combination of mass flux and quality. The condensation data collected in the present study were primarily in the wavy and annular flow regimes.

During supercritical cooling, the sharp variations in thermophysical properties in the vicinity of the critical temperature resulted in sharp peaks in the heat transfer coefficients and sudden jumps in the pressure drop. Based on the characteristics of the specific work of thermal expansion (contraction), the data from the supercritical tests were grouped into three regimes: liquid-like, pseudo-critical transition and gas-like regimes.

Flow regime-based heat transfer and pressure drop models were developed for both condensation and supercritical cooling. For condensation, the overall heat transfer model predicts 98% of the data within ±15% while the overall pressure drop model predicts 87% of the data within ±15%. For supercritical cooling, the heat transfer model predicted 88% of the data within ±25% while the pressure gradient model predicts 84% of the data within ±25%.

CHAPTER 1 INTRODUCTION

The objective of this study is to investigate near-critical pressure heat transfer and pressure drop of low-critical-temperature refrigerant blend R410A during cooling. The need for this study arises from the recent interest in vapor-compression systems for high temperature-lift space-conditioning and water heating applications, and concerns about the depleting stratospheric ozone levels. This chapter provides a brief discussion of the significance of this research and its importance to the air-conditioning and refrigeration industry.

1.1 Need for Refrigerant Blend R410A

The ozone layer in the stratosphere acts as a shield to protect us from the harmful effects of ultraviolet light by absorbing much of it. Ozone is created by collisions of oxygen molecules (O_2) and oxygen atoms (O) and destroyed by similar collisions of O_3 molecules and O atoms, resulting in pairs of O_2 molecules. It is believed that, due to the extraordinary stability of CFC compounds, CFCs are contributing to the deterioration of the ozone layer. CFC (Chlorofluorocarbon) molecules are made of chlorine, fluorine, and carbon, while HCFC (Hydrochlorofluorocarbon) molecules also have hydrogen atoms attached. These compounds do not break down in the lower atmosphere. Furthermore, although heavier than air, traces of CFCs have been found in the upper atmosphere (stratosphere) and predicted to last for 100 years or more due to their high stability. However, once affected by ultraviolet radiation, these CFC traces slowly decompose and release chlorine (Cl_2). Since ozone is an oxidizer, with the presence of sunlight, chlorine catalytically decomposes ozone, and forms chlorine oxide (which is unstable) and oxygen. The unstable chlorine oxide then breaks down to again form

chlorine and oxygen. This process keeps repeatedly attacking the ozone and causes ozone destruction to happen faster than ozone creation. This depletion of the ozone layer due to the release of chlorine from CFC and HCFC refrigerants has raised serious concerns about using them in vapor compression systems. These concerns led to the Montreal Protocol in 1987. Based on the amended version of the protocol, CFCs were phased out by January 1996, except for essential users, and HCFCs are to be eliminated by 2020. This generates a need for the investigation of zero ozone-depletion-potential (ODP) refrigerants or refrigerant blends with properties similar to CFCs and HCFCs to be used as replacements in existing systems and also for the design of newer air-conditioning and refrigeration systems. R410A is among this newer brand of refrigerant blends, with zero ODP. R410A is an azeotropic mixture of equal proportion by mass of HFC refrigerants R32 (CH2F2, difluoromethane) and R125 (HF2C-CF3, pentafluoroethane) with properties similar to those of HCFC R22. (An azeotropic blend is a mixture of two or more refrigerants with similar boiling points and acts like a single fluid. Azeotropic blends do not have a temperature glide: the temperature difference between the vapor and liquid state during evaporation or condensation at constant pressure. Near-azeotropic mixtures have small temperature glides, while zeotropic mixtures have larger temperature glides than 5°C.) Hydrofluorocarbons (HFCs) are made of hydrogen, fluorine, and carbon atoms. Because they have no chlorine, they do not interact with the ozone layer once they break down. Therefore, R410A is benign to the ozone layer. Also R410A is particularly chosen for this study due to its usage as a replacement fluid in space-conditioning and refrigeration applications and the lack of

systematic information about its heat transfer and pressure drop characteristics at high reduced pressures.

1.2 High Temperature Lift Systems

To achieve the desired heat rejection temperatures for high temperature-lift space-conditioning and water heating applications, the refrigerant blend R-410A must either be condensed at pressures close to its critical pressure, or cooled at pressures exceeding its critical pressure. The critical temperature and pressure of R410A are 71.36°C and 4903 kPa respectively. In comparison, the critical temperature and pressure for R22 are 96.15°C and 4990 kPa, respectively (Lemmon *et al.*, 2002). Table 1.1 shows the liquid and vapor-phase properties of R410A and R22 at representative saturation temperatures of 35 and 50°C. Phase change at such near-critical pressures in refrigerant blends is not well understood. While it is known that heat transfer coefficients and pressure drop in convective condensation are strong functions of vapor quality, few predictive methods are reported in the literature for refrigerant blends at near-critical pressures.

Quasi single-phase gas cooling above critical pressures is accompanied by sharp changes in fluid properties such as specific heat in the vicinity of the vapor-liquid dome

Table 1.1 Representative Phase Change Properties of R410A and R22

Fluid	h_{fg}	ρ_l	ρ_v	$\mu_l \times 10^6$	$\mu_v \times 10^6$	$C_{p,l}$	$C_{p,v}$	k_l	k_v
	kJ/kg	kg/m^3		kg/m-s		kJ/kg-K		W/m-K	
$T_{sat} = 35^oC$									
R410A	169.1	1006	88.46	105.7	15.43	1.841	1.671	0.089	0.018
R22	172.3	1150	57.99	146.92	13.01	1.308	0.949	0.079	0.012
$T_{sat} = 50^oC$									
R410A	136.2	908	140.4	83.89	17.41	2.249	2.391	0.080	0.024
R22	154.2	1082	85.95	122.96	13.95	1.419	1.113	0.072	0.014

(Figure 1.1), as the fluid experiences a gas-like to liquid-like transition. The heat transfer coefficients and pressure drops during cooling are expected to vary substantially along the length of the heat exchanger because of the sharp spikes in specific heat and rise in density and viscosity during gas-like to liquid-like transition. In addition, fluid property variations from the bulk temperature to the tube surface temperature assume much greater significance. For example, Shitsman (1963), Krasnoshchekov *et al.* (1970) and Tanaka *et al.* (1971), have reported that in supercritical cooling of carbon dioxide, when the bulk fluid is above the critical temperature, and the tube wall temperature is below the critical point, there is an improvement in the heat transfer coefficient.

1.3 Objectives of the Present Study

As discussed above, heat transfer and pressure drop are strong functions of vapor

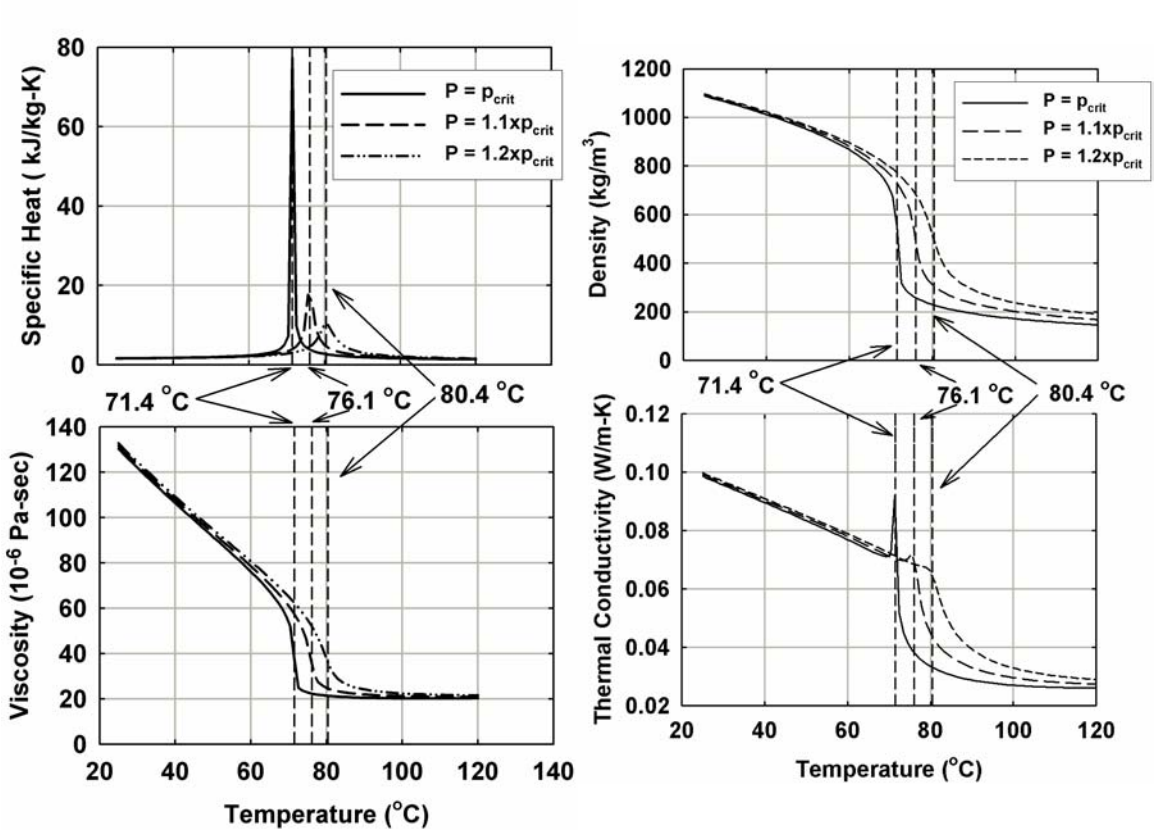

Figure 1.1 R410A Properties at and above Critical Pressure

quality and mass flux in convective condensation, and are expected to be affected significantly by sharp changes in fluid properties at supercritical pressures. However, few studies and predictive methods are reported for refrigerant blends at such near-critical and supercritical pressures. Much of the literature available for predicting condensation heat transfer and pressure drop is at relatively low operating pressures, and the validity of extrapolating these models to near-critical pressures is not well established. Similarly, much of the available literature on supercritical heat transfer and pressure drop is focused on pure fluids such as steam or carbon dioxide with properties different from those of R410A (Table 1.2). Also most of the studies are on supercritical heating. Therefore, the present study attempts to provide a thorough understanding, through careful experiments and analyses, of heat transfer and pressure drop characteristics during condensation at near-critical pressures and supercritical cooling of the refrigerant blend R410A. The

Table 1.2 Representative Phase Change Properties of R410A, Carbon Dioxide and Steam at Critical Pressure

Fluid	Temperature °C	Pressure kPa	ρ kg/m^3	$\mu \times 10^6$ kg/m-s	C_p kJ/kg-K	k W/m-K	Pr
Liquid-Like							
R410A	30	4903	1064	1.22E-04	1.65	0.096	2.10
CO_2	0	7377	959	1.09E-04	2.28	0.117	2.11
Steam	250	22064	818	1.11E-04	4.67	0.643	0.81
Pseudo-Critical Transition							
R410A	71	4903	637	4.80E-05	12.75	0.074	8.26
CO_2	31	7377	575	4.20E-05	39.17	0.097	17.05
Steam	374	22064	391	4.69E-05	214.60	0.528	19.04
Gas-Like							
R410A	120	4903	146	2.04E-05	1.37	0.026	1.07
CO_2	80	7377	144	1.96E-05	1.42	0.027	1.03
Steam	620	22064	59	3.49E-05	2.80	0.102	0.96

models resulting from this research are expected to provide tools essential for the design of condensers/gas coolers for high-temperature-lift vapor-compression systems. The objectives and major tasks of this project are as follows:

- Experimentally determine local (over small quality change; typically $\Delta x < 0.2$) condensation heat transfer coefficients and pressure drops of R410A in smooth round tubes at pressures 80 and 90% of the critical pressure for the mass flux range $200 < G < 800$ kg/m^2-s over the entire quality range. The tests are conducted in commercially available smooth round copper tubes of 9.4 and 6.2 mm I.D.
- Experimentally determine the quasi single-phase (in small temperature increments) heat transfer coefficients and pressure drops of R410A in smooth round tubes at $p = p_{critical}$, $1.1 \times p_{critical}$, and $1.2 \times p_{critical}$ for $200 < G < 800$ kg/m^2-s over a temperature range of 30 to 120°C. The temperature intervals are chosen to track the steep changes in supercritical heat transfer and pressure drop phenomena with a high resolution.
- Compare the data with the limited local condensation and supercritical heat transfer and pressure drop correlations in the literature, and provide explanations for agreement/disagreement of the existing models with the present data. These comparisons are used to understand and identify the most significant parameters and phenomena that influence heat transfer and pressure drop, and also to explain the shortcomings in the existing models.

- Develop flow mechanism-based condensation and quasi single-phase heat transfer and pressure drop models from the data collected in the present study in terms of dimensionless flow, property, and geometric parameters.
- The conditions investigated in this study are summarized in Table 1.3. The wide range of test conditions at various pressures and tube diameters yield models that capture the relevant physical phenomena accurately.

Table 1.3 Test Conditions

	Two-Phase	Critical/Supercritical
Tube Size	9.4, 6.2 mm I.D.	9.4, 6.2 mm I.D.
Pressure	3922, 4413 kPa	4903, 5393, 5883 kPa
Temperature	~61.1, 66.6°C	30-110°C
Mass Flux	200-800 kg/m^2-s	200-800 kg/m^2-s
Quality	0-1	----

1.4 Organization of the Dissertation

The organization of the dissertation is as follows. Chapter 2 provides a review of the literature on condensation and supercritical heat transfer and pressure drop, and identifies the deficiencies in the understanding of these phenomena. The experimental set-up and procedures for determining condensation and supercritical heat transfer coefficients and pressure drops are described in Chapter 3. Data analysis and uncertainty analysis techniques are discussed in Chapter 4. Chapter 5 discusses the results of the condensation experiments, agreement/disagreement between the available models in the literature and the experimental data, and the development of local heat transfer and pressure drop models. Supercritical heat transfer and pressure drop experimental results are discussed in Chapter 6 along with the comparison with the literature and the development of the models. Chapter 7 provides the conclusions from this study and recommendations for further research.

CHAPTER 2 LITERATURE REVIEW

This chapter presents a review of the relevant literature on in-tube condensation and supercritical heat transfer and pressure drop. The approaches used in these studies are described, along with a discussion of the key results, models, and discrepancies between the results of different investigators. The chapter is broadly divided into two sections: in-tube condensation and supercritical heat transfer. The in-tube condensation part focuses on studies on flow regime mapping, heat transfer and pressure drop during two-phase flow and phase change of air-water mixtures and a variety of refrigerants in different tube sizes. The supercritical heat transfer part summarizes studies on heat transfer and pressure drop above the critical pressure.

2.1 Prior Investigations of In-Tube Condensation

2.1.1 Flow regimes

During in-tube condensation, the vapor and liquid are in simultaneous motion in a variety of flow mechanisms governed by phase flow velocities, properties, and tube geometry. These flow patterns provide a mechanism for transport of heat, and due to the different interactions between the vapor and liquid phases and the tube wall, affect the pressure drop. Based on such flow regime observations, condensation inside horizontal tubes has typically been treated as being governed by a combination of gravity forces and interfacial shear stresses, the relative contributions of which change with the geometry and fluid conditions. While the annular flow pattern is associated with high vapor shear stresses, stratifying and wavy flows appear when gravity forces dominate.

Taitel and Dukler (1976) developed theoretically derived flow regime transition criteria based on gas and liquid mass flow rates, properties of the fluids, pipe diameter

and angle of inclination. Their transition criteria divided two-phase flows into five different flow regimes: intermittent, stratified smooth, stratified wavy, dispersed bubble and annular with dispersed liquid flow. Various non-dimensional parameters for the transitions between these regimes were developed and these parameters were plotted against the Martinelli parameter to delineate the different flow patterns. The primary application of the Taitel and Dukler (1976) map, however, has been for air-water *two-phase* flow, as opposed to *phase-change* condensation, which is of interest here.

Breber *et al.* (1980) used refrigerants R11, R-12, R113, and steam and n-Pentane to develop a simplified flow map. They found that the ratio of shear-to-gravity forces and the ratio of vapor volume-to-liquid volume are the main parameters affecting flow patterns in horizontal tubes. Hence the flow regime domain in horizontal tubes was thought of as four quadrants on a two-dimensional map with the y-axis as a function of the ratio of shear-to-gravity forces, and the x-axis as a function of the liquid volume fraction. However, the true liquid volume fraction in the tube cannot be readily determined for all regimes because the slip between the two phases cannot be theoretically determined. Therefore, they replaced the volume fraction on the x-axis with the Martinelli parameter. Similarly, the ratio of the two forces for the y axis was found to be a function of the dimensionless gas velocity, which was therefore used as the ordinate. The resulting dimensionless gas velocity versus Martinelli parameter map was divided into 4 quadrants: Annular and Mist Annular, Bubble, Wavy and Stratified, and Slug and Plug flows. The authors also recommended the heat transfer coefficients to be used for each flow regime. The Taitel and Dukler (1976) flow regime map was also tested in this study with the condensation data bank, and good agreement was found for tube diameters

ranging from 4.8 mm to 22 mm I.D. However, for small diameter tubes, the agreement was not good. The investigators thought that the surface tension effect, which was not accounted for in the Taitel and Dukler (1976) map, had an important role in the discrepancies at the small diameters. They also noted that the Taitel and Dukler (1976) map showed excellent agreement and relatively good agreement for annular and stratified-wavy flows, respectively. However at high liquid loading, with Martinelli parameter greater than 0.5, the slug flow and the wavy flow boundaries were not well predicted. An empirical shift of those boundaries produced better results.

Tandon *et al.* (1985) conducted an experimental study of flow patterns during forced convective condensation for various compositions of a mixture of R22 and R12 inside horizontal tubes of 10 mm I.D. The flow patterns were divided into Annular flow, Semiannular flow, Wavy flow, Slug flow and Plug flow. Several flow maps, including the Breber *et al.* (1980) map, were compared with their data. They considered the Breber *et al.* (1980) map to be similar to the Taitel and Dukler (1976) map with modified flow pattern boundaries based on condensation data for pure refrigerants. They found that the annular and slug flow data were predicted well by the Breber *et al.* (1980) map; however, semi-annular and wavy flow data were not predicted well.

Dobson and Chato (1998) studied heat transfer and flow regimes during condensation of refrigerants R12, R22, R32/R125 and R134a in horizontal tubes ranging from 3.14 to 7.04 mm I.D., and $0.21 < p_r < 0.57$. The authors broadly classified the flow regimes into two categories, those that occur at low void fractions, and those at high void fractions. Stratified flow, wavy flow, wavy-annular flow, annular flow and annular-mist flow were in the first category, whereas slug, plug and bubbly flow belonged to the

second category. In the first category, stratified and wavy flows were considered to be gravity dominated, whereas annular and annular-mist flows were considered to be shear-dominated. Transitions in the second category of flow regimes were determined by amount of liquid present in the two-phase flow. In addition to shear and gravity forces, the mass flux, quality, fluid properties, tube diameter and surface tension also affected the flow regimes for smaller diameter tubes. They observed smooth stratified flow over the entire range of qualities at an extremely low mass flux of G = 25 kg/m^2-s. As mass flux was increased to G = 75 kg/m^2-s, interfacial waves developed and wavy flow was observed for the entire quality range. The flow regimes were not affected by changes in diameter or refrigerant for these mass fluxes. As the mass flux increased to G = 150 and 300 kg/m^2-s, several different flow regimes were observed. As the quality was increased, wavy flow followed by wavy-annular and annular flow was observed. At high mass fluxes, the flow regimes included slug flow at low qualities followed by wavy-annular, annular, and annular-mist flow as the quality was increased. The fluid properties and tube diameters played a secondary role in the flow regime determination, with their influence mostly seen at intermediate mass fluxes of G = 150 to 300 kg/m^2-s. The fluid properties that affected the flow regimes were the vapor and liquid densities, viscosities, the ratio between the two quantities, and surface tension. They compared their data with those of Mandhane *et al.* (1974) , the Taitel and Dukler (1976) map, and the Soliman (1982; 1986) transition criteria. They found that the Mandhane *et al.* (1974) map exhibited considerable differences from their data, and the Taitel and Dukler (1976) map had success only with the annular flow data. However, the agreement with the Mandhane *et al.* (1974) map improved considerably when the superficial vapor velocity axis was

transformed using square root of vapor to air density ratio multiplier ($\sqrt{\rho_g / \rho_a}$). The Soliman (1982; 1986) transition criteria for wavy or slug flow to annular flow, and annular flow to mist flow were found to agree better with the data. The authors used the Soliman (1982) modified Froude number (Equation 2.1), which is the ratio between inertial and gravitational forces, to define their flow regimes.

$$Fr_{so} = \begin{cases} 0.025 \cdot Re_l^{1.59} \left[\frac{1 + 1.09 X_{tt}^{0.039}}{X_{tt}} \right]^{1.5} \frac{1}{Ga^{0.5}} & \cdots \; Re_l \le 1250 \\ 1.26 \cdot Re_l^{1.04} \left[\frac{1 + 1.09 X_{tt}^{0.039}}{X_{tt}} \right]^{1.5} \frac{1}{Ga^{0.5}} & \cdots \; Re_l > 1250 \end{cases} \tag{2.1}$$

For the purpose of heat transfer model development (discussed in section 2.1.2), they divided the various flow regimes into annular or non-annular groups. The delineation of these two groups of flow regimes was based on either a Soliman (1982) modified Froude number of 20, or a mass flux of G = 500 kg/m^2-s.

Ewing *et al.* (1999) conducted flow visualization experiments on horizontal two-phase flow patterns in a transparent circular channel of 19 mm I.D. using adiabatic mixtures of air and water. Their data agreed with the Breber *et al.* (1980) map in general, but there were some deviations in the transitions from wavy and stratified to slug and plug flow, and between slug and plug to bubbly flow.

Coleman (2000) and Coleman and Garimella (2000b; 2000a; 2003) developed flow regime maps for condensation of R134a in round, square and rectangular tubes ($1 < d_h < 5$ mm) over the mass flux range $150 < G < 750$ kg/m^2-s. Based on the analysis of condensation video frames, they classified the flow into intermittent, wavy, annular and dispersed flow regimes. Each flow regime was further subdivided into flow patterns

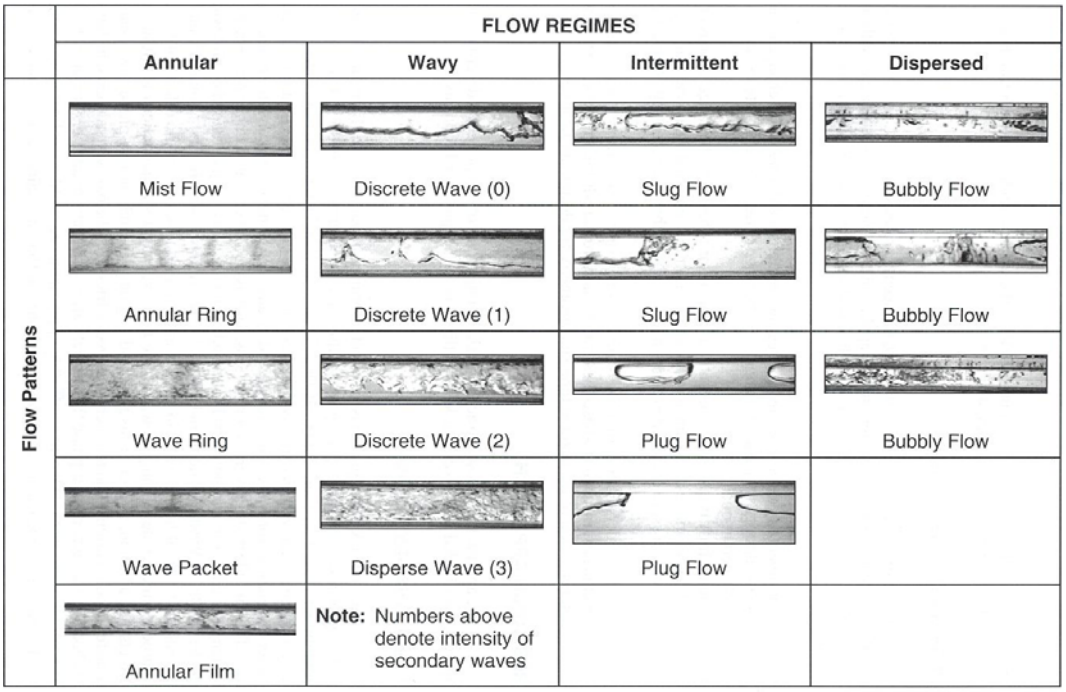

Figure 2.1 Flow Regime Classification of Coleman and Garimella (2003)

within these regimes to provide a more precise description of the flow mechanisms as shown in Figure 2.1. They found that in the annular flow regime, a liquid film coats the circumference of the wall, and the vapor flows through the core with or without liquid droplet entrainment. The wavy flow regime was subdivided into two categories: discrete wave flow and disperse wave flow. In discrete-wave flow, the liquid flows primarily on the bottom of the tube, while the vapor flows above a wavy vapor-liquid interface. They emphasized that even in this regime, a thin liquid film exists around the vapor at the top of the tube. Disperse-wave flow is characterized by a large number of secondary waves with no dominant wavelength or amplitude. As the gas velocity increases in wavy flow, the interface becomes more unstable and the intensity of the waves increase until disperse-wave flow is achieved. The mist-flow pattern is characterized by a uniform vapor mist with liquid droplets entrained in the vapor. This flow pattern does not have a

clearly discernible film. The intermittent flow regime is characterized by discontinuities in the liquid and vapor phases, with vapor plugs or slugs surrounded by a liquid film and interrupted by alternating slugs of liquid. They also developed transition criteria between these various regimes and patterns for each of the tube geometries investigated.

El Hajal *et al.* (2003) and Thome *et al.* (2003) developed a flow pattern map for condensation based on an earlier evaporation flow regime map developed by their research group (Kattan *et al.*, 1998b, a, c). They classified the flow into fully-stratified, stratified-wavy, intermittent, annular, mist and bubbly flow regimes. The maps consist of flow regime transition curves that delineate one flow pattern from another on mass flux versus quality graphs (it should be noted that the transition curves are implicit equations with respect to mass flux). The void fraction for high reduced pressures is estimated using the homogeneous model, and at low pressures using the Rouhani-Axelsson (1970) void fraction equation. They combine these equations using a logarithmic mean technique to obtain the void fraction over a wide range of reduced pressures. The logarithmic void fraction equation was validated by comparing heat transfer predictions for annular flow from several different researchers. The range of applicability of this map is as follows: $16 < G < 1532$ kg/m^2-s, $3.14 < d < 21.4$ mm, $0.02 < p_r < 0.8$, $76 < (We/Fr)_L < 884$.

2.1.2 Heat Transfer

Condensation inside horizontal tubes is governed by a combination of gravity forces and interfacial shear stresses, the relative contributions of which change with the geometry and fluid conditions. For smaller diameter tubes, surface tension forces also play an increasing role, as demonstrated by Coleman and Garimella (2000a; 2003). While

the annular flow pattern is associated with high vapor shear stresses, stratified and wavy flows appear when gravity forces dominate.

Many of the widely used condensation heat transfer correlations were developed for annular flow. Traviss *et al.* (1973) proposed an annular flow model by applying the momentum and heat transfer analogy using the von Karman universal velocity distribution to describe the liquid film. Assuming the liquid film is thin over the tube length, a flat plate approximation could be used for the liquid film. The interfacial shear stress was assumed to be approximately equal to the wall shear stress. By assuming the turbulent Prandtl number was unity and the heat flux at the interface was approximately equal to the wall heat flux, the heat transfer equation was represented as a function of turbulent film thickness, which in turn is a function of the liquid Reynolds number. The results were compared with experimental data on R12 and R22 in an 8 mm ID tube. The experiments were conducted at mass fluxes ranging from 161 – 1532 kg/m^2-s, and at saturation temperatures between 25 and 58°C. They found good agreement between the predictions and the data for qualities as low as 0.1. For qualities less than 0.1, a linear extrapolation between the model and a single-phase heat transfer correlation was found to yield good results. For higher qualities at which $X_{tt} < 0.16$ and mist flow is expected, the authors raised the power of the function of X_{tt} ($F(X_{tt})$) from 1 to 1.15 for better predictions.

Shah (1979) developed a correlation for film condensation inside tubes based on his previous work on evaporative heat transfer (Shah, 1976). He argued that, as long as the entire tube surface remains wetted, the mechanisms for heat transfer during film condensation were similar to evaporation without nucleate boiling. Similar to his

evaporation correlation, he developed a new two-phase multiplier using a large set of condensation data (473 data points from 21 independent experimental studies). The fluids included R-11, R-12, R-22, R-113, water, methanol, ethanol, benzene, toluene, and trichloroethylene condensing inside tubes as well as an annulus with various tube orientations. The parameter ranges were as follows: $11 < G < 211$ kg/m^2-s, $7 < d < 40$ mm, $0.002 < p_r < 0.44$. He noted that the application of this model should be restricted to the operating ranges of the data considered, and for $1 < Pr_l < 13$. The model is also restricted to $Re_l > 350$ due to limited data at lower Re_l values. This correlation was found to predict all the data considered with a mean deviation of 17%.

Kosky and Staub (1971) studied annular flow condensation of steam inside a horizontal 12.57 mm copper tube at 20 – 152 kPa. The mass flux range covered was 2.712 – 149.2 kg/m^2-s. Assuming the film is thin and smooth, and entrainment is negligible, they proposed an analytical model based on the modified Martinelli analogy (Martinelli, 1947) between heat and momentum transfer in turbulent flow to calculate the thermal resistance of a flowing film of condensate. They suggested that the annular flow heat transfer coefficient could be related to the frictional pressure gradient through the shear velocity. In their study, an empirical pressure drop relation was used to fit their own data, and data from an independent investigation. The model was developed for annular flow and therefore the tube orientation is irrelevant, provided that there is sufficient vapor shear at the liquid-vapor interface to maintain annular flow.

Jaster and Kosky (1976) used data from Kosky and Staub (1971) supplemented by additional measurements in the annular-stratified transition and fully stratified flow regimes. For the mass flux range 12.6 – 145 kg/m^2-s, they observed three different flow

regimes: annular, annular-stratified transition and stratified. They suggested that the annular-to-stratified transition was a function of the ratio of axial shear force to gravitational body force, F. Thus, for $F < 5$, the flow was considered to be stratified flow. For $F > 29$, the flow was considered annular. A transition region between annular and stratified flow was defined as $5 < F < 29$. They also presented heat transfer correlations for annular and stratified flow. For fully annular flow, the heat transfer was governed by boundary layers whose thermal resistance could be found using the Martinelli analogy as modified in Kosky and Staub (1971). Assuming the heat transfer in the liquid pool is negligible, a simplified model from Rufer and Kezios (1966) was suggested for the fully stratified flow. For the transition region between fully annular and stratified flow, they suggested that a linear interpolation was a good approximation. The comparison between the experiments and predictions showed that the errors were of the same order of magnitude as those of the annular and stratified models.

Eckels and Pate (1991) conducted condensation heat transfer experiments on R134a and R12 for $30 < T_{sat} < 50°C$ and $125 < G < 400$ kg/m^2-s. *Average* heat transfer coefficients (over a quality change of 90% to 10%) were measured, and were found to decrease with an increase in temperature (saturation pressure). They found that heat transfer coefficients for R134a were higher than those for R-12.

Singh *et al.* (1996) measured local condensation heat transfer coefficients for R134A for $50 < G < 300$ kg/m^2-s at 35°C in a smooth tube of 12.7 mm O.D. They classified their data into annular, wavy to annular transition and stratified-wavy flow regimes. A strong dependence of heat transfer coefficient on the mass flux was found in the wavy-annular and annular regimes. However, the dependence was lower in the low

mass flux and high heat flux region (generally wavy-stratified flow) due to an increased condensate thickness. They developed an empirical model for heat transfer coefficients during condensation for stratified-wavy flow by assuming that the heat transfer in the top part of the tube is due to film condensation and that in the bottom part is due to forced convection through the condensate layer. For film condensation, they used the correlation proposed by Chato (1962) for condensation inside horizontal smooth tubes. For the forced convection part, they used the single phase liquid heat transfer coefficient with a multiplier that was a function of the Martinelli parameter. The single-phase liquid heat transfer coefficient was calculated using the Gnielinski (1976) correlation for $Re_l > 2300$ and a modified form of the Dittus-Boelter correlation for $Re_l \leq 2300$. The predictions using the above approach were within ±7.5% of the data.

More recent attempts at modeling condensation heat transfer in pure fluids and blends have yielded correlations that are based on the specific flow pattern that exists for the applicable conditions. Dobson and Chato (1998) conducted flow visualization and heat transfer experiments on R12, R22, R134a and R32/R125 condensing at saturation temperatures between 35 and 45°C in smooth tubes for the diameter range $3.14 < d < 7.04$ mm. Stratified, wavy, wavy-annular, annular, annular-mist and slug flow regimes were observed. They found that mass flux and quality are the dominant factors in establishing the relevant flow regime. They also reported that, at low mass fluxes (25 and 75 kg/m^2-s), the flow regime was not affected by tube diameter or refrigerant type, while at 150 and 300 kg/m^2-s, these parameters must be taken into account. They proposed a heat transfer correlations for annular and wavy flows, treating them as shear-dominated and gravity-dominated flow regimes, respectively. For the gravity driven

correlation, they argued that the heat transfer in the liquid pool might not be negligible at high mass flux and low quality situations due to the convective heat transfer in the bottom part of the tube. Thus they developed a wavy flow correlation that accounted for both film condensation and liquid pool forced convection. The shear driven correlation was based on a two-phase multiplier approach, and agreed well with data from the literature. They suggested that for $G > 500$ kg/m^2-s, the annular flow correlation should be used; whereas for $G < 500$ kg/m^2-s, the annular flow correlation should be used for modified Froude numbers (as defined by Soliman (1982)), $Fr > 20$, and the wavy-stratified flow correlation should be used for $Fr < 20$. The applicability of this model by Dobson and Chato (1998) was extended for use with R407C by Sweeney (1996) , who proposed simple mass flux-based modifications to Dobson and Chato's annular and wavy Nusselt numbers. Boissieux *et al.* (2000) investigated condensation heat transfer for R404A, R407C, and Isceon 59 in a smooth horizontal tube (d = 9.5 mm), for $150 < G < 400$ kg/m^2-s, at saturation temperatures between 15°C and 35°C. They concluded that their test results were in good agreement with the correlations from Dobson and Chato (1998) and Shah (1979), and recommended that the Dobson and Chato correlation could be used for R404A.

Ebisu and Torikoshi (1998), Han and Lee (2001) and Cavallini *et al.* (2001; 2002b) investigated condensation heat transfer characteristics of the refrigerant blend R410A. For $150 < G < 300$ kg/m^2-s, a saturation temperature of 50°C, and $0.2 < x < 0.8$, Ebisu and Torikoshi (1998) found that the pressure drops for R410A were about 30% lower than those for R22. In addition, the heat transfer coefficients for R410A were also found to be lower than those for R22, particularly in the low quality region. They stated

that the heat transfer coefficients for $x > 0.4$ were in good agreement with the correlation developed by Haraguchi *et al.* (1994). Han and Lee (2001) conducted tests on R410A and R22 in 7 and 9.52 mm O.D. smooth and microfin tubes, and found that the heat transfer coefficients are slightly larger, and the pressure drops are slightly lower, for R410A than R22. They stated that their data for the 7 mm smooth tube were within ±30% of the values predicted by the correlations of Shah (1979), Traviss *et al.* (1973), and Cavallini and Zecchin (1974).

Kwon and Kim (2000) conducted an experimental and theoretical investigation of condensation heat transfer for R22 and R410A in smooth round tubes of 9.52 mm O.D. The experiments for determining local heat transfer coefficients were conducted at a saturation temperature of 31°C and mass fluxes of 97, 144, 202 kg/m^2-s. They developed an analytical model for annular flow including the effects of interfacial shear stress, liquid entrainment and turbulent eddy viscosity, and found good agreement with the heat transfer coefficient of R410A. In a later study, Kwon *et al.* (2001) presented the predictions of their model with and without liquid entrainment for condensation of refrigerant R22. The predictions for R22 were better than the predictions for R410A in the earlier paper.

Cavallini *et al.* (2001) measured heat transfer coefficients and pressure drops during condensation inside an 8 mm I.D. smooth tube with pure and nearly azeotropic HFC refrigerants for $30 < T_{sat} < 50$°C, $100 < G < 750$ kg/m^2-s, and $0.15 < x < 0.85$. The tests also covered a wide range of operating pressures as determined by the saturation conditions: low pressure (R236ea), mid-pressure (R134a, R22) and high pressure (R32, R125, R410A). In general, they found that at the same mass flux and quality, the high

pressure fluids have lower pressure drops, and recommended that the Friedel (1980) correlation should be used to compute the pressure drop, even though this correlation was found to slightly over predict the pressure drop for high pressure fluids. They found that the model by Kosky and Staub (1971) should be used for heat transfer in the annular flow regime, while the correlation proposed by Jaster and Kosky (1976) should be used for the stratified flow regime for R32, R125, and R410A. In a follow up paper (Cavallini *et al.*, 2002b) they compared their experimental heat transfer coefficient data and other independent experimental data collected by different researchers with several theoretical or semi-empirical condensation heat transfer models for annular and gravity dominated flows (Akers et al. (1959), Akers and Rosson (1960), Dobson and Chato (1998), Jaster and Kosky (1976), Haraguchi *et al.* (1994), Tang (1997), Shah (1979)). This comparison showed that quite a few of their data were outside the validity ranges for these models, especially for the high-pressure refrigerants such as R125, R32 and R410A. The correlation by Akers *et al.* (1959) was found to underestimate the heat transfer coefficient, while the subsequent model by Akers and Rosson (1960) overestimated the data for 3 mm tubes. For the most part, they found that the conditions of interest for high-pressure refrigerants fall outside the ranges of validity of the Cavallini and Zecchin (1974) equation and the Haraguchi *et al.* (1994) models. The Dobson and Chato (1998) model was found to strongly over-predict the heat transfer coefficients for the high-pressure fluids, particularly at the higher values of Nusselt number, although the predictions under wavy-stratified conditions were found to be better. Similarly, the Shah (1979) correlation also over-predicted the data for high-pressure fluids, whereas the Tang (1997) model yielded better predictions. Cavallini *et al.* (2002b) noted that Shah (1979)

and Tang (1997) models can only be applied to annular flow, and would not be appropriate for stratified, wavy-stratified and slug flow. Their overall conclusion, therefore, was that either the available models and correlations do not address the conditions of interest for high-pressure refrigerants, or, even if the stated range of applicability is adequate, the resulting predictions are considerably different from the measured values for these fluids.

Based on the above observations, Cavallini *et al.* (2002b) proposed a new model for condensation heat transfer and pressure drop for pure fluids and refrigerant blends, notably including the high-pressure fluids. They used their own data and those of other researchers to develop three submodels to include annular flow, annular-stratified transition and stratified flow, and stratified-slug transition and slug flow. The transition criteria between different flow regimes were based on dimensionless vapor velocity J_G and Martinelli parameter X_{tt}. Thus, for $J_G > 2.5$, they suggested that the annular flow model be used. For $J_G < 2.5$, when $X_{tt} < 1.6$, the annular-stratified flow transition and stratified flow model is applicable, while for $X_{tt} > 1.6$, the stratified-slug and slug flow model is recommended. The annular flow model was based on the theoretical model of Kosky and Staub (1971), in which the heat transfer coefficient is related to the frictional pressure gradient (based on the Friedel (1979) correlation) through the interfacial shear stress. The stratified model accounted for the Nusselt type condensation in the upper region, and a convective term that computed the liquid pool heat transfer at the bottom of the tube. The heat transfer coefficient for slug flow was calculated with a two-phase multiplier applied to the corresponding single-phase heat transfer coefficient. The model yielded excellent agreement with their own data as well as those of many other

investigators, and was recommended for halogenated refrigerants in tubes with $3 < D < 21$ mm, $p_r < 0.75$, and $\rho_L/\rho_G > 4$. However, as pointed out in Cavallini *et al.* (2002a), the slug flow model does not smoothly approach the heat transfer coefficient calculated from the annular-stratified flow transition and stratified flow model, resulting in some cases in abrupt jumps in the predicted heat transfer coefficients as vapor quality varies. Therefore, Cavallini *et al.* (2002a) suggested that, when $J_G < 2.5$ and $X_{tt} > 1.6$, the heat transfer coefficient should be calculated as a linear interpolation between the coefficient calculated at $X_{tt} = 1.6$ and the coefficient obtained if the entire flow was liquid flow only.

El Hajal *et al.* (2003) and Thome *et al.* (2003) in the second part (first part discussed in section 2.1.1) of their two-part paper developed models to predict local heat transfer coefficient data from various sources for $24 < G < 1022$ kg/m^2-s, $0.02 < p_r < 0.8$, $0.03 < x < 0.97$, and $3.1 < d < 21.4$ mm. The flow regimes identified by the authors in the first part of the paper are grouped into annular type flow (includes annular, mist and intermittent flow), stratified-wavy and fully stratified flow. Annular flow is considered to be governed by convective condensation, whereas stratified and stratified-wavy flows are considered to be composed of both film and convective condensation, with the relative contribution determined by the angle subtended by the liquid pool at the bottom of the tube. Film condensation is modeled using Nusselt falling film theory on the inside of the tube (similar to Dobson and Chato (1998)). For the convective condensation part, the authors rearranged the liquid pool in the tube to have uniform thickness, and a turbulent film equation similar to the Dittus-Boelter equation is used with appropriate correction factors to take into account the interfacial waves. With the above formulation, the authors found that 85% of the data were predicted within ±20%.

In a recent review paper, Cavallini *et al.* (2003) presented the available experimental data for new ozone-friendly refrigerants with well-established heat transfer prediction models. The authors stated that, according to Cavallini *et al.* (2001), the heat transfer coefficient in the stratified flow regime was affected by the wall-saturation temperature difference (T_s-T_w), while the heat transfer coefficient for annular flow only varied with mass flux, quality and saturation temperature. According to their review of the literature, for annular flow, semi-empirical models from Shah (1979), Kosky and Staub (1971), Traviss *et al.* (1973), Tang (1997), Cavallini and Zecchin (1971; 1974) and Boyko and Kruzhilin (1967) are available. For stratified flow, heat transfer through the thin film is often analyzed by Nusselt theory (Nusselt, 1916). Jaster and Kosky (1976) suggested that the heat transfer in the liquid pool may be neglected compared to the film condensation. However, as discussed by Dobson and Chato (1998), the convection in the liquid pool may be substantial and could not be neglected at high mass fluxes. Dobson and Chato (1998) and Haraguchi *et al.* (1994) also proposed heat transfer models that cover both annular and stratified-wavy flow. The model proposed by Cavallini *et al.* (2002b) covers annular, stratified-wavy and slug flow. This model was developed from a large data bank and could be used for in-tube condensation of halogenated refrigerants with $3 < D < 21$ mm, $P_r < 0.75$, and $\rho_L/\rho_G > 4$. They also compared the experimental data from Cavallini *et al.* (2001) with the models by Cavallini *et al.* (2002b), Shah (1979) and Dobson and Chato (1998) for R134a, R22, R410A and R32 in a 8 mm smooth tube. It was shown that the model by Cavallini *et al.* (2002b) resulted in lower heat transfer coefficients while the models by Shah (1979) and Dobson and Chato (1998) strongly

over predict the data. The model by Haraguchi *et al.* (1994) was not applicable for most of the conditions considered.

2.1.3 Pressure drop

The frictional pressure drop during condensation in a uniform horizontal tube is due to the resistance to flow imposed by the walls of the tube on the respective phases and the interactions between the two phases. To calculate this frictional component of the pressure drop, the quantities that must be known include the flow rates of the liquid and vapor, the nature of flow of each phase (e.g., laminar or turbulent), the area of the tube wetted by each phase, the cross section of tube occupied by each phase, and the nature of interactions between the phases. However, often, one or more of these parameters are not known to an adequate degree, primarily due to the difficulty in fully describing (quantitatively) the respective flow mechanisms at the different operating conditions. Because of this, investigators have developed methods to reference the two-phase pressure drop to the corresponding single-phase pressure drop through the use of two phase multipliers as follows:

$$\phi_L{}^2 = \frac{(dP_f / dz)}{(dP_f / dz)_L} \tag{2.2}$$

$$\phi_G{}^2 = \frac{(dP_f / dz)}{(dP_f / dz)_G} \tag{2.3}$$

$$\phi_{LO}{}^2 = \frac{(dP_f / dz)}{(dP_f / dz)_{LO}} \tag{2.4}$$

$$\phi_{GO}{}^2 = \frac{(dP_f / dz)}{(dP_f / dz)_{GO}} \tag{2.5}$$

where subscripts L, G, LO and GO refer to the flow of the liquid phase alone in the channel, vapor phase alone, total flow having liquid properties, and total flow having vapor properties, respectively.

Also during condensation, the vapor (generally at a higher velocity due to the low density) condenses to liquid (generally at a lower velocity). This causes an overall decrease in the velocity of the flow, leading to a deceleration pressure rise. This pressure rise acts in a direction opposite to that of the frictional pressure drop, thereby reducing the overall pressure drop. The deceleration component is obtained from the force-momentum balance of the flow in the axial direction as follows:

$$\left|\frac{dP_d}{dz}\right| = \left|\left(\frac{1}{A}\right)\cdot\frac{d}{dz}\left[\frac{G^2\cdot x^2\cdot A}{\rho_v\cdot\alpha}+\frac{G^2\cdot(1-x)^2\cdot A}{\rho_l\cdot(1-\alpha)}\right]\right| \qquad (2.6)$$

An appropriate void fraction (α) model is required to enable this computation. The overall pressure drop during condensation is given by:

$$\left|(dP/dz)\right| = \left|(dP_f/dz)\right| - \left|(dP_d/dz)\right| \qquad (2.7)$$

The classical correlation for two-phase frictional pressure drop in tubes is that of Lockhart and Martinelli (1949), who related ϕ_G and ϕ_L to the parameter X, defined in the equations below:

$$X^2 = \frac{(dP_f/dz)_L}{(dP_f/dz)_G} \qquad (2.8)$$

$$\phi_L = \left(1+\frac{C}{X}+\frac{1}{X^2}\right)^{1/2} \qquad (2.9)$$

$$\phi_G = \left(1+CX+CX^2\right)^{1/2} \qquad (2.10)$$

where the constant C depends on the flow regimes (laminar or turbulent) associated with the flow of the vapor and the liquid alone in the tube. This model was developed for air, benzene, kerosene, water and various oils in tubes with diameter from 1.49 – 25.83 mm. However, the Lockhart-Martinelli correlations do not closely represent phase-change data and have large systematic errors. Also, they do not adequately represent the physical property effects. Since then, a large number of other correlations have been published. Most of them, such as models by Chisholm (1973) and Friedel (1979), can be regarded as simple data fits. The Chisholm (1973) correlation is :

$$\phi_{LO}^2 = 1 + [Y^2 - 1][Bx^{\frac{2-n}{2}}(1-x)^{\frac{2-n}{2}} + x^{2-n}] \tag{2.11}$$

where n is the power to which Re is raised in the single-phase friction factor (For example, n = 0.25 for Blausius equation). The parameter B is defined as a piecewise function of mass flux and parameter Y given by:

$$Y^2 = \frac{(dP/dz)_{f,GO}}{(dP/dz)_{f,LO}} \tag{2.12}$$

Based on a database of 25,000 points, Friedel (1979) proposed a two-phase multiplier correlation for ϕ_{LO} for upward vertical and horizontal flow in circular tubes as a function of vapor quality, mass flux, tube diameter and physical properties.

$$\phi_{LO}^2 = C_1 + \frac{3.24 C_2}{Fr^{0.045} We^{0.035}} \tag{2. 13}$$

where Fr and We are the Froude number and the Weber number, respectively.

$$Fr = \frac{G}{gD\rho_{tp}^2} \tag{2.14}$$

$$We = \frac{G^2 D}{\rho_{tp}\sigma} \tag{2.15}$$

$$C_1 = (1-x)^2 + x^2\left(\frac{\rho_l}{\rho_v}\right)\left(\frac{f_{GO}}{f_{LO}}\right) \tag{2.16}$$

$$C_2 = x^{0.78}(1-x)^{0.24}\left(\frac{\rho_l}{\rho_v}\right)^{0.91}\left(\frac{\mu_v}{\mu_l}\right)^{0.19}\left(1-\frac{\mu_v}{\mu_l}\right)^{0.7} \tag{2.17}$$

$$\rho_{tp} = \left(\frac{x}{\rho_v} + \frac{1-x}{\rho_l}\right)^{-1} \tag{2.18}$$

It should be noted that despite the complexity of the Friedel (1979) correlation, it showed considerable scatter when compared with the data bank he used (Hewitt *et al.*, 1994).

Recently, several researchers (Mishima and Hibiki, 1996; Tran *et al.*, 2000; Lee and Lee, 2001; Kawahara *et al.*, 2002) have developed pressure drop models for small diameter tubes by modifying the classical pressure drop correlations such as the Lockhart and Martinelli (1949) and Chisholm (1973) correlations. Mishima and Hibiki (1996) studied flow regime, void fraction, rise velocity of slug bubbles and frictional pressure loss for air-water flows in capillary tubes with inner diameters in the range from 1 to 4 mm. They found that the boundaries of the flow regimes were in good agreement with the model by Mishima and Ishii (1984), although flow regimes peculiar to a capillary tube (concentration of bubbles along tube axis, spiral train of small bubbles, etc) were also observed. They also found that, instead of being a constant, as the tube diameter decreases, the parameter C in the Lockhart and Martinelli (1949) model (Equation 2.9) decreases. Similar results were obtained by other researchers (Sugawara *et al.*, 1967; Mishima *et al.*, 1993) . Based on this observation, the authors proposed a correlation for C as a function of tube hydraulic diameter. The authors showed that for all the data considered except for those of ammonia-vapor flow, the prediction was within ±12%.

For ammonia-vapor flow, the error becomes ±25%. It should also be noted that the parameter C becomes zero when the hydraulic diameter is as small as 0.2 mm.

Lee and Lee (2001) studied two-phase pressure drop for air-water flow at atmospheric pressure through horizontal rectangular channels with small gaps between 0.4 to 4 mm, while the channel width was constant at 20 mm. The superficial air and water velocities ranged from 0.05-18.7 and 0.03-2.39 m/s, respectively. They suggested that the parameter C in the Lockhart and Martinelli (1949) model (Equation 2.9) could be expressed in terms of dimensionless parameters λ, ψ and Re_{LO} as follows:

$$C = A\lambda^{q}\psi^{r}\,Re_{LO}^{s} \tag{2.19}$$

$$\lambda = \frac{\mu_l^{2}}{\rho_l \sigma D} \tag{2.20}$$

$$\psi = \frac{\mu_l^{2} j}{\sigma} \tag{2.21}$$

where j is the liquid slug velocity. The constants A q, r and s were determined through data regression based on the applicable flow regime (laminar or turbulent) of the liquid and vapor phases. By comparing the model with their own experimental data, the authors concluded that the Lockhart and Martinelli (1949) model with a modified C parameter could cover a wide range of Martinelli parameters ($0.303 < X < 79.4$) and liquid-only Reynolds numbers ($175 < Re_{LO} < 17700$).

Kawahara *et al.* (2002) investigated two-phase pressure drop in a 100 μm diameter circular tube with superficial velocities of water and nitrogen gas at 0.02 – 4 and 0.1 – 60 m/s. They compared their data with a homogeneous flow model (homogeneous friction factor) with various two-phase viscosities available in the literature (McAdams, 1954; Cicchitti *et al.*, 1960; Owens, 1961; Dukler *et al.*, 1964; Beattie and Whalley,

1982; Lin *et al.*, 1991) and found the agreement was generally poor except for the model of Dukler *et al.* (1964) (within ±20%). They also compared their data with the two-phase multiplier models developed by Mishima and Hibiki (1996) and Lee and Lee (2001) and found significant improvement in predictions with an error band of ±10%.

Tran *et al.* (2000) studied pressure drops for R134a, R12 and R113 during phase-change inside three different tubes: two circular, 2.46 and 2.92 mm I.D. and one rectangular channel, 4.06×1.7 mm. The operating pressures ranged from 138 to 856 kPa. They proposed a new two-phase pressure drop model during flow boiling in small channels based on the Chisholm (1973) correlation. The B-coefficient in the Chisholm (1973) correlation was only a function of mass flux and parameter Y, but not the tube dimension and fluid properties. The authors argued that tube dimension and fluid surface tension were important factors in phase-change pressure drop, especially in refrigerants. Therefore, they suggested that, to better reflect the physics of flow boiling in small tubes, the B-coefficient should be replaced with a dimensionless number – confinement number, introduced by Cornwell and Kew (in (Pilavachi, 1993)),

$$N_{conf} = \frac{1}{D}\left[\frac{\sigma}{g(\rho_l - \rho_v)}\right]^{0.5} \tag{2.22}$$

They also included a constant C = 4.3 before the Y parameter to scale the difference in pressure gradient between small and large tubes. A comparison between the model and their own data showed that, most of the data were predicted within ±20%, and 93.8% of the data were predicted within ±30%.

Han and Lee (2001) studied pressure drop for R410A and R22 in smooth round tubes. They found that the pressure drop increased with a decrease in saturation

temperature due to the increase in specific volume of the vapor, which in turn increases the vapor velocity. They found that the pressure drops for R410A were 30 to 40% lower than those of R22 for all tubes under similar experimental conditions. This was attributed to the lower viscosity and specific volume of the R410A vapor. Ebisu and Torikoshi (1998) also found that for $150 < G < 300$ kg/m^2-s, saturation temperature of 50°C and $0.2 < x < 0.8$, the pressure drops for R410A were about 30% lower than those for R22 due to the larger vapor density of R410A.

Cavallini *et al.* (2001) conducted pressure drop experiments during condensation inside an 8 mm I.D. smooth tube with pure and nearly azeotropic HFC refrigerants R236ea, R134a, R22, R32, R125, R407C and R410A for $30 < T_{sat} < 50$°C and $100 < G < 750$ kg/m^2-s, over the entire vapor quality range. Using these data, Cavallini *et al.* (2002b) proposed a new flow regime-based pressure drop correlation that can be obtained from the momentum equation. They suggested that for the gas-phase non-dimensional superficial velocity $J_G \geq 2.5$, a modified version of the Friedel (1979) correlation can be used to compute the frictional pressure gradient, while for $J_G < 2.5$, the original Friedel (1979) correlation should be used.

2.2 Prior Investigations of Supercritical Heat Transfer and Pressure Drop

The flow of refrigerant at or above critical pressure is a quasi-single phase flow process, accompanied by significant property variations due to the temperature variation across the cross-section of flow. This abrupt property variation takes place across a temperature (defined in a subsequent section) known as the transition temperature. The transition temperature is unique for each supercritical pressure. As discussed in section 1.2 and shown in Figure 1.1 the property variations lead to a sharp peak in specific heat

and drop in viscosity and density at temperatures above the transition temperature. The peak in specific heat leads to a peak in local heat transfer coefficient in the vicinity of this region. The drop in density leads to increased flow velocities, thereby increasing the pressure drop. However, few predictive methods in the literature take into account these effects for refrigerant blends. Almost all the supercritical heat transfer and pressure drop papers have focused on steam or carbon dioxide.

Shitsman (1963; 1974) reported that supercritical carbon dioxide experiences a gas-like to liquid-like transition in fluid properties as the temperature is changed. These effects are crucial in determining the variation in heat transfer coefficients along the length of a heat exchanger. In addition, fluid property variations from the bulk temperature to the tube surface temperature could assume much greater significance. Shitsman (1963) , Krasnoshchekov *et al.* (1970) and Tanaka *et al.* (1971) observed that if the bulk fluid is above the critical temperature, and the tube wall is below the critical temperature, the heat transfer coefficient increases. Krasnoshchekov *et al.* (1970) attributed this to the formation of a lower temperature liquid-like layer near the wall of the tube. The liquid-like layer having a higher thermal conductivity than the bulk fluid increases the heat transfer coefficient. Based on this rationale, Krasnoshchekov *et al.* (1970) proposed a heat transfer model using the Petukhov-Popov-Kirilov Nusselt number equation with wall-to-bulk density and average-to-wall specific heat ratio corrections.

Ghajar and Asadi (1986) compared the existing empirical approaches for forced-convective heat transfer in the near-critical region. They concluded that the most significant discrepancy in existing correlations developed for forced convection when applied to the near-critical region may be due to the property variations, influences of

heat flux and buoyancy, and the differences in properties used by various investigators. Using a data bank from previous literature for water and carbon dioxide heating in the supercritical region, seven different types of forced convective heat transfer correlations were proposed. The data that they collected from the literature were for near-critical and supercritical heating of CO_2 and steam with reduced pressure range from 0.018 to 1.88. The heat fluxes for the database were from 0.8 to 1100 W/cm^2 for CO_2 and 18.7 to 2320 W/cm^2 for steam. The bulk-to-critical temperature ratio ranged from 0.43 to 1.31. The mass fluxes studied were from 1.7 to 300 kg/m^2-s. To compare the correlations based on the same physical property inputs, the constants proposed were determined by curve fitting the data based on revised values of the physical property inputs. Their results showed that the convective heat transfer in the supercritical region could be predicted by a Dittus-Boelter type equation combined with property ratio multipliers to account for the large property variations in this region as follows:

$$\mathrm{Nu_b} = \mathrm{a\,Re_b}^{\mathrm{e}}\,\mathrm{Pr_b}^{\mathrm{c}}\left(\frac{\rho_w}{\rho_b}\right)^{\mathrm{d}}\left(\frac{\overline{C}_p}{C_{pb}}\right)^{\mathrm{n}} \tag{2.23}$$

where subscripts w and b represent wall and bulk temperature, respectively, and a, c, d, and e are curve-fit constants for different fluids. $\overline{C}_p$ is the integrated mean specific heat, defined as a function of wall and bulk enthalpies and temperatures:

$$\overline{C}_p = \frac{h_w - h_b}{T_w - T_b} \tag{2.24}$$

The exponent n was proposed by Jackson and Fewster (1975):

$$n = \begin{cases} 0.4 & T_b < T_w < T_{crit} \text{ and } T_w > T_b \geq 1.2T_{crit} \\ 0.4 + 0.2(T_w / T_{crit} - 1) & T_b \leq T_{crit} < T_w \\ 0.4 + 0.2(T_w / T_{crit} - 1)[1 - 5(T_b / T_{crit} - 1)] & T_{crit} \leq T_b \leq 1.2T_{crit} \text{ and } T_b < T_w \end{cases} \tag{2.25}$$

Ghorbani-Tari and Ghajar (1985) investigated free convection in the near-critical region. They used a data bank for horizontal and vertical free convection of CO_2 and water, with Rayleigh number ranges from $0.2–1.04\times10^{13}$. They found that many free convective heat transfer correlations showed discrepancies when applied in the near-critical region. According to the authors, these discrepancies appeared to be due to 1) the reference temperature used for the evaluation of the physical properties, 2) the physical properties selected in reducing the dimensional experimental data to dimensionless variables, and 3) the differences in the values of the physical properties used in the literature. Five different types of free-convection heat transfer correlations were proposed. To compare the correlations based on the same physical property inputs, the constants proposed were determined by curve-fitting the data based on consistent values of the physical property inputs. For horizontal wires and vertical plates with a wide range of Rayleigh numbers, the authors proposed the following correlation.

$$Nu_\infty = a(Gr_\infty\, Pr_\infty)^b \left(\frac{\rho_w}{\rho_\infty}\right)^c \left(\frac{\overline{C}_p}{C_{p\infty}}\right)^d \left(\frac{k_w}{k_\infty}\right)^e \left(\frac{\mu_w}{\mu_\infty}\right)^f \tag{2.26}$$

where $\overline{C}_p$ is defined as in Equation (2.24), and a, b, c, d, e and f are curve-fit constants. The authors also found that when using the free-stream temperature to evaluate the fluid properties, the predictions were better. They argued that the effect of tube diameter was reduced if heat transfer coefficients were expressed as $hD^{0.25} = NukD^{-0.75}$.

Pitla *et al.* (1998) conducted a critical review of the literature on supercritical heat transfer for carbon dioxide. The review focused on studies of thermophysical properties in the supercritical region, factors influencing in-tube forced convection heat transfer, correlations for in-tube heat transfer and friction factor and numerical methods for the

calculation of supercritical heat transfer. From the review, they found that heat transfer is enhanced during supercritical cooling (due to the formation of a higher thermal conductivity liquid layer near the wall) and deteriorated during heating (conversely, due to the formation of a gas layer near the wall). The deterioration in heat transfer during heating became worse for pressures closer to the critical pressure, increase in heat flux, and substantial decrease of inlet enthalpy below the critical point. They also noted that at very low Reynolds number, buoyancy effects cause a secondary flow at the top of the horizontal tube causing enhancement in heat transfer at the bottom of the tube and deterioration at the top. They found that the most common method of correlating heat transfer or friction factor in supercritical flow was to use property corrections on single phase Nusselt number or friction factor correlations.

More recently, Pitla *et al.* (2001b; 2001a) conducted a combined experimental and numerical study of the heat transfer and pressure drop of in-tube cooling of carbon dioxide. The numerical model is based on the Favre-averaged, parabolized Navier-Stokes equations and an appropriate turbulence model. Favre decomposition was applied to the velocities and the enthalpy, and Reynolds decomposition was applied to thermophysical properties and pressure to account for the highly turbulent flow and large property variations. Both Nikuradse's mixing length model and the k-ε turbulence model were used and found to agree within ±1%. Simulations were performed for supercritical cooling of CO_2 inside a 4.52 mm tube with a constant wall temperature of 30°C. The length of the test tube was 2 m. The inlet temperature and pressure of the fluid were assumed to be 122°C and 10 MPa, respectively. The inlet fluid velocity was 9.65 m/s, corresponding to a Reynolds number of 3.2×10^5. The simulations showed that the heat

transfer coefficient decreases rapidly in the entrance region, but increases steadily after that. At the temperature corresponding to the pseudocritical temperature of CO_2, the heat transfer coefficient reaches a peak value which is mainly due to the peak in the bulk specific heat. Then, the heat transfer coefficient decreases sharply. The simulation also showed that the friction factor decreases as the fluid cools down and finally approaches a constant value corresponding to that of compressed liquid CO_2. They also conducted experiments to measure supercritical cooling of carbon dioxide inside a 4.72 mm I.D. tube at pressures ranging from 8 to 12 MPa ($0.71 - 1.11 \times p_{crit}$). The test fluid was cooled from 120°C to 25°C. The authors compared the numerical solutions with their experimental results and found that they were within ±10% of each other. The comparison therefore verified the accuracy of the numerical model. Based on the numerical solution, Pitla *et al.* (2002) proposed the following correlation for in-tube supercritical cooling of carbon dioxide.

$$Nu = \left(\frac{Nu_{wall} + Nu_{bulk}}{2} \right) \frac{k_{wall}}{k_{bulk}} \tag{2. 27}$$

where Nu_{wall} and Nu_{bulk} are evaluated using the Gnielinski (1976) correlation at the wall and bulk temperatures, respectively:

$$Nu = \frac{(f/8)(Re - 1000)\,Pr}{12.7(f/8)^{0.5}(Pr^{2/3} - 1) + 1.07} \tag{2.28}$$

The Petukhov (Incropera and DeWitt, 2002) correlation was used to evaluate the friction factor in the above equation. The authors found that the best results are obtained by using the inlet velocity to compute the Reynolds number at the wall irrespective of location, and by using the local mean velocity to compute the bulk Reynolds number.

In a two-part paper, Kurganov (1998a; 1998b) investigated the heat transfer and pressure drop of carbon dioxide under supercritical pressures in different tube diameters and orientations based on a series of experimental studies. In part I , he suggested that considering the drastic change in CO_2 properties near the critical region, it was advisable to divide the temperature (or enthalpy) into three regions based on the specific work of thermal expansion (defined below): liquid-like, pseudophase transition and gas-like states.

$$E_o = \left(\frac{P \partial V}{\partial h} \right)_P = \frac{P\beta}{\rho c_p} \tag{2.29}$$

In the liquid-like state, the behavior of the fluid is the same as that of a liquid. The change in properties is gradual and insignificant. In this region, E_o is of the order of 10^{-2}, which is typical for liquids. In the pseudophase transition region, the density and viscosity of the fluid decrease sharply, and the specific heat, Prandtl number, and volume expansion coefficient β pass through a maximum. In this region, E_o increases sharply. The steep rise in E_o begins when $E_o > 0.02–0.03$. Therefore, these values could be considered as boundary values when determining the transition from the liquid-like state to the pseudophase transition region. The fluid is considered to be in a gas-like state when $E_o > R/C_p$, which is typical for a substance in an ideal gas state.

The author also found that, for CO_2 under supercritical heating conditions in horizontal tubes, besides the negative pressure gradient due to thermal acceleration of flow, stratification of the liquid density and of the gravity forces in the vertical direction took place. This stratification was stable near the top portion of the tube, but unstable near the bottom portion of the tube. For supercritical heating at low heat fluxes, normal heat transfer was observed. However, with the increase of heat flux beyond a certain

value, as the fluid changes from liquid to vapor state, a deteriorated heat transfer was observed. The author also pointed out that, due to the nonuniform wall temperature distribution along the tube circumference caused by buoyancy, the heat transfer coefficients varied around the tube circumference. Near the top of the tube, heat transfer deterioration and wall superheating took place, while near the bottom of the tube, heat transfer was enhanced, resulting in the wall temperature being lower than average. He proposed the following friction factor correlation:

$$\xi/\xi_{01} = (\mu_w/\mu_1)^a (\rho_w/\rho_1)^b \tag{2.30}$$

For the pseudophase region, Equation (2.30) reduces to Popov's correlation with a = 0, and b = 0.25. For the gas-like region, the exponent b reduces to ~0.3-0.25 while *a* remains at 0. For the liquid-like region, typical values for carbon dioxide can be *a = 1/5* and *b = 1/3*. The heat transfer equation correlation is as follows:

$$St = \frac{q_w}{\overline{\rho \cdot u}(h_w - h_1)} = \frac{\xi/8}{1 + 900/Re_1 + 12.7 \cdot \sqrt{\xi/8} \cdot \left(\overline{Pr}^{2/3} - 1\right)} \tag{2.31}$$

where, the ξ is the friction factor given by Equation (2.30).

2.3 Deficiencies in the Literature and Need for Research

The above reviews of the literature on in-tube condensation and supercritical heat transfer are summarized in Tables 2.1 and 2.2.

2.3.1 In-tube Condensation

It is clear from Table 2.1 that, for condensation heat transfer, most early investigations (Kosky and Staub, 1971; Traviss *et al.*, 1973; Shah, 1979) focused on heat transfer for pure refrigerants based on the annular flow assumption. Jaster and Kosky (1976) extended Kosky and Staub's (1971) investigation to stratified-wavy flow and

proposed flow transition criteria based on the ratio of axial shear force to gravitational body force. However, for stratified-wavy flow, they assumed that the heat transfer in the liquid pool was negligible compared to the film condensation in the upper portion of the tube. This assumption is reasonable for the low mass flux range in his study, but might not be true for higher mass flux, low quality situations where wavy or stratified wavy flow could prevail in the presence of substantial convective heat transfer in the bottom of the tube.

Some recent studies (Sweeney, 1996; Dobson and Chato, 1998; Ebisu and Torikoshi, 1998; Boissieux *et al.*, 2000; Cavallini *et al.*, 2001; Han and Lee, 2001; El Hajal *et al.*, 2003; Thome *et al.*, 2003) have started to investigate condensation heat transfer for pure refrigerants and refrigerant blends. These studies have yielded correlations that are based on the specific flow pattern that exists for the applicable conditions. However, most of these studies on high pressure refrigerants focused on R410A at low reduced pressures (low saturation temperatures). Although the studies by El Hajal *et al.* (2003) and Thome *et al.* (2003) were for pure and refrigerant blends at saturation temperatures between 27 and 60°C, the saturation temperature range for high pressure pure refrigerants and blends (R32, R125, R410A) was $28 < T_{sat} < 52$°C. Boissieux *et al.* (2000) studied R404A in a similar tube diameter as in the present study, but the saturation temperature range for their study was $15 < T_{sat} < 35$°C. Cavallini *et al.* (2002a) used a data bank taken from literature for heat transfer in tube diameter range 3 – 21 mm to develop flow regime based heat transfer and pressure models. But they recommend that their model can be used only for reduced pressures up to 0.75 due to the lack of data at higher reduced pressures. Also, as discussed in the above review, several

of these correlations result in unrealistic abrupt transitions in the heat transfer coefficients as the flow regimes change with quality, mass flux, and other parameters.

Table 2.1 also shows that most two-phase pressure drop studies have been conducted on air-water or gas-water mixtures instead of refrigerants. Tran *et al.* (2000) studied the pressure drop for pure refrigerants, but their study was for evaporation at a much lower reduced pressure range. Thus, there is little literature available on heat transfer and pressure drop at saturation pressures approaching the critical pressure. Many of the commonly used condensation heat transfer and pressure drop correlations result in significant discrepancies when predicting the heat transfer coefficients for the higher pressures of interest in the present study.

Table 2.1 Summary of Literature on In-Tube Condensation

Type	Author	Fluids	D (mm)	G (kg/m2s)	P_r or T_{sat} (^oC)	HT and ΔP Models/ Flow Maps
Pure Fluids	Kosky and Staub (1971)	Steam	12.57	2.7 – 149.2	$0 < P_r < 0.007$	Annular flow heat transfer model
	Traviss *et al*. (1973)	R-12, R-22	8.00	161 – 1532	$25 < T_{sat} < 58$	Annular flow heat transfer model
	Jaster and Kosky (1976)	Steam	12.5	12.6 – 145	$0 < P_r < 0.007$	Annular, stratified and transition flow models
	Taitel and Dukler (1976)	Air-water				Theoretically developed flow regime map based on several non-dimensional parameter
	Shah (1979)	R-11, R-12, R-22, R-113, water, methanol, ethanol, benzene, toluene, trichloroethylene	7 – 40	11 – 211	$0.002 < P_r < 0.44$	Empirical heat transfer model for $1 < Pr_l < 13$

Table 2.1 (*Continued*)

Type	Author	Fluids	D (mm)	G (kg/m2s)	P_r or T_{sat} (^oC)	HT and ΔP Models/ Flow Maps
Pure fluids	Breber *et al.* (1980)	R11, R-12, R113, Steam and n-Pentane	4.8 – 22, 50.8	17.63 – 990, 1600		Flow maps based on shear to gravity forces. Simplified HTC model for annular and wavy/stratified flow
	Eckels and Pate (1991)	R134a, R12	8	125 - 400	$30 < T_{sat} < 50$	
	Nitheanandan and Soliman (1994)	Steam				Theoretically derived transition criteria from Stratified to non stratified regime
	Singh *et al.* (1996)	R134A	12.7	50 – 300	$T_{sat} = 35$	Empirical HTC model for stratified-wavy flow
	Coleman (2000)	R134a	$1 < d_h < 5$	150 - 750		Flow regime transition criteria based on modified Soliman Froude number
Refrigerant Blends	Tandon *et al.* (1982, 1985)	binary mixtures of R22 and R12	10			Developed flow regime maps
	Dobson & Chato (1998)	R-134a, R-12, R-22 R-32/R-125	3.14, 4.57, 7.04	25 – 800	$35 < T_{sat} < 45$	Annular and wavy flow heat transfer models
	Sweeney (1996)	R-407C		150 – 400		Modified Dobson & Chato (1998) models
R404A and other fluids	Boissieux, *et al*. (2000)	R-404A, R-407C, Isceon 59	9.5	150, 300	$15 < T_{sat} < 35$	Dobson & Chato (1998) models recommended
R410A and other pure and refrigerant blends	Ebisu & Torikoshi (1998)	R-410A, R-407C, R-22	6.4	100 – 400	$T_{sat} = 50$	Haraguchi et al. (1994) correlation recommended for R410A for $x \geq 0.4$.

Table 2.1 (*Continued*)

Type	Author	Fluids	D (mm)	G (kg/m2s)	P_r or T_{sat} (^oC)	HT and ΔP Models/ Flow Maps
R410A and other pure and refrigerant blends	Han & Lee (2001)	R-410A, R-22	7, 9.52	100 – 400	T_{sat} = 30, 40	
	Kwon and Kim (2000, 2001)	R22, R410A	9.52 O.D.	97, 144, 202	T_{sat} = 31	Analytical model for annular flow
	Cavallini *et al.* (2001)	R-22, R-134a, R-125, R-32, R-410A, R-236ea	8	100 – 750	30 < T_{sat} < 50	Kosky and Staub (1971) model for annular flow, Jaster and Kosky (1976) model for stratified flow
	Cavallini *et al.* (2002)	Data bank taken from literature	3 – 21		P_r < 0.75	Annular, stratified and slug flow heat transfer and pressure drop model
	El Hajal, Thome, Cavallini (2003)	Data bank taken from literature	3.1 – 21.4	24 – 1022	0.02 < P_r < 0.8	Flow regime Maps developed along with stratified, wavy-stratified and annular models
Adiabatic flow	Lockhart & Martinelli (1949)	Air, benzene, kerosene, water, oils	1.49 – 25.83		110.3 – 358.5 kPa	Liquid and vapor two-phase multiplier
	Chisholm (1973)					Liquid only two-phase multiplier
	Friedel (1979)	Data bank in the literature				Liquid only two-phase multiplier pressure drop model
	Mishima and Hibiki (1996)	Air-water mixture	1 – 4			Press drop modified Lockhart and Martinelli two-phase multiplier

Table 2.1 (*Continued*)

Type	Author	Fluids	D (mm)	G (kg/m2s)	P_r or T_{sat} (^oC)	HT and ΔP Models/ Flow Maps
Adiabatic flow	Ju Lee and Yong Lee (2001)	Air-water mixture	0.4 – 4			Modified Lockhart and Martinelli two-phase multiplier pressure drop model
	Kawahara et al. (2002)	Water-nitrogen mixture	0.1			Mishima and Hibiki (1996) and Lee and Lee (2001) pressure drop model recommended
Phase-change	Tran *et al.* (2000)	R134a, R12 and R113	2.46 and 2.92 and rectangular	33 - 832	0.04 < P_r < 0.23	ΔP model for flow boiling by modifying Chisholm's B-coefficient correlation

2.3.2 Supercritical Heat Transfer and Pressure Drop

Table 2.2 shows that most prior investigations on supercritical heat transfer and pressure drop have been conducted on carbon dioxide or steam. Furthermore, most of these studies have focused on the heating process (Ghorbani-Tari and Ghajar, 1985; Ghajar and Asadi, 1986; Kurganov, 1998a, b). Most studies attributed the changes in heat transfer coefficients to the large variation in properties, especially specific heat, near the vicinity of the critical point. Therefore, many researchers developed or recommended heat transfer correlations based on single-phase turbulent flow with property corrections to account for the large property variations near the critical region. There is little literature available on the supercritical cooling process for refrigerant blends. Extrapolating from heat transfer correlations developed for CO_2 mostly under heating conditions may result in significant discrepancies.

Therefore, the present study investigates heat transfer and pressure drop during condensation and supercritical cooling of refrigerant R404A and R410A in horizontal smooth tubes (9.4 and 6.2 mm diameter) for $0.8 < p_r < 1.2$. Data are subdivided into categories based on the expected flow regimes predicted from the information available in the literature. Heat transfer and pressure drop models are developed based on appropriate flow regimes using the data obtained in the present study. The following chapter discusses the experimental approach and the test facility used in the present study.

Table 2.2 Summary of Supercritical Heat Transfer and Pressure Drop Studies

Type	Author	Fluids	Flow Conditions	P_r or T (^oC)	HT and ΔP Models
Single-phase flow	Gnielinski (1976)		Single-phase turbulent flow		Modified Petukhov (1970) correlation
	Churchill (1977)		Single-phase fully developed, near isothermal flow		Combination of various heat transfer and friction factor models into one expression
Free convection	Ghorbani-Tari and Ghajar (1985)	CO_2, water	Free convection near critical region data bank from literature	$0.2 < Ra < 1.04\times10^{13}$	Free convection HT correlation with property corrections
Supercritical heating and cooling	Krasnoshchekov (1970)	CO_2	Supercritical cooling in horizontal tubes	30 – 215^oC	Single-phase turbulent correlation with property corrections
	Kuraeva and Protopopov (1974)		In-tube flow of supercritical fluids		Separate equations for friction factors neglecting and considering effect of free convection
	Ghajar & Asadi (1986)	CO_2, water	Supercritical heating data bank from literature	$0.018 < P_r < 1.46$	Dittus-Boelter-type HT correlation with property corrections
	Kurganov (1998a)	CO_2	Supercritical heating		Flow regime transition criteria
	Kurganov (1998b)	CO_2	Supercritical heating		Generalized Petukhov-Kirillov correlation recommended

Table 2.2 (*Continued*)

Type	Author	Fluids	Flow Conditions	P_r or T (^oC)	HT and ΔP Models
Supercritical heating and cooling	Pitla et al. (2001b)	CO_2	Supercritical cooling in horizontal tubes	T_{wall} = 30^oC P_{in}= 10 MPa	Numerical heat transfer models
	Pitla et al. (2001a)	CO_2	Supercritical cooling in horizontal tubes	$T_{test\ in}$ = 120^oC $T_{test\ out}$ = 5^oC	Experimentally validate the numerical model in Pitla et al. (2001a)
	Pitla et al. (2002)	CO_2	Numerical predictions from Pitla et al. (2001b)		Average of wall and bulk heat transfer based on Gnielinski (1976) correlation with property corrections

CHAPTER 3 EXPERIMENTAL APPROACH

This chapter provides a detailed description of the requirements and experimental approach used for measuring heat transfer coefficients and pressure drops close to the critical pressure. Heat transfer coefficient and pressure drop are measured for seven different mass fluxes ranging between 200 and 800 kg/m^2-s at five different pressures: $0.8\times P_{crit}$, $0.9\times P_{crit}$, P_{crit}, $1.1\times P_{crit}$, and $1.2\times P_{crit}$. Tests at the first two pressures are phase-change (condensation) tests, while the tests at the remaining three pressures are quasi single-phase (gas cooling) tests. For each mass flux of the phase change tests, experiments are conducted with nominal local test-section qualities from 0.9 to 0.1. For quasi single-phase tests, at each mass flux, data points are taken with nominal test-section inlet temperatures from 30 to 110°C in nominally 10°C increments. Therefore, the test facility must allow the heat transfer coefficient and pressure drop to be measured in small increments over the entire quality or temperature range. Furthermore, the test facility must also withstand the highest pressure under consideration (5883 kPa). The overall test conditions of this study is shown in Table 1.3

3.1 Requirements for Heat Transfer Coefficient Determination

The requirements for heat transfer coefficient determination are discussed here in detail for the phase-change tests. The approach developed for addressing these requirements is also applicable for supercritical tests. The primary focus in this study is to measure *local* heat transfer coefficient and pressure drop during condensation near critical pressure and gas cooling above critical pressure. *Local* here refers to small quality decrements, typically 5 to 10%, or small temperature drops across the test section, which enables the collection of data at high resolution. However, the vapor-liquid dome

converges toward the critical point (Figure 3.1) as the reduced pressure increases. This implies that the enthalpy differences for identical decreases in quality decrease as the reduced pressure increases. For example, for refrigerant R410A, at $P_r = 0.2$, $\Delta h = 43$ kJ/kg for $\Delta x = 0.2$, whereas at $P_r = 0.9$, it is 14.5 kJ/kg. These small enthalpy differences result in a significant decrease in the heat duty across the test section for such incremental changes in quality.

To accurately determine local heat transfer coefficients at such conditions, the test section inlet quality (enthalpy), outlet quality (enthalpy), and heat transfer rate need to be accurately determined. Second, the techniques used must also ensure the establishment of a wide range of quality and temperature for each mass flux. In addition, small condensation (phase-change tests) or cooling (supercritical tests) heat duties, i.e., small

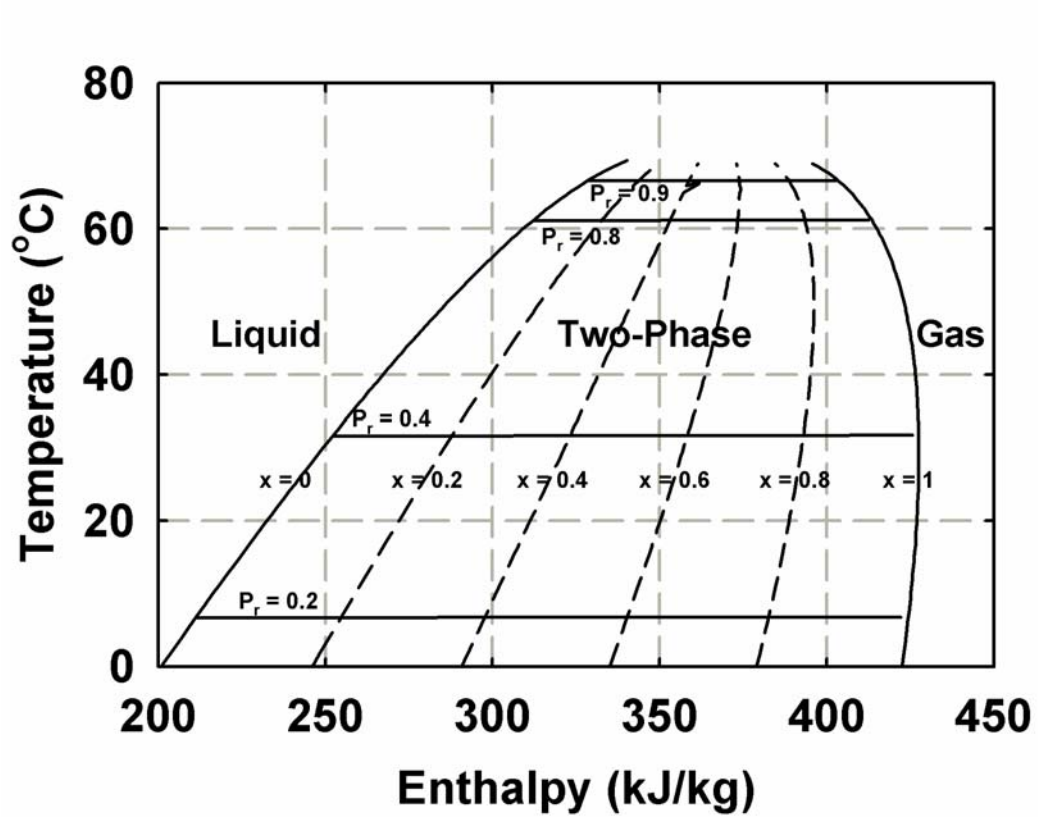

Figure 3.1 Liquid Vapor Dome for Refrigerant R410A

quality or temperature increments, are needed to represent local phenomena. Finally, the heat transfer coefficient must be accurately determined from measured heat duty and UA values.

However, in this study, heat transfer rate and heat transfer coefficient determination pose somewhat opposing requirements. Thus, the coolant flow rate and temperature rise must be measured very accurately to yield the coolant heat duty. While the coolant flow rate can be measured very accurately (± 0.15%) using a Coriolis mass flow meter, an appreciable coolant-side temperature rise is needed for acceptable uncertainties. As explained above, for the small quality or temperature increments desired to represent local phenomena, the coolant heat duties are very small. Therefore, extremely low flow rates are needed to maintain a measurable coolant temperature rise. However, a low coolant flow rate results in low coolant-side heat transfer coefficients, which make the coolant-side the governing resistance, leading to very poor and even unacceptable uncertainties in the refrigerant-side heat transfer coefficients. To solve these conflicting constraints, the heat duty determination and resistance ratio issues were decoupled, as described below.

3.2 Experimental Facility

A photograph of the experimental facility used in this study is shown in Figure 3.2. An overview of the experimental technique and the details of the test facility are provided below.

3.2.1 Thermal Amplification Technique

A novel thermal amplification technique developed by Garimella and Bandhauer (2001) is used in this study to decouple the issues pertaining to the accurate determination

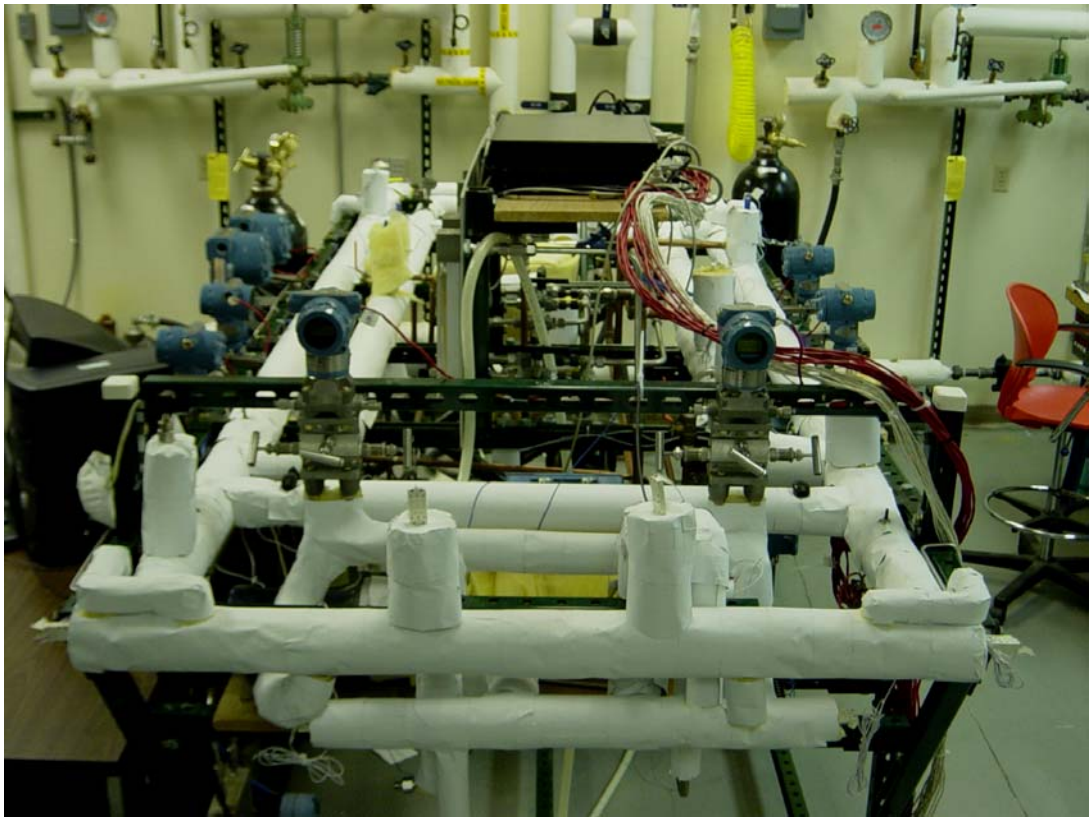

Figure 3.2 Photograph of the Test Section Side of the Test Facility

of heat duty and heat transfer coefficient. A schematic of the technique is shown in Figure 3.3. Refrigerant flows through the inner tube of the test section, while being condensed/cooled by a primary closed-loop water stream flowing in counterflow. The small gap in the annulus, and the high flow rate of the primary coolant ensures that the dominant heat transfer resistance in the test section is on the refrigerant side. This primary coolant in turn rejects heat to an open-loop city water stream in a shell-and-tube heat

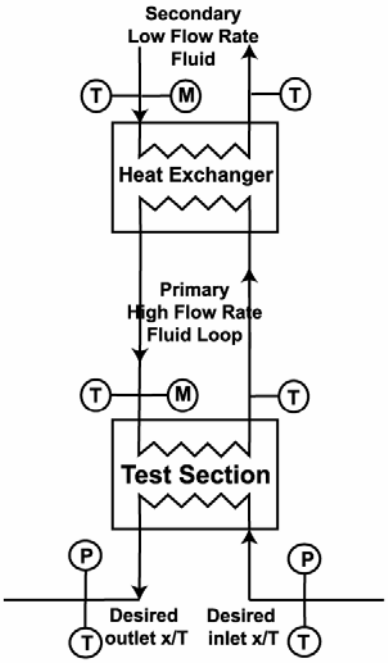

Figure 3.3 Thermal Amplification Technique

exchanger. The test section heat duty is then determined from the secondary coolant, which flows at very low flow rates. The low secondary coolant flow rate ensures a large temperature rise, resulting in low uncertainties in the test section heat duty. The secondary coolant flow rate is adjusted as the test conditions change to maintain a reasonable ΔT and also small condensation duties in the test section.

It should be noted that this approach depends upon the minimization of spurious heat losses and gains from/to the primary coolant loop so that the test section heat duty can be calculated accurately from a measurement of the secondary coolant heat load. Thus, it is essential that the primary coolant circulation pump heat dissipation and the ambient heat loss are small fractions of the secondary loop duty, and also that they be estimated with reasonable accuracy. This ensures that the test section heat load is relatively insensitive to pump heat addition and ambient heat loss, as will be demonstrated in a subsequent section. Low thermal conductivity insulation and small temperature differences between the primary coolant and the ambient minimize the heat loss to the ambient. Similarly, using a pump with extremely low heat dissipation minimizes the heat addition to this loop. This technique of decoupling the determination of heat duty and heat transfer coefficient through thermal amplification is described in greater detail in Garimella and Bandhauer (2001).

3.2.2 Test Loop Description

The schematic of the test facility is shown in Figure 3.4. Subcooled liquid refrigerant was pumped through a coiled tube-in-tube evaporator (Exergy Model # 00528) where the steam flowed counter-current to the refrigerant to boil and heat it to a desired superheated state. This superheated state of the refrigerant was ensured by a

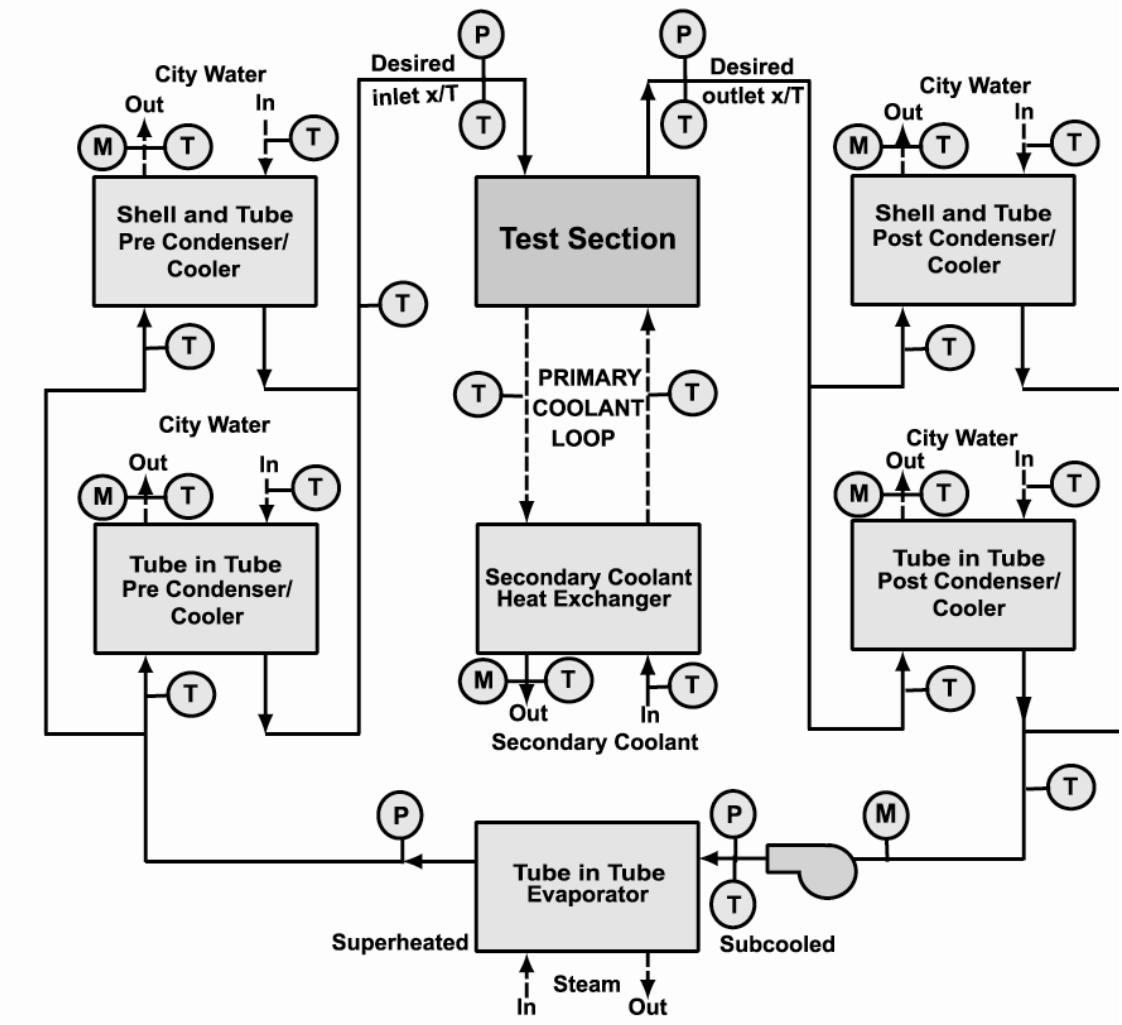

Figure 3.4 Test Loop Schematic

combination of a sight glass and temperature and pressure measurements. These temperature and pressure measurements also determine the refrigerant enthalpy. The superheated vapor entered one of two pre-condensers/coolers, where city water at the desired (variable) flow rate was used to partially condense/cool the vapor. One of the pre-condensers/coolers is a tube-in-tube heat exchanger whereas the other is a shell-and-tube heat exchanger (Exergy Model# 00256-1). These heat exchangers are switched back and forth during testing depending on the amount of pre-condensation/cooling required. For example, if high test-section qualities/temperatures are required, the tube-in-tube heat

exchanger is used, while for lower qualities/temperatures, the shell-and-tube heat exchanger, which has a higher cooling capacity, is used. Details of all the heat exchangers in the test loop are provided in Tables 3.1 and 3.2. These pre-condensers/coolers, with their different heat transfer surface areas, and variable cooling water flow rates, establish a wide range of refrigerant conditions at the test section inlet.

Refrigerant and coolant temperature and pressure measurements were also taken at the exit of the pre-condenser/cooler. For the condensation tests, the refrigerant temperature and pressure measurements ensured that the measured temperature corresponded to the saturation temperature at the measured pressure. The coolant measurements were used to compute the pre-cooler/condenser heat duty. An energy balance across the pre-condenser/cooler was then used to calculate the refrigerant

Table 3. 1 Tube-in-Tube Heat Exchanger Dimensions

Tube		Material	Length (m)	Tube O.D. (mm)	Wall Thickness (mm)	Manufacturer
Test Section Heat Exchanger						
9.4 mm	Inner Tube	Copper	0.292	12.7	1.65	In house
	Outer Tube	Stainless Steel		19.1	1.65	In house
6.2 mm	Inner Tube	Copper	0.292	9.5	1.65	In house
	Outer Tube	Stainless Steel		15.9	1.25	In house
Pre-Condenser/Cooler						
Short	Inner Tube	Stainless Steel	0.56	6.35	0.89	In house
	Outer Tube	Stainless Steel		12.70	0.89	In house
Post-Condenser/Cooler						
Short	Inner Tube	Stainless Steel	0.56	6.35	0.89	In house
	Outer Tube	Stainless Steel		12.70	0.89	In house
Evaporator						
Inner Tube		Stainless Steel	5.90	12.70	1.65	Exergy Model 00528
Outer Tube		Stainless Steel	5.90	25.40	1.65	

Table 3. 2 Shell-and-Tube Heat Exchanger Dimensions

Length (m)	Material	Shell-Side		Tube-Side		Tube Count	Baffle Count	HT Area (m^2)	Manufacturer
		O.D. (mm)	Wall (mm)	O.D. (mm)	Wall (mm)				
Secondary Heat Exchanger									
0.248	Stainless Steel	25.4	1.25	3.18	0.32	19	9	0.04	Exergy Model 00540-4
Pre-Condenser/Cooler									
0.565	Stainless Steel	41	1.65	3.18	0.32	55	11	0.27	Exergy Model 00256-1
Post-Condenser/Cooler									
0.311	Stainless Steel	41	1.65	3.18	0.32	55	7	0.13	Exergy Model 00256-2

enthalpy at the exit of the pre-cooler/condenser. For the phase-change tests, this enthalpy was used to calculate the quality at the exit of the pre-cooler/condenser. For the supercritical tests, this calculated enthalpy was validated against the enthalpy obtained from the refrigerant temperature and pressure readings at the test section inlet. Similar measurements at the adjacent inlet of the test section ensured that there was no heat loss between the exit of the pre-condenser/cooler and the inlet of the test section.

Refrigerant exiting the pre-condensers/coolers entered the test section, a counterflow tube-in-tube water-cooled heat exchanger. Temperatures and pressures were also measured at the exit of the test section. After flowing through the test section, one of two post-coolers/condensers (one tube-in-tube and one shell-and-tube (Exergy Model# 00256-2)) downstream of the test section was used to completely condense and subcool the refrigerant. A temperature reading was also taken at the inlet of the post-condensers/coolers to ensure that there was no heat loss between the exit of the test section and inlet of the post-condensers/coolers. Pressure and temperature readings at the end of these heat exchangers provided the outlet enthalpy of the refrigerant. The

subcooled refrigerant enthalpy at the exit of the post-cooler/condenser, and an energy balance on the post-cooler/condenser, were used to deduce the refrigerant enthalpy and quality at the outlet of the test section. The test section quality is the average of the test section inlet and outlet qualities.

The refrigerant was circulated around the test loop using a magnetic gear pump (Micropump, Table 3.3). Two pump heads were used to obtain the full range of mass fluxes under consideration. A coriolis mass flow meter (Micromotion, Model # CFM025) was placed at the inlet of the pump to measure the refrigerant mass flow rate. A bladder-type accumulator (Accumulator Inc. Model #A1-3100, 1 gal, 3000 psid) was located upstream of the evaporator to maintain the system pressure at a desired constant value. A nitrogen tank connected to the accumulator was used to vary the bladder pressure to obtain the desired system pressures.

Table 3. 3 Refrigerant Pump Specifications

Pump Head					
Model	**Maximum Flow Rate (gpm)**	**Maximum System Pressure (psig)**	**Differential Pressure (psi)**	**Material**	**Manufacturer**
220/56C	1	1500	100	Stainless Steel	Micropump
219/56C	0.466	1500	100	Stainless Steel	Micropump

Motor						
Frame	**HP**	**Speed (rpm)**	**Voltage (V)**	**Frequency (Hz)**	**Phase**	**Manufacturer**
56C	1/2	1725	230/460	60	3	Reliance
56C	1/2	3450	230/460	60	3	Reliance

Variable Frequency Drive					
Model	**HP**	**kW**	**Input**	**Output**	**Manufacturer**
Series 15P Mini Inverter	0.5	0.37	115 V/1 Phase	230 V/3 Phase	Baldor Motors and Drives

A shell-and-tube heat exchanger (Exergy Model# 0.00540-4) was used to transfer heat from the primary coolant to the secondary coolant. The coolant in the primary loop was circulated at a high flow rate using a variable speed magnetic gear pump (pump head Micropump Model # 500.750/56C). A ½ hp, 2500 rpm motor and a variable speed drive by Leeson electric was used with the pump. Open-loop cooling water was pumped in the secondary loop using a magnetic gear pump (Cole Parmer S/N 75225-00) with a variable speed drive. For the water flow in the pre- and post-heat exchangers, a ½ hp centrifugal pump at 3450 rpm was used. Refrigerant was circulated in the test loop by a set of two magnetic gear pump heads, two motors and a pulse-width-modulated variable frequency controller. The following pump heads from Micropump were used:

- Model # 2200/56C (0-2 gpm): 9 mm tube.
- Model # 219/56C (0.08-0.466 gpm): 7 mm tube

Two ½ hp, 3-ϕ, 1725 and 3450 rpm motors were used along with the pump heads to establish the entire range of mass fluxes in the present study.

3.2.3 Test Section

The test section is a counter-flow tube-in-tube heat exchanger. Refrigerant flows through the inner tube while being condensed/cooled by the coolant in the annulus. A picture of the test section is shown in Figure 3.5. Two test sections, each 11.5 inches (0.292 m) long were used, with the following dimensions:

- ***9 mm case:*** Inner tube: 12.7 mm OD, 1.65 mm wall thickness copper tube (I.D. = 9.4 mm); Outer tube: 19.1 mm OD, 1.65 mm wall thickness (I.D. = 15.8 mm) stainless steel tube.

- ***7 mm case:*** Inner tube: 9.5 mm OD, 1.65 mm wall thickness copper tube (I.D. = 6.3 mm); Outer tube: 15.9 mm OD, 1.25 mm wall thickness (I.D. = 13.4 mm) stainless steel tube.

In addition to determining the refrigerant heat transfer coefficients from the measured UA using the thermal amplification technique described above, a redundant method for obtaining the refrigerant heat transfer coefficients based on the refrigerant-to-wall temperature difference was utilized. To measure these wall temperatures, three 26-gauge T-type thermocouples for the 9.4 mm tube, and six for the 6.2 mm tube (Figure 3.6) were soldered to the outer wall of the refrigerant tube. For the 9.4 mm tube, the first thermocouple was placed 1.59 mm (1/16 inch, same for 6.2 mm tube) from the refrigerant inlet as shown in Figure 3.7, with the second and third thermocouples placed further downstream, at intervals of 144.5 mm i.e 5.69 inch (for 6.2 mm tube subsequent thermocouples were placed 57.79 mm i.e 2.275 inches apart). In addition, the thermocouples were placed 120° apart from each other in the circumferential direction as shown in Figure 3.7 to account for temperature variations due to potential stratification. The refrigerant-to-wall temperature difference (after subtracting the ΔT from the inner wall to the outer wall) provided an additional estimate of the refrigerant heat transfer coefficient for the phase-change and supercritical tests. The agreement between these two methods of obtaining the refrigerant heat transfer coefficients is described in Chapter 4.

3.2.4 Instrumentation and Data Acquisition

The measurement ranges and accuracies of the instrumentation used in this study are summarized in Table 3.4. The refrigerant and secondary coolant flow rates were measured using Coriolis mass flow meters (Micromotion Elite flow sensor model number

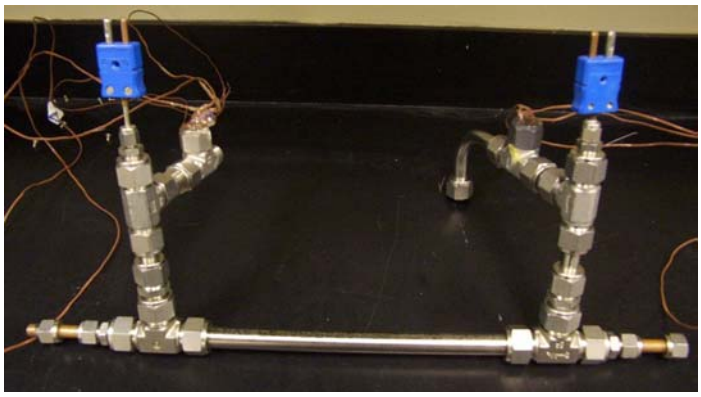

Figure 3. 5 A 6.2 mm I.D. Test Section

Figure 3. 6 The Test Section Inner Tube with Thermocouples

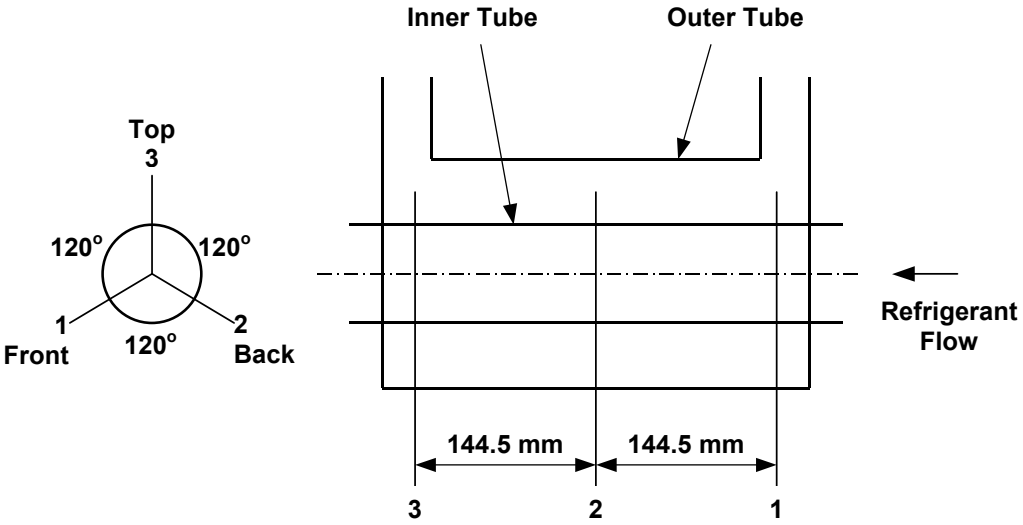

Figure 3. 7 Schematic of Wall-Mounted Thermocouple Locations for the Test Section

Table 3. 4 Instrumentation Specifications

Fluid	Manufacturer	Model	Range	Accuracy
Temperature				
R410A and Water	Omega	Pr-13	0 – 100ºC	±0.5ºC
Water	Thermocouple	T		±1.0ºC or ±0.75% Reading
Mass Flow Rate				
R410A	Micromotion	CFM025	0 – 0.3 kg/s	±0.10% Reading
Water (secondary loop)	Micromotion	D6	0 – 0.015 kg/s	±0.15% Reading
Volumetric Flow Rate				
Water (post heat exchangers)	Gilmont	Accucal	0.1 – 0.78 lpm	±2% Reading
	Gilmont	Accucal	0.2 – 2.2 lpm	±2% Reading
	Gilmont	Accucal	0.2 – 4.5 lpm	±2% Reading
Water (primary and pre HX)	Rosemount	8711 TSE-30-FS1 Flow Tube and 8712C magnetic Flow Transmitter	0 – 25.02 lpm	±0.5% Reading
Pressure				
R410A	Rosemount	2088 (absolute)	0 – 5515.8 kPa	±13.79 kPa
R410A	Rosemount	3051 (absolute)	0 – 13790 kPa	±0.075 % of span
R410A	Rosemount	3051C (dP)	0-248.2 kPa	±0.075 % of span
R410A	Rosemount	3051C (dP)	0-62.27 kPa	±0.075 % of span
R410A	Rosemount	3051C (dP)	0-6.227 kPa	±0.1 % of span

CFM025 and Micromotion type D6 sensor), with accuracies of ±0.10% and 0.15% of the reading, respectively. The primary coolant volumetric flow rate was measured using a Rosemount series 8711 magnetic flowmeter flowtube coupled with series 8712C transmitter. This flowmeter provided an accuracy of ±0.5% for flow velocities of 1 to 10 m/s and 0.005 m/s for velocities less than 1 m/s. The cooling water flow rates for the post-condensers/coolers were measured using a set of three Gilmont Accucal flow

meters, with flow rate ranges of 0.2 to 4.5 liter per minute, 0.2 to 2.2 liter per minute, and 0.1 to 0.78 liter per minute. The accuracies of these flow meters were ±2% of the reading, or ±1 scale division, whichever is greater. For each data point, the cooling water was routed through the rotameter that yields the highest accuracy. The pre-condenser/cooler side water flow rate was measured using a Rosemount magnetic flowmeter similar to the one in primary loop.

Rosemount model 2088 absolute and gage pressure transmitters with an accuracy of ±0.25% of the calibrated span were used to measure pressures of the refrigerant at various locations. The maximum span for these transducers is 0 to 5,515.8 kPa (0 – 800 psi). However, $P_r = 1.2$ was beyond the range of these transducers. Therefore a new set of Rosemount series 3051 absolute smart pressure transmitters with a variable span up to 13790 kPa (2000 psi) was used for these cases. The 3051 series transducers have an accuracy of ±0.075% of span. Pressure drops were measured using a bank of 3 Rosemount model 3051C differential pressure transmitters with the following spans: 0-248.2, 0-62.27, and 0-6.227 kPa. The differential pressure transducers with maximum spans of 0-248.2, 0-62.27 kPa have an accuracy of ±0.075% of the span, whereas the transducer with maximum span of 0-6.227 kPa has an accuracy of ±0.1% of the span. For each data point, the measurement is taken using the transducer that yields the highest accuracy. Temperatures were measured using a combination of Platinum RTDs (Omega PR-13, accuracy: ±0.5°C for 0 – 100°C) and type-T thermocouples (accuracy: ±1.0°C or ±0.75% of the reading, whichever is greater).

All data were recorded using a TEMPSCAN data acquisition system (Iotech TempScan/1100 High Speed Temperature Measurement system with an expansion

chassis Exp/10A. This system can record up to 992 inputs for temperature, pressure, flow rate, and other signal measurements, at speeds of up to 960 channels per second for real-time data analysis. The data acquisition system communicated with the computer through an RS-232/RS-422 serial port. TempView and ChartView software was used to read signals from the data acquisition system. Measured temperatures, flow rates, and pressures were continuously displayed and plotted as a function of time to ensure that steady state conditions are reached. Once steady state was achieved, the sight glasses, and pressure and temperature readings were inspected to ensure an adequate degree of superheat and subcooling. Two data points were recorded for each case, with each data point representing an average of 120 scans taken every second for a two-minute period. The averages of these two data points were used for data analysis.

3.3 Experimental Procedures

3.3.1 System Charging

Several taps were provided in the system for evacuation and charging of different sections of the loop. The refrigerant-side of the test facility was initially pressurized with nitrogen gas and a trace amount of R134A. An electronic leak detector (CPS model L-709a) was used to detect any possible leaks around all of the fittings. The test facility was evacuated to a system pressure of 150 microns (20.03 Pa) using a vacuum pump (J/B Industries model DV-85N). A Thermal Engineering vacuum gauge (model 14571) with the capability of measuring pressures as low as 10 microns (1.33 Pa) was used to measure the vacuum pressure. At 150 microns, the vacuum pump was shut off, and the system was isolated for 24 hours to check for any pressure rise, which indicated leaks in the system. Any such leaks were fixed and the loop was again evacuated. The system was

charged with approximately 3.5 kg of R410A immediately after evacuation, and the system pressure was monitored over a 24-hour period to verify system integrity. The system was also charged with cooling water in the primary loop and leak-tested. A relief valve in the primary loop was used to purge the air from this loop.

3.3.2 System Start-up and Operation

Testing commenced with the pre- and post-condenser/cooler water flow, refrigerant flow, primary and secondary water flow, and steam flow being turned on in this order. The desired refrigerant mass flow rate was achieved through a combination of needle valves and a variable frequency drive on the pump. The desired refrigerant testing pressure was maintained by controlling the external pressure to the accumulator by a nitrogen tank.

Based on the mass flux under consideration and the desired test section inlet quality (or temperature for supercritical tests), one of the two available large and small pre-condensers/coolers and the coolant flow rate, as well as the volumetric flow meter that yielded the highest accuracy were selected. For example, at low refrigerant mass flux and high test section inlet quality (or inlet temperature for supercritical tests), the small pre-condenser/cooler (tube-in-tube heat exchanger) was selected. For phase-change tests, using the superheated refrigerant inlet enthalpy and mass flow rate, and the measured water-side heat duty, the pre-condenser outlet quality (also the test section inlet quality) was calculated through an energy balance.

The test-section primary-coolant flow rate was selected to obtain a low coolant heat transfer resistance and pump heat addition. With the secondary coolant inlet temperature fixed by the city water temperature, the flow rate determined the outlet

temperature, and thus the temperature difference available for heat transfer between the primary and secondary coolants. Therefore, secondary flow rate indirectly controlled the cooling duty across the test section, i.e. test section outlet quality for phase-change tests or temperature for supercritical tests. This flow rate was therefore carefully selected to obtain a large temperature difference across the secondary heat exchanger, which allows for the test section heat duty to be measured accurately. One out of the two post-condensers/coolers and the water flow rate were selected to fully condense and subcool the refrigerant while maintaining a measurable temperature difference at the outlet of the post-cooler. Again, for phase-change tests, an energy balance in the post-condenser was used to derive the post-cooler inlet (also the test section outlet) vapor quality. The subcooled refrigerant was also measured by a coriolis flow meter and pumped back to the evaporator.

The system pressures, temperatures, and flow rates were constantly monitored during the test. Steady state conditions took between 30 minutes and 3 hours to obtain, depending on the specific test condition under consideration. After steady state was established, sight glasses at the exit of the evaporator and at the inlet of the refrigerant pump were checked to ensure that the refrigerant was superheated and subcooled at these respective locations, and the data point was recorded. Water flow rates for the pre- and post-coolers and the primary and secondary coolants (as necessary) were then adjusted to obtain another average test section condition at the same refrigerant flow rate. This process was repeated until all the data points needed in this study were completed.

For supercritical tests, temperatures and pressures were measured directly at the test section inlet and outlet to evaluate refrigerant enthalpies and ensure that the desired

conditions were established. Pre- and post-cooler energy balances were also computed to independently validate these conditions while the test was in progress. The temperature increments were reduced near the transition temperatures so that the sharp variations in these heat transfer coefficients could be tracked with higher resolution.

CHAPTER 4 DATA ANALYSIS

This chapter provides a detailed description of the data reduction and uncertainty analyses used to analyze data obtained with techniques described in Chapter 3. *Engineering Equation Solver* (EES) software (Klein (2003)) was used to analyze the data, and the refrigerant properties were obtained from *REFPROP* (Lemmon *et al.* (2002)) using the *EES-REFPROP* interface. The chapter is divided into three sections. The first section describes the phase-change heat transfer and pressure drop analyses using a sample data point for illustration. The second section provides a description of the uncertainty analysis for the sample point in the previous section. The third section provides details of the additional analyses for the supercritical tests. The sample calculations for phase-change and supercritical conditions are also tabulated in Appendices A through E.

4.1 Condensation Data Analysis

The representative phase-change case demonstrated here is for a data point of G = 302 kg/m^2-s, x = 0.66, and p = 0.8×P_{crit}. For a 9.4 mm I.D. tube, with a flow area of 6.94×10^{-5} m^2, this corresponds to a refrigerant flow rate of 2.1×10^{-2} kg/s. Table 4.1 shows a summary of the measured data for this case.

4.1.1 Average Test Section Quality

4.1.1.1 Test Section Inlet Quality

The measured quantities for required calculations are the inlet and outlet temperatures, as well as the pressure and flow rate of the water-side of the pre-cooler, in addition to the refrigerant flow rate, inlet temperature and pressure. The water-side heat duty of the pre-condenser was calculated using the following equation:

Table 4.1 Measured Data for the Representative Case

	Variable, units	***Value***
Pre Condenser:		
Inlet water temperature	$T_{pre,w,in}$, °C	14.74
Inlet water pressure (assumption)	$P_{pre,w,in}$, kPa (psia)	413.7 (60)
Outlet water temperature	$T_{pre,w,out}$, °C	58.22
Outlet water pressure (assumption)	$P_{pre,w,out}$, kPa (psia)	137.9 (20)
Water flow rate	$Vol_{pre,w}$, m^3/s (gpm)	1.223×10^{-5} (0.194)
Inlet refrigerant temperature	$T_{pre,r,in}$, °C	105.77
Inlet refrigerant pressure	$P_{pre,r,in}$, kPa (psia)	3822.8 (554.5)
Outlet refrigerant temperature	$T_{pre,r,out}$, °C	59.64
Outlet refrigerant pressure	$P_{pre,r,out}$, kPa (psia)	3820.9 (554.2)
Post Condenser:		
Inlet water temperature	$T_{post,w,in}$, °C	13.89
Inlet water pressure (assumption)	$P_{post,w,in}$, kPa (psia)	413.7 (60)
Outlet water temperature	$T_{post,w,out}$, °C	20.31
Outlet water pressure (assumption)	$P_{post,w,out}$, kPa (psia)	137.9 (20)
Water flow rate	$Vol_{post,w}$, m^3/s (gpm)	7.17×10^{-5} (1.14)
Inlet refrigerant temperature	$T_{post,r,in}$, °C	59.13
Inlet refrigerant pressure	$P_{post,r,in}$, kPa (psia)	3821.8 (554.31)
Outlet refrigerant temperature	$T_{post,r,out}$, °C	46.14
Outlet refrigerant pressure	$P_{post,r,out}$, kPa (psia)	3808.5 (552.38)
Test Section:		
Inlet refrigerant temperature	$T_{test,r,in}$, °C	59.78
Inlet refrigerant pressure	$P_{test,r,in}$, kPa (psia)	3820.9 (554.18)
Outlet refrigerant temperature	$T_{test,r,out}$, °C	59.64
Outlet refrigerant pressure	$P_{test,r,out}$, kPa (psia)	3821.8 (554.30)
Refrigerant flow rate	$\dot{m}_{refg}$, kg/s (lbm/min)	2.097×10^{-2} (2.77)
Universal Refrigerant flow rate	G, kg/m^2-s	302
Secondary Heat Exchanger:		
Inlet tube water temperature (Primary)	$T_{prim,w,in}$, °C	34.97
Outlet tube water temperature (Primary)	$T_{prim,w,out}$, °C	34.32
Inlet shell water temperature (Secondary)	$T_{sec,w,in}$, °C	14.11
Outlet shell water temperature (Secondary)	$T_{sec,w,out}$, °C	25.47
Shell water flow rate (Secondary)	$\dot{m}_{sec}$, kg/s (lbm/min)	1.182×10^{-2} (1.56)
Average water pressure (assumption)	$P_{test,w}$, kPa (psia)	275.8 (40)
Primary Loop:		
Inlet test section water temperature	$T_{test,w,in}$, °C	34.32
Outlet test section water temperature	$T_{test,w,out}$, °C	34.97
Volumetric water flow rate	$Vol_{prim,w}$, m^3/s (gpm)	1.146×10^{-4} (1.816)
Average water pressure (assumption)	$P_{prim,w}$, kPa (psia)	413.7 (60)
Ambient Temperature: T_{amb} = 23°C (assumption)		
Critical Pressure : P_{crit} = 4920.6 kPa		

$$Q_{pre} = \dot{m}_{water,pre}\, \Delta h_{water,pre} \tag{4. 1}$$

where $\dot{m}_{water,pre}$ and $\Delta h_{water,pre}$ are the mass flow rate and enthalpy change of the cooling water in the pre-condenser, respectively. The water properties needed to calculate the mass flow rate and the enthalpies were evaluated at the mean water temperature and pressure. Since the refrigerant enters the pre-condenser as superheated vapor, its enthalpy $h_{refg,pre,i}$ can be calculated using the refrigerant temperature and pressure measurements at the inlet of the pre-condenser. This refrigerant enthalpy, in conjunction with the heat duty obtained from the water-side, yields the test section inlet quality:

$$\begin{aligned} Q_{pre} &= \dot{m}_{refg}(h_{refg,in} - h_{refg,out}) \\ x_{test,in} &= x_{pre,out} = x(P_{pre,out}, h_{refg,out}) \end{aligned} \tag{4. 2}$$

Thus, for the representative case, with the pre-condenser water flow rate at 1.223×10^{-5} m^3/s, and measured inlet and outlet temperatures of 14.74 and 58.22°C, the pre-condenser water density is 993.6 kg/m^3, resulting in a mass flow rate of 1.22×10^{-2} kg/s and a heat duty of 2.21 kW. The measured refrigerant temperature and pressure at the inlet of the pre-condenser are 105.77°C and 3822.8 kPa, respectively, resulting in an enthalpy of 494.3 kJ/kg. From equations (4.1) and (4.2), the refrigerant enthalpy at the pre-condenser outlet (test section inlet) is 388.9 kJ/kg. Here, it is assumed that the heat loss from the pre-cooler outlet to the test section inlet is negligible. For a measured pre-condenser outlet pressure of 3820.9 kPa, the refrigerant quality at the test section inlet is 0.75.

4.1.1.2 Test Section Outlet Quality

The test section outlet quality was determined using a method similar to that described in the previous section. Instead of pre-condenser water heat duty, the post-condenser water heat duty was used to calculate the test section outlet quality as follows.

$$Q_{post} = \dot{m}_{water,post}\,\Delta h_{water,post} \tag{4. 3}$$

$$\begin{aligned} Q_{post} &= \dot{m}_{refg}(h_{refg,in} - h_{refg,out}) \\ x_{test,out} &= x(P, h_{refg,in}) \end{aligned} \tag{4. 4}$$

The post-condenser water flow rate is 7.17×10^{-5} m^3/s, with measured inlet and outlet temperatures of 13.89 and 20.31°C, respectively. With a density of 998.9 kg/m^3 and a mass flow rate of 7.16×10^{-2} kg/s, the post-condenser heat duty is calculated to be 1.92 kW. The refrigerant leaves the post-condenser as a subcooled liquid, allowing the refrigerant enthalpy to be determined from the measured temperature and pressure. Thus, with the refrigerant temperature and pressure at the outlet of the post-condenser of 46.14°C and 3808.5 kPa, the refrigerant enthalpy at the post-condenser outlet is 277.2 kJ/kg. Using Equations (4.3) and (4.4), the refrigerant enthalpy at the post-condenser inlet (test section outlet) is determined to be 368.9 kJ/kg. For a measured pressure of 3821.8 kPa, the refrigerant quality at test section outlet is calculated as 0.56. Again, it is assumed that the heat loss from the test section outlet to the post-cooler inlet is negligible. With the test section inlet and outlet qualities of 0.75 and 0.56, the average test section quality is 0.66.

4.1.2 Test Section Heat Duty

The test section heat duty was calculated using an energy balance between the test section and the secondary loop (Figure 3.4) expressed as follows:

$$Q_{w,test} = Q_{w,sec} + Q_{ambient} - Q_{pump} \quad (4.5)$$

where $Q_{w,test}$, $Q_{w,sec}$, $Q_{ambient}$, and Q_{pump} are test section heat duty, secondary water heat duty, ambient heat loss and pump heat addition, respectively. Figure 4.1 shows a schematic of the relationship between $Q_{w,test}$, $Q_{w,sec}$, $Q_{ambient}$, and Q_{pump}. The secondary water heat duty can be calculated as follows, with the properties evaluated at the mean temperature and pressure:

$$Q_{w,sec} = \dot{m}_{w,sec} \cdot C_{p,w,sec}(T_{w,sec,o} - T_{w,sec,i}) \quad (4.6)$$

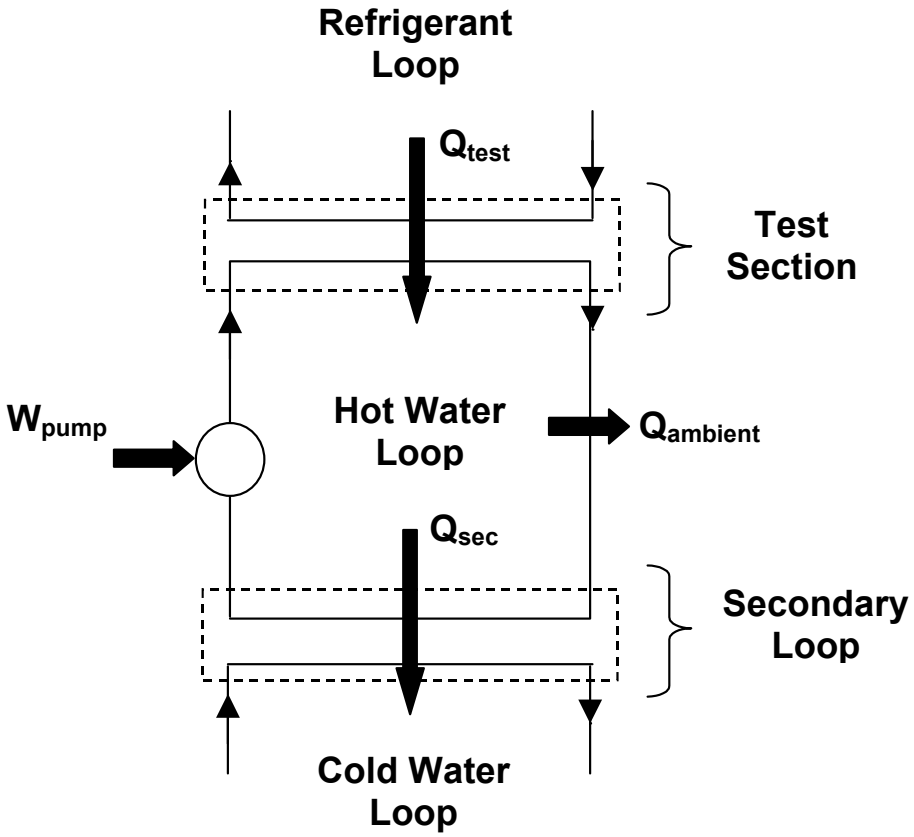

Figure 4.1 Primary and Secondary Loop Heat Duties

For a measured secondary flow at 1.18×10^{-2} kg/s, with inlet and outlet temperatures at 14.11 and 25.47°C, the secondary water heat duty is calculated as 0.561 kW. The detailed procedures of calculating the pump heat addition and ambient heat loss of the primary loop are discussed in the following sub-sections.

4.1.2.1 Pump Heat Addition

To calculate the pump heat addition, the pressure drop in the primary loop must be calculated first to determine the pumping power required for water circulation. The pressure drop in the primary loop includes the pressure drops in the tubing and fittings, primary flow meter, annulus side pressure drop of the test section, and the shell side pressure drop of the secondary shell and tube heat exchanger. The heat exchanger and tubing dimensions, and types of the fittings involved in the discussion below are summarized in Table 4.2. A detailed calculation is also shown in Appendix B.

4.1.2.1.1 Pressure loss in tubing

The pressure loss in the tubing includes frictional and minor losses. For the stainless steel tubing with an inner diameter of 10.92 mm (12.70 mm O.D. with wall thickness of 0.89 mm) and a measured volumetric flow rate of 1.146×10^{-4} m^3/s, the velocity of the circulating water in the tube was calculated as 1.22 m/s, resulting in a Reynolds number of 18,269 (water properties are evaluated at the average temperature of the circulating fluid). With a roughness for drawn tubing of 0.0015 mm (Munson *et al.*, 1998) and the Reynolds number calculated above, the Churchill (1977b) correlation yields a friction factor of 0.0296. The pressure drop in the tubing is calculated as follows:

$$\Delta P_{\text{friction,tube}} = \frac{1}{2}\cdot f\cdot \rho\cdot V^2\cdot\frac{L_{\text{tube}}}{(\text{I.D.})_{\text{tube}}} \qquad (4.7)$$

For 2.54 m of tubing in the primary loop, the pressure drop is 5.12 kPa. The minor losses due to the fittings are calculated as follows, where K_{total} is the total K-factor (see Table 4.2) of the fittings (Munson *et al.*, 1998).

$$\Delta P_{minor,tube} = \frac{1}{2}\rho V^2 K_{total} \tag{4. 8}$$

Assuming the fluid velocity is the same as in the tubing, the total minor loss is 15.7 kPa. Thus, from equations (4.7) and (4.8), the total pressure drop in the tubing due to frictional and minor losses is 20.77 kPa.

4.1.2.1.2 Pressure loss in the flow meter

Table 4.2 Tubing Geometry and Fitting Type

Tubing	
Tube O.D. (mm)	$(O.D.)_{tubing} = 12.70$
Tube thickness (mm)	$w_{tubing} = 0.89$
Tube roughness (mm)	Drawn tubing, $\varepsilon = 0.0015$
Tube length (m)	$L_{tube} = 2.54$
Test Section	
Outer Tube O.D (mm)	$(O.D.)_{outer} = 19.05$
Outer tube thickness (mm)	$w_{outer} = 1.65$
Outer tube roughness (mm)	Drawn tubing, $\varepsilon = 0.0015$
Inner Tube O.D. (mm)	$(O.D.)_{inner} = 12.70$
Inner tube thickness (mm)	$w_{inner} = 1.65$
Test section length (m)	$L_{test} = 0.292$
Secondary Heat Exchanger	
Shell O.D. (mm)	$(O.D.)_{shell} = 25.4$
Shell thickness (mm)	$w_{shell} = 1.25$
Heat exchanger length (m)	$L_{sec} = 0.173$
Fittings	
90° threaded elbow	×5, K=1.5/each
Tee, branch flow, threaded	×6, K=2/each
Ball valve fully opened	×1, K=.05/each
180° return bend, threaded	×1, K=1.5/each

Based on the specifications of the Rosemount 8711 magnetic flow meter and flow tube, the inner volume of the tube was found to be equivalent to 0.54 m of 10.92 mm I.D. primary loop tubing. The pressure drop across the flow tube was then computed from Equation (4.7) with the same friction factor and velocity as that of the primary loop. Thus, for a 1.816 gpm (1.146×10^{-4} m^3/s) primary coolant flow rate, the pressure loss in the flow meter is 1.08 kPa.

4.1.2.1.3 Pressure loss in the test section

The primary water flows through the annulus side of the test section. The hydraulic diameter of the annulus can be calculated using the inner tube O.D. and the outer tube I.D.

$$D_{h,annulus} = \frac{4A_{f,annulus}}{P} = (I.D.)_{outer} - (O.D.)_{inner} \qquad (4.9)$$

where $A_{f,annulus}$ and P are the free flow area and perimeter of the annulus side, respectively. With an outer tube I.D. of 15.75 mm and a inner tube O.D. of 12.70 mm, the free flow area is 6.82×10^{-5} m^2, the perimeter is 89.38 mm and the hydraulic diameter is 3.05×10^{-3} mm. At a primary coolant flow rate of 1.146×10^{-4} m^3/s, the flow velocity and Reynolds number are 1.68 m/s and 7,014, respectively. The annulus-side friction factor can be calculated using curve fits for the laminar and turbulent friction factor data of Kays and Leung (1963) by Garimella and Christensen (1995). The transition between laminar and turbulent flow was determined using curve fits to the lower (transition from laminar) and upper (transition to turbulent) critical Reynolds numbers for different annulus radius ratios reported by Walker *et al.* (1957). The transition Reynolds number for an annulus is a function of the radius ratio, which is defined as follows:

$$r^* = \frac{(\text{O.D.})_{\text{inner}}}{(\text{I.D.})_{\text{outer}}} \tag{4. 10}$$

For the current sample conditions, the lower and upper transition Reynolds numbers are 2,643 and 3,233, respectively. The flow in the annulus is in the turbulent region, with a friction factor is 0.0365. The annulus-side frictional pressure drop (in the test section) can be calculated as follows:

$$\Delta P_{\text{annulus}} = \frac{1}{2} \cdot f_{\text{annulus}} \cdot \rho \cdot V_{\text{annulus}}^{\ 2} \cdot \frac{L_{\text{test}}}{D_{\text{h,annulus}}} \tag{4. 11}$$

Thus, the primary water pressure drop in the test section is 4.9 kPa.

4.1.2.1.3 Pressure loss in the secondary shell and tube heat exchanger

The primary water flows through the shell side of the secondary heat exchanger. According to the manufacturer, the shell side pressure drop (in psi) is a function of volumetric flow rate (in gpm) as follows:

$$\Delta P_{shell}(\text{in psi}) = 0.49157(\text{Actual Flowrate in gpm})^{1.9} \tag{4. 12}$$

For a primary water flow rate of 1.146×10^{-4} m^3/s (1.816 gpm), the pressure loss in the shell side of the secondary heat exchanger is 10.5 kPa (1.527 psi).

4.1.2.1.4 Pump efficiency

From the above calculations, the total pressure loss for the primary water is given by:

$$\begin{aligned} \Delta P_{primary} &= \Delta P_{tube} + \Delta P_{flow\,meter} + \Delta P_{annulus} + \Delta P_{shell} \\ &= 20.77 + 1.08 + 4.9 + 10.5 = 37.3 kPa \end{aligned} \tag{4. 13}$$

The ideal pump work is a function of the total water pressure drop and is given by:

$$W_{\text{ideal}} = \text{Water Flow Rate} \cdot \Delta P_{\text{primary}} \tag{4. 14}$$

The operating shaft work is given by:

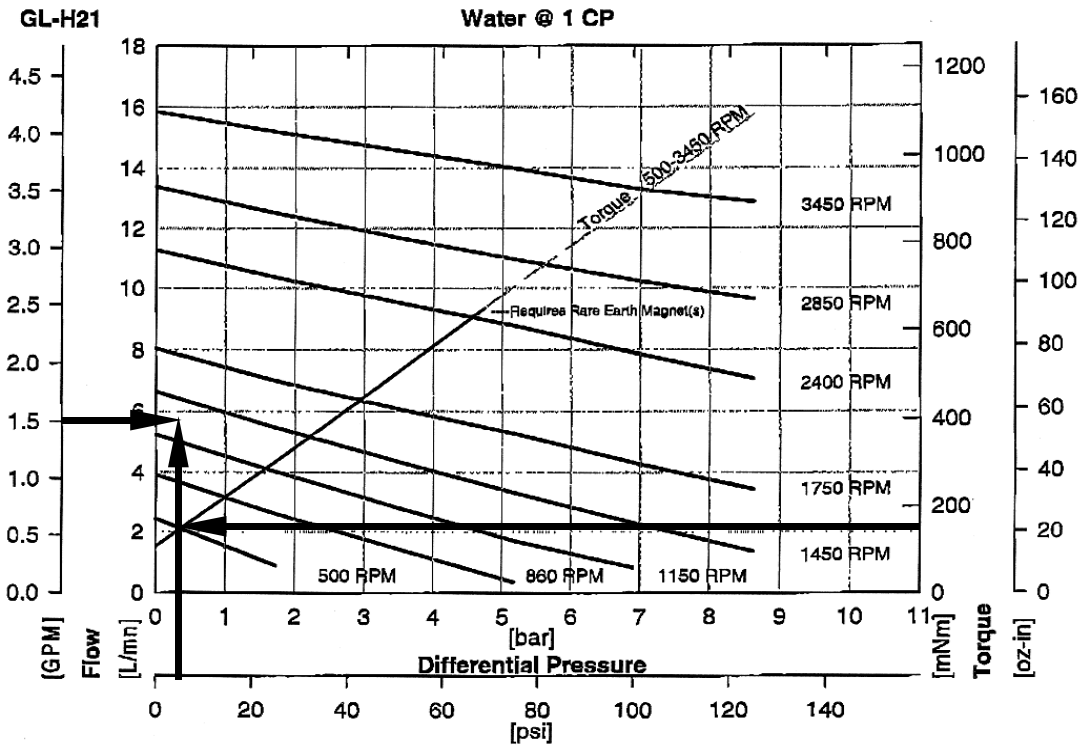

Figure 4. 2 Micropump Series 5000 H21 Pump Curve

$$W_{shaft} = \tau \cdot \omega \tag{4. 15}$$

The applied torque and shaft rotational speed are supplied by the manufacturer (Micropump), as shown in Figure 4.2 for the Micropump Series 5000 H21 pump head model. The applied torque is a function of the primary water loop pressure drop (or pump pressure rise). The pump shaft rotational speed is the function of the actual flow rate and pressure drop. For a primary water flow rate of 1.146×10^{-4} m3/s (1.816 gpm) and a total pressure loss in the primary loop of 37.3 kPa (5.4 psi), the ideal pump work is 4.27 W. The applied torque and the shaft rotational speed are 0.15 N-m and 1700 rpm according to the manufacturer's specification, resulting in a shaft work of 26.69 W. The pump efficiency and the pump heat addition can be calculated using the following equations.

$$\eta = \frac{W_{ideal}}{W_{shaft}} \tag{4. 16}$$

$$Q_{pump} = (1-\eta) \cdot W_{shaft} \quad (4.17)$$

According to the above equations, the pump efficiency is 16%, and the pump heat addition is 22.42 W (Here, it is assumed that all the pump losses are rejected into the coolant as heat). Figure 4.3 shows the pump heat addition as a function of the volumetric flow rate. A power series curve fit was developed from the data in Figure 4.3 as follows:

$$\dot{Q}_{pump} = 10.66 \cdot VolFlo_{prim,w,gpm}^{1.2474} \quad (4.18)$$

For the representative data point, with a primary flow rate of 1.146×10^{-4} m^3/s (1.816 gpm), the pump heat addition calculated from equation (4.18) is 22.44 W.

4.1.2.2 Ambient Heat Losses

Ambient heat losses were minimized by using fiberglass insulation for the test section and the primary and secondary coolant loops. Furthermore, the small temperature

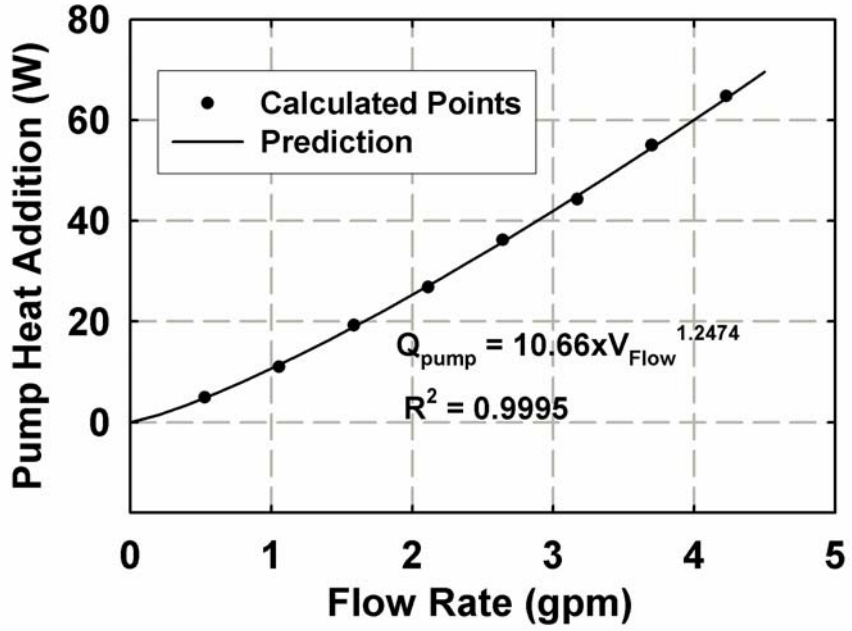

Figure 4. 3 Pump Heat Addition vs. Flow Rate for Micropump Series 5000 H21 Pump

differences between the fluid and the ambient (ΔT = 11.65°C) lead to low heat losses. The heat loss from the primary coolant to the ambient consists of losses from three locations: test section heat exchanger, secondary heat exchanger, and the rest of the plumbing in the primary loop. The heat is assumed to be lost from the average coolant temperature to the ambient temperature (~23°C). A detailed heat loss calculation is also shown in Appendix A.

4.1.2.2.1 Test Section Heat Loss

For the test section, the heat flows through the following resistances: water side convection, outer tube wall, insulation, natural convection, and radiation. Figure 4.4 shows a schematic of the heat transfer resistance network. The annulus-side heat transfer coefficient is calculated using curvefits developed by Garimella and Christensen (1995) for laminar and turbulent Nusselt numbers in annuli reported by Kays and Leung (1963).

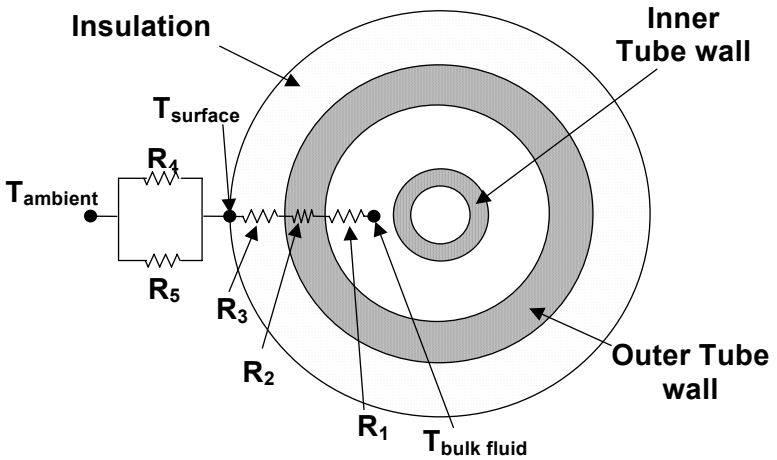

Figure 4. 4 Resistance Network for the Ambient Heat Loss Calculation

The transition between laminar and turbulent flow was determined using curve fits to the lower and upper critical Reynolds numbers for different annulus radius ratios reported by Walker *et al.* (1957). For a primary flow rate of 1.146×10^{-4} m^3/s, the Reynolds number in the annulus of the test section is 7,014. With the lower and upper transition Reynolds numbers of 2,643 and 3,233, respectively, and a radius ratio of 0.8065, the heat transfer coefficient in the annulus of the test section is 11,143 W/m^2-K. Thus, the water-side convective heat transfer resistance can be calculated as follows:

$$R_{conv} = \frac{1}{h_{annulus} \cdot A_{eff,annulus}} \tag{4. 19}$$

where, $A_{eff,annulus}$ is the annulus-side heat transfer area defined in the following equation:

$$A_{eff,annulus} = \pi (I.D.)_{outer} L_{test} \tag{4. 20}$$

For a 15.75 mm inner diameter of the outer tube, and a 0.292 m test section length, the annulus-side heat transfer area is 1.445×10^{-2} m^2, resulting in a water-side convective heat transfer resistance of 6.21×10^{-3} K/W. The tube-wall resistance is calculated as follows:

$$R_{wall} = \frac{\ln\left[\frac{(O.D.)_{outer}}{(I.D.)_{outer}}\right]}{2\pi L_{test} k_{wall}} \tag{4. 21}$$

where, $(I.D.)_{outer}$ and $(O.D.)_{outer}$ are the inner and outer diameters of the outer tube wall. For the 0.292 m test section of the stainless steel tube (k = 15.02 W/m-K) with outer and inner diameters of 19.05 mm and 15.75 mm, respectively, the wall resistance is 6.90×10^{-3} K/W. The resistance of the insulation is calculated in a similar manner. With an insulation thickness of 26.67 mm (O.D. = 72.39 mm, I.D. = 19.05 mm) and a thermal

conductivity of 0.043 W/m-K, the resistance of the insulation $R_{insulation}$ is 16.92 K/W. Heat transfer from the insulation to the ambient air is due to natural convection and radiation. The natural convection resistance is based on the Rayleigh number, which is defined as follows:

$$\mathrm{Ra} = \frac{g\beta(T_{surface} - T_{\infty})D_{insulation}^{3}\rho^{2}\,\mathrm{Pr}}{\mu^{2}} \tag{4. 22}$$

where $D_{insulation}$ is the outer diameter of the insulation, g is the acceleration due to gravity, β is the volumetric coefficient of thermal expansion, and ρ, μ and Pr are air properties evaluated at the fluid temperature defined as follows:

$$T_{fluid} = \frac{T_{surface} + T_{\infty}}{2} \tag{4. 23}$$

$T_{surface}$ and T_{∞} are the surface temperature of the insulation and ambient temperature, respectively. Assuming a value of $T_{surface}$, the correlation suggested by Churchill and Chu (1975) was used to determine the natural convection heat transfer coefficient h_{nc}. Through the energy balance in (equation 4.5), the surface temperature $T_{surface}$ and thus the ambient heat loss through the test section heat exchanger can be determined iteratively.

$$\begin{aligned} Q_{ambient,test} &= \frac{\left(T_{water} - T_{surface}\right)}{R_{conv} + R_{wall} + R_{insulation}} \\ &= h_{nc}A\left(T_{surface} - T_{ambient}\right) + \sigma\varepsilon A\left(T_{surface}^{4} - T_{ambient}^{4}\right) \end{aligned} \tag{4. 24}$$

where the heat transfer area A on the surface of the insulation is defined as, $A = \pi D_{insulation} L_{test}$. For a test section length of 0.292 m and an insulation outer diameter of 72.39 mm, the resulting natural convection heat transfer coefficient is 2.271 W/m^2-K. The surface temperature and the test section ambient heat loss were iteratively solved to

yield 24.26°C and 0.61 W, respectively. Of the 0.61 W from the surface, 0.42 W is attributed to radiation. It was assumed that the insulation has an emissivity of 0.85.

4.1.2.2.2 Secondary Heat Exchanger Heat Loss

The ambient heat loss through the primary-to-secondary shell-and-tube heat exchanger can be calculated in a manner similar to that described for the test section ambient heat loss. The primary water flows through the shell side of the secondary heat exchanger, and the wall is assumed to be at the bulk temperature. Hence, only the wall and insulation resistances are used in Equation (4.24). This assumption is reasonable because of the large water-side heat transfer coefficient. The secondary heat exchanger has a shell outer diameter of 25.4 mm and a wall thickness of 1.25 mm. With a heat exchanger length of 0.173 m and an average water temperature of 19.79°C, the heat lost to the ambient is -0.11 W. The negative sign here indicates that since the water temperature inside the heat exchanger was below the ambient temperature the heat flow (even though minimal) was actually from the ambient to the water.

4.1.2.2.3 Primary Loop Tubing Heat Loss

The ambient heat loss through the rest of the primary loop is also calculated as described above. However, in this case, the water flow is through a single tube instead of an annulus. The Dittus and Boelter equation is used to calculate the water-side convection heat transfer resistance.

Thus, for the tube O.D. and wall thickness of 12.70 and 0.89 mm, respectively, and a primary water flow rate of 1.146×10^{-4} m^3/s, the flow velocity is found to be 1.22 m/s. The corresponding Reynolds number and Nusselt number are 18,269 and 95.58, respectively, which yields a water-side heat transfer coefficient of 5339 W/m^2-K. The

iterative procedure described in previous sections was used to calculate the ambient heat loss in the rest of the primary loop plumbing. The total tubing length used here includes tubing that connects the primary-to-secondary heat exchanger to the test section heat exchanger, as well as "equivalent" lengths for the pump housing and flow meter which are defined as follows,

$$L_{equivalent} = \frac{A}{\pi D_{tubing}} \tag{4. 25}$$

Figure 4.5 shows the outside of the pump housing, which has a total surface area of 0.0451 m^2. The resulting equivalent length of 12.70 mm tubing for the pump housing is 1.133 m. Similarly the flow tube's O.D and length of 90 and 55 mm resulted in an equivalent length of 0.54 m of 12.7 mm tubing. Hence, the total length of the primary loop tubing is 4.22 m, with an ambient heat loss of 8.35 W. Therefore, the total heat lost to the ambient from the entire primary loop is 8.85 W.

The test section heat duty can now be readily derived:

$$\begin{aligned} Q_{w,test} &= Q_{w,sec} + Q_{ambient} - Q_{pump} \\ &= 561.1 + 8.85 - 22.44 = 547.5\,W \end{aligned} \tag{4. 26}$$

4.1.3 Heat Transfer Coefficient Calculation

The condensation heat transfer coefficient is determined from the measured test section heat duty (discussed above), the applicable temperature difference, and the other thermal resistances. The calculations are illustrated using the same data point as was used for the explanation of the test section quality and heat duty calculations. A detailed calculation procedure is included in Appendix A.

The primary coolant flows through the annulus side of the test section. For heat

transfer from the refrigerant to the water, the annulus-side resistance can be calculated as follows:

$$R_{wall} = \frac{\ln\left[(O.D.)_{inner} / (I.D.)_{inner}\right]}{2\pi \cdot k_{wall} L_{test}} \tag{4. 27}$$

where $(I.D.)_{inner}$ and $(O.D.)_{inner}$ are the inner and outer diameter of the inner tube of the test section, and L_{test} is the length of the test section heat exchanger. The logarithmic temperature difference between the primary water and the refrigerant of the test section heat exchanger is calculated using the following equation,

$$LMTD = \frac{(T_{refg,i} - T_{water,o}) - (T_{refg,o} - T_{water,i})}{\ln[(T_{refg,i} - T_{water,o}) / (T_{refg,o} - T_{water,i})]} \tag{4. 28}$$

where all the temperatures are measured quantities. The overall UA and the total heat transfer resistance of the test section can be calculated as

$$UA = \frac{Q_{w,test}}{LMTD} \tag{4. 29}$$

$$R_{total} = \frac{1}{UA} \tag{4. 30}$$

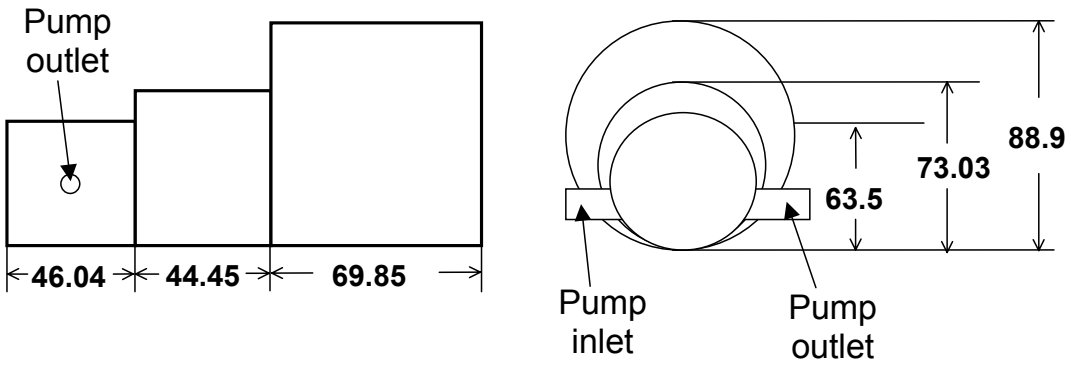

Figure 4.5 Side (a) and Front (b) View Sketches of the Micropump Series 5000 Model H21 Pump Housing (Measurements are in mm; Drawing Not to Scale)

The refrigerant-side heat transfer resistance, and thus the heat transfer coefficient, can be deduced from the total heat transfer resistance as follows:

$$R_{refg} = R_{total} - R_{annulus} - R_{wall} \tag{4. 31}$$

$$h_{refg} = \frac{1}{R_{refg}\left[\pi \cdot (I.D.)_{inner} L_{test}\right]} \tag{4. 32}$$

As reported in the previous sections, the heat transfer coefficient in the annulus for this representative point is 11,143 W/m^2-K, resulting in a thermal resistance of 7.7×10^{-3} K/W. The calculated tube-wall resistance is 4.12×10^{-4} K/W. With measured primary coolant and refrigerant inlet and outlet temperatures of the test section at 34.32, 34.97, 59.78 and 59.64°C, respectively, the corresponding LMTD is 25.06°C. The overall UA, and thus the total heat transfer resistance, are 21.85 W/K and 4.58×10^{-2} K/W. The refrigerant-side resistance is calculated from the measured overall conductance of the test section and the coolant-side and tube-wall resistances, and for this case is 3.776×10^{-2} K/W. This yields a condensation heat transfer coefficient of 3,079 W/m^2-K. For the above representative case, $R_{refg}/R_{coolant}$ =4.9.

As mentioned in Chapter 3, outer wall temperatures of the inner tube were measured by three thermocouples for the 9.4 mm tube (6 for 6.2 mm tube) and used to derive redundant refrigerant heat transfer coefficients to validate the refrigerant heat transfer coefficients obtained from the above method using water-side, wall and total heat transfer resistances. The average deviation between the wall-mounted thermocouples was 1.39°C (range: 0.4 – 2.9°C) and 0.36°C (range: 0.0 – 1.3°C) in the 9.4 and 6.2 mm tubes, respectively. Figure 4.6 shows some cases of measured wall temperatures for P_r = 0.8. By assuming that the wall temperature is the average of the thermocouple measurements,

the logarithmic temperature difference between the wall of the test section and the refrigerant is calculated using the following equation:

$$LMTD_{refg-wall} = \frac{(T_{refg,i} - T_{wall}) - (T_{refg,o} - T_{wall})}{\ln[(T_{refg,i} - T_{wall})/(T_{refg,o} - T_{wall})]} \quad (4.\ 33)$$

The UA and R based on $LMTD_{refg\text{-}wall}$ and the test section heat duty can be calculated as follows:

$$UA_{refg-wall} = \frac{Q_{w,test}}{LMTD_{refg-wall}} \quad (4.\ 34)$$

$$R_{total,refg-wall} = \frac{1}{UA_{refg-wall}} \quad (4.\ 35)$$

The refrigerant-side heat transfer resistance, and thus the heat transfer coefficient, was calculated from this resistance by subtracting the tube-wall resistance, as follows:

$$R_{refg,wall\ based} = R_{total,refg-wall} - R_{wall} \quad (4.\ 36)$$

$$h_{refg,wall\ based} = \frac{1}{R_{refg-wall}\left[\pi \cdot (I.D.)_{inner} L_{test}\right]} \quad (4.\ 37)$$

For this representative data point, with measured wall temperatures of the test section at 37.8 (inlet), 36.3 (center) and 35.3°C (outlet), the average wall temperature is 36.47°C. The corresponding $LMTD_{refg\text{-}wall}$ is 23.22°C. The overall $UA_{refg\text{-}wall}$, and thus the total heat transfer resistance, are 23.58 W/K and 4.24×10^{-2} K/W, respectively. The refrigerant-side resistance is calculated from the measured overall conductance of the test section and the tube-wall resistances, and for this case is 4.2×10^{-2} K/W. This yields a condensation heat transfer coefficient of 2,761 W/m^2-K. Thus, for this data point, the refrigerant heat transfer coefficient based on wall temperature measurements is 10.33%

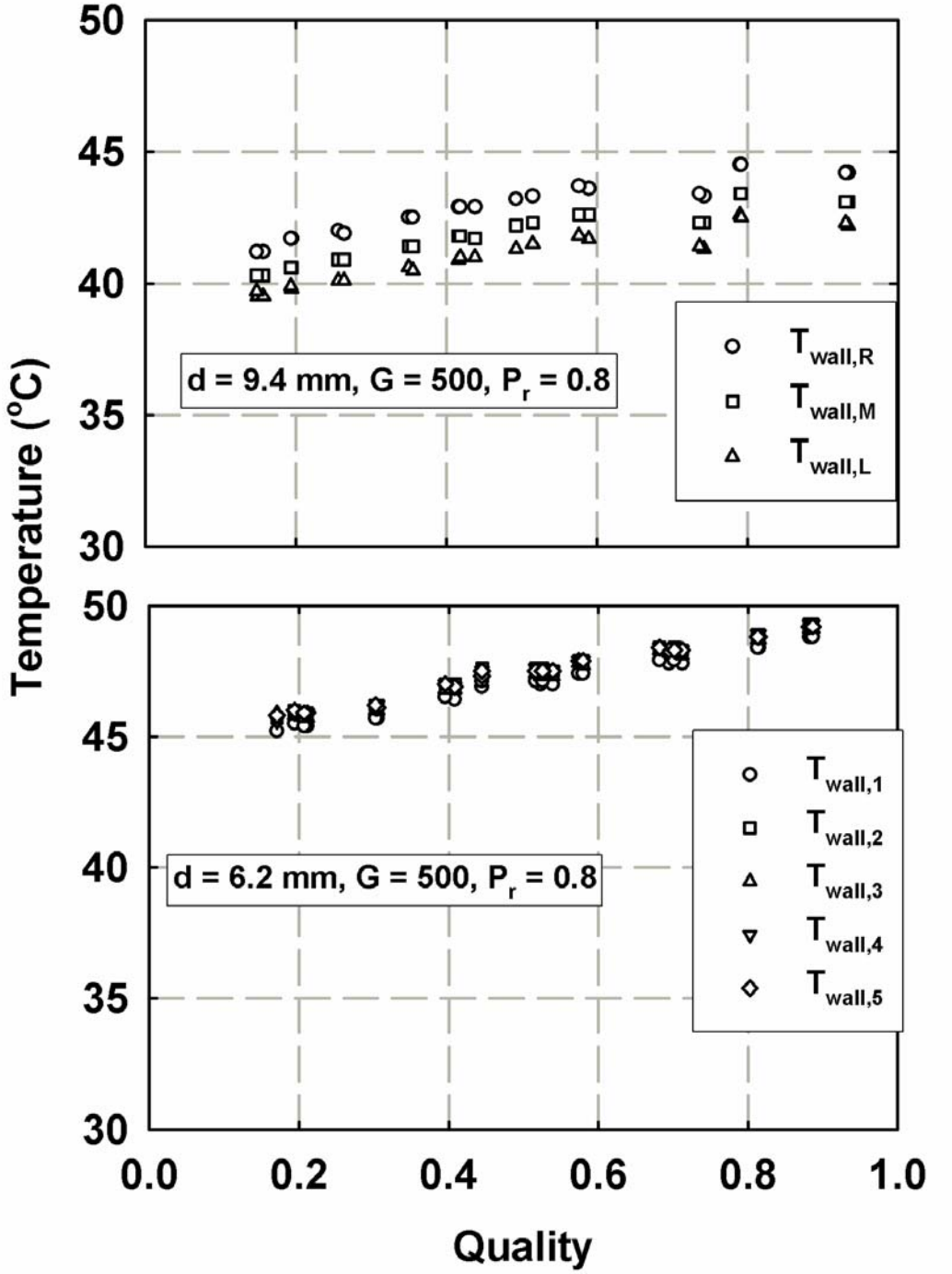

Figure 4.6 Wall Temperature versus Quality (Sample Cases)

less than the refrigerant heat transfer coefficient of 3,079 W/m^2-K determined from the overall UA. For the entire phase change data, the average difference between the refrigerant heat transfer coefficients obtained using the resistance ratio and wall temperature methods was 10.7% (5-18% range) and 10.4% (4.8-19.2% range) for 9.4 and 6.2 mm tubes, respectively.

4.2 Uncertainty Analysis

An uncertainty analysis (Taylor and Kuyatt, 1994) was conducted to estimate the uncertainty in the refrigerant heat transfer coefficient using the error propagation approach. An Engineering Equation Solver (EES) (Klein, 2003) program was developed to evaluate all the uncertainties needed in this study .

4.2.1 Average Test Section Quality

From equation (4.1), the uncertainty in the test section inlet quality is deduced from the pre-cooler heat duty as follows:

$$U_{Q_{pre}}{}^2 = \left(\frac{\partial Q_{pre}}{\partial Vol_{w,pre}} U_{Vol_{w,pre}} \right)^2 + \left(\frac{\partial Q_{pre}}{\partial h_{w,pre,out}} U_{h_{w,pre,out}} \right)^2 + \left(\frac{\partial Q_{pre}}{\partial h_{w,pre,in}} U_{h_{w,pre,in}} \right)^2 \quad (4.38)$$

where $Vol_{w,pre}$, $h_{w,pre,in}$ and $h_{w,pre,out}$ are the measured volumetric flow rate, and inlet and outlet enthalpies of the pre-condenser cooling water, respectively. The influence of density (needed for mass flow rate calculation of cooling water) on uncertainty was neglected in the above calculation. The relative uncertainty in the volumetric flow rate is ±0.5% of the reading according to the manufacturer (see Table 3.4). The uncertainty in coolant enthalpy is given by:

$$U_h{}^2 = \left(\frac{\partial h}{\partial T} U_T \right)^2 = \left(c_p U_T \right)^2 \quad (4.39)$$

where the uncertainty in temperature measurements is ±0.5°C (see Table 3.4), which results in an uncertainty in the enthalpy of 2.09 kJ/kg. For the representative data point, the pre-condenser heat duty and the associated uncertainty is 2.21±0.037 kW. From equation (4.2), the uncertainty of the refrigerant enthalpy at the pre-condenser outlet can be calculated using the following equation:

$$U_{h_{refg,pre,out}}{}^2 = \left(\frac{\partial h_{refg,pre,out}}{\partial h_{refg,pre,in}} U_{h_{refg,pre,in}}\right)^2 + \left(\frac{\partial h_{refg,pre,out}}{\partial Q_{pre}} U_{Q_{pre}}\right)^2 + \left(\frac{\partial h_{refg,pre,out}}{\partial \dot{m}_{refg}} U_{\dot{m}_{refg}}\right)^2 \quad (4.40)$$

The uncertainty in the pre-condenser inlet enthalpy is as follows:

$$U_{h_{refg,pre,in}}{}^2 = \left(\frac{\partial h}{\partial T} U_T\right)^2 + \left(\frac{\partial h}{\partial P} U_P\right)^2 \quad (4.41)$$

where

$$\frac{\partial h}{\partial T} = \frac{h_{T+U_T,P} - h_{T-U_T,P}}{2U_T} \quad (4.42)$$

$$\frac{\partial h}{\partial P} = \frac{h_{T,P+U_P} - h_{T,P-U_P}}{2U_P} \quad (4.43)$$

With a refrigerant mass flow rate uncertainty of 2.097×10^{-5} kg/s, and a pre-condenser refrigerant inlet enthalpy of 494.3±0.667 kJ/kg for the representative data point, the uncertainty in the pre-condenser outlet enthalpy is 388.9±1.914 kJ/kg.

The test section inlet quality is a function of enthalpy and pressure, with the corresponding uncertainty given by:

$$U_{x_{test,in}}{}^2 = \left(\frac{\partial x_{test,in}}{\partial h_{refg,pre,out}} U_{h_{refg,pre,out}}\right)^2 + \left(\frac{\partial x_{test,in}}{\partial P} U_P\right)^2 \quad (4.44)$$

where,

$$\frac{\partial x_{test,in}}{\partial h} = \frac{x_{h+U_h,P} - x_{h-U_h,P}}{2U_h} \quad (4.45)$$

and,

$$\frac{\partial x_{test,in}}{\partial P} = \frac{x_{h,P+U_P} - x_{h,P-U_P}}{2U_P} \quad (4.46)$$

For the representative data point, the test section inlet quality and the associated uncertainty is 0.75±0.018. Similarly, the test section outlet quality and the associated uncertainty is 0.56±0.098, resulting in a test section average quality of 0.66±0.05.

4.2.2 Test Section Heat Duty

To estimate the uncertainty in test section heat duty, uncertainties in secondary water heat duty, pump heat addition and ambient heat loss are calculated as shown in the following equation:

$$U_{Q_{w,test}}^2 = \left(\frac{\partial Q_{w,test}}{\partial Q_{w,sec}} U_{Q_{w,sec}}\right)^2 + \left(\frac{\partial Q_{w,test}}{\partial Q_{ambient}} U_{Q_{ambient}}\right)^2 + \left(\frac{\partial Q_{w,test}}{\partial Q_{pump}} U_{Q_{pump}}\right)^2 \quad (4.47)$$

The heat load in the secondary heat exchanger is calculated using the mass flow rate of the coolant (measured using a Coriolis mass flowmeter) and the inlet and outlet temperatures. The thermal amplification provided by the low flow rate of the secondary coolant (1.181×10^{-2} kg/s) is evident from the temperature rise in this fluid. Thus, the secondary coolant temperature rise for this data point is 11.36°C, while the primary coolant ΔT is only 0.7°C. The corresponding primary and secondary water flow rates are 0.114 and 1.181×10^{-2} kg/s respectively. This large temperature rise, coupled with the high-accuracy flow rate measurement, yields a low uncertainty in the secondary coolant duty, ±6.23%, (561.1±34.95 W). A very conservative uncertainty of ±50% was assumed for pump heat dissipation and ambient heat loss. For this representative case of G = 302.4 kg/m^2-s, x = 0.6581, and p = $0.8\times P_{crit}$, the pump heat addition and ambient heat

loss were estimated using this procedure to be 22.44±11.22 W and 8.85±4.43 W, respectively. Because the net contribution of the ambient heat loss (1.6%) and pump heat addition (4.1%) terms is small by design, the relatively high assumed uncertainties in these terms are not very significant in determining the test section heat duty. Thus, the resulting test section heat duty is 547.5±36.97 W. With a log mean temperature difference of 25.06±0.79°C, the overall heat transfer conductance, UA, is 21.85±1.56 W/K.

4.2.3 Heat Transfer Coefficient

Neglecting the uncertainties in the heat transfer area and wall resistance, the uncertainty in the refrigerant-side heat transfer coefficient is as follows:

$$U_{h_{refg}}{}^2 = \left(\frac{\partial h_{refg}}{\partial UA} U_{UA} \right)^2 + \left(\frac{\partial h_{refg}}{\partial h_{annulus}} U_{h_{anulus}} \right)^2 \qquad (4.48)$$

With an assumed coolant-side heat transfer coefficient uncertainty of ±25%, the refrigerant-side heat transfer coefficient can be estimated to be 3,079±320 W/m^2-K, i.e., an uncertainty of ±10.39%. It should be noted that for this data point, $R_{refg}/R_{coolant}$ = 4.9, which ensures that the condensation side presents the governing thermal resistance and effectively minimizes the sensitivity of the calculated condensation heat transfer coefficient to the coolant-side thermal resistance. The resistance ratios ranged from 2.16 to 13.51 for all the data points in this study with an average of 5.8. Similarly, the uncertainties in the heat transfer coefficients ranged from 2.64% to 21.17% for all the data points with an average of 10.7%.

4.3 Pressure Drop

The test section pressure loss was directly measured using banks of Rosemount differential pressure transducers with a maximum uncertainty of ±0.075 to ±0.1% (±0.075% for 0-248.2 and 0-62.27 kPa range and ±0.1% for 0-6.227 kPa range) of the span. The pressure gradient was calculated from this measured pressure drop and the known test section length.

4.4 Supercritical Gas-Cooling

For each data point, the test section temperature was taken as the average of the measured inlet and outlet temperatures. The test section heat duty and heat transfer coefficient are derived using the same techniques described above for condensation tests. The detailed procedure for test section heat duty and heat transfer coefficient calculations for this supercritical case is included in Appendix C. Again, an uncertainty analysis was performed on each calculated quantity using the error propagation approach (Taylor and Kuyatt, 1994). For the whole set of data points, the uncertainty in the test section average temperature is ±0.35°C. The heat transfer coefficients and pressure gradients were derived using the technique described in the condensation heat transfer sections. Throughout the test conditions, the heat transfer coefficients varied from 1556±12.75% W/m^2-K at G = 198.4 kg/m^2-s, T = 61.15°C for the 9.4 mm tube to 11,067±17.21%W/m^2-K at G = 798.8 kg/m^2-s, T = 72.2°C for the 6.2 mm tube. It should be noted that refrigerant properties were evaluated using REFPROP 7.0 Lemmon *et al.* (2002). Uncertainties in the critical region for these properties were not considered when computing these uncertainties. Thus, in reality, the uncertainties in heat transfer

coefficients and Nusselt numbers could be higher, depending on the uncertainties in the properties.

CHAPTER 5 CONDENSATION HEAT TRANSFER AND PRESSURE DROP RESULTS AND MODEL DEVELOPMENT

This chapter provides a detailed discussion of the experimental results, model development and predictions of the phase-change data, obtained and analyzed using techniques described in Chapters 3 and 4. The data are interpreted in terms of the respective physical phenomena, which are used as the bases for model development. The high reduced pressure conditions are shown in Table 5.1. The experimental results and model development are each discussed separately in the following sections.

Table 5.1 In-Tube Condensation Test Conditions

Refrigerant	R410A
Tube Size	9.4, 6.2 mm I.D.
Pressure	3922, 4413 kPa
Temperature	~61.1, 66.6°C
Mass Flux	200-800 kg/m^2-s
Quality	0-1

5.1 In-Tube Condensation Results

This section discusses the heat transfer coefficients, pressure drops, flow regime assignment for the data, and the agreement/discrepancies between the present data and the models in the literature.

5.1.1 Heat Transfer Coefficient

The local heat transfer coefficients and uncertainties for all the experimental conditions in Table 5.1 are shown in Figures 5.1-5.2. It can be seen from these figures that the heat transfer coefficients increase with an increase in either quality or mass flux. The rate of increase in the heat transfer coefficient with mass flux is larger at the higher qualities. At the higher mass fluxes, shear-controlled condensation leads to the increase in heat transfer coefficient with quality, because of the increase in interfacial shear as the vapor-phase velocity increases, and the decrease in liquid film thickness. At low mass fluxes and qualities, gravity forces dominate, resulting in film condensation at the top of

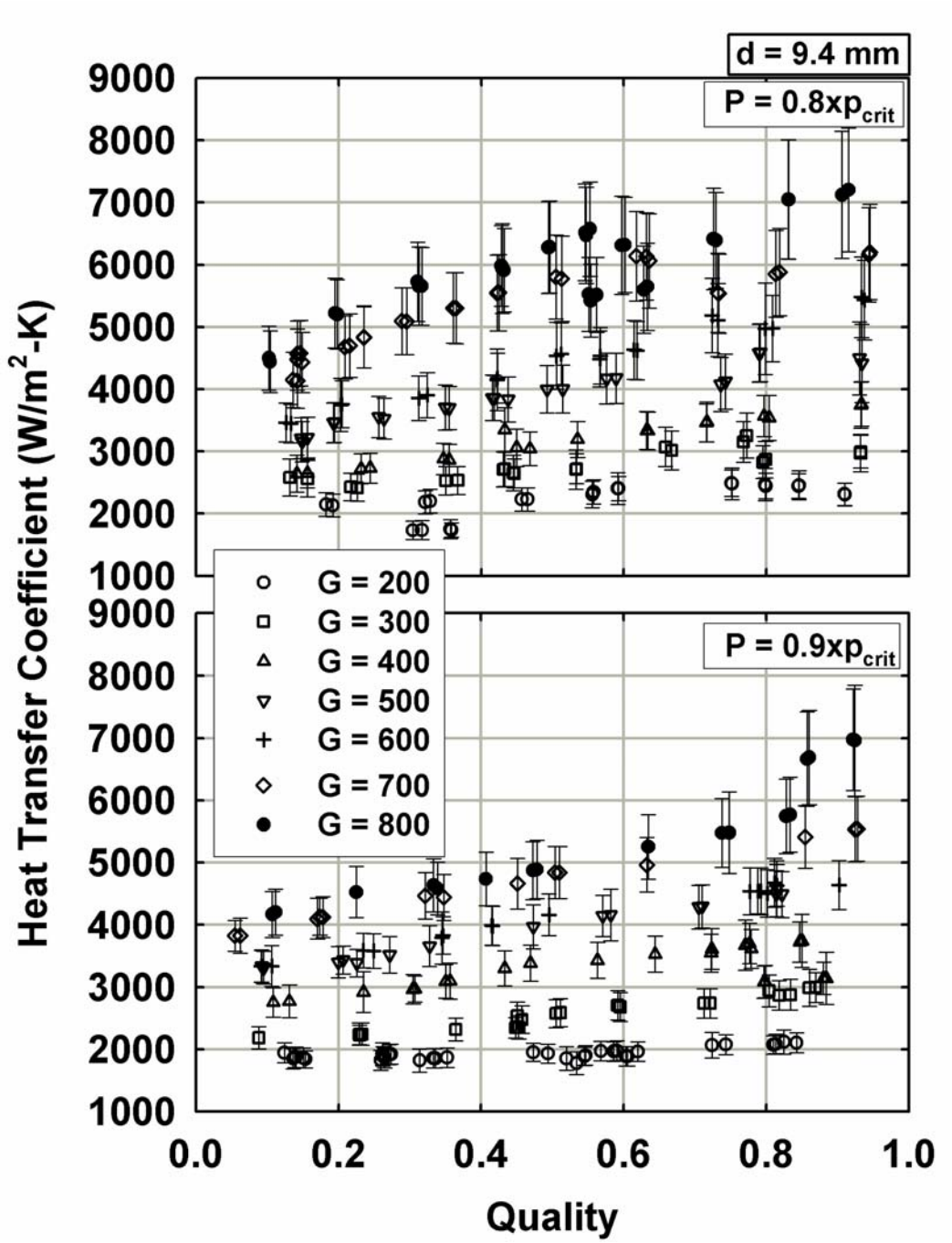

Figure 5. 1 Heat Transfer Coefficients and Uncertainties for 9.4 mm Tube

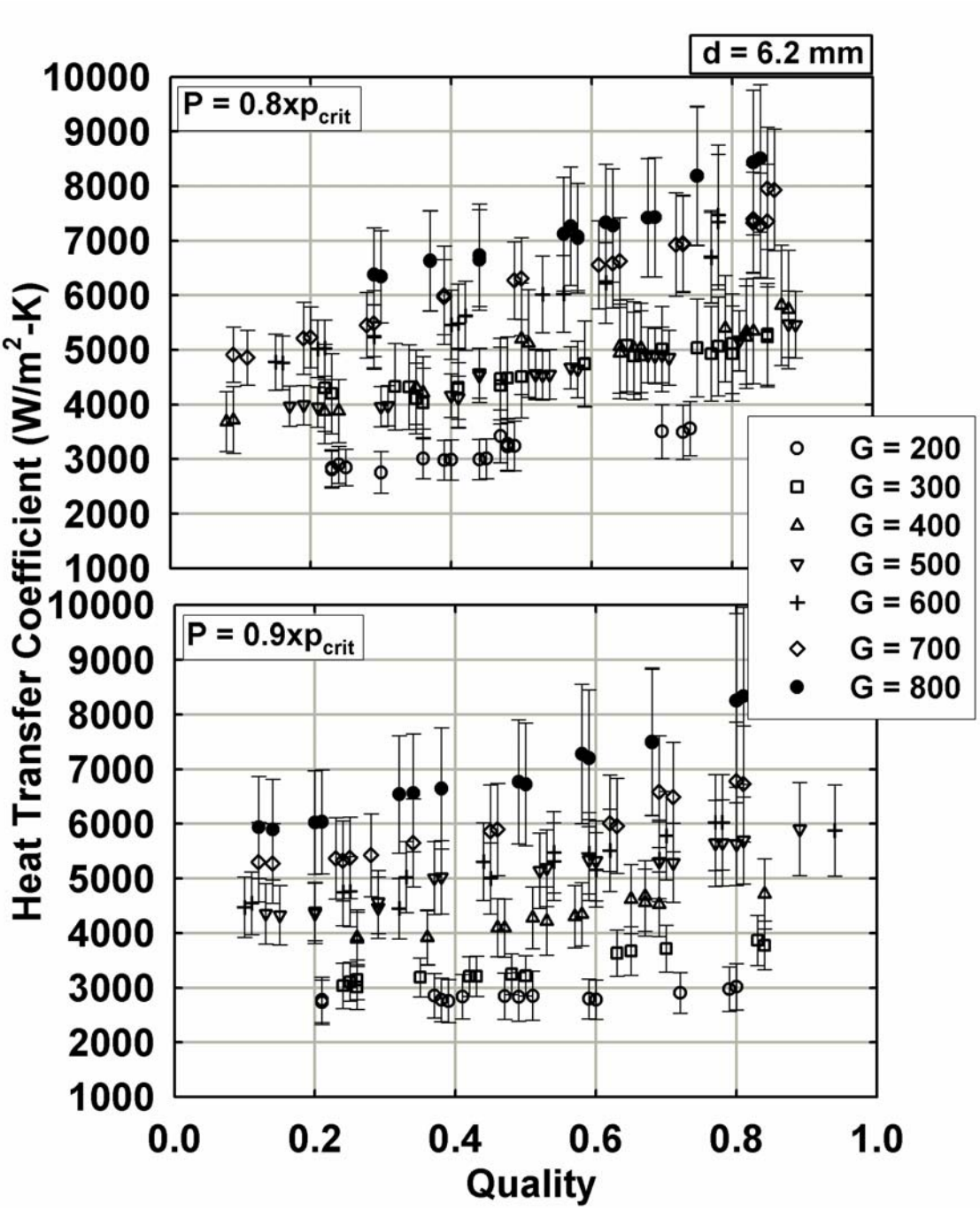

Figure 5. 2 Heat Transfer Coefficients with Uncertainties for 6.2 mm Tube

the tube, and forced-convective heat transfer in the pool of liquid at the bottom. This explains the relatively lower sensitivity of the heat transfer coefficient to quality in this regime. The average change in quality across the test section and uncertainties in heat transfer coefficients are shown in Table 5.2 for all the cases studied. It is clear from this table that the experiments were able to capture local heat transfer phenomena effectively. The quality increments across the test section were generally higher for the 6.2 mm I.D. tube as compared to the 9.4 mm I.D. tube. This may be attributed to the larger heat transfer coefficients (Figures 5.1-5.2) in the smaller diameter tube, which increase the condensation rates (per unit mass flow rate) and greater quality changes over the same length of the tube. The uncertainty in the heat transfer coefficients for the 6.2 mm tubes (~14%) is greater than the uncertainty for the 9.4 mm tube (~10%) because the refrigerant-to-coolant resistance ratio is correspondingly lower.

Table 5.2 Average Quality Increments and Uncertainties

Fluid	Tube	Conditions	Δx (%)	Uncertainty in h (%)
R410A	9.4 mm I.D.	$P = 0.8 \times p_{crit}$	8.60	10.4
		$P = 0.9 \times p_{crit}$	14.6	8.7
	6.2 mm I.D.	$P = 0.8 \times p_{crit}$	18.0	13.7
		$P = 0.9 \times p_{crit}$	24.0	14.0

Figure 5.3 shows the resistance ratio between the refrigerant side and the coolant side for all the data taken in this study. It is clear that the experimental techniques used result in the refrigerant presenting the dominant resistance for all the experiments. The resistance ratios are typically higher at low mass fluxes and decrease as the mass flux increases, because of the higher refrigerant heat transfer coefficients at the higher mass fluxes. Also, the resistance ratios are lower for the 6.2 mm tube, because of the higher refrigerant heat transfer coefficients in this tube. It should be noted that for the cases with high refrigerant heat transfer coefficients, the coolant flow rate could not be raised

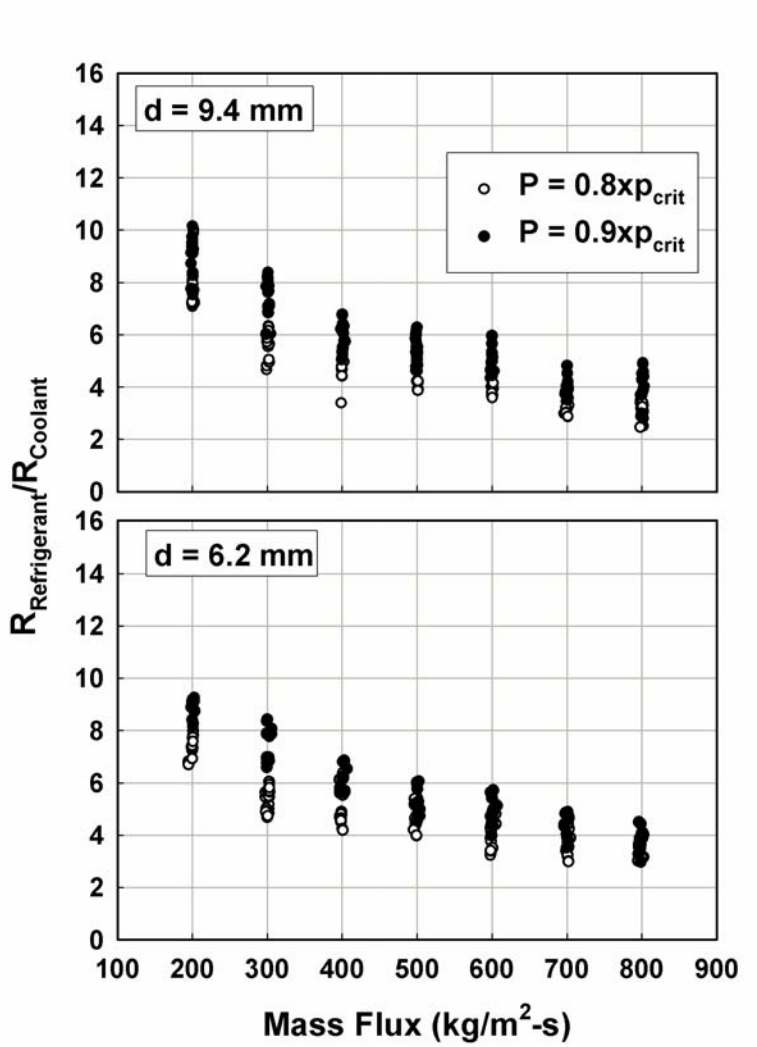

Figure 5. 3 Refrigerant-to-Coolant Resistance Ratios for all Cases

indefinitely to increase the resistance ratio. This is because a higher coolant flow rate increases the pump heat dissipation, and makes it a more significant fraction of the test section heat duty, adding to the uncertainties in heat duty determination. Therefore, the coolant flow rate for any data point was chosen based on the tradeoff between resistance ratio increase and the uncertainty in heat duty determination.

Figure 5.4 shows heat transfer coefficients derived from the above resistance-ratio analysis as well as from the wall-mounted thermocouple measurements for representative cases. It can be seen that there is very good agreement between the results from the two

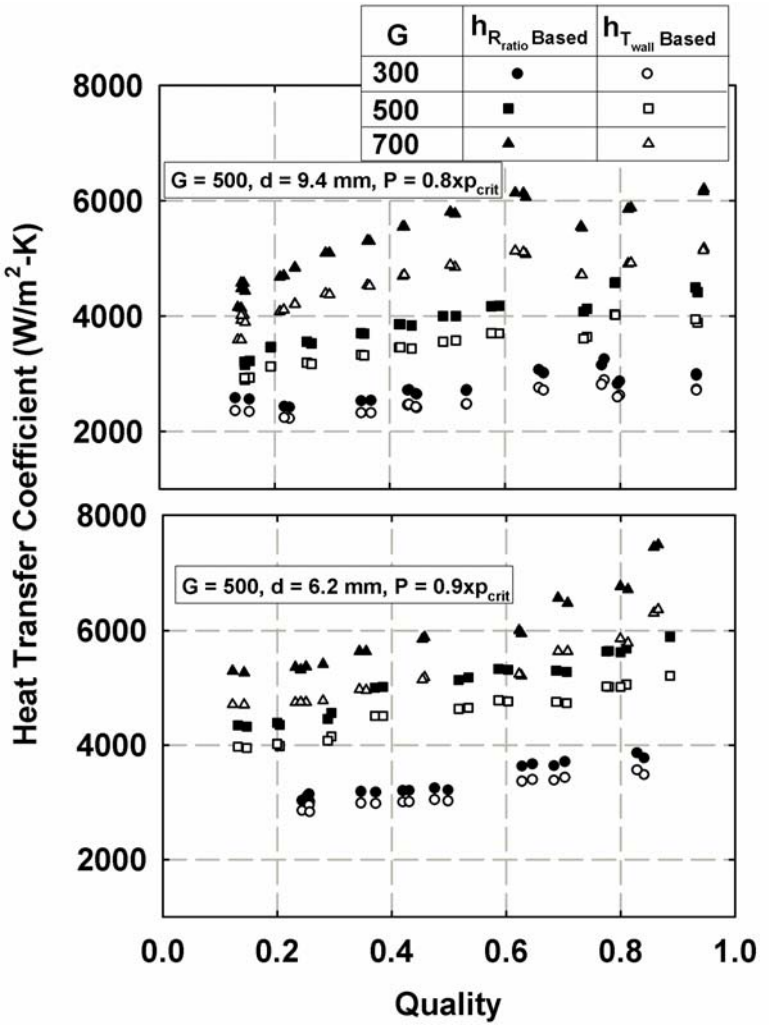

Figure 5.4 Phase-Change Heat Transfer Coefficients from Resistance Ratio Analysis and Wall-Temperature Measurements

techniques. For the entire phase-change data set, the average deviation between the two heat transfer coefficients was 10.7% (5-18% range) and 10.4% (4.8-19.2% range) for the 9.4 and 6.2 mm tubes, respectively.

The effect of reduced pressure on heat transfer coefficients is shown in Figure 5.5. There is a slight decrease in the heat transfer coefficient with an increase in the reduced pressure, particularly at high qualities. This is probably because of the compensating effects of an increase in specific heat of the two phases by a factor of about 1.7-1.9, coupled with a decrease in the latent heat by a factor of 1.33 as the pressure increases

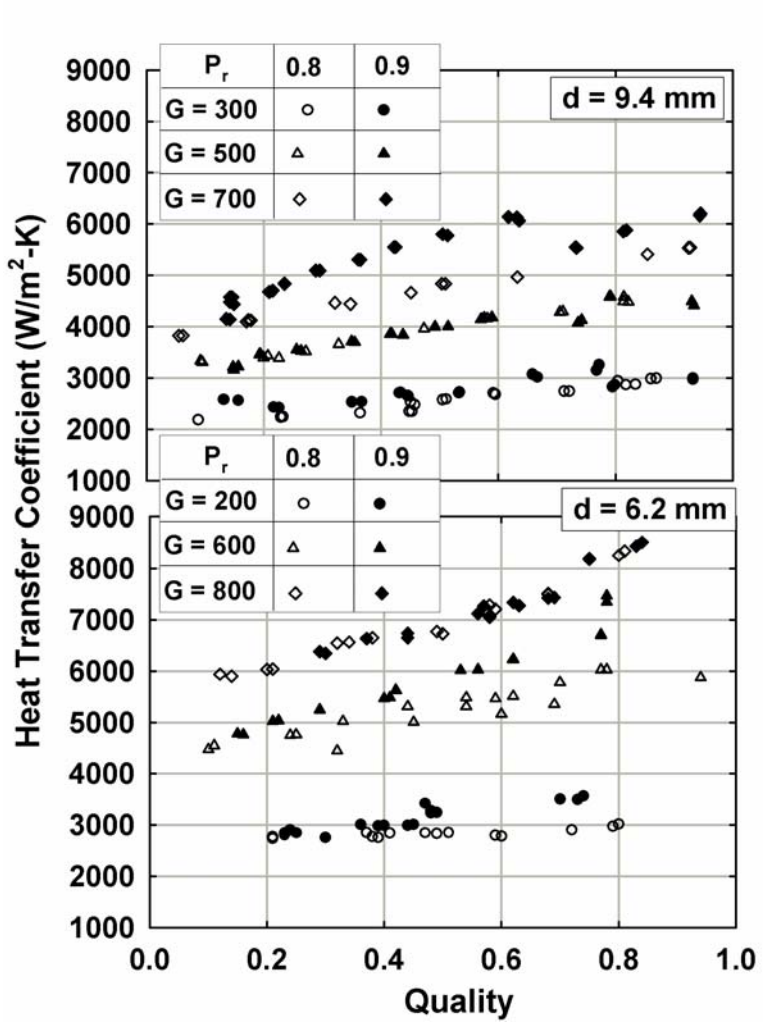

Figure 5. 5 Effect of Reduced Pressure on Heat Transfer Coefficients

from 0.8 to 0.9×p_{crit}. At low qualities, where the heat transfer coefficients are insensitive to changes in flow parameters, the effect of reduced pressure is almost negligible. Figure 5.6 shows the comparison of the heat transfer coefficients for the 9.4 and 6.2 mm tubes. As expected, the smaller diameter of the 6.2 mm tube leads to larger heat transfer coefficients under identical mass flux and pressure conditions.

5.1.2 Pressure Drop

The measured pressure drop per unit length is shown in Figures 5.7-5.8 as a function of quality for all the experimental conditions investigated. These figures show

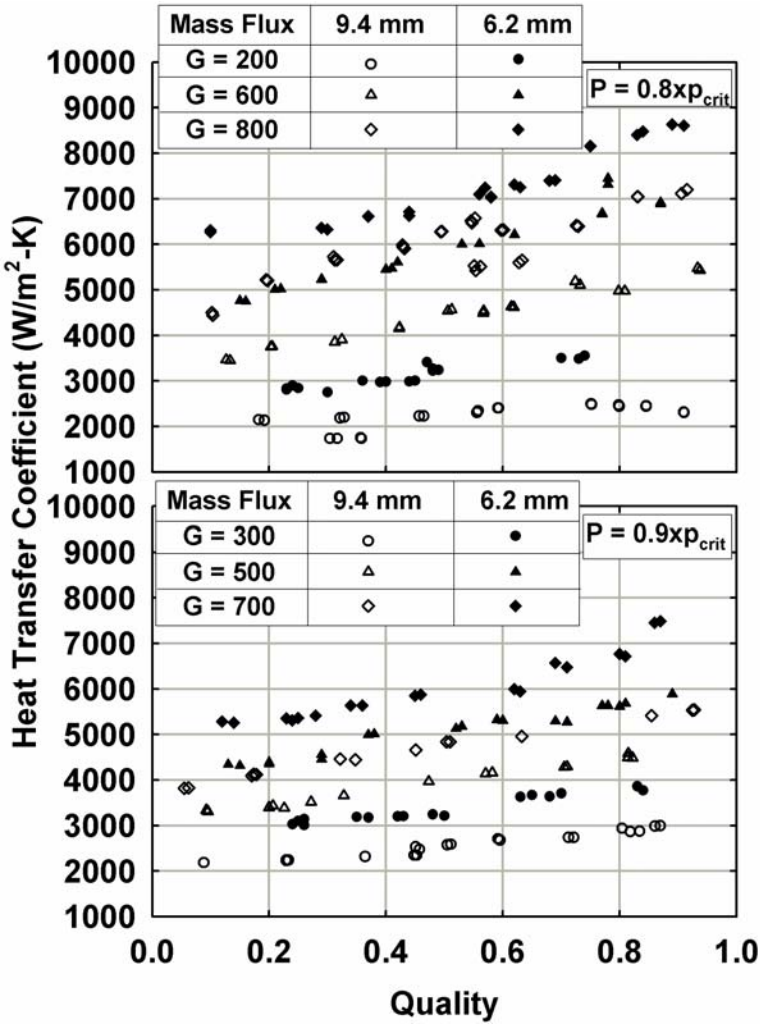

Figure 5. 6 Heat Transfer Coefficients in the 9.4 mm and 6.2 mm Tubes

that as expected, the pressure drop increases with an increase in quality and mass flux. The increased shear between the phases at the higher qualities, and the higher flow velocities at the higher mass fluxes are responsible for these trends. The increase in reduced pressure has a more pronounced effect on the pressure drop (Figure 5.9) than on the heat transfer coefficients (Figure 5.5). For the same mass flux and vapor quality, the higher the reduced pressure, the lower the pressure gradient, with this effect becoming stronger as the mass flux increases. This is because as p_r increases, the difference between the vapor and liquid properties such as density and viscosity decreases (ρ_l/ρ_v =

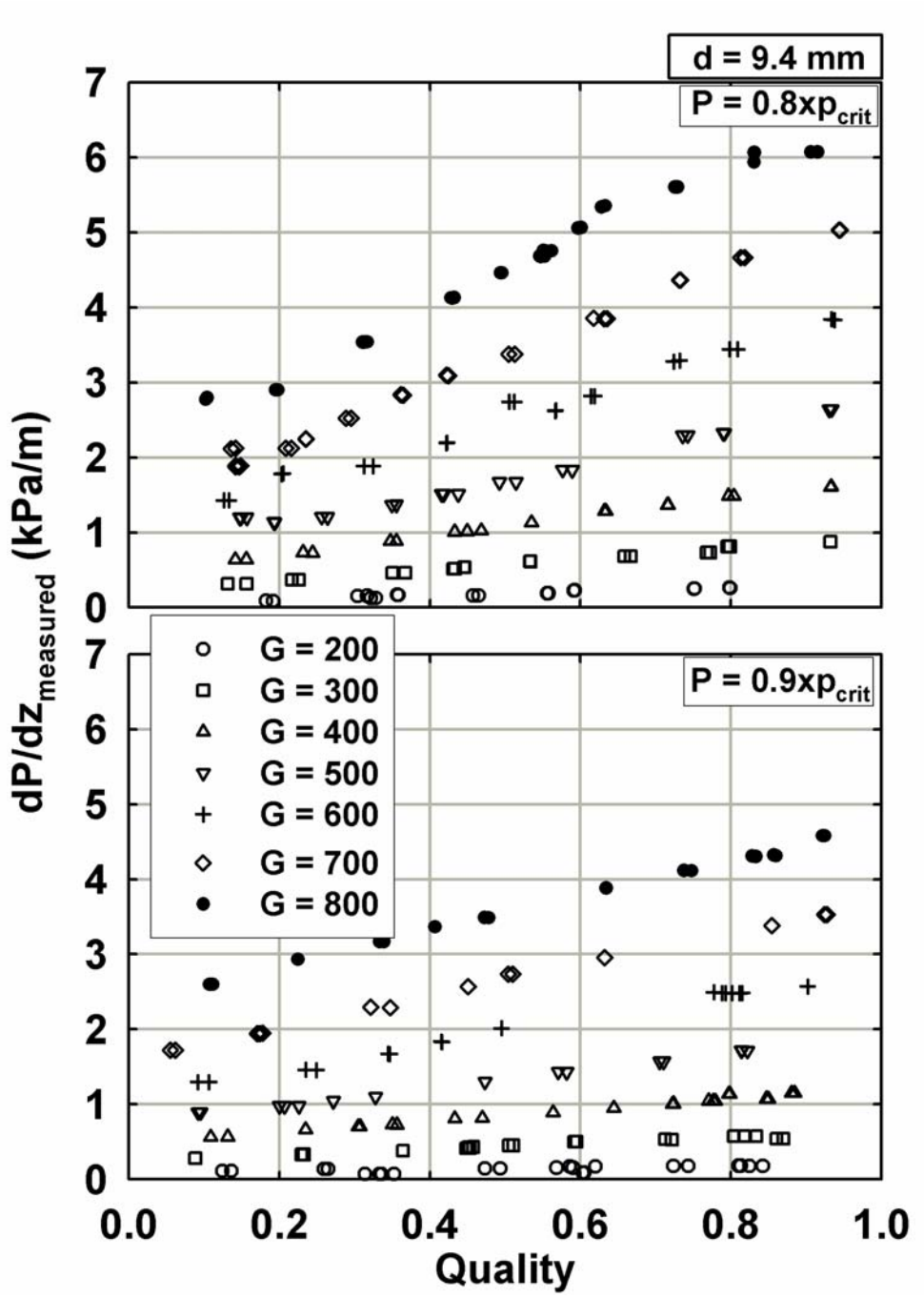

Figure 5. 7 Measured Pressure Drops in 9.4 mm Tube

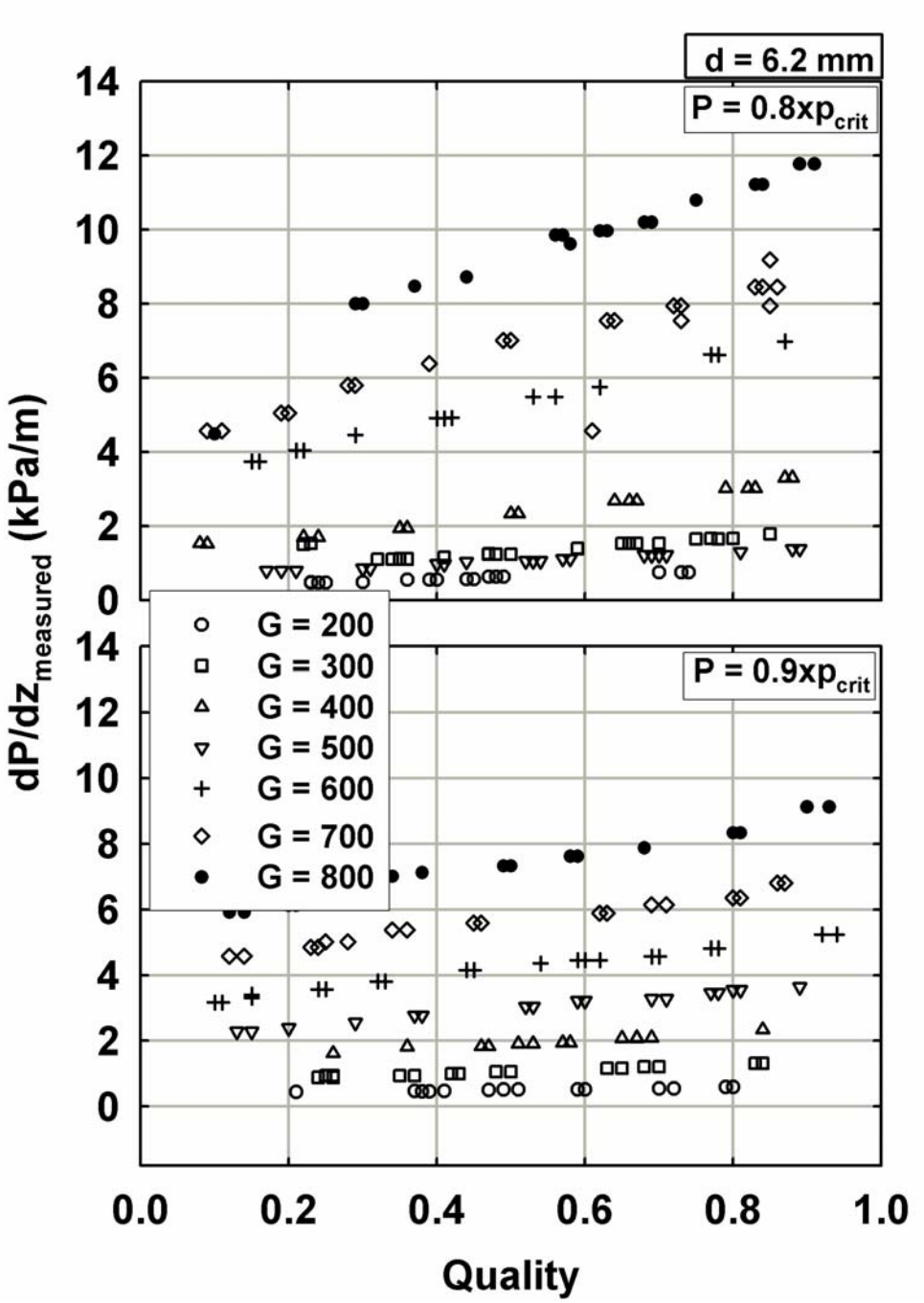

Figure 5. 8 Measured Pressure Drops in 6.2 mm Tube

2.69, μ_l/μ_v = 2.54 at p_r = 0.9; ρ_l/ρ_v = 3.85, μ_l/μ_v = 3.36 at p_r = 0.8.). This decrease in the difference between the properties of the two phases reduces the shear between the phases, and therefore the pressure drop. The more pronounced effect of reduced pressure at higher mass fluxes also supports this conclusion because at the higher mass fluxes, the flow would tend toward annular flow, which is governed by vapor shear.

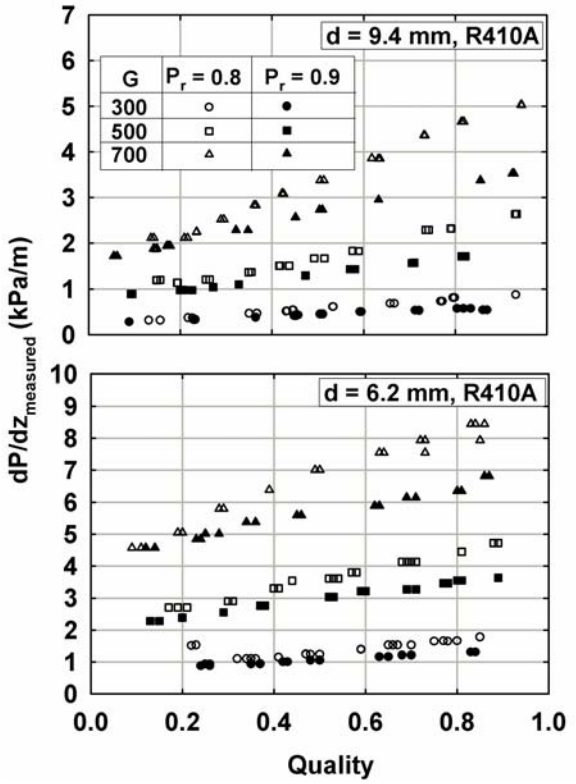

Figure 5. 9 Effect of Reduced Pressure on Condensation Pressure Drop

Figure 5.10 shows a comparison of the pressure drop for R410A in the two tubes. As expected, the pressure drop at similar mass flux and quality conditions is higher for the smaller diameter tube due to the larger L/D ratio for this tube.

5.1.3 Flow Regimes

A flow regime-based analysis was conducted to understand the heat transfer coefficient and pressure drop trends discussed above in terms of the applicable flow regimes. However, due to the absence of maps in the literature for condensation of refrigerant blends at high reduced pressures, the available flow regime maps for somewhat similar situations were used to predict the possible regimes for the conditions in the present study.

Breber et al. (1980)

The data are plotted on the Breber *et al.* map, in which transitions between flow regimes occur at constant Martinelli parameters and dimensionless gas velocities, as shown in Figure 5.11. The dimensionless gas velocity (J_g^*) is a function of the ratio of the vapor axial shear gradient to the gravity radial gradient and the friction factor at the two-phase interface. Thus, the Breber *et al.* (1980) map, which used the Taitel and Dukler (1976) map as a starting point, was based on the argument that the ratio of shear force-to-gravity force on the condensate film, and the ratio of vapor volume-to-liquid volume are the main factors in establishing transitions between the respective regimes. This map was particularly chosen for comparison here because it is applicable for a wide range of tube diameters (4.8-50.8 mm), pressures (108.1-2489 kPa) and refrigerants (R12, R113, steam, n-Pentane, R11), and acknowledges that the transitions do not occur abruptly, but over regions with some overlap. At a constant mass flux, the condensation path on the Breber map generally moves from the top left corner (high qualities) where annular/mist flows, prevail to the bottom right corner (at low qualities) of the map where the slug and plug flows dominate. Also as the mass flux increases, the dimensionless gas velocity increases, resulting in a

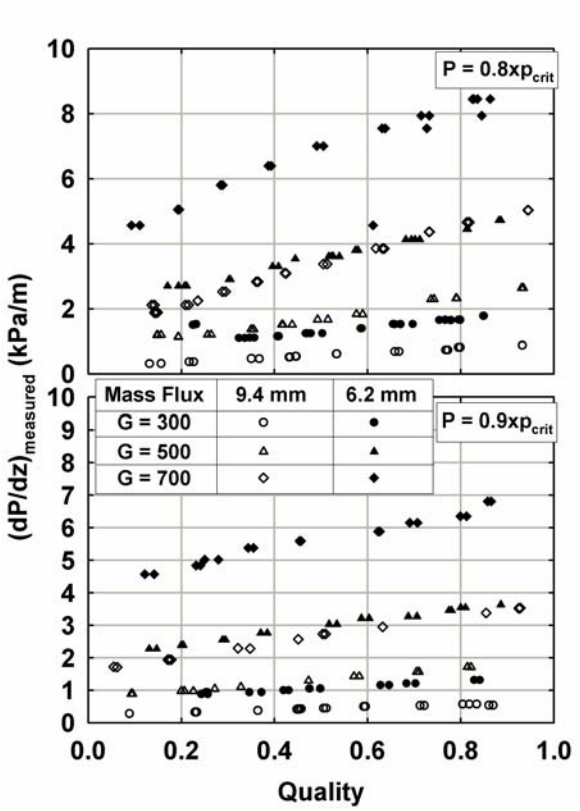

Figure 5.10 Effect of Diameter on Condensation Pressure Drop

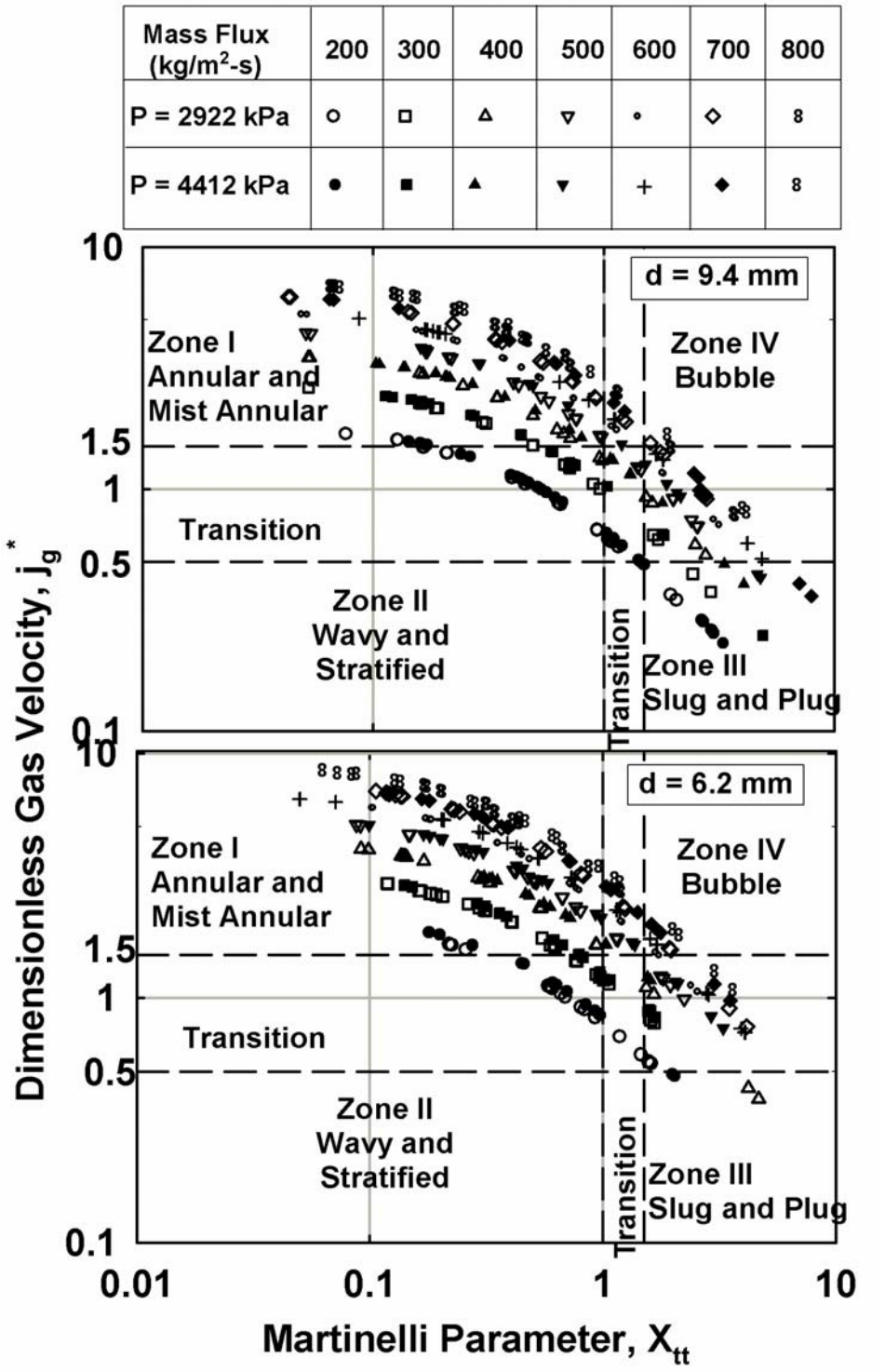

Figure 5.11 Present Data Plotted on Breber *et al.* (1980) Flow Regime Map

shift of the curve to higher y-axis values. Figure 5.11 shows that a large portion of the data from the present study are in the annular and mist regions, with some points falling in the transition region between the four primary regimes, and relatively few points in the slug and plug flow regimes (few 9.4 mm tube data points), according to the Breber *et al.* map. It can also be seen that even though none of the data points fall in the wavy-stratified regions, many data lie in the transition region between annular/mist and wavy-stratified flows. The change in reduced pressures does not seem to affect the flow regimes in these maps, since the condensation paths lie on the same curve for both pressures.

Coleman and Garimella (2003)

The data from the present study are plotted on the flow regime maps developed by Coleman and Garimella (2003) in Figure 5.12. Their maps were developed for condensation of refrigerant R134a in circular, square and rectangular tubes (1 mm < d_h < 5 mm) for the mass flux range 150 < G < 750 kg/m^2-s at $p_r \cong 0.34$. The low reduced pressures and slightly lower diameters used in their study might lead to some differences between the regimes predicted by their criteria and those exhibited by R410A under the conditions of interest in the present study. But these criteria were in fact developed for condensation of refrigerants (rather than boiling experiments or simulations using air-water two-phase flow) and addressed the mass flux range of interest in this study; and are therefore deemed to provide some guidance. These graphs show that the data points exhibit the discrete and disperse wave flow, and annular flow (G > 400 kg/m^2-s and x > 0.5) patterns, with a few points at low qualities being in the intermittent regime. Upon comparison of the flow regimes predicted by the Breber *et al.* (Figure 5.11) and the

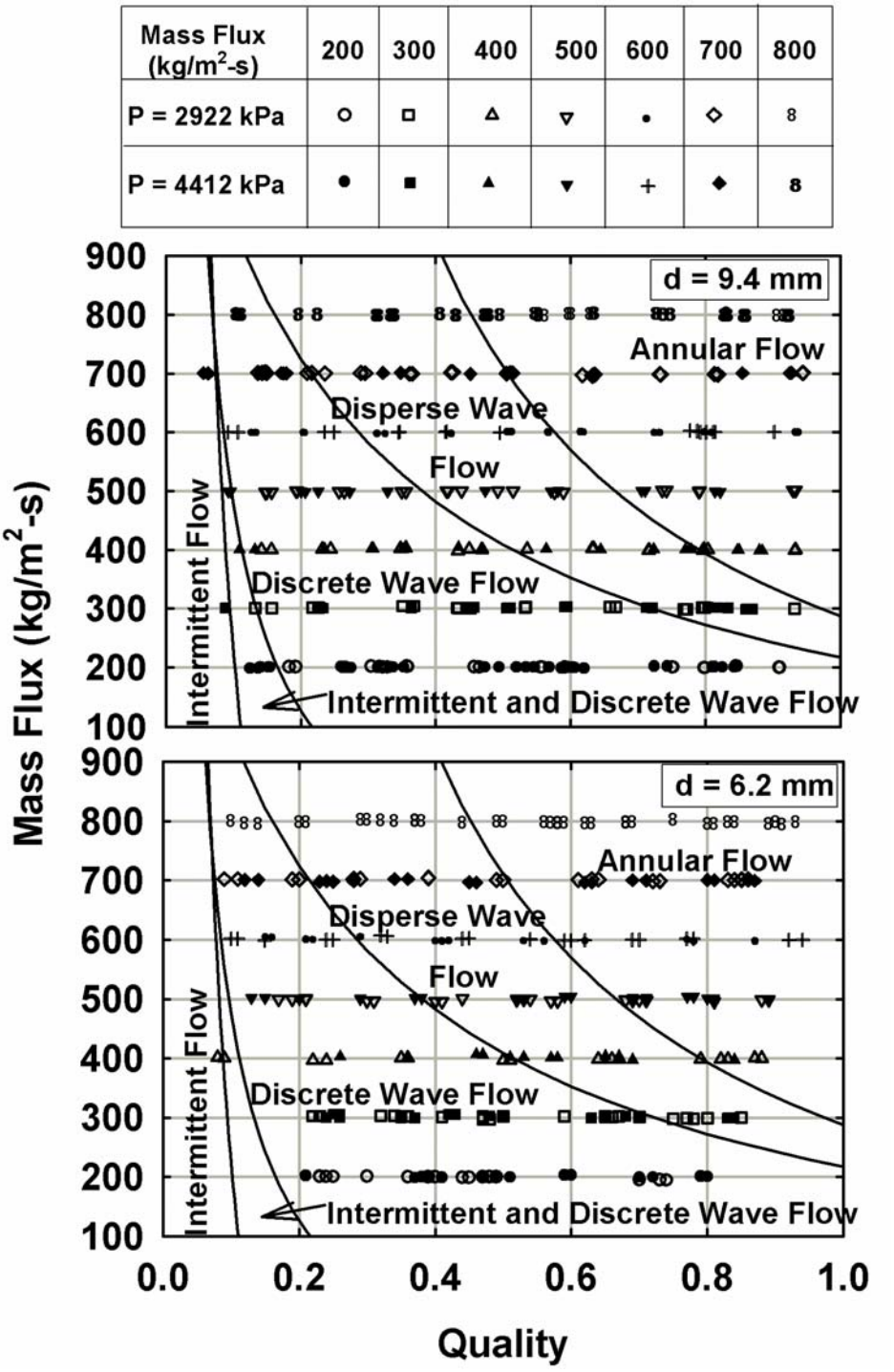

Figure 5.12 Present Data Plotted on the Coleman and Garimella (2003) Flow Regime Map

Coleman and Garimella (Figure 5.12) maps, it can be seen that these two maps from the literature predict similar flow regimes for the present data, except that the data predicted to be in the discrete and disperse wave regimes by Coleman and Garimella appear in the transition and slug and plug flow regions in the Breber map. It should be noted that differences in definitions and categorizations of different kinds of flows, details of which are available in the respective papers, could be responsible for some of these differences in the assignment of flow regimes.

Dobson and Chato (1998)

The data from the present study are plotted along with the annular to wavy flow transition criteria proposed by Dobson and Chato (1998) in Figure 5.13. The authors consider the flow to be annular for all G > 500 kg/m^2-s. For G < 500 kg/m^2-s the flow is considered annular for modified Soliman Froude number (Equation 5.1), Fr_{SO} > 20 and wavy for Fr_{SO} < 20. The plots in Figure 5.13 show that the majority of the data points are in the annular flow regime with a few (but not insignificant) points below G = 500 kg/m^2-s in the wavy flow regime. These transition criteria were developed for condensation in tubes with diameters ranging from 3.14 to 7.04 mm and hence fall within the range of tube diameters used in this study.

El Hajal et al. (2003)

The recent El Hajal *et al.* (2003) map was also considered for the assignment of flow regimes to the data points from the current study (Figure 5.14). In their approach, Hajal *et al.* used their earlier map (Kattan *et al.*, 1998a) developed for evaporation and adiabatic flow in small diameters tubes. According to their map, data from the present

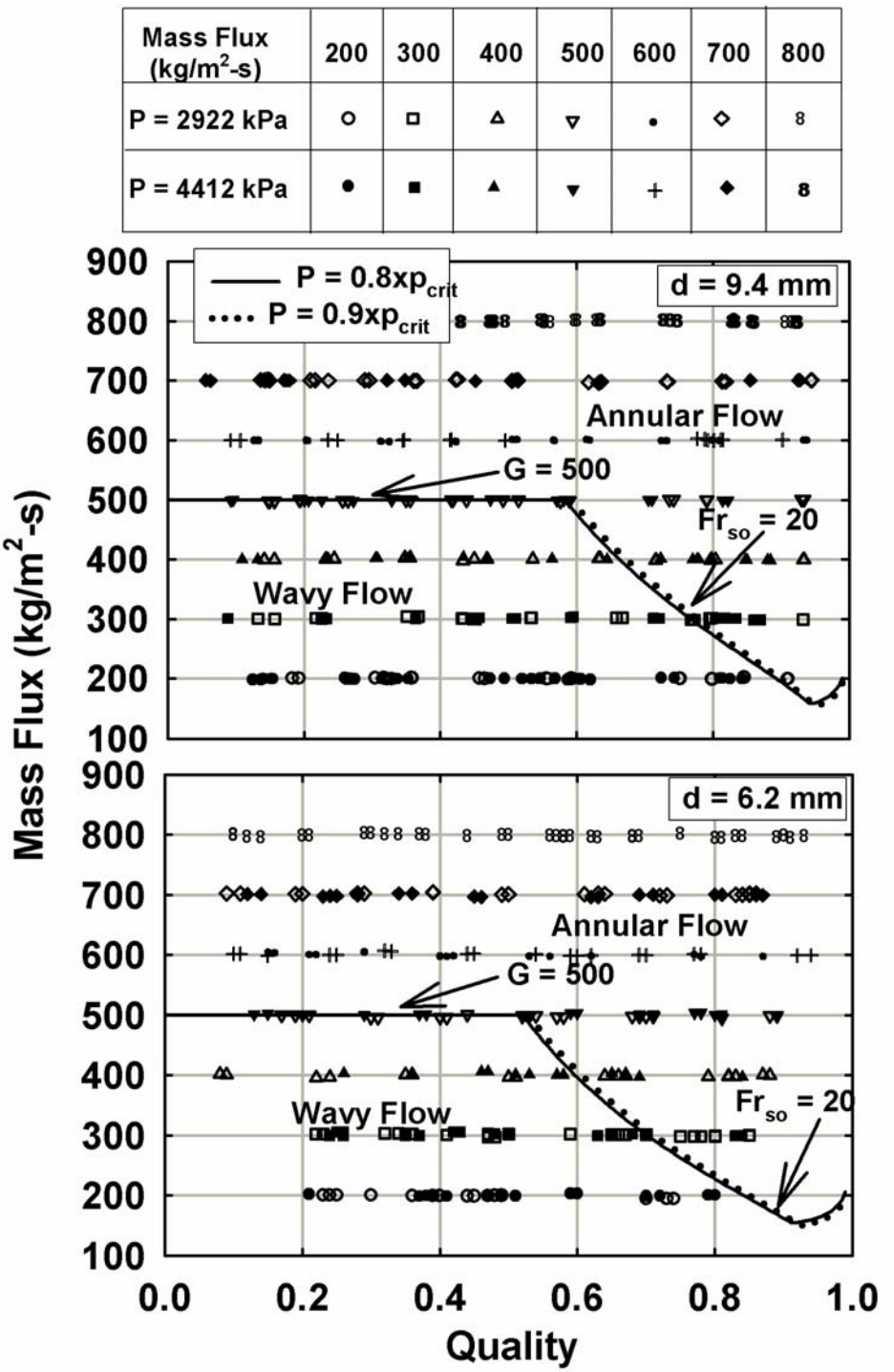

Figure 5.13 Present Data Plotted with Dobson and Chato (1998) Flow Regime Transition Criteria

study were primarily in the intermittent and annular flow regimes, with few data in stratified-wavy flow and no fully stratified flow data. However, the definitions of these flows are not explicitly stated by them. It is possible that they consider intermittent flow to be similar to annular flow, because the same heat transfer correlation developed in the second part of this work (Thome *et al.*, 2003) is used for the intermittent, annular and mist flows. The wavy or stratified flow regimes for the El Hajal *et al.* map (Figure 5.14) requires mass fluxes to be around or less than 200 kg/m^2-s, which were either at the borderline or beyond the test conditions of the present study. The flow predictions from this map were quite different from those of the Coleman and Garimella (2003) map (Figure 5.12), which showed a considerable amount of data from the present study to be in the wavy flow regime.

The Coleman and Garimella map (Figure 5.12), however results in transitions similar to those predicted by Dobson and Chato (1998) (Figure 5.13). Since the heat transfer models developed in the present study used an approach similar to that of Dobson and Chato (1998), it is more appropriate to use a flow regime map that is similar to their map to delineate the data. Because the Coleman and Garimella (2003) criteria yielded transitions similar to those predicted by Dobson and Chato (1998), lead to consistency in the heat transfer models, and are easy to implement, they were chosen for the assignment of flow regimes to the data points in this study.

5.1.4 Literature Comparison

To assess the validity of models in the literature for these high-pressure refrigerant blends when operating at near-critical pressures, the heat transfer coefficients from the present study were compared with the predictions of the relatively recent

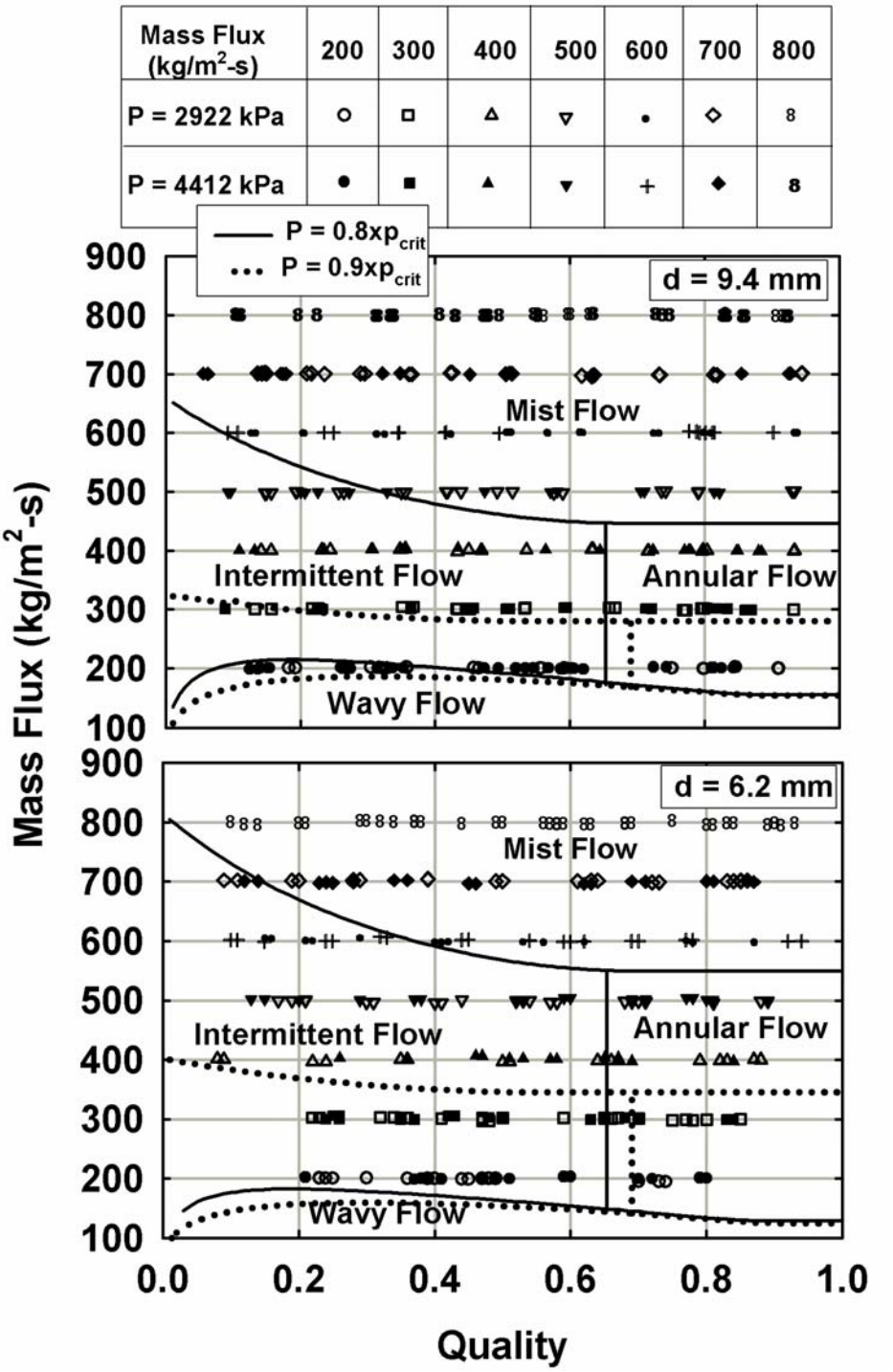

Figure 5.14 Present Data Plotted on El Hajal *et al.* (1998) Flow Regime Map

correlations. It should be noted that none of the heat transfer and pressure drop models in literature are based on data encompassing conditions under investigation in the present study. Therefore, the comparisons are presented here for the purpose of understanding whether these correlations can be extrapolated to the test conditions of interest in this study. It is believed that understanding the discrepancies between these models and the current data is necessary for the development of better predictive models.

Dobson and Chato (1998)

Comparisons with the models of Dobson and Chato (1998) models are shown in Figures 5.15-5.16. For shear-driven annular flow ($G < 500$ kg/m^2-s and $Fr_{so} > 20$, or $G > 500$ kg/m^2-s), the Dobson and Chato (1998) model is essentially a simplified version of the Traviss *et al.* (1973) correlation, and applies a two-phase multiplier (which is a function of the Martinelli parameter) to the Dittus-Boelter single-phase equation. The wavy flow model considers film condensation (similar to Nusselt condensation) on the top of the tube and forced convection in the liquid pool at the bottom of the tube. The forced convection Nusselt number is again a Dittus- Boelter type equation multiplied with a two-phase multiplier which is a function of the Martinelli parameter and the Froude number. The film condensation part is a Nusselt condensation equation over a horizontal cylinder with a multiplier to account for enhancement due to interfacial waves. The liquid angle subtended from the top of the tube to the liquid level is evaluated using the void fraction by Zivi (1964).

In general, the experimental values from the present study are between the predictions of the annular and wavy-stratified submodels of Dobson and Chato: their annular model strongly over predicts the current data, while the wavy-stratified model

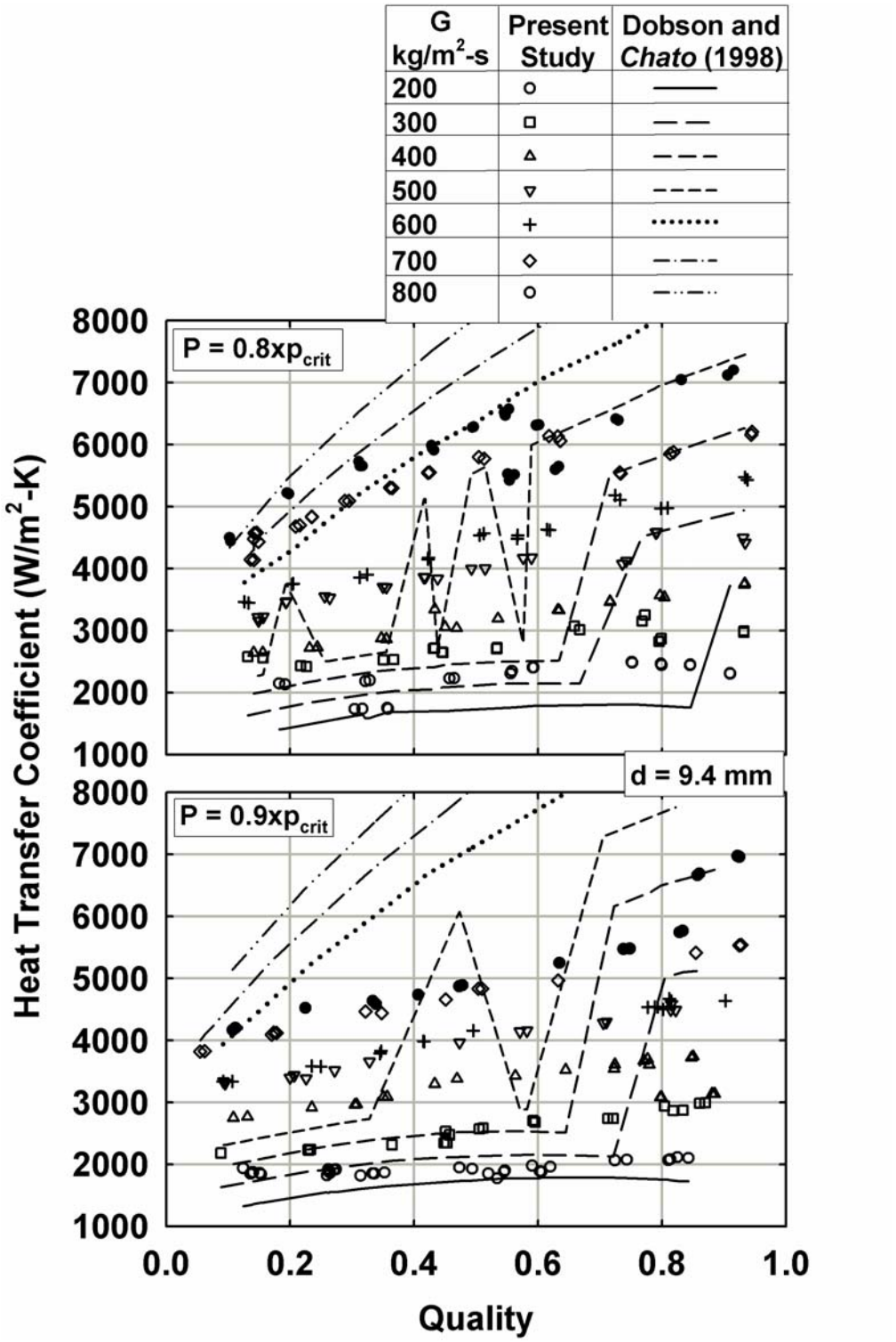

Figure 5.15 Comparison of Measured Condensation Heat Transfer Coefficients with the Dobson and Chato (1998) Predictions (9.4 mm Tube)

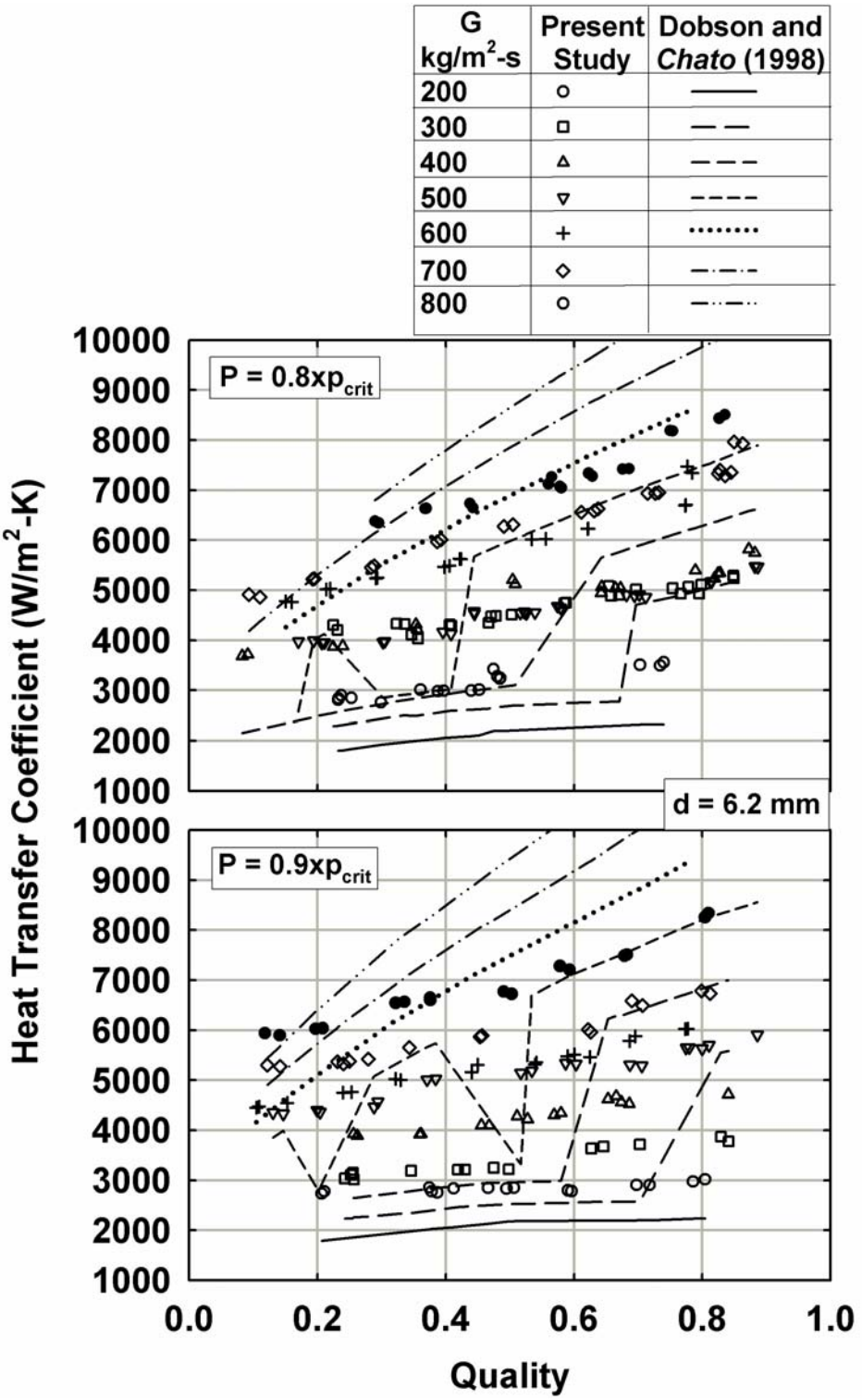

Figure 5.16 Comparison of Measured Condensation Heat Transfer Coefficients with the Dobson and Chato (1998) Predictions (6.2 mm Tube)

slightly under-predicts the data. This overall result is understandable based on the expectation from the discussion above that the current data are mostly in the discrete and disperse wave regions according to Coleman and Garimella (2003) or in the transition regions between the annular and wavy region according to Breber *et al.* (1980). Even though the models were developed for diameters ($3.14 < d < 7.04$ mm) comparable to present study, it appears that the low reduced pressures ($p_r < 0.57$) in their study contribute to the differences from the present data. The under-predictions of the wavy flow may be because of the assumption that the film condensation is the dominant mechanism of heat transfer and that the heat transfer in the bottom of the pool is significant only at high mass fluxes. They neglect the effect of vapor shear at intermediate quality cases; however, even though the vapor shear is not significant enough to cause annular flow, it may still move some of the condensed film tangentially. Also, the Zivi (1964) void fraction model used in their correlation may not be applicable to the present conditions. The abrupt and unrealistic jump in heat transfer coefficient from the wavy-stratified to the annular region predicted by their model limits its usefulness to the conditions under study here. In addition, the Dobson and Chato (1998) model predicts an increase in heat transfer coefficient for an increase in reduced pressure (At a representative data point of $G = 800$ kg/m^2-s, $d = 9.4$ mm, $x = 0.63$, for an increase in p_r from 0.8 to 0.9, the predicted heat transfer coefficient increases from 8989 to 10113 W/m^2-K, whereas the experimental heat transfer coefficient decreases from 5647 to 5252 W/m^2-K), which appears unrealistic and is different from the trends in the present experimental data.

Cavallini et al. (2002a; 2002b)

The predictive capabilities of the heat transfer and pressure drop models of Cavallini *et al. (2002a; 2002b)* are shown in Figures 5.17-5.18. As stated in the literature review section of this report, these models consist of submodels for annular flow, annular-stratified flow transition and stratified flow, and stratified-slug and slug flow. It can be seen that the predictions of this model are in better agreement with the present data than the predictions of the models described above. The heat transfer models under-predict the data with the average deviations ranging from 13% in the 9.4 mm tube (p_r = 0.8) to 37% in 6.2 mm tube (p_r = 0.9). The somewhat better predictions of these models is not surprising given that this model is applicable for condensation of halogenated refrigerants in tubes with $3 < d < 21$ mm, $p_r < 0.75$, and $\rho_l/\rho_g > 4$. The conditions for the present study, p_r = 0.8 and 0.9, and $2.93 < \rho_l/\rho_g < 4.72$, are only slightly outside the range of applicability of their model. Some of the discrepancies in the heat transfer model may also be due to the fact that the interfacial shear stress (approximated as the wall shear stress) in the model is obtained from the frictional pressure drop model - significant discrepancies in the pressure drop model might have led to deviations in the heat transfer model.

The (total) pressure drop model proposed by Cavallini *et al.* (2002a) was based on the original (for $J_G < 2.5$) and modified (for $J_G > 2.5$) Friedel (1979) correlation. The measured pressure drop data from the present study are plotted with the predictions of these models in Figures 5.19-5.20. It can be seen that the agreement between their model and the current data is not as good as the corresponding agreement of the heat transfer data. Their model under-predicts the experimental values, especially for higher mass

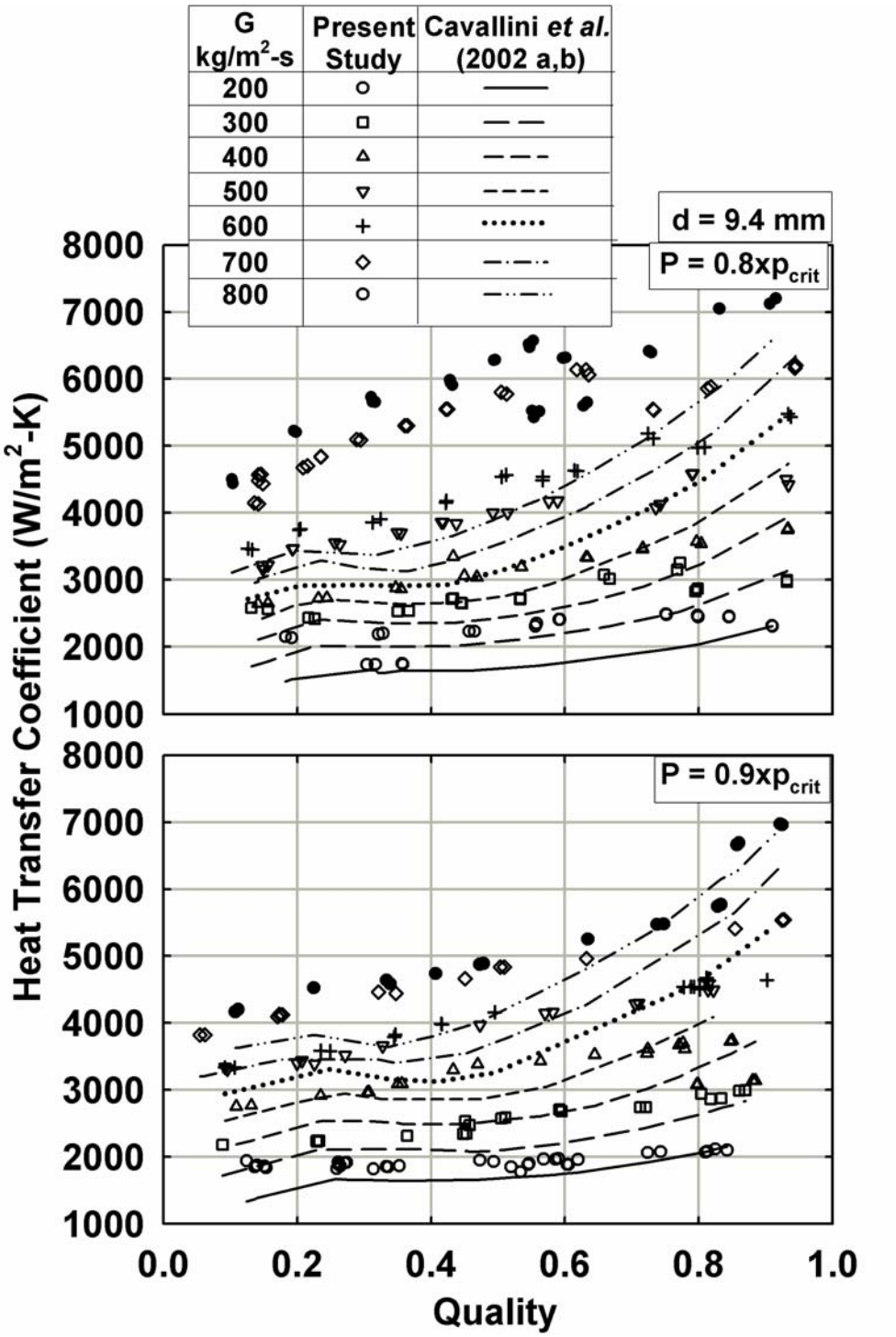

Figure 5. 17 Comparison of the Measured Condensation Heat Transfer Coefficients with the Cavallini *et al.* (2002 a,b) Predictions (9.4 mm Tube)

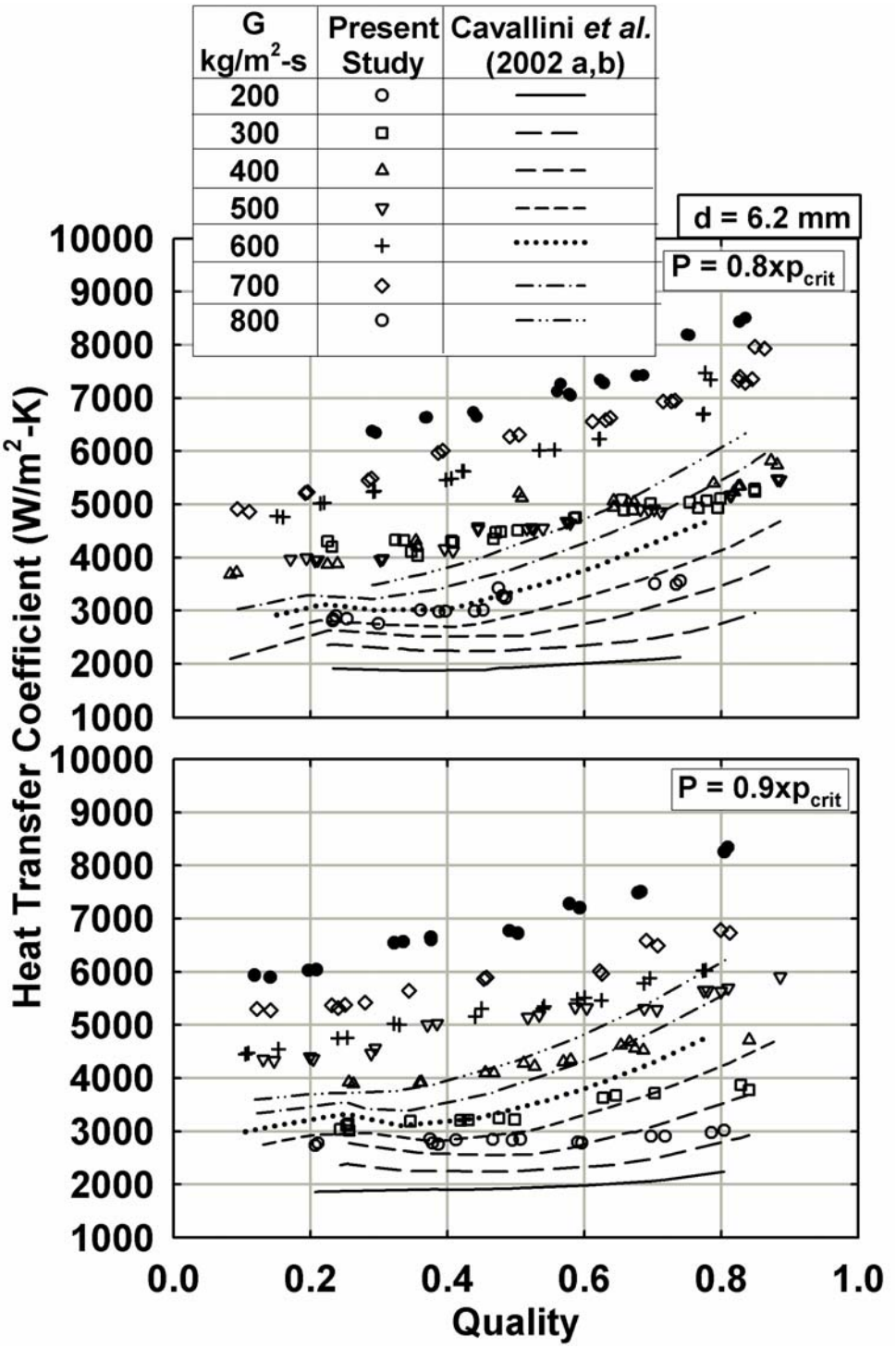

Figure 5.18 Comparison of the Measured Condensation Heat Transfer Coefficients with the Cavallini *et al.* (2002 a,b) Predictions (6.2 mm Tube)

fluxes. It can also be seen that the original Friedel (1979) correlation for $J_G < 2.5$ yields much better predictions than the modified version proposed by them. Furthermore, the abrupt transitions between the two submodel correlations are unrealistic. It was discussed above that pressure drop values in the current study are more sensitive to reduced pressure than heat transfer data, which was explained based on the variations in the phase properties. Hence this larger discrepancy in pressure drops between their model and the current data is understandable. Also, the increasing discrepancy as the reduced pressure deviates from their maximum value of 0.75 to 0.9 in this study corroborates this explanation.

El Hajal et al. (2003) and Thome et al. (2003)

The current data are plotted with the predictions of the heat transfer models in the second part of the two part paper of El Hajal *et al.* (2003) and Thome *et al.* (2003) in Figures 5.21-5.22. The models predict the data fairly well for the refrigerant at $p_r = 0.8$ in the 9.4 mm tube (10.7%). However, for other pressures and diameters, the deviations are high with the maximum deviation being 30% in the 6.2 mm tube at $p_r = 0.8$. In addition, this model predicts an increase in the heat transfer coefficient with an increase in reduced pressure (similar to the model of Dobson and Chato(1998)), whereas the trend should show decreases in heat transfer coefficient as the reduced pressure rises. For example, for a representative data point of G = 800 kg/m^2-s, d = 9.4 mm, x = 0.63, for an increase in p_r from 0.8 to 0.9, the predicted heat transfer coefficient increases from 5869 to 6832 W/m^2-K, whereas the experimental heat transfer coefficient decreases from 5647 to 5252 W/m^2-K.

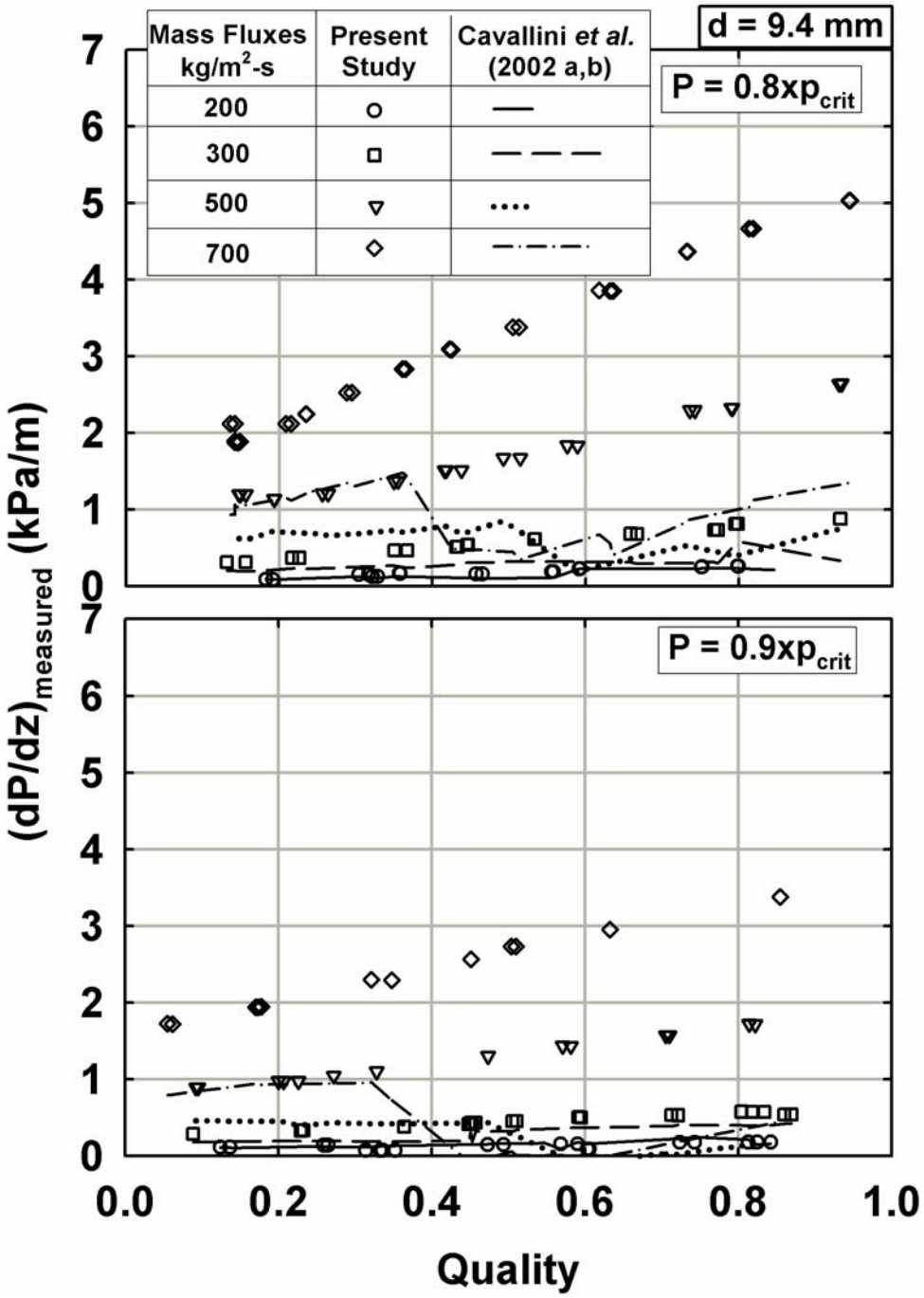

Figure 5. 19 Comparison of the Measured Condensation Pressure Drops with the Cavallini *et al.* (2002 a,b) Predictions (9.4 mm Tube)

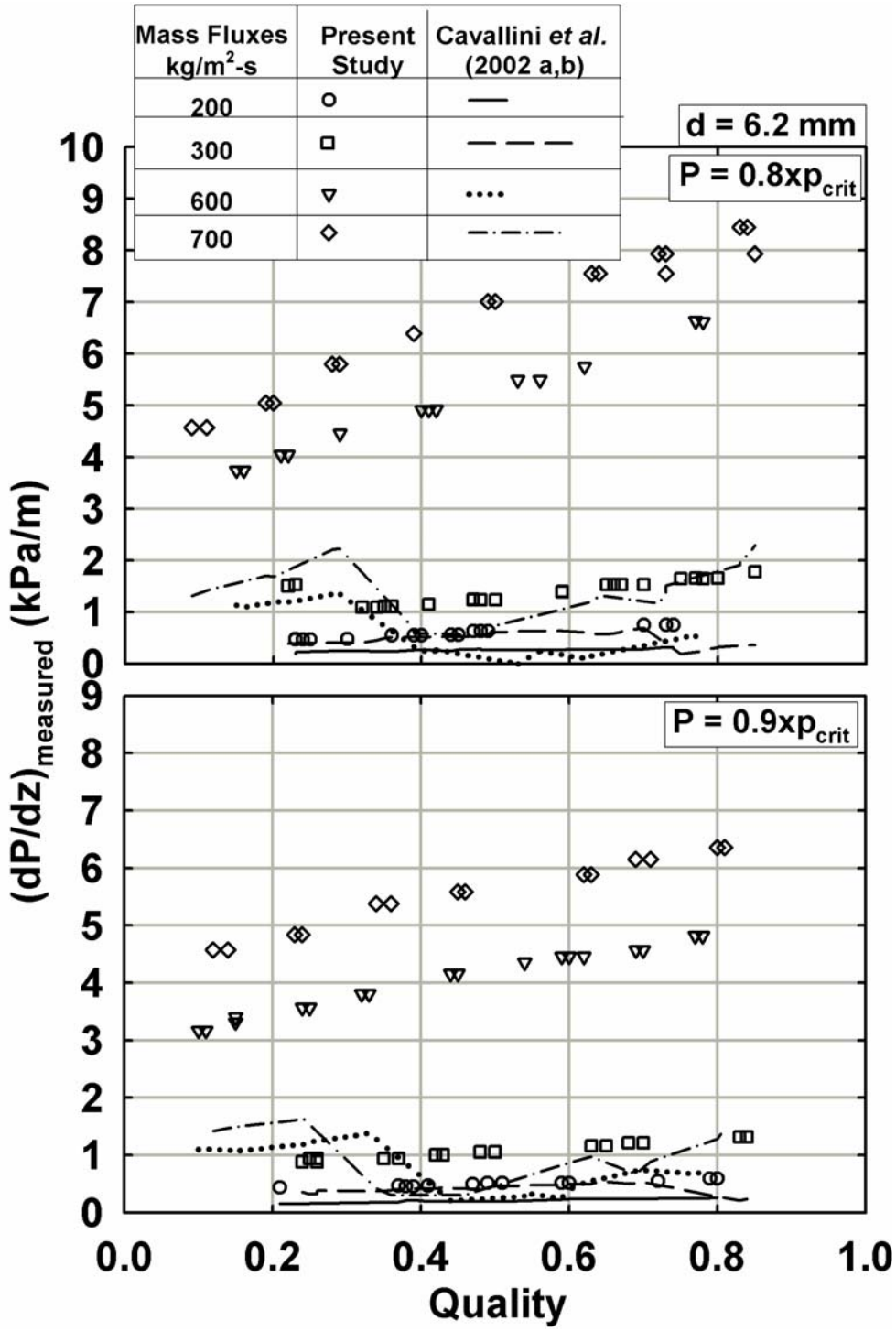

Figure 5. 20 Comparison of the Measured Condensation Pressure Drops with the Cavallini *et al.* (2002 a,b) Predictions (6.2 mm Tube)

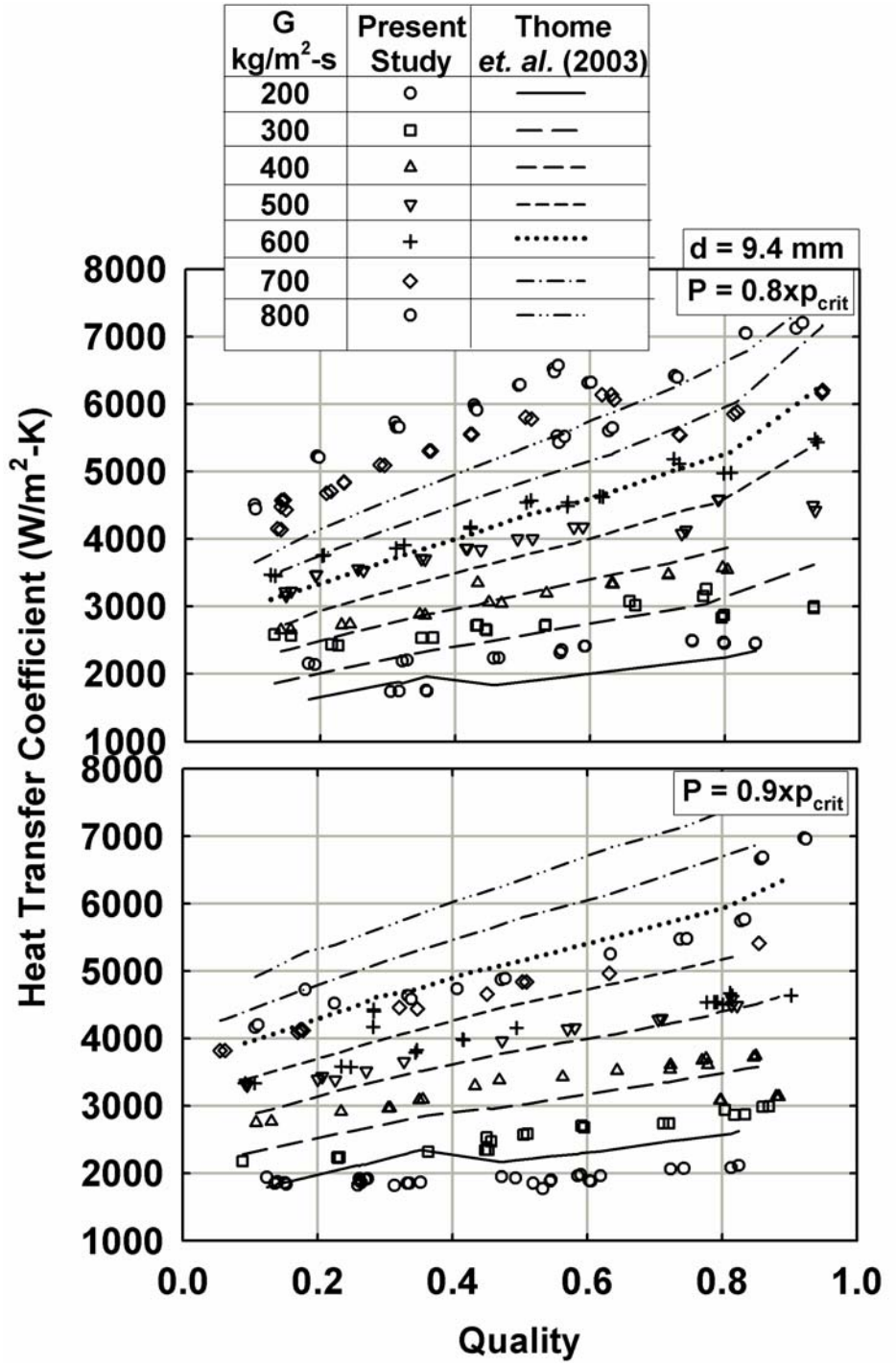

Figure 5. 21 Comparison of the Measured Condensation Heat Transfer Coefficients with the Thome *et al.* (2003) Predictions (9.4 mm Tube)

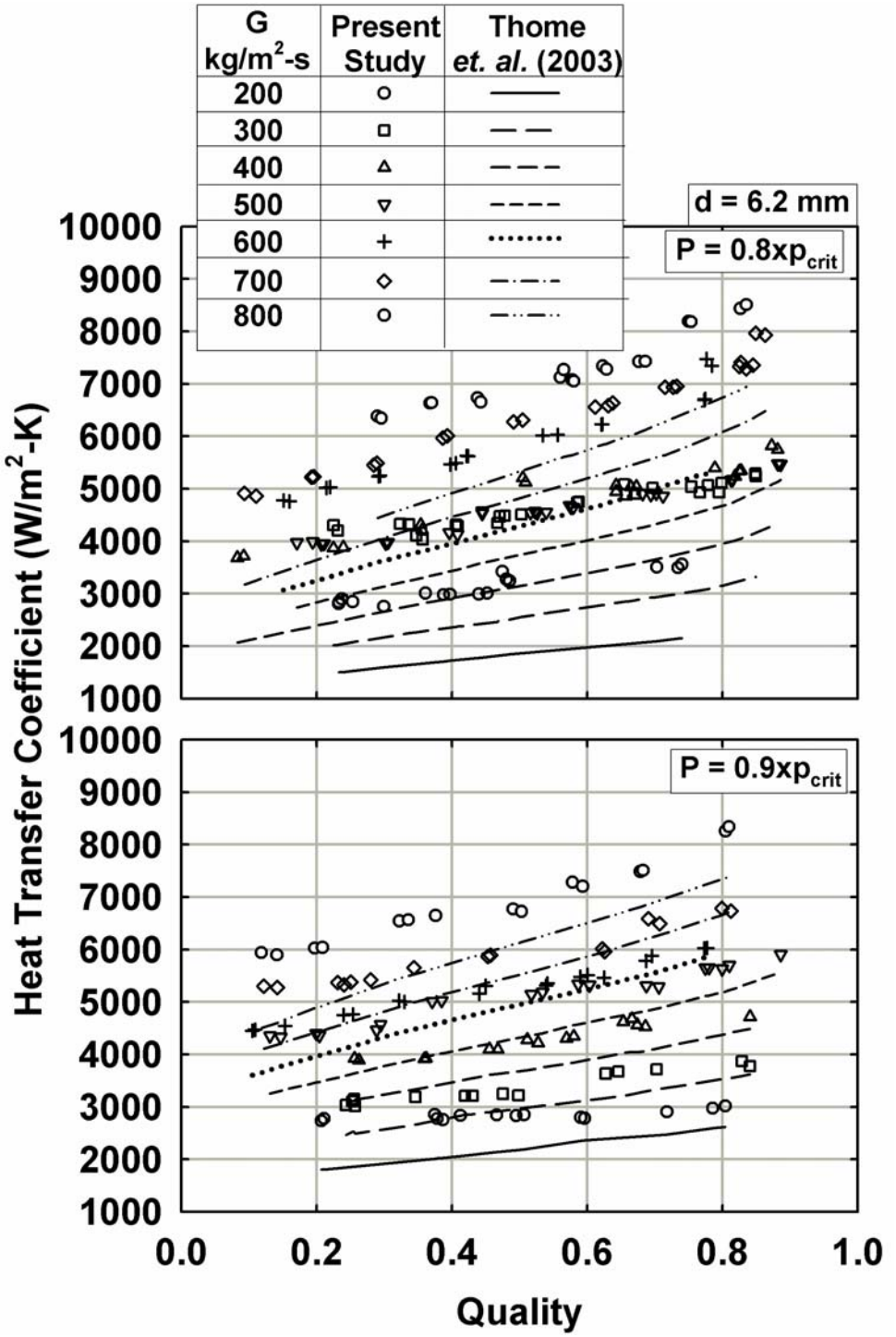

Figure 5.22 Comparison of the Measured Condensation Heat Transfer Coefficients with the Thome *et al.* (2003) Predictions (6.2 mm Tube)

5.2 Model Development

In this section, the development of condensation heat transfer and pressure drop models from the experimental data and insights from the comparisons with the literature is presented. The heat transfer and pressure drop are considered to occur due to two types of mechanisms: wavy flow and annular flow. The transition criteria proposed by Coleman and Garimella (2003) are used to classify the data into wavy flow and annular flow regimes. Film condensation at the top of the tube and convection at the bottom of the tube are considered as the primary modes of heat transfer and pressure drop in wavy flow. The annular flow is considered to be driven by a shear force at the vapor liquid interface. Sudden transitions of one mechanism of heat transfer and pressure drop to another result in abrupt discontinuities at the transition point, as discussed above, and were deemed to be unrealistic. Therefore, a transition region between the wavy and annular flow was introduced, where the flow is considered to be a consequence of the combined effects of wavy and annular flow. A detailed discussion of the details of the models and the respective predictions is provided below.

It should be noted that a companion study on refrigerant R404A in 9.4 mm diameter tubes was conducted by another researcher (Jiang, 2004) in the same laboratory. The models presented below were developed using data for both fluids. However, the discussion below focuses on R410A data collected by the author of this dissertation.

5.2.1 Heat Transfer Coefficient Models

Annular Flow Model

The data from this study with modified Soliman Froude number (shown below) $Fr_{so} \geq 18$ were used for the development of the annular flow model. Here Fr_{so} is defined as follows:

$$Fr_{so} = \begin{cases} 0.025 \cdot \mathrm{Re}_l^{1.59} \left[\dfrac{1+1.09 X_{tt}^{0.039}}{X_{tt}} \right]^{1.5} \dfrac{1}{Ga^{0.5}} & \cdots \quad \mathrm{Re}_l \leq 1250 \\ 1.26 \cdot \mathrm{Re}_l^{1.04} \left[\dfrac{1+1.09 X_{tt}^{0.039}}{X_{tt}} \right]^{1.5} \dfrac{1}{Ga^{0.5}} & \cdots \quad \mathrm{Re}_l > 1250 \end{cases} \tag{5. 1}$$

where

$$X_{tt} = \left(\frac{\rho_g}{\rho_l} \right)^{0.5} \left(\frac{\mu_l}{\mu_g} \right)^{0.1} \left(\frac{1-x}{x} \right)^{0.9} \tag{5. 2}$$

$$Ga = \frac{g \rho_l (\rho_l - \rho_g) D^3}{\mu_l^2}, \text{ and} \tag{5. 3}$$

$$\mathrm{Re}_l = \frac{GD(1-x)}{\mu_l} \tag{5. 4}$$

According to Dobson *et al.* (1994), the annular flow model developed by Traviss *et al.* (1973) could be reduced to a two-phase multiplier provided that $\mathrm{Re}_l > 1125$. The authors argued that the Nusselt number could be written in the following form:

$$Nu = \frac{D^+ \mathrm{Pr}_l}{F_2(\mathrm{Re}_l, \mathrm{Pr}_l)} \tag{5. 5}$$

where the term D^+ is the non-dimensional tube diameter scaled by the turbulent length scale, $\nu_l / \sqrt{\tau_w / \rho_l}$. F_2 is a dimensionless heat transfer resistance. This resistance increases as the dimensionless film thickness as well as the liquid Prandtl number

increase. Under the assumption of a symmetric annular film with no entrainment, the liquid Reynolds number Re_l uniquely specifies the dimensionless film thickness. Because of the piecewise nature of the universal velocity profile, F_2 is a piecewise function of liquid Reynolds number. For $Re_l < 50$, the annular film is so thin that it is entirely contained in the laminar sublayer. For $50 < Re_l < 1125$ and $Re_l > 1125$, the annular film ends in the buffer layer and fully turbulent region, respectively. Dobson *et al.* (1994) further pointed out that the liquid film in annular flow was seldom so thin that the fully turbulent region is not reached. With the F_2 confined to values of $Re_l > 1125$, therefore, the piecewise definition of F_2 was generally not necessary. They then proposed a power law function of Re_l and Pr_l for F_2. For the range of Re_l from 1125 to 10,000 and Pr_l from 1 to 10, F_2 can be well approximated by:

$$F_2 \equiv 10.25\,\mathrm{Re}_l^{\,0.0605}\,\mathrm{Pr}_l^{\,0.592} \tag{5. 6}$$

By assuming the Lockhart and Martinelli (1949) two-phase liquid multiplier approach for pressure drop correlation, equation (5.5) was reduced to the following form:

$$Nu = 0.0194\,Re_l^{\,0.815}\,Pr_l^{\,0.408}\,\phi_l(X_{tt}) \tag{5. 7}$$

which is similar to the approach used by Shah (1979).

For the present study, the liquid Reynolds number Re_l ranges from 2,676 to 72,613 implying that the film is always in the fully turbulent region. Thus, the two-phase multiplier approach was adopted to correlate the annular flow heat transfer data. The following correlating form was selected:

$$Nu_{Annular} = a \cdot Re_l^{\,b} \cdot Pr_l^{\,0.3}\left[1 + \left(\left(\frac{x}{1-x}\right)\cdot\left(\frac{\rho_l}{\rho_v}\right)\right)^c\right]\cdot\left(\frac{d_{actual}}{d_{baseline}}\right)^d \tag{5. 8}$$

Here, $d_{baseline}$ refers to the baseline diameter of 9.4 mm and d_{actual} is the diameter of the tube under consideration in mm. The values of constants and exponents a, b, c and d were determined through regression analysis on the measured annular Nusselt numbers to yield the following correlation with $R^2 = 0.90$:

$$Nu_{Annular} = 0.0134 \cdot \mathrm{Re}_l^{0.84} \cdot \mathrm{Pr}_l^{0.3} \left[1 + \left(\left(\frac{x}{1-x} \right) \cdot \left(\frac{\rho_l}{\rho_v} \right) \right)^{0.80} \right] \cdot \left(\frac{d_{actual}}{d_{baseline}} \right)^{-0.32} \qquad (5.9)$$

The Reynolds number Re_l used in the above equation is the liquid Reynolds number given by Equation 5.4.

Wavy Flow Models

The data from this study with modified Soliman Froude number $Fr_{so} < 18$ were used for the development of the wavy flow models. A schematic of the wavy flow pattern used for the development of this model is shown in Figure 5.23. In wavy flow, heat transfer occurs in the upper portion of the tube by filmwise condensation and in the liquid pool at the bottom of the tube by forced convective condensation, as shown in Figure 5.23. Film condensation is due to slow moving vapor condensing upon contact with a cold surface and flowing down vertically due to gravity to be collected in a liquid pool. The thickness of the liquid film grows as the condensed vapor descends from the top of the tube. This condensation occurs down to angle θ (Figure 5.23), the half angle of the portion of the tube covered by film

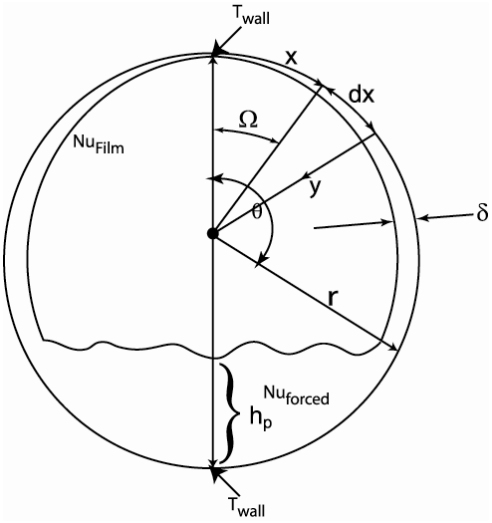

Figure 5. 23 Schematic of the Wavy Flow Model

condensation. Beyond this half angle θ, the liquid pool starts where the heat transfer mechanism is due to forced convection. The liquid pool moves axially due to the imposed pressure gradient. At low vapor velocities, the liquid pool at the bottom of the tube is relatively quiescent, and heat transfer at the bottom of the tube is much smaller than the heat transfer due to film condensation. In addition, the vapor flow has little effect on the liquid film on the top portion of the tube, and Nusselt-type film condensation on a cylinder can be used to model this process. However, as vapor velocities increase, the heat transfer in the liquid pool also increases due to the increasing waviness of the pool, and may be too significant to neglect. Furthermore, the interfacial shear exerted by the vapor on the condensate film at the top also increases as the vapor velocities increase. In view of these considerations, an additive model for predicting the local heat transfer coefficient was proposed by combining the heat transfer through film condensation on the top of the tube and forced convection in the liquid pool.

Assuming that the convective terms can be neglected, an energy balance on a differential element dx of the film requires that

$$h_{lv} \cdot \frac{d\dot{m}'}{dx} = \frac{k_l \cdot \left[T_{sat}(P_v) - T_w\right]}{\delta} \tag{5. 10}$$

Similarly a momentum balance across the differential element in direction y yields:

$$(\delta - y) \cdot dx \cdot (\rho_l - \rho_v) \cdot g \cdot \sin(\Omega) = \mu_l \cdot \left(\frac{du}{dy}\right) \cdot dx \tag{5. 11}$$

Integrating the above equation from 0 to y, with u = 0 at y = 0 (wall) results in the following velocity profile:

$$u = \frac{(\rho_l - \rho_v) \cdot g \cdot \sin(\Omega)}{\mu_l} \left(y \cdot \delta - \frac{y^2}{2} \right) \tag{5. 12}$$

The condensate mass flow rate per unit tube length is obtained by integrating the above velocity profile from y = 0 to δ as follows:

$$\dot{m}' = \rho_l \cdot \int_0^{\delta} u \cdot dy = \frac{\rho_l \cdot (\rho_l - \rho_v) \cdot \delta^3 \cdot g \cdot \sin(\Omega)}{3 \cdot \mu_l} \tag{5. 13}$$

Combining Equations (5.13) and (5.10), replacing x with r·Ω, and integrating the mass flow rate per unit length of the tube from 0 to $\dot{m}'$ and the angle Ω from 0 to θ results in the following expression:

$$\dot{m}' = \left(\frac{2}{3}\right)^{3/4} \left(\frac{1}{3}\right)^{1/4} \left[\frac{D^3 k_l{}^3 (T_{sat} - T_{wall})^3}{h_{fg}{}^3} \frac{\rho_l (\rho_l - \rho_v) g}{\mu_l}\right]^{1/4} \left[\int_0^{\theta_l} \sin^{1/3}\theta d\theta\right]^{3/4} \tag{5. 14}$$

Considering that condensation occurs on both sides of the tube, the following expression can be written:

$$2 \cdot h_{fg} \cdot \dot{m}' = \theta \cdot d \cdot \bar{h} \cdot (T_{sat} - T_w) \tag{5. 15}$$

which, on replacing $\dot{m}'$ from Equation (5.14) and replacing the average heat transfer coefficient $\bar{h}$ by the film Nusselt number results in the following expression for film condensation:

$$Nu_{film} = \frac{1.122}{\theta} \cdot \left[\int_0^{\theta} \sin^{1/3}\theta \cdot d\theta\right]^{3/4} \cdot \left(\frac{Ra}{Ja}\right)^{1/4} \tag{5. 16}$$

where the angle θ is evaluated using the following expression:

$$\theta = \pi - \arccos(2\alpha - 1) \tag{5. 17}$$

and the void fraction α is obtained from the Baroczy (1965) correlation in the absence of void fraction models for the conditions under study.

For the modeling of the Nusselt number of the liquid pool at the bottom of the tube, a hydraulic diameter of the pool $d_{h,lp}$ is first defined as follows:

$$d_{h,lp} = \frac{4 \cdot A}{P} = \frac{\left[\pi - \theta\left(1 - \frac{sin(2 \cdot \theta)}{(2 \cdot \theta)}\right)\right]}{\left[\pi - \theta\left(1 - \frac{sin(\theta)}{(\theta)}\right)\right]} \cdot d_{actual} \tag{5. 18}$$

The Reynolds number for the liquid pool is therefore calculated as follows:

$$Re_{lp} = \frac{G \cdot (1 - x) \cdot d_{h,lp}}{\mu_l} = Re_l \cdot \left(d_{h,lp} / d_{actual}\right) \tag{5. 19}$$

The forced convection in the liquid pool was considered analogous to turbulent single-phase flow of liquid in a tube of the hydraulic diameter $d_{h,lp}$ defined above, suggesting a Dittus-Boelter type equation with a two-phase multiplier as follows:

$$W_F = \left[1 + \left(\frac{x}{1 - x}\right) \cdot \left(\frac{\rho_l}{\rho_v}\right)\right] \tag{5. 20}$$

A diameter ratio was also used to account for the different diameters of the tubes under consideration. Thus final form of the forced convection correlation used to model the data from the present study is given as follows:

$$Nu_{Forced} = a \cdot {Re_{lp}}^{b} \cdot {Pr_l}^{0.3} \left[1 + \left(\left(\frac{x}{1 - x}\right) \cdot \left(\frac{\rho_l}{\rho_v}\right)\right)\right] \cdot \left(\frac{d_{actual}}{d_{baseline}}\right)^{c} \tag{5. 21}$$

Parameters a, b and c were obtained through a regression analysis, resulting in the following equation for the forced-convective term:

$$Nu_{Forced} = 0.005 \cdot {Re_{lp}}^{0.97} \cdot {Pr_l}^{0.3} \left[1 + \left(\left(\frac{x}{1 - x}\right) \cdot \left(\frac{\rho_l}{\rho_v}\right)\right)\right] \cdot \left(\frac{d_{actual}}{d_{baseline}}\right)^{-0.56} \tag{5. 22}$$

The film condensation (Eq. 5.16) and forced convection (5.22) Nusselt numbers are combined using a summation of the heat transferred in the different regions of the tube as follows:

$$q_{total} = q_{top} + q_{bottom} \tag{5. 23}$$

where q_{total}, q_{top}, q_{bottom} are given as follows:

$$q_{total} = \bar{h} \cdot A \cdot \Delta T = \frac{Nu_{total} \cdot k_l}{d} \cdot A \cdot \Delta T \tag{5. 24}$$

$$q_{top} = \bar{h} \cdot \theta \cdot d \cdot L_{test} \cdot \Delta T = \bar{h} \cdot A \cdot \frac{\theta}{\pi} \cdot \Delta T = \frac{\theta}{\pi} \cdot \frac{Nu_{top} \cdot k_l}{d} \cdot A \cdot \Delta T \tag{5. 25}$$

$$q_{bottom} = \bar{h} \cdot (\pi - \theta) \cdot d \cdot L_{test} \cdot \Delta T = \bar{h} \cdot A \cdot \frac{(\pi - \theta)}{\pi} \cdot \Delta T = \left(1 - \frac{\theta}{\pi}\right) \cdot \frac{Nu_{bottom} \cdot k_l}{d_h} \cdot A \cdot \Delta T \tag{5. 26}$$

Substituting Equations (5.24), (5.25) and (5.26) into Equation (5.23) yields

$$Nu_{total} = \frac{\theta}{\pi} \cdot Nu_{top} + \left(1 - \frac{\theta}{\pi}\right) \cdot \frac{Nu_{bottom}}{d_h / d} \tag{5. 27}$$

Transition Region

It is believed that the transitions between different flow patterns are not abrupt but rather gradual in reality. Therefore, a transition region between annular and wavy flow was defined based on the Soliman modified Froude number (Soliman, 1982) Fr_{so}. Therefore, a transition region $14 < Fr_{so} < 24$ was defined to represent the band where contributions of both types of flow were apparent. The heat transfer coefficients for this region are calculated using an interpolation between the annular and wavy flow heat transfer models as follows:

$$Nu = \left(\frac{Fr_{so} - Fr_{so,wavy}}{Fr_{so,annular} - Fr_{so,wavy}}\right) \cdot Nu_{annular} + \left(\frac{Fr_{so,annular} - Fr_{so}}{Fr_{so,annular} - Fr_{so,wavy}}\right) \cdot Nu_{wavy} \tag{5. 28}$$

where $Fr_{so,wavy} = 14$ and $Fr_{so,annular} = 24$. In this equation, it should be noted that at $Fr_{so} = Fr_{so,wavy}$, the contribution of $Nu_{annular}$ toward the overall Nusselt number is zero, indicating fully wavy flow and at $Fr_{so} = Fr_{so,annular}$ the contribution of Nu_{wavy} toward the overall Nusselt number is zero indicating fully annular flow.

Model Predictions

Figure 5.24 shows the experimental heat transfer coefficients with the predictions of the comprehensive model described above. Overall, 98% of the 513 data points are predicted within ±15%, with an average absolute deviation between the data and predictions of 5.91%. Details of the predictions for each tube and each reduced pressure are shown in Table 5.3. Predictions for each pressure are plotted in Figures 5.25-5.26, and show an excellent agreement between the data and the predictions. The relatively larger discrepancies for G = 800 kg/m^2-s for 0.9×p_{crit} in the 9.4 mm tube may be due to the high heat transfer coefficients at these mass fluxes, which lead to larger experimental uncertainties in the data. It should also be pointed out that the 300 kg/m^2-s, 0.8×p_{crit} case for R410A in the 6.2 mm tube was omitted from the model development because the

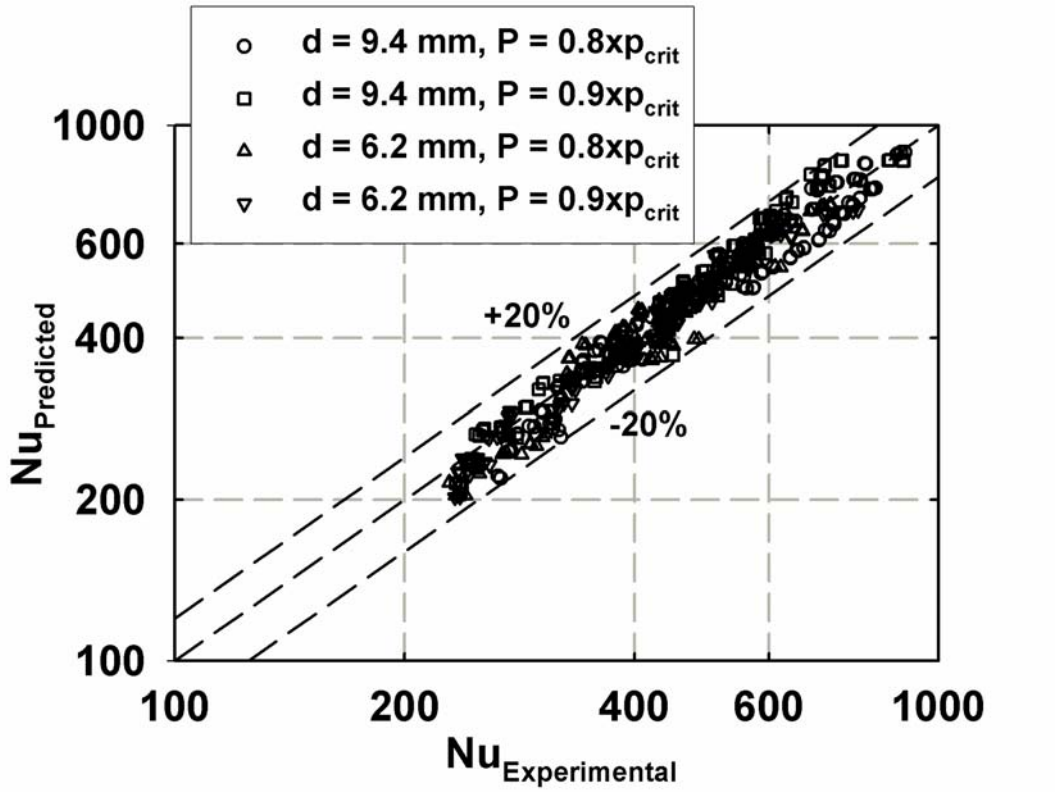

Figure 5.24 Predictions of the Comprehensive Annular, Wavy and Transition Region Heat Transfer Model

Table 5.3 Heat Transfer Coefficient Prediction Capabilities

Reduced Pressure	Tube Size (mm)	Average Deviation	Number of Points	Points below 15%
0.8	9.4	6.59%	153	98%
0.9	9.4	5.97%	117	96%
0.8	6.2	6.54%	121	98%
0.9	6.2	4.40%	122	100%
Overall		**5.91 %**	**513**	**98%**

measured heat transfer coefficients for this case were unreasonably and inexplicably high.

The effect of reduced pressure on the heat transfer coefficient predictions at representative mass fluxes is shown in Figure 5.27. These figures show the expected and physically reasonable trend of slightly higher heat transfer coefficients at the lower reduced pressure.

5.2.2 Pressure Drop Models

As discussed in section 2.1.3, the pressure drop in two phase flow in horizontal tubes consists of frictional and deceleration pressure components as shown in the expression below:

$$\left|\left(dP/dz\right)\right| = \left|\left(dP_f/dz\right)\right| - \left|\left(dP_d/dz\right)\right| \tag{5. 29}$$

The deceleration component in the above equation for uniform cross-sectional area along the length of the test section is given as follows:

$$\left|\frac{dP_d}{dz}\right| = \left|G^2 \cdot \frac{d}{dz}\left[\frac{x^2}{\rho_v \cdot \alpha} + \frac{(1-x)^2}{\rho_l \cdot (1-\alpha)}\right]\right| \tag{5. 30}$$

The accounting of the deceleration component in the pressure drop is extremely important as it can, in certain cases, be up to as much as much as 100% of the actual measured pressure drop. A plot of the deceleration pressure drop as a percentage of the

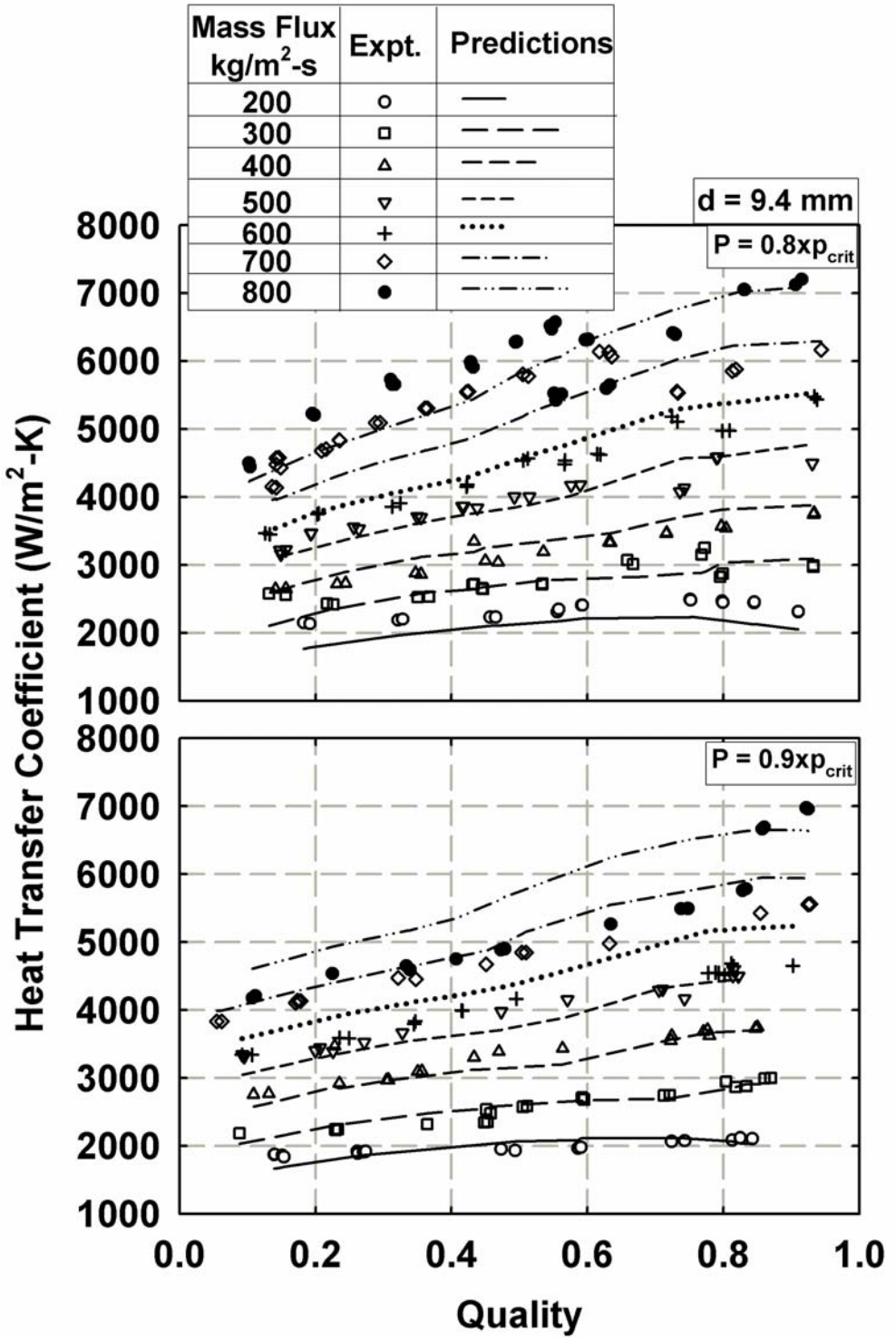

Figure 5. 25 Heat Transfer Model Predictions (9.4 mm Tube)

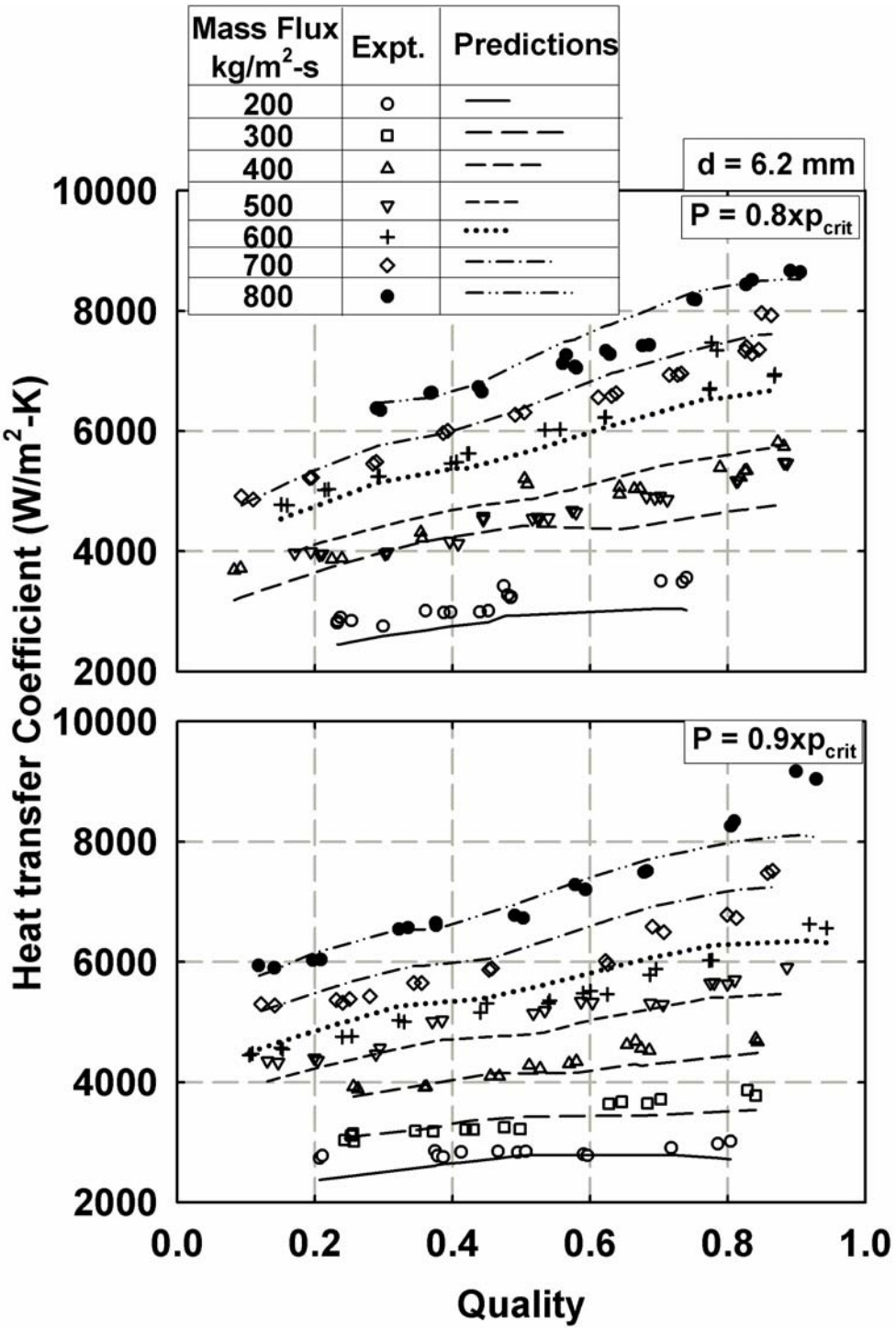

Figure 5. 26 Heat Transfer Model Predictions (6.2 mm Tube)

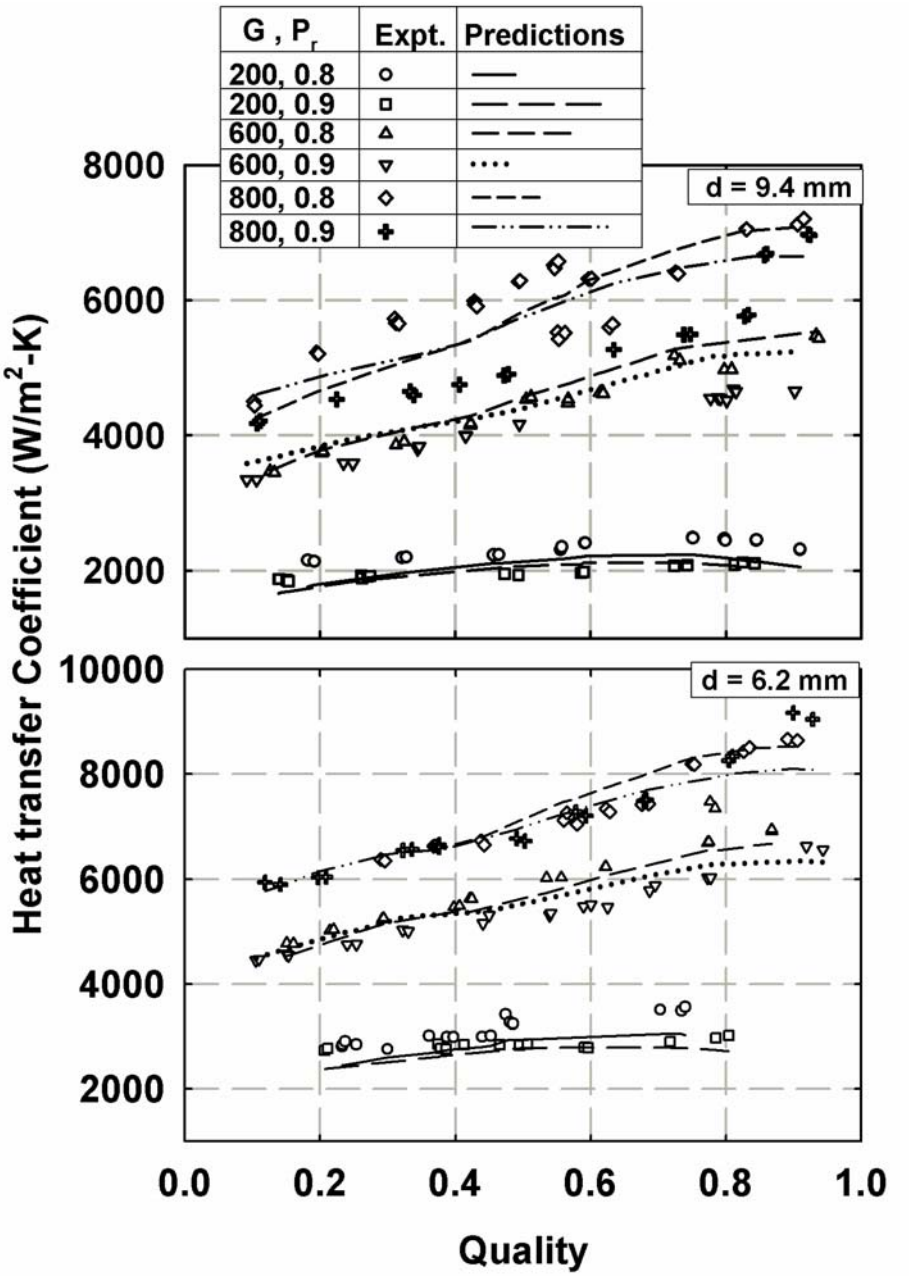

Figure 5. 27 Effect of Reduced Pressure on Heat Transfer Coefficient

measured pressure drop for various mass fluxes for R410A is shown in Figure 5.28. The deceleration pressure drop ranged from 0.5-96.5% of the total measured pressure drop for all the data points. The larger contributions of the deceleration pressure drop typically occur for the lower total measured pressure drops (i.e., lower mass fluxes). This is attributed to the fact that at lower mass fluxes, the frictional pressure drop is lower, while the deceleration pressure drop is determined by the quality change across the test section. Representative values of the measured, deceleration and frictional pressure drops versus quality at a mass flux of 500 kg/m^2-s are shown in Figure 5.29. It should be noted that these pressure drops were recorded in tests where the change in quality across the test section varied from $\Delta x = 0$ to $\Delta x = 0.41$ with $\Delta x < 0.20$ for 71 % (321 out of 452) data points. The frictional pressure drop obtained from this approach is used for subsequent analysis and model development.

The frictional pressure drop is evaluated using a two-phase multiplier approach based on the Tran *et al.* (2000) two-phase multiplier for boiling in small channels, which in turn is based on the Chisholm (1983) B-coefficient method. Thus, the frictional pressure drop is given by:

$$\left(\frac{dP}{dz}\right)_f = \Phi_{LO}^2 \left(\frac{dP}{dz}\right)_{LO} \tag{5. 31}$$

where the two phase liquid only multiplier (Φ_{LO}^2) developed by (Tran *et al.*, 2000) is:

$$\phi_{LO}{}^2 = 1 + (CY^2 - 1)[N_{conf} x^{0.875}(1-x)^{0.875} + x^{1.75}] \tag{5. 32}$$

where C is a constant, C = 4.3, and N_{conf} is a dimensionless confinement number that includes the effects of density and surface tension as follows:

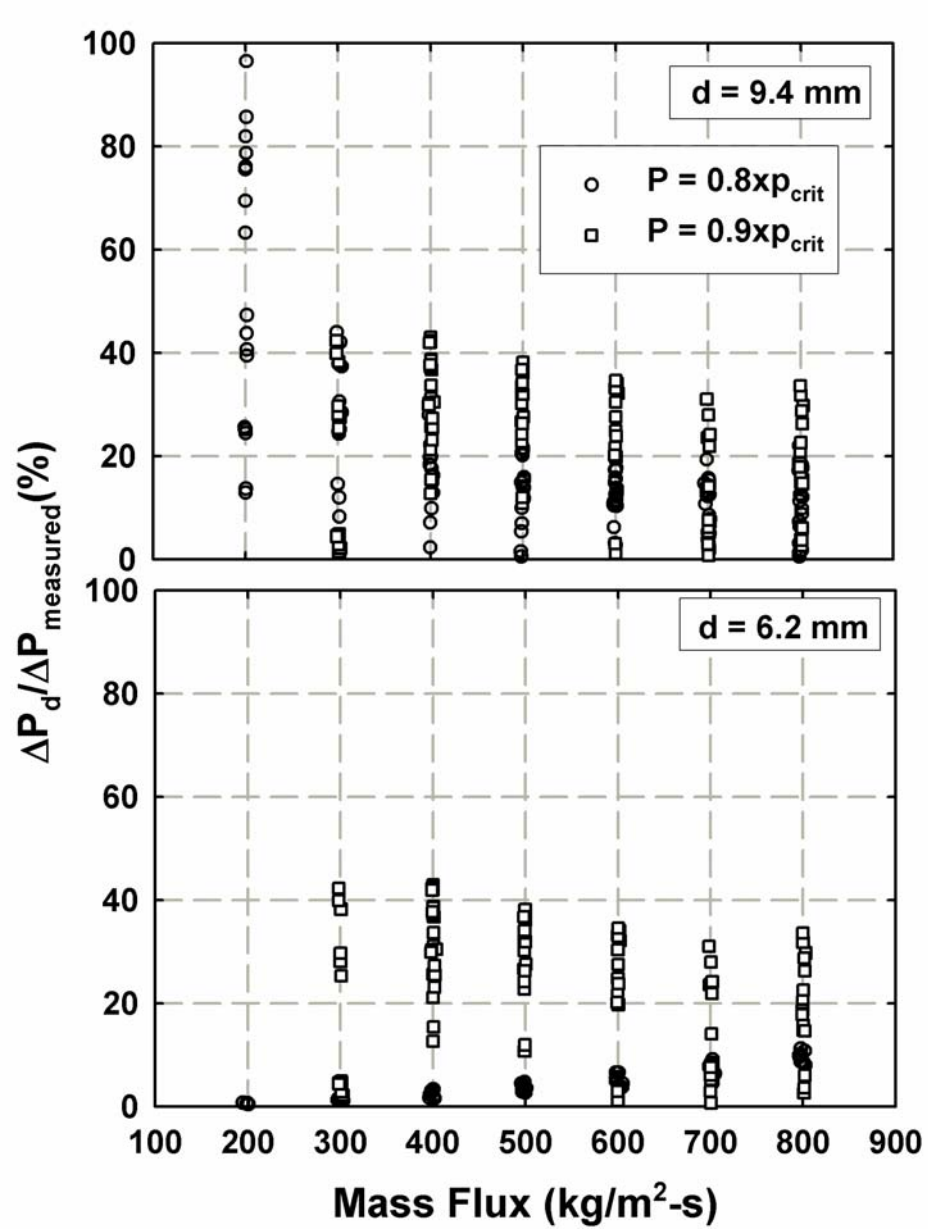

Figure 5.28 Deceleration Pressure Drop as a Percentage of Measured Pressure Drop

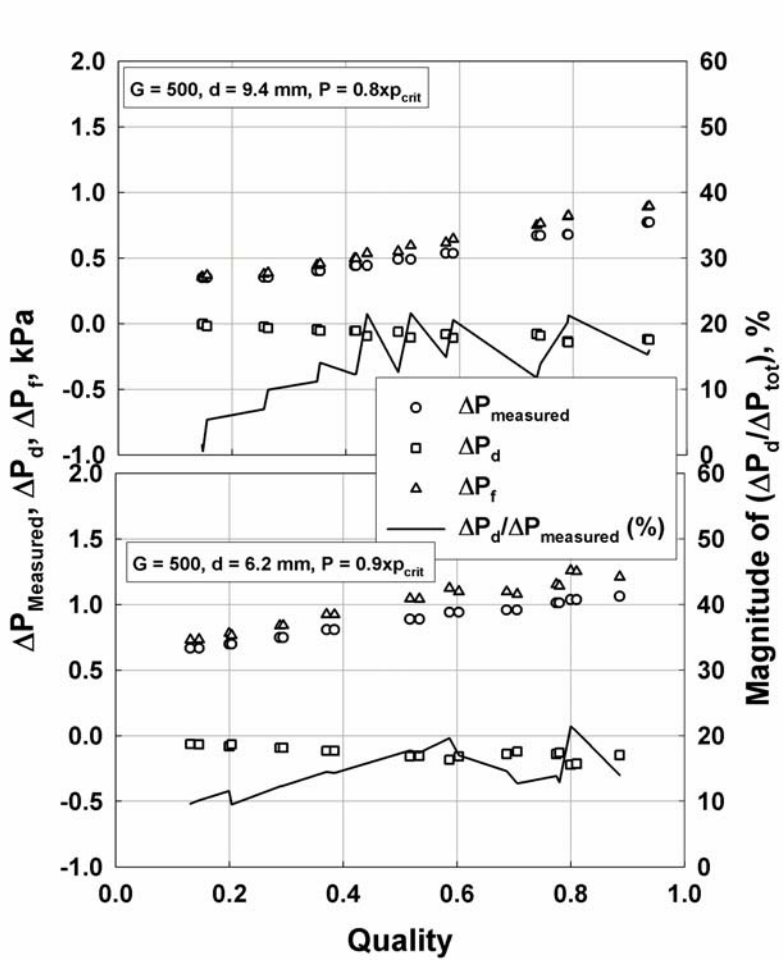

Figure 5.29 Representative Measured, Deceleration and Frictional Pressure Drops (Phase-Change Tests)

$$N_{conf} = \frac{1}{d} \cdot \left[\frac{\sigma}{g(\rho_l - \rho_v)} \right]^{0.5} \tag{5. 33}$$

Due to the larger tubes used in this study, the confinement numbers are fairly small (0.025-0.059), but not negligible, and are more or less fixed by the reduced pressure (properties) and tube diameter. The confinement number increases with a decrease in tube diameter and a decrease in reduced pressure, as can be seen in Figure 5.30. Y^2 in the Tran *et al.* (2000) model is given by:

$$Y^2 = \frac{(dP/dz)_{f,GO}}{(dP/dz)_{f,LO}} \tag{5. 34}$$

The $(dP/dz)_{f,GO}$ and $(dP/dz)_{f,LO}$ terms are the frictional pressure gradients for vapor only and liquid only flows, defined as follows:

$$(dP/dz)_{f,GO} = 2f_{GO}G^2/(D\rho_v) \tag{5.35}$$

$$(dP/dz)_{f,LO} = 2f_{LO}G^2/(D\rho_l) \tag{5.36}$$

where

$$\mathrm{Re}_{GO} = \frac{GD}{\mu_v} \quad \text{and} \quad \mathrm{Re}_{LO} = \frac{GD}{\mu_l} \tag{5.37}$$

$$f_{GO} = \begin{cases} 16/\mathrm{Re}_{GO} & \mathrm{Re}_{GO} < 2300 \\ 0.079\,\mathrm{Re}_{GO}^{-0.25} & 2300 < \mathrm{Re}_{GO} < 20000 \\ 0.046\,\mathrm{Re}_{GO}^{-0.2} & \mathrm{Re}_{GO} > 20000 \end{cases} \tag{5.38}$$

$$f_{LO} = \begin{cases} 16/\mathrm{Re}_{LO} & \mathrm{Re}_{LO} < 2300 \\ 0.079\,\mathrm{Re}_{LO}^{-0.25} & 2300 < \mathrm{Re}_{LO} < 20000 \\ 0.046\,\mathrm{Re}_{LO}^{-0.2} & \mathrm{Re}_{LO} > 20000 \end{cases} \tag{5.39}$$

The following modified form of the two-phase multiplier ϕ_{LO}^2 was used to correlate the frictional pressure drops in the present study:

$$\phi_{LO}^2 = 1 + [C(x,P_r)Y^2 - 1][N_{conf}x^{\frac{2-n}{2}}(1-x)^{\frac{2-n}{2}} + x^{2-n}] \tag{5.40}$$

where C may be a function of quality and reduced pressure, and n is the absolute value of the power to which Re_{LO} is raised in the single-phase friction factor as shown in equation (5.38) and (5.39):

$$n = \begin{cases} 1 & \mathrm{Re}_{LO} < 2300 \\ 0.25 & 2300 < \mathrm{Re}_{LO} < 20000 \\ 0.2 & \mathrm{Re}_{LO} > 20000 \end{cases} \tag{5.41}$$

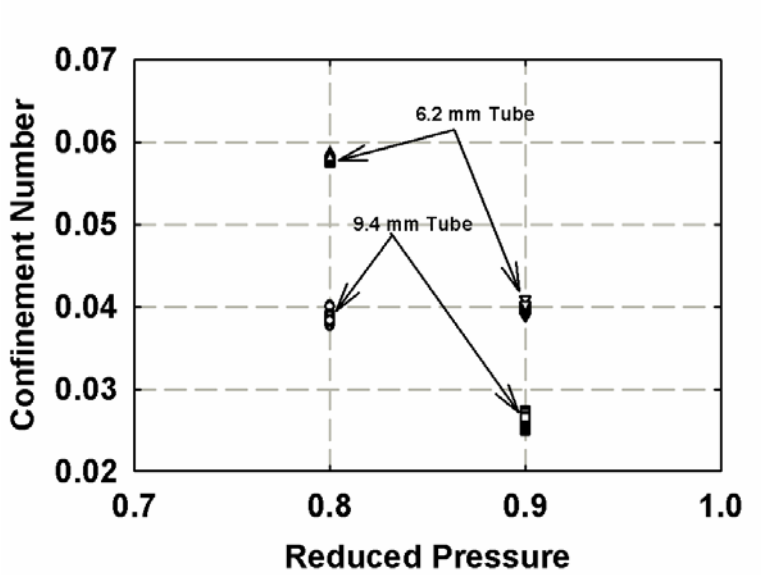

Figure 5. 30 Confinement Numbers for R410A versus Reduced Pressure

The scaling factor C was found to be largely independent of reduced pressure, but was a function of quality and diameter, as can be seen in Figure 5.31. Regression analysis was used to develop the following expressions for C in the annular and wavy flow regimes:

$$C(x)=\begin{cases}\left(18.22-31.97x+17.21x^2\right)\left(\dfrac{d_{actual}}{d_{baseline}}\right)^{-0.34} & \text{For Annular Flow}\\ \left(\dfrac{0.12}{x^2}+\dfrac{2.9}{x}-0.76\right)\left(\dfrac{d_{actual}}{d_{baseline}}\right)^{-0.77} & \text{For Wavy Flow}\end{cases} \tag{5. 42}$$

The frictional pressure drops can now be obtained using equations (5.31, 5.32 and 5.42). In addition to these models, the transition region was addressed using the same interpolation technique that was described above for the heat transfer data, with the various regions delineated as follows:

$$\begin{cases}\text{Annular Flow Regime} & 24 < Fr_{so} < 65\\ \text{Annular to Wavy Transition} & 14 < Fr_{so} < 24\\ \text{Wavy Flow Regime} & 1.75 < Fr_{so} < 14\end{cases} \tag{5. 43}$$

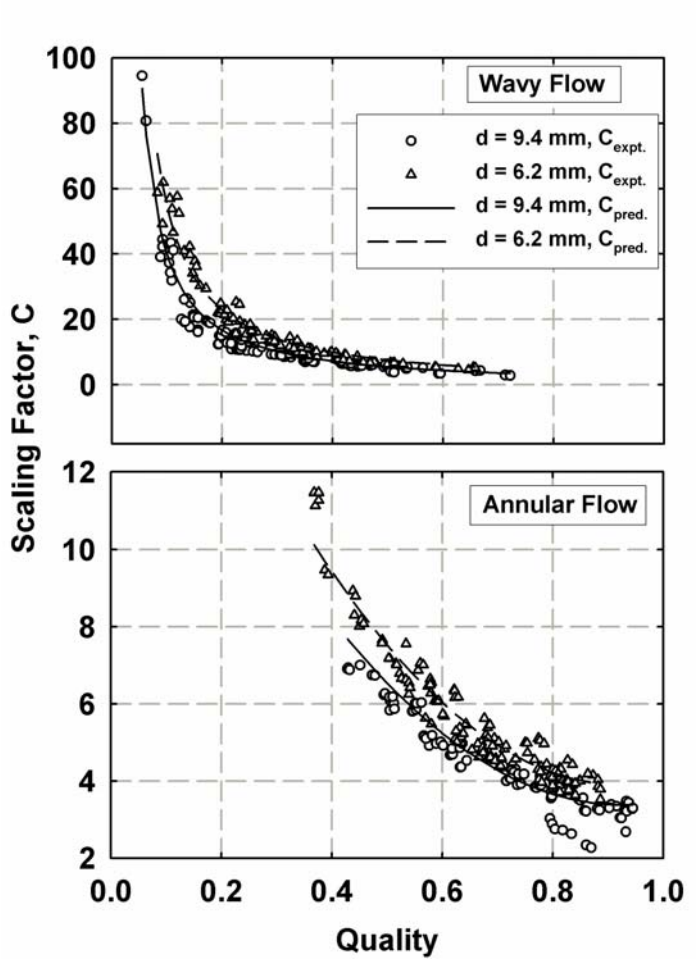

Figure 5.31 Scaling Factor, C as a function of Quality

The overall predictions of this comprehensive condensation pressure drop model are shown in Figure 5.32, with the statistics for the individual cases shown in Table 5.4. There is excellent agreement between the model and the data, with 87% of the 452 data points being predicted within ±15%, and an absolute average deviation of 7.75%. Figures 5.33-5.34 show predicted and experimental frictional pressure gradients as a function of quality for the entire data set. These graphs further illustrate the predictive capabilities of the model, and demonstrate smooth transitions between the wavy and annular regimes. The detailed calculation of condensation pressure drop models developed in the present study is included in Appendix F.

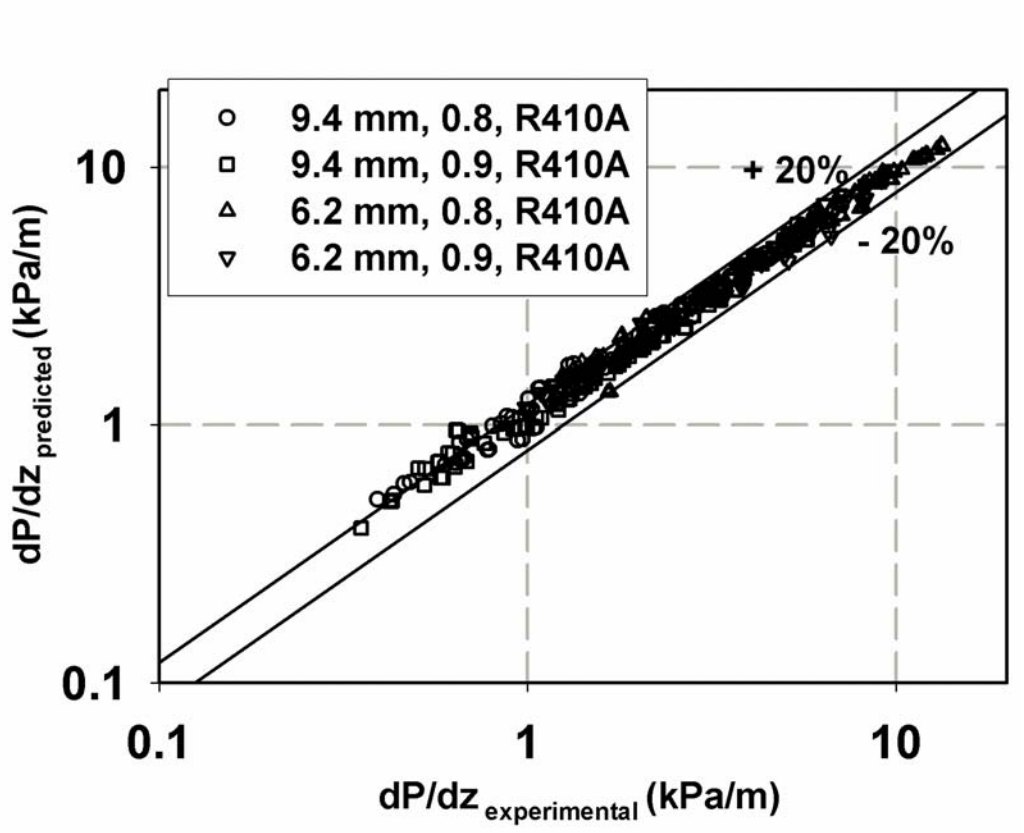

Figure 5. 32 Condensation Pressure Drop Model Predictions

Table 5.4 Condensation Pressure Drop Model Predictions

Reduced Pressure	Tube Size (mm)	Average Deviations	Number of Points	Points below 15%
0.8	9.4	8.47%	129	83%
0.9	9.4	7.81%	100	86%
0.8	6.2	7.15%	122	88%
0.9	6.2	7.50%	101	90%
Overall		**7.75%**	**452**	**87%**

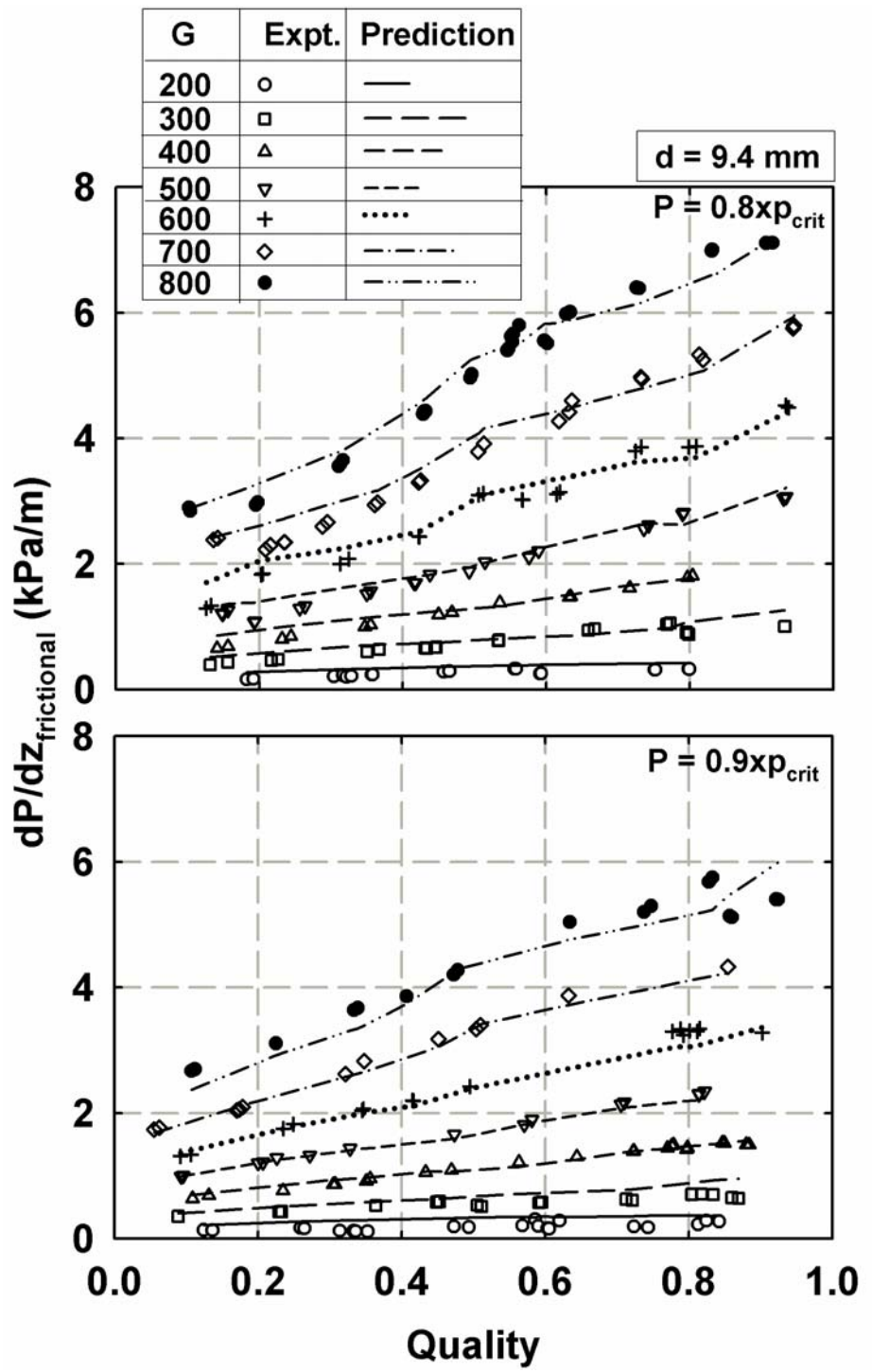

Figure 5. 33 Condensation Pressure Drop Model Predictions (9.4 mm Tube)

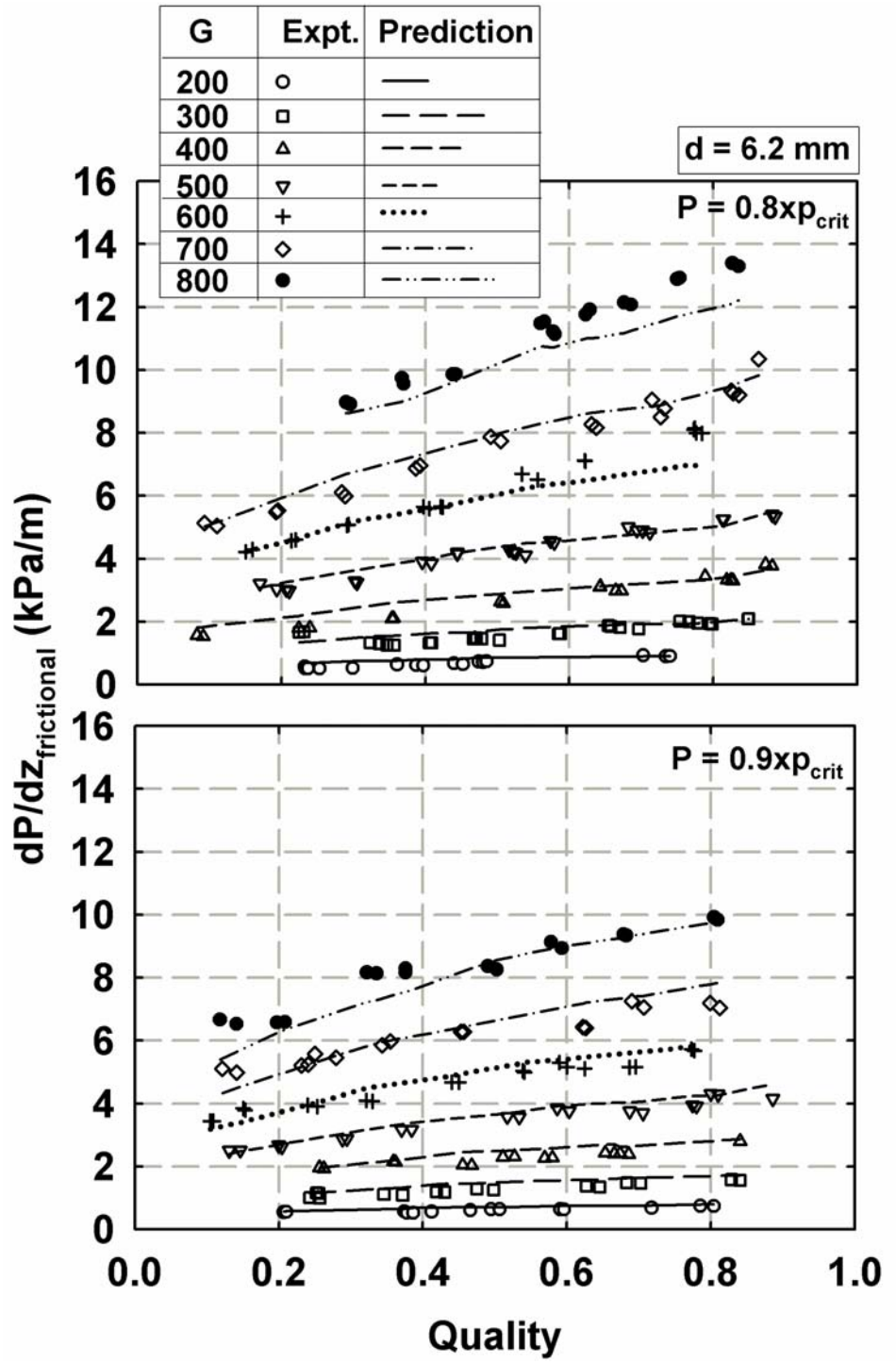

Figure 5. 34 Condensation Pressure Drop Model Predictions (6.2 mm Tube)

CHAPTER 6 SUPERCRITICAL HEAT TRANSFER AND PRESSURE DROP RESULTS AND MODEL DEVELOPMENT

This chapter provides a detailed discussion of the experimental results, comparison with the literature, model development and predictions of the critical and supercritical heat transfer and pressure drop data, obtained and analyzed using techniques described in Chapters 3 and 4.

It should be noted that a companion study on refrigerant R404A in 9.4 mm diameter tubes at supercritical pressure conditions was also conducted by another researcher (Jiang, 2004) in the same laboratory. The models in the model development section (6.3) of this chapter were developed using data for both fluids. However, the discussion below focuses on R410A data collected by the author of this dissertation.

6.1 Supercritical Heat Transfer and Pressure Drop Results

This section discusses the heat transfer and pressure drop results and compares them with the few available correlations in the literature. Possible explanations for agreement and discrepancies between the data and predictions are provided.

6.1.1 Local Heat Transfer Coefficients

The measured local heat transfer coefficients are plotted versus temperature for all the mass fluxes and pressure conditions in Figures 6.1-6.2. The average uncertainties in the measured heat transfer coefficients are 7.7% in the 9.4 mm tube and 13% in the 6.2 mm tube. The larger uncertainties in the smaller diameter tube were attributed to the relatively lower resistance ratios at the correspondingly higher refrigerant heat transfer coefficients, and the increased uncertainty arising from the larger pump heat addition necessary to maintain the resistance ratios at acceptable levels. The refrigerant-to-coolant resistance ratios for all the data points taken in the supercritical tests are shown in

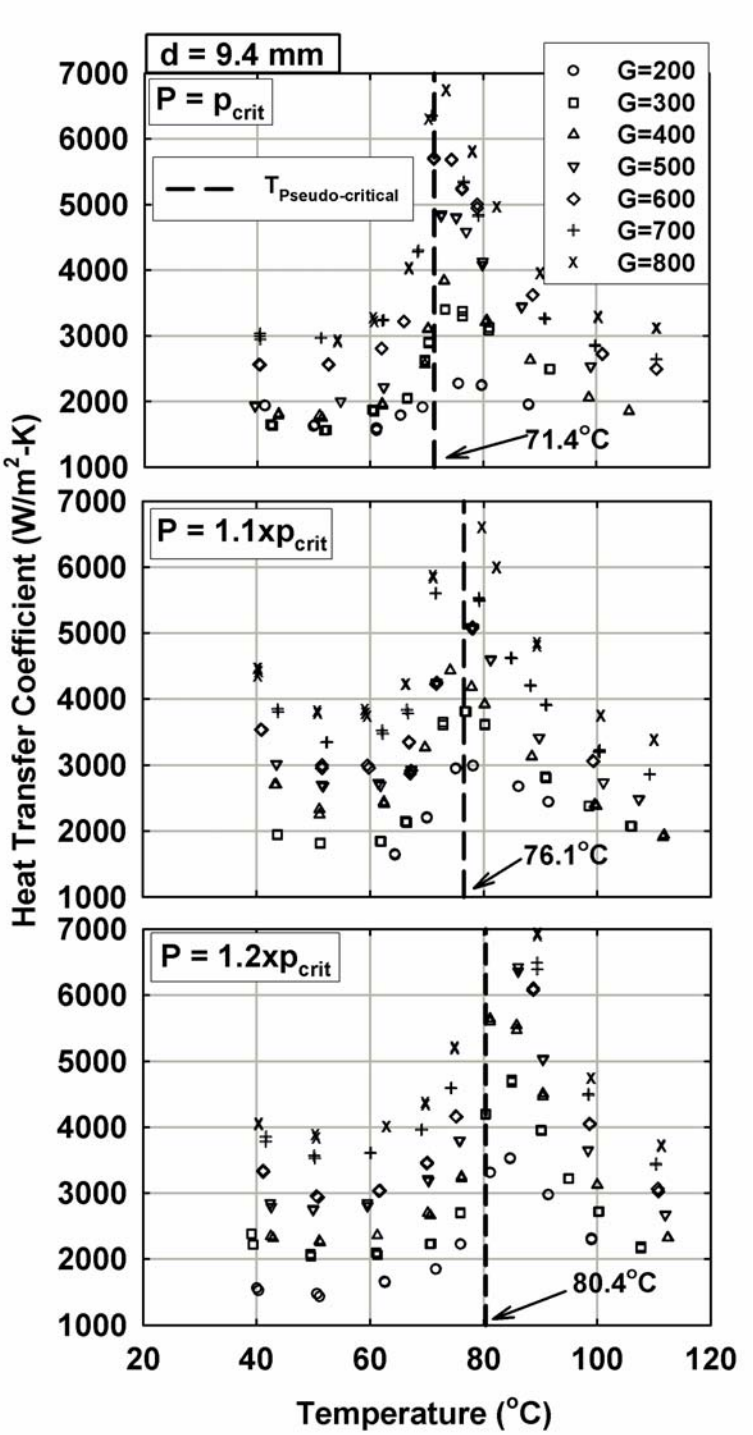

Figure 6.1 Supercritical Heat Transfer Coefficients (9.4 mm Tube)

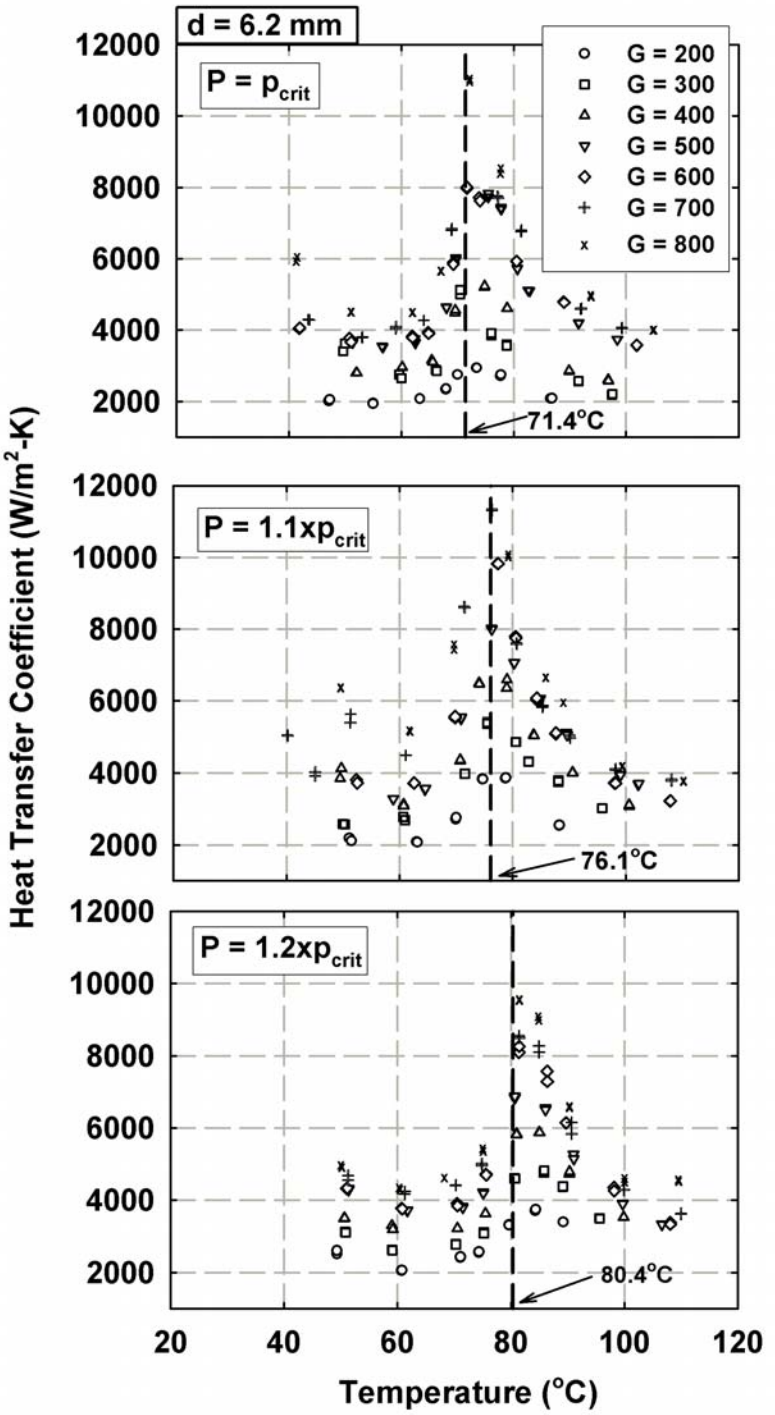

Figure 6.2 Supercritical Heat Transfer Coefficients (6.2 mm Tube)

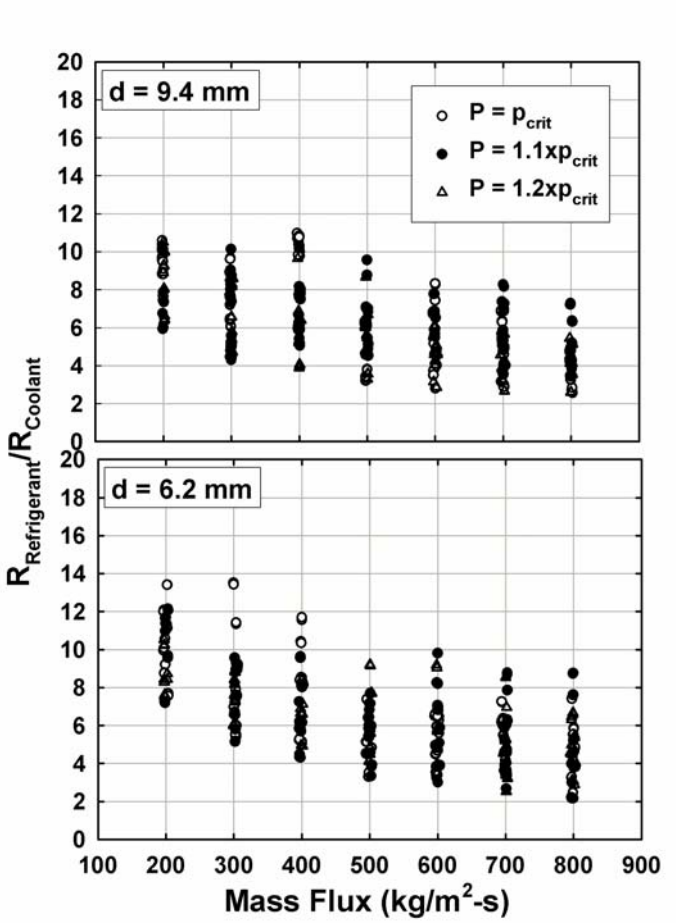

Figure 6.3 Resistance Ratios for all Supercritical Test Conditions

Figure 6.3. The high heat transfer coefficients (6000-10000 W/m^2-K) in the pseudo-critical region near the vapor-liquid dome for all mass fluxes lead to low refrigerant-to-coolant resistance ratios. This resistance ratio ranged from 2.16 – 13.51, with only 28 out of 667 data points with resistance ratios < 3. Figure 6.4 shows heat transfer coefficients derived from the wall-mounted thermocouple measurements for G = 300, 500 and 700 kg/m^2-s for P_r = 1.1. It can be seen that the heat transfer coefficients derived using the two different methods agreed well. For the entire supercritical data set, the average deviation between the two heat transfer coefficients was 10.77%, with minimum and maximum deviations of 1.2% and 23%, respectively.

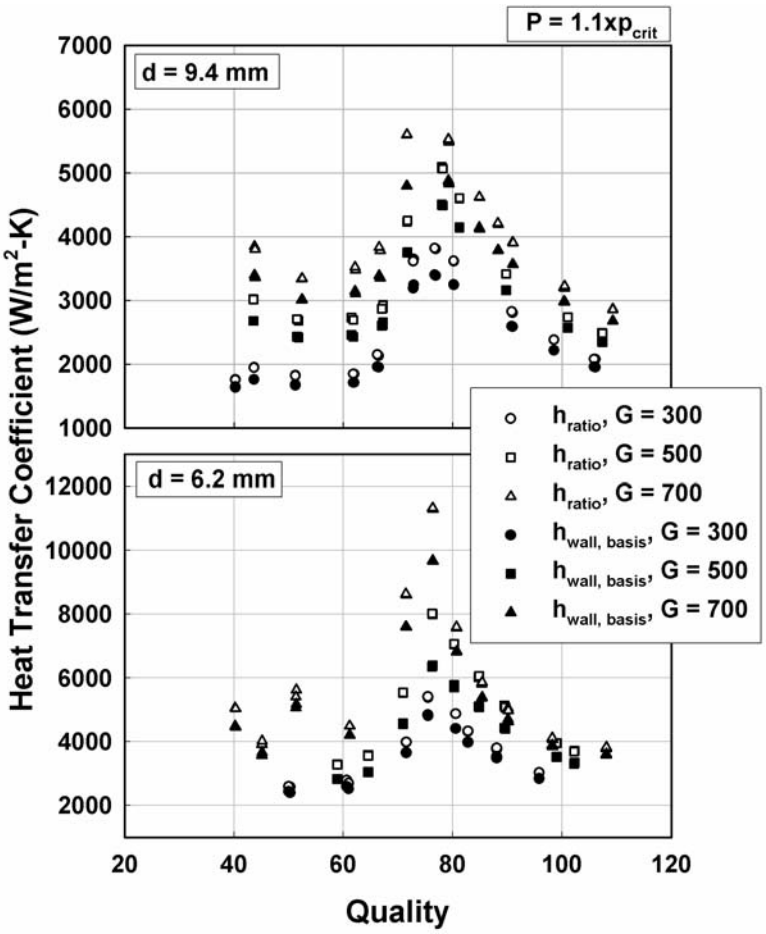

Figure 6.4 Comparison of Supercritical Heat Transfer Coefficients from Water-Side Resistance Analysis and Wall-Temperature Measurements

The heat transfer coefficients in Figures 6.1-6.2 show a sharp peak in the vicinity of the pseudo-critical temperature, $T_{Pseudo\text{-}critical}$, the temperature corresponding to the peak in specific heat. The $T_{Pseudo\text{-}critical}$ of R410A for the three pressures under consideration is:

$$T_{Pseudo-critical,R410A} = \begin{cases} 71.4°C & for \quad p = 1.0 \times p_{crit} \\ 76.1°C & for \quad p = 1.1 \times p_{crit} \\ 80.4°C & for \quad p = 1.2 \times p_{crit} \end{cases} \tag{6. 1}$$

A drastic change in thermo-physical properties due to a change from gas-like to liquid-like behavior across this temperature, as shown in Figure 1.1 in Chapter 1, leads to these peaks in heat transfer coefficients. Thus, for example, for the 9.4 mm tube at P =

p_{crit}, G = 500 kg/m^2-s, for the data point at T = 62.31^{o}C, the C_p = 2.516 kJ/kg-K, whereas at T = 72.59^{o}C, C_p = 13.56 kJ/kg-K. The density falls abruptly from 843 to 340 kg/m^3 across this same temperature, while the viscosity decreases from 7.24×10^{-5} to 2.60×10^{-5} kg/m-s, and the thermal conductivity decreases from 0.075 W/m-K to 0.057 W/m-K. At the same mass flux, the decrease in viscosity leads to an increase in Reynolds number (from 64,695 to 179,641). The combination of property changes leads to an increase in Prandtl number from 2.42 to 6.18. The net effect of these changes is that the Nusselt number increases from 277 to 798, leading to an increase in heat transfer coefficient from 2219 to 4851 W/m^2-K. Similar variations can be seen at the supercritical ($p = 1.1\times p_{crit}$ and $p = 1.2\times p_{crit}$) cases. As the temperature at these pressures increases well beyond $T_{Pseudo\text{-}critical}$ (for example, beyond T > 90^{o}C), several properties such as C_p, ρ, μ decrease gradually to more or less stable ideal gas values, resulting in the lower heat transfer coefficients characteristic of gas-phase flow. It should also be noted that the Nusselt number maintains high values and peaks at about 77^{o}C for $p = p_{crit}$, 81^{o}C for $p = 1.1\times p_{crit}$ and 88°C for $p = 1.2\times p_{crit}$, but the heat transfer coefficients start decreasing at somewhat lower temperatures because of the concurrent decrease in thermal conductivity. Similar trends are observed throughout the range of mass fluxes investigated in this study, with the peak being sharper at the higher mass fluxes. The effect of temperature on heat transfer coefficient is further illustrated by noting that the controlled variation in mass flux in this study was from G = 200 to 800 kg/m^2-s, a factor of 4, while at a representative mass flux of 500 kg/m^2-s for the 9.4 mm tube at critical pressure, simply changing the temperature from about 40 to 100^{o}C, keeping G constant, increases the Reynolds number by a factor of 4.9 (from Re = 43,734 to Re = 229,536). Thus,

temperature variation in the supercritical region has a much more significant effect on heat transfer than the independent variation of mass flux, because it affects thermal properties as well as the flow-related Reynolds number substantially. It should also be noted that, as the pressure increases, the variations in properties decreases, resulting in less variation in the heat transfer coefficients.

At the same mass flux, the heat transfer coefficients in the 6.2 mm tube are higher than those in the 9.4 mm tube (Figures 6.1 and 6.2). Under similar mass flux and temperature conditions, the Reynolds number for the 6.2 mm tube is lower than that of the 9.4 mm tube by a factor of ~ 1.5 (the diameter ratio). At lower Re values, the Nusselt number decreases, but due to the typical exponent on Re < 1, the decrease is by a smaller amount than the diameter ratio, which is reflected as a higher heat transfer coefficient.

6.1.2 Pressure Drops

The measured pressure drops per unit length are plotted as a function of temperature in Figure 6.5 for the representative 9.4 mm tube for all the conditions tested. The pressure gradients for all the critical and supercritical cases at the lowest mass flux (G = 200 kg/m^2-s) were very small. For all the data points at this mass flux, the measured pressure gradients ranged from (-0.078) – 0.555 kPa/m with 71% (68 out of 96) of the data in the range of (-0.078) – 0.2 kPa/m. Since the uncertainty in the differential pressure transducer was constant (0.00623 kPa), the uncertainties in measured pressure gradients for the G = 200 kg/m^2-s were relatively high, i.e. ±3.84% at dP/dz = 0.555 kPa/m and ±355% at dP/dz = (-0.006) kPa/m. The average uncertainty in pressure gradient for the entire set of data points for both tubes for all mass fluxes including the G = 200 kg/m^2-s data was ±5.74%, with maximum and minimum uncertainties

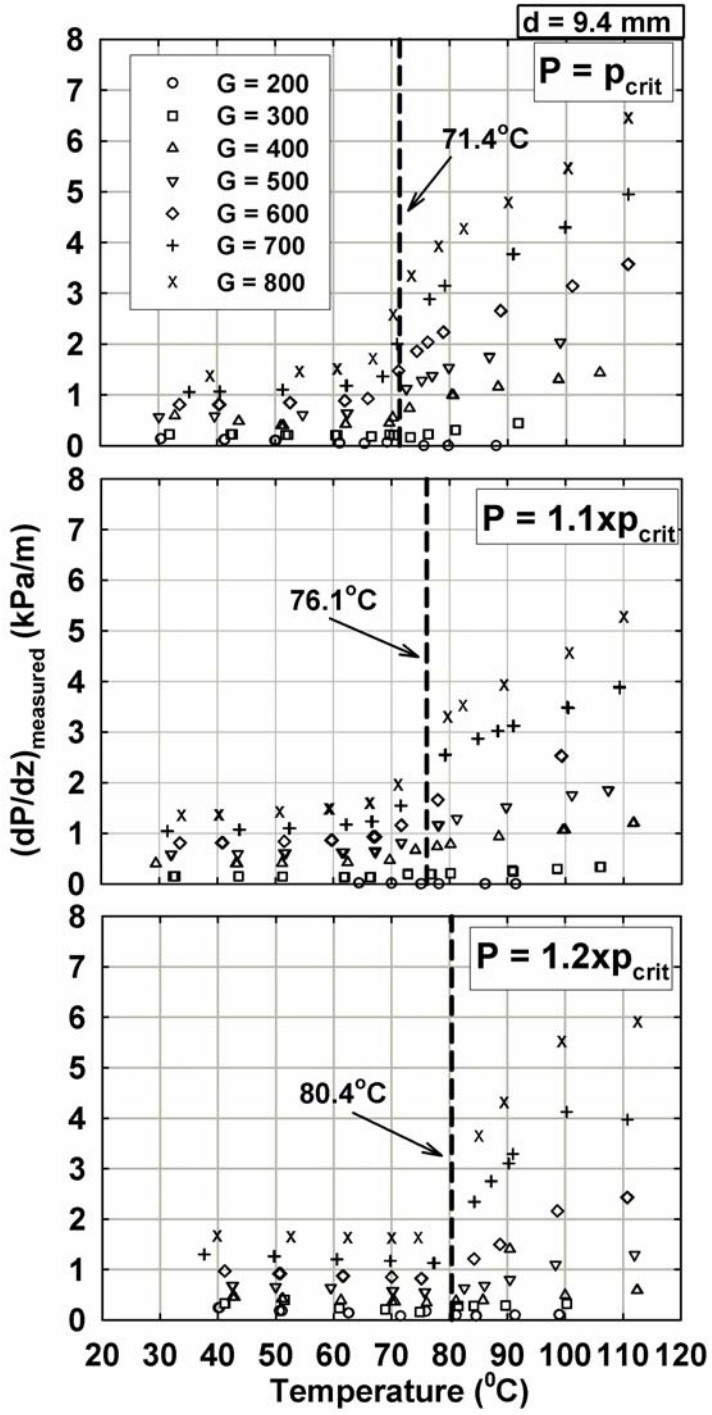

Figure 6.5 Measured Supercritical Pressure Drops (9.4 mm Tube)

of ±354% at dP/dz = (-0.006) kPa/m and ±0.13% at dP/dz = 16 kPa/m, respectively. For the data set without G = 200 kg/m^2-s, the average uncertainty in pressure gradient was ±2.36%, with maximum and minimum uncertainties of ±15.74% and ±0.13%, respectively. For the data points with G = 200 kg/m^2-s, the average uncertainty in pressure gradient was ±31.57%, with maximum and minimum uncertainties of ±355% and ±3.84%, respectively. Based on these uncertainties, it was decided that the measured pressure gradients for the G = 200 kg/m^2-s should not be used for model development.

As discussed above, the density varies significantly with temperature at critical and supercritical conditions. This variation is even more significant in the vicinity of $T_{Pseudo\text{-}critical}$ where a small temperature drop across the test section could cause a substantial decrease in flow velocity due to the transition from gas-like to liquid-like behavior. For example at G = 500 kg/m^2-s and p_r = 1.0, at an average test section temperature of 72.6°C, the temperature difference across the test section is 3.2°C. Even for such a small temperature drop, the density variation in the test section is from 292 to 661 kg/m^3. This causes a decrease in velocity from 1.7 to 0.75 m/s (56%) over a short length, with a corresponding pressure recovery that counteracts to some extent the frictional pressure drop. The measured pressure drop is divided into frictional and deceleration pressure drop components in the following manner:

$$\left|\partial P/\partial z\right|_{measured} = \left|\partial P/\partial z\right|_{frictional} - \left|\partial P/\partial z\right|_{deceleration} \tag{6.2}$$

where the frictional component across the test section is given by:

$$\left|\partial P/\partial z\right|_{frictional} = \frac{1}{2}\cdot f_{friction}\cdot\frac{G^2}{\rho_{average}}\cdot\frac{1}{d_{test}} \tag{6.3}$$

For the deceleration component, the rate of change of momentum across the test section is evaluated as follows:

$$dF = \int_{inlet}^{outlet} \dot{m} \cdot dv \tag{6.4}$$

In the above equation, the mass flow rate $\dot{m} = G \cdot A = \rho \cdot v \cdot A$ is a constant across the test section, which yields the following expression for the momentum change:

$$dF = \dot{m} \int_{inlet}^{outlet} dv = \rho \cdot v \cdot A \int_{inlet}^{outlet} dv = \left[\rho_{out} \cdot {v_{out}}^2 - \rho_{in} \cdot {v_{in}}^2 \right] \cdot A \tag{6.5}$$

Converting this to an expression for pressure drop, we have:

$$\left| \partial P / \partial z \right|_{deceleration} = \left| \frac{dF}{A} \right| = \left| G^2 \cdot \left(\frac{1}{\rho_{in}} - \frac{1}{\rho_{out}} \right) \cdot \frac{1}{L_{test}} \right| \tag{6.6}$$

For the 500 kg/m^2-s mass flux case in the vicinity of the critical point at $p_r = 1.0$ considered above, the deceleration component of the pressure drop was found to be 1.62 kPa/m, which was in fact higher than the measured pressure drop of 1.12 kPa/m. The deceleration component of the pressure drop is plotted for representative R410A data in Figures 6.6-6.7. It can be seen that in the gas-like region (high temperature region), the magnitude of $(\Delta P)_{deceleration}$ was small due to the relatively small change in density. Similar results were observed for the liquid-like region (low temperature region). Near the critical region (temperature close to the critical value), due to the sudden decrease in fluid density, $(\Delta P)_{deceleration}$ shows a sudden increase. Also the deceleration component of pressure drop is higher for lower mass fluxes due to the lower flow velocities causing a larger temperature drop across the test section.

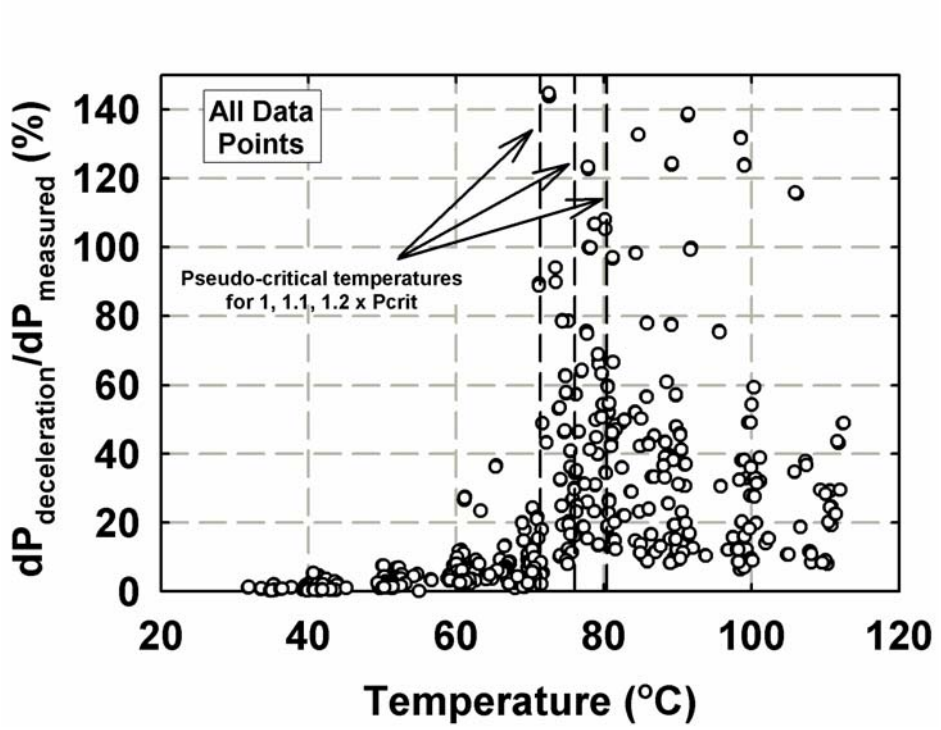

Figure 6.6 Variation of Deceleration Pressure Drop with Temperature

The variation in the frictional pressure gradient of the refrigerant with temperature is shown in Figures 6.8-6.9. It can be seen that the variation of pressure drop is not very significant below the transition temperature, i.e., in the liquid-like region. The pressure gradient abruptly drops as the temperature is decreased across the transition temperature due to the sudden change in refrigerant properties from the gas-like to the liquid-like properties and the corresponding decrease in velocities. Thus, for example, for the p_{crit}, G = 500 kg/m^2-s case discussed above, the velocity decreases from 2.83 m/s at 99^{o}C to 1.46 m/s at just above the pseudo-critical temperature, to 0.59 m/s in the liquid-like region. These variations in velocities are reflected in the pressure drop trends seen in Figures 6.8-6.9.

Frictional pressure drops in the 9.4 mm tube at the three different reduced pressures and three mass fluxes are shown in Figure 6.10. For a given mass flux and

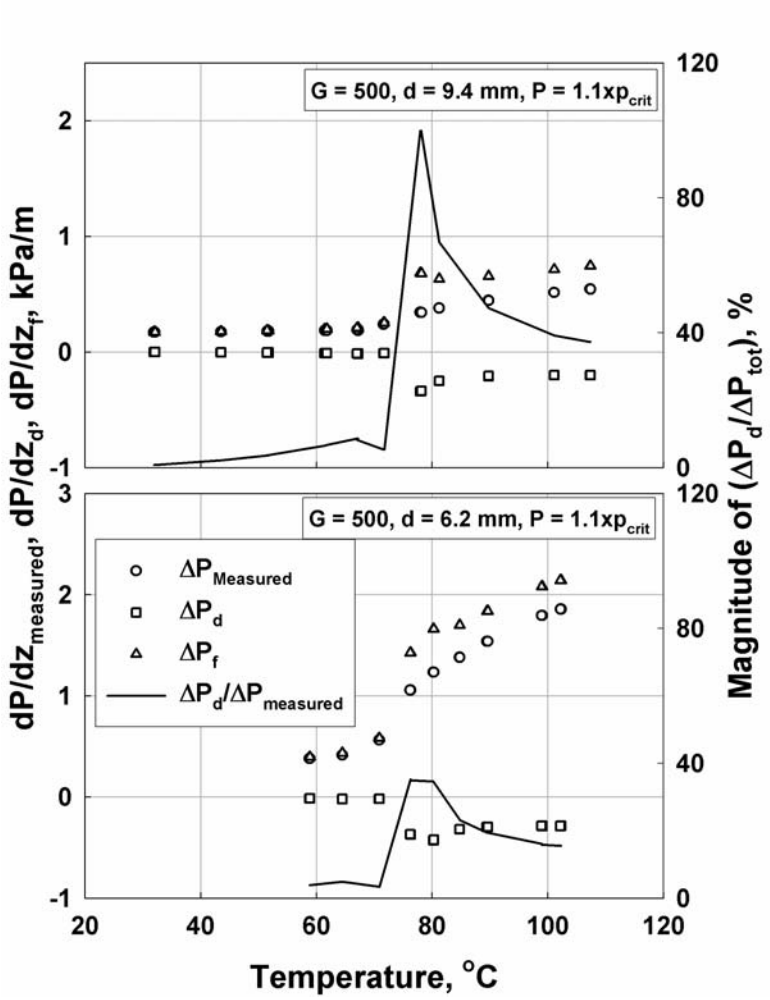

Figure 6.7 Representative Magnitudes of Measured, Deceleration and Frictional Pressure Drops (P_r = 1.1)

temperature, the pressure drops in the liquid-like phase are approximately the same at different pressures. In the gas-like phase beyond the transition, however, the pressure drop decreases as the pressure increases. This is because, as the pressure increases, while in the liquid-like phase, the fluid density remains approximately constant (for T = 40.83°C, ρ = 1007 kg/m^3 at P = p_{crit} and 1018 kg/m^3 at P = 1.2×p_{crit}), in the gas-like phase, the density increases with increased pressure (for T = 90.4°C, ρ = 191.5 kg/m^3 at P = p_{crit} and 285.6 kg/m^3 at P = 1.2×p_{crit} see Figure 1.1 in Chapter 1), resulting in velocities

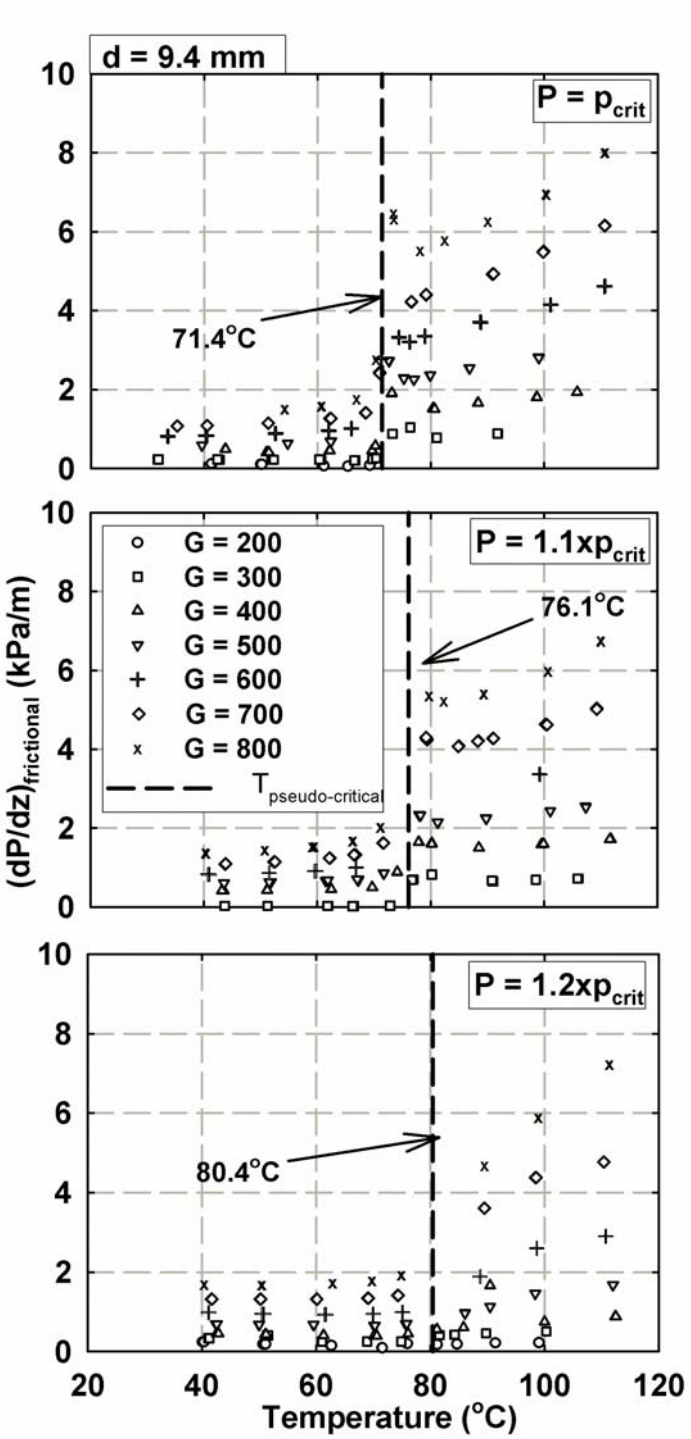

Figure 6.8 Frictional Supercritical Pressure Drops (9.4 mm Tube)

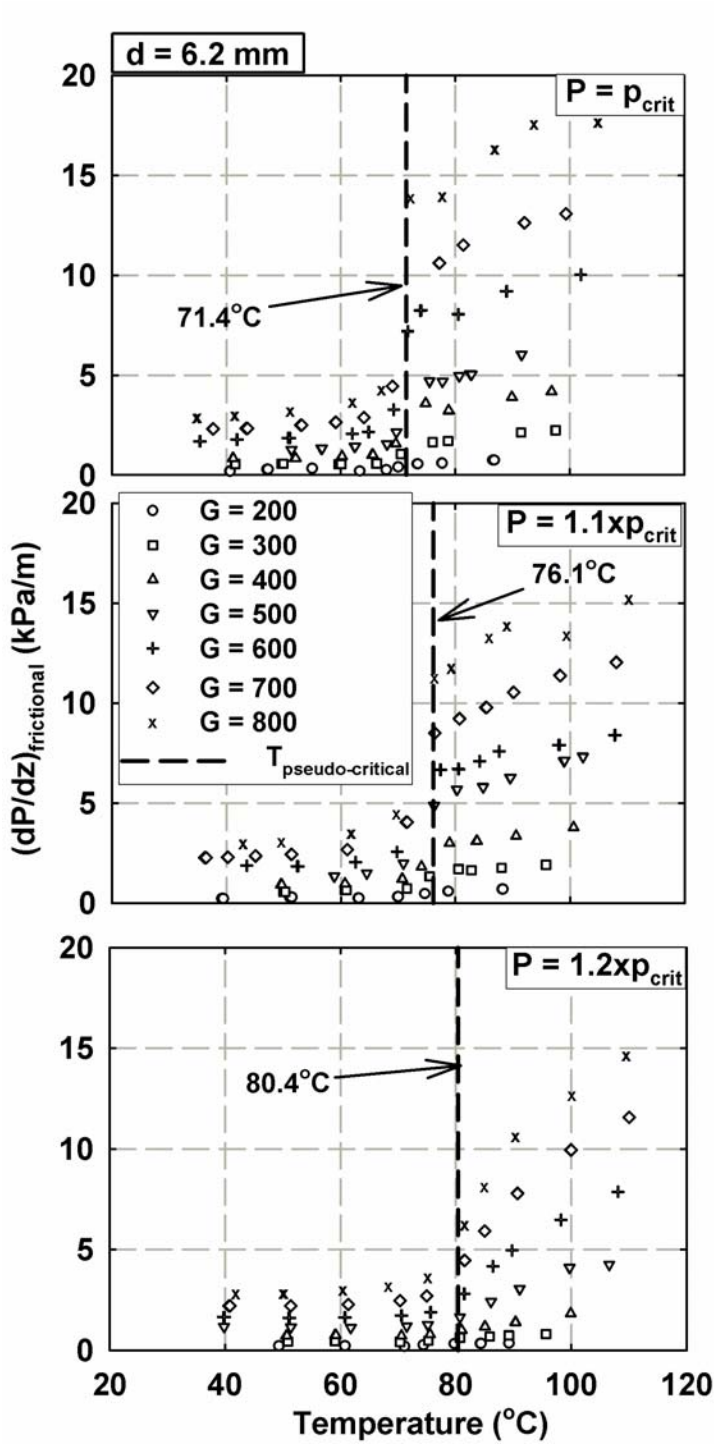

Figure 6.9 Frictional Supercritical Pressure Drops (6.2 mm Tube)

of 2.83 m/s (ρ = 175.5 kg/m^3) at 99.03^{o}C at P = p_{crit}, 2.66 m/s (ρ = 200.7 kg/m^3) at 101.1^{o}C (P = 1.1×p_{crit}), and 2.43 m/s (ρ = 243.4 kg/m^3) at 98.37^{o}C (P = 1.2×p_{crit}). These progressive decreases in flow velocity in the gas phase lead to the decreases in pressure drop in the gas-like phase seen in Figure 6.10.

6.2 Comparison with the Literature

As discussed in Section 2.2, the available heat transfer and pressure drop correlations in the supercritical region are either single-phase turbulent flow correlations, or those developed for supercritical CO_2. Data from the present study are compared with the predictions of these models to assess their applicability to the current work, and/or guide the development of new models.

6.2.1 Gnielinski (1976)

The Gnielinski (1976) correlation shown below is valid for turbulent conditions ($3000 < Re < 5\times10^6$) and $0.5 < Pr < 2000$).

$$Nu = \frac{(f/8)(\mathrm{Re}-1000)\,\mathrm{Pr}}{1+12.7(f/8)^{0.5}(\mathrm{Pr}^{2/3}-1)} \tag{6. 7}$$

In the above equation, the friction factor f is calculated using the Petukhov (1970) correlation given by:

$$f = [0.790\ln(\mathrm{Re}) - 1.64]^{-2} \tag{6. 8}$$

The data from the present study are compared with the predictions of the Gnielinski (1976) in Figure 6.11. It is evident that most of the data are under predicted by more than 30%. A comparison of the trends of the Gnielinski correlation with those the current data for representative conditions is shown in Figure 6.12. The figure shows that the Gnielinski correlation is in reasonable agreement with the data for G < 500

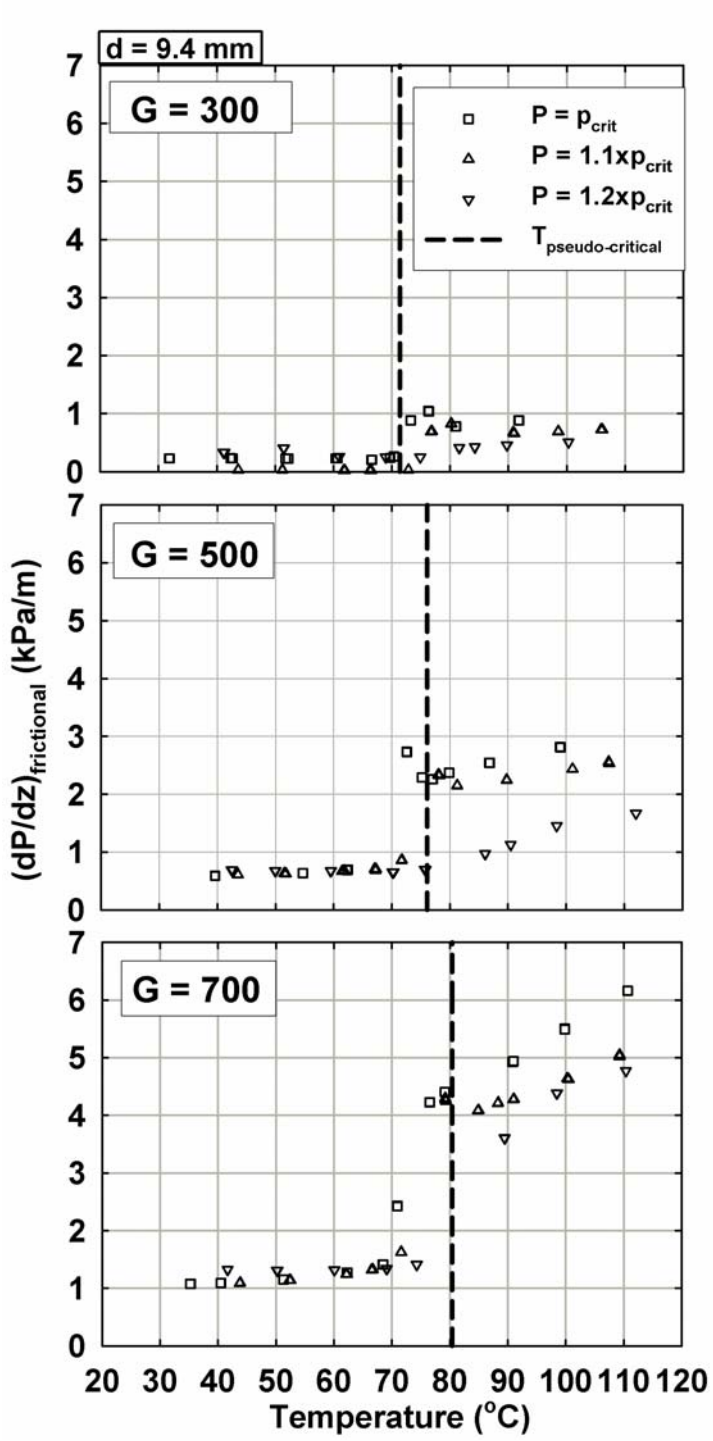

Figure 6.10 Effect of Reduced Pressure on Frictional Pressure Drop (9.4 mm Tube)

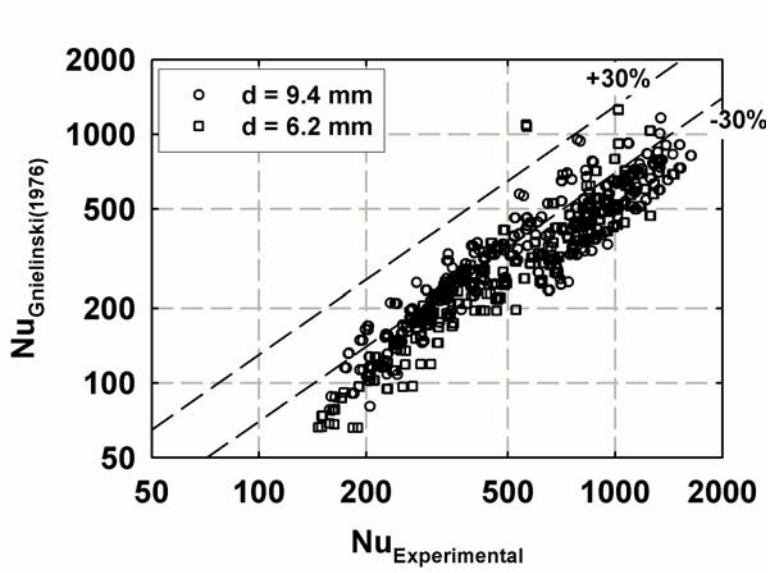

Figure 6.11 Overall Predictions of Gnielinski (1976) Correlation

kg/m^2-s, while the data are considerably under predicted for G > 500 kg/m^2-s. For the whole set of data, the mean absolute deviation from this correlation is 40%.

6.2.2 Krasnoshchekov *et al.* (1970) and Pitla *et al.* (2002)

Correlations developed by these authors use property ratio multipliers to single-phase convective correlations for the modeling of supercritical cooling of carbon dioxide. Krasnoshchekov *et al.* (1970) used density and specific heat ratio multipliers for the wall Nusselt number as follows:

$$Nu_b = Nu_w \left(\frac{\rho_w}{\rho_b} \right)^n \left(\frac{\bar{c}_p}{c_{pw}} \right)^m \tag{6. 9}$$

The constants m and n are provided graphically by the authors as a function of reduced pressure. The wall Nusselt number Nu_w is obtained from the Petukhov (1970) single phase heat transfer correlation. Pitla *et al.* (2002) used an average of Nusselt numbers at wall and bulk temperatures and applied a conductivity multiplier as follows:

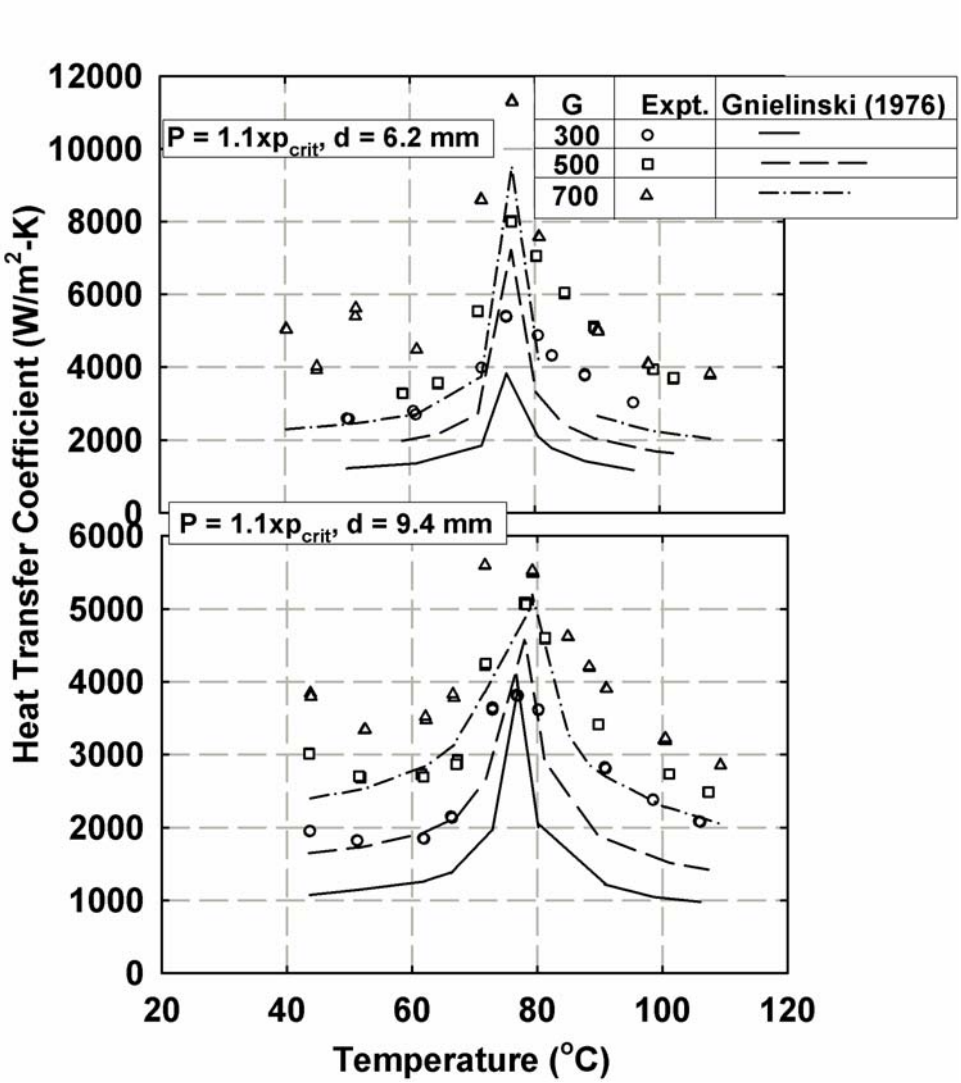

Figure 6.12 Representative Trends Predicted by Gnielinski (1976) Correlation

$$Nu = \left(\frac{Nu_{wall} + Nu_{bulk}}{2} \right) \frac{k_{wall}}{k_{bulk}} \qquad (6.\ 10)$$

where Nu_{wall} and Nu_{bulk} are evaluated using the Gnielinski (1976) correlation at the wall and bulk temperatures, respectively. The overall predictions of these models are shown in Figure 6.13. The Krasnoshchekov *et al.* (1970) correlation considerably under predicts most of the data (mean absolute deviation of 42%) , while the Pitla *et al.* (2002) correlation results in large under- and over- predictions throughout the range of data

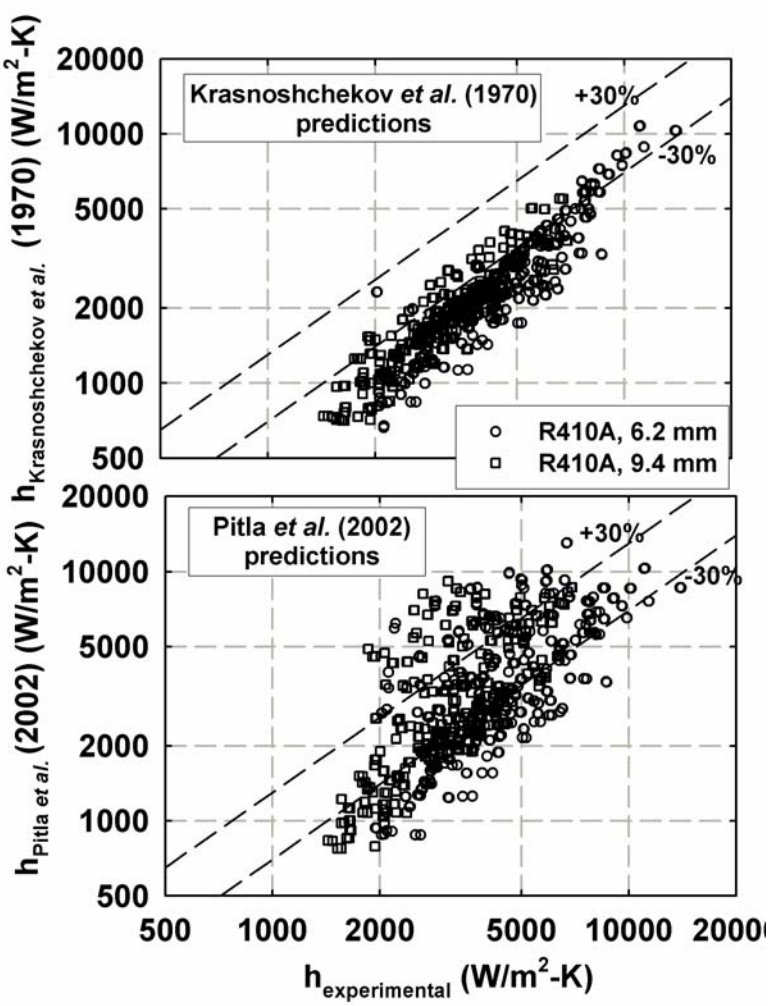

Figure 6.13 Overall Predictions of Krasnoshchekov *et al.* (1970) and Pitla *et al.* (2002) Correlations

(mean absolute deviation of 40%). The predictive trends of these correlations are further investigated for representative data in Figure 6.14. It appears that even though the Krashnoshchekov *et al.* model under-predicted almost all the data, it follows the heat transfer coefficient trends well. The discrepancies in this model may therefore be due to constants in the correlation being based on Carbon dioxide - a pure fluid with properties much different from the refrigerant blends under consideration. The Pitla *et al.* model results in unrealistic predictions above the pseudo–critical temperature: instead of a decrease in heat transfer coefficients, a steady rise is seen. This is attributed to the fact

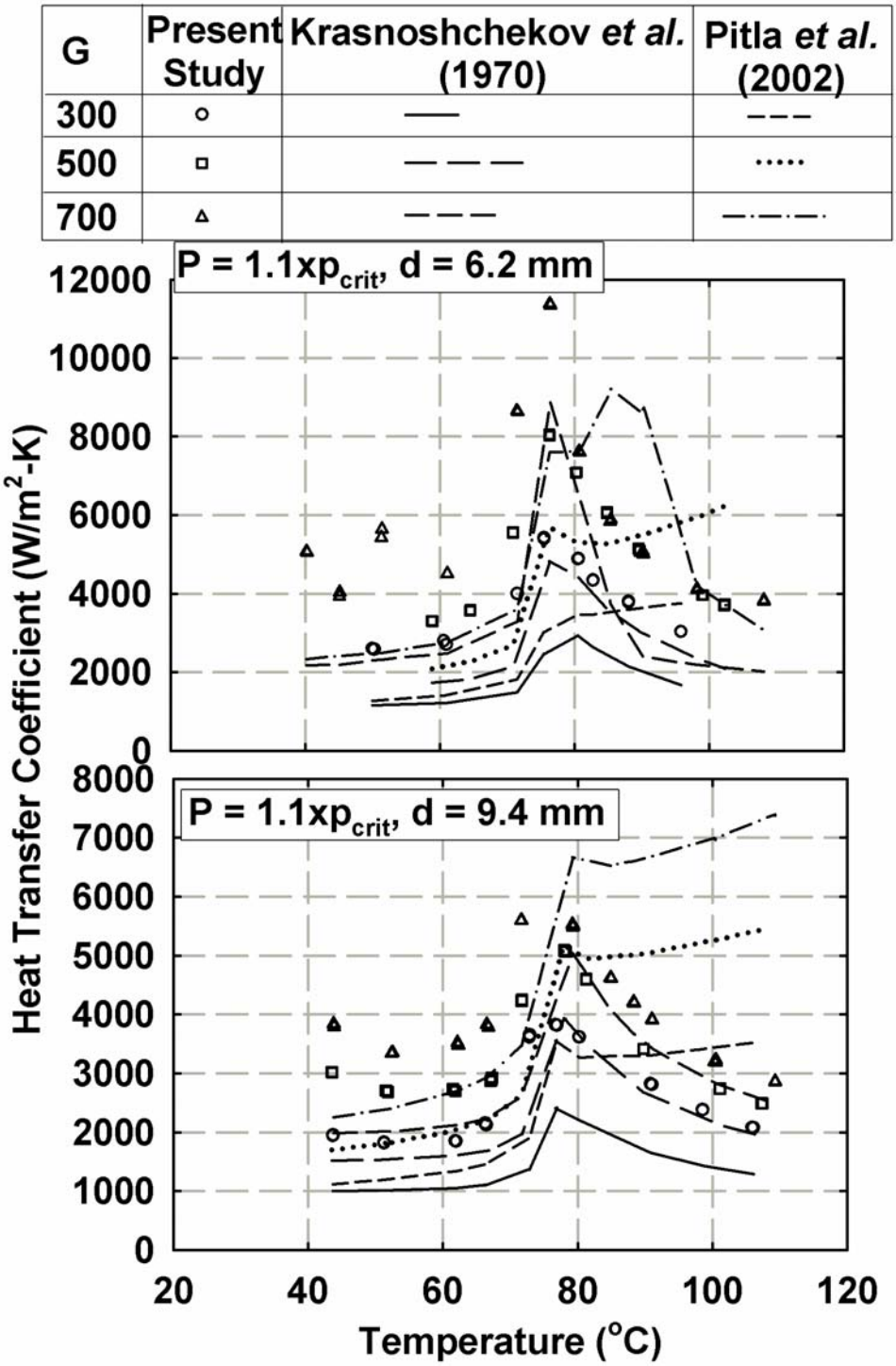

Figure 6.14 Representative Trends Predicted by Krasnoshchekov *et al.* (1970) and Pitla *et al.* (2002) Correlations

that the model uses an average of bulk and wall Nusselt numbers. Above $T_{Pseudo\text{-}critical}$, the specific heat decreases, leading to lower bulk heat transfer coefficients, however T_{wall} might still be less than $T_{Pseudo\text{-}critical}$, resulting in an increase in wall specific heat and heat transfer coefficients. The abrupt variations in heat transfer coefficient and the multiple inflection points in these plots occur because Nu_{wall} and Nu_{bulk} reach peak values at different fluid temperatures, leading to these unrealistic predictions.

6.2.3 Kuraeva and Protopopov (1974) and Churchill (1977b)

Kuraeva and Protopopov (1974) developed a correlation for friction factor of supercritical fluids based on Filonenko's (1954) correlation for single-phase flow. They used wall-to-bulk viscosity correction factors and included a consideration of natural convection effects to propose the following correlation:

$$f = \begin{cases} f_0 \cdot (\mu_w/\mu_l)^{0.22} & Gr/\mathrm{Re}^2 < 5\times 10^{-4} \\ f_0 \cdot (\mu_w/\mu_l)^{0.22} \times 2.15 \cdot \left(Gr/\mathrm{Re}^2\right)^{0.1} & 5\times 10^{-4} < \left(Gr/\mathrm{Re}^2\right)^{0.1} \end{cases} \qquad (6.\ 11)$$

where f_0 is given by Filonenko's (1954) correlation for $Re > 10^5$, and $f_0 = 0.02$ for $Re < 10^5$. The Churchill (1977b) friction factor correlation is for single-phase (laminar, transition and turbulent) flow of fluids. Both models under-predict the data (Figure 6.15), with the Kuraeva and Protopopov correlation resulting in somewhat better predictions (mean average deviation of 44%) than those of the Churchill correlation (mean average deviation of 64%). Pressure drop trends predicted by these models are shown in Figure 6.16 for representative conditions. The Kuraeva and Protopopov model shows better agreement for the 9.4 mm tube data than for the 6.2 mm tube data. Although the Churchill correlation results in larger errors (under predictions), it appears to follow the trends in the data better.

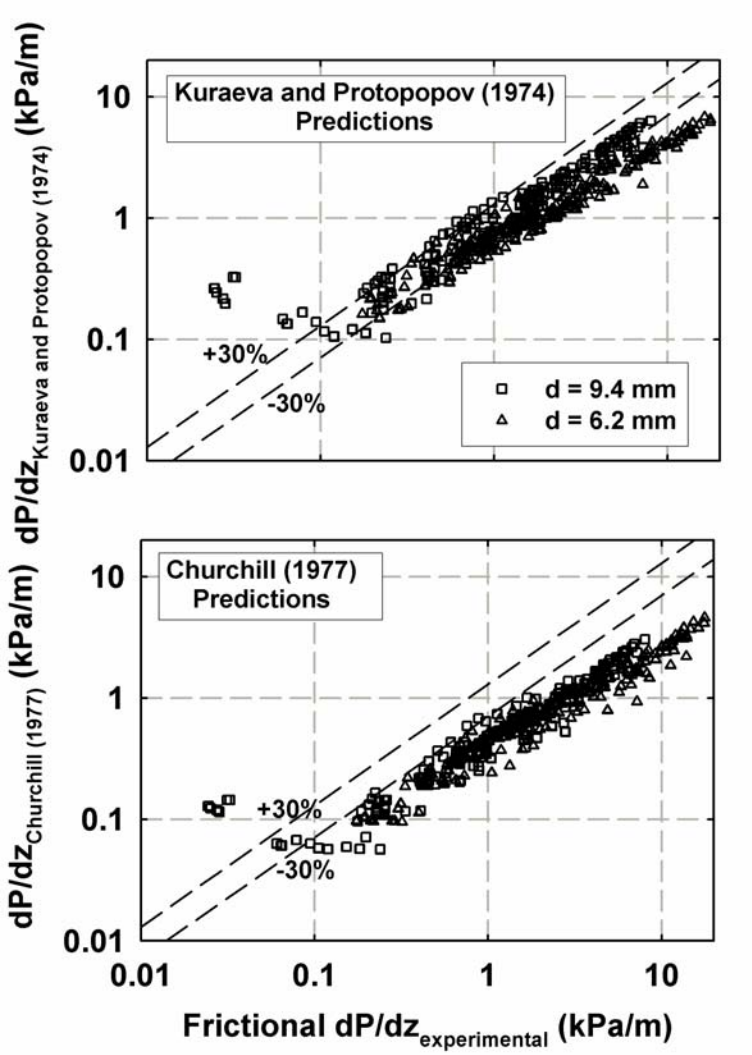

Figure 6.15 Overall Predictions of Kuraeva and Protopopov (1974) and Churchill (1977) Pressure Drop Correlations

6.3 Model Development

6.3.1 Flow Region Definition

As stated above, based on the variations in the thermodynamic and thermophysical properties, the supercritical conditions can be divided into three regimes, liquid-like, pseudo-critical transition, and gas-like. In the liquid-like regime, the refrigerant behaves very much like a liquid at subcritical pressures. The viscosity changes the most with the temperature. As the temperature increases, the viscosity

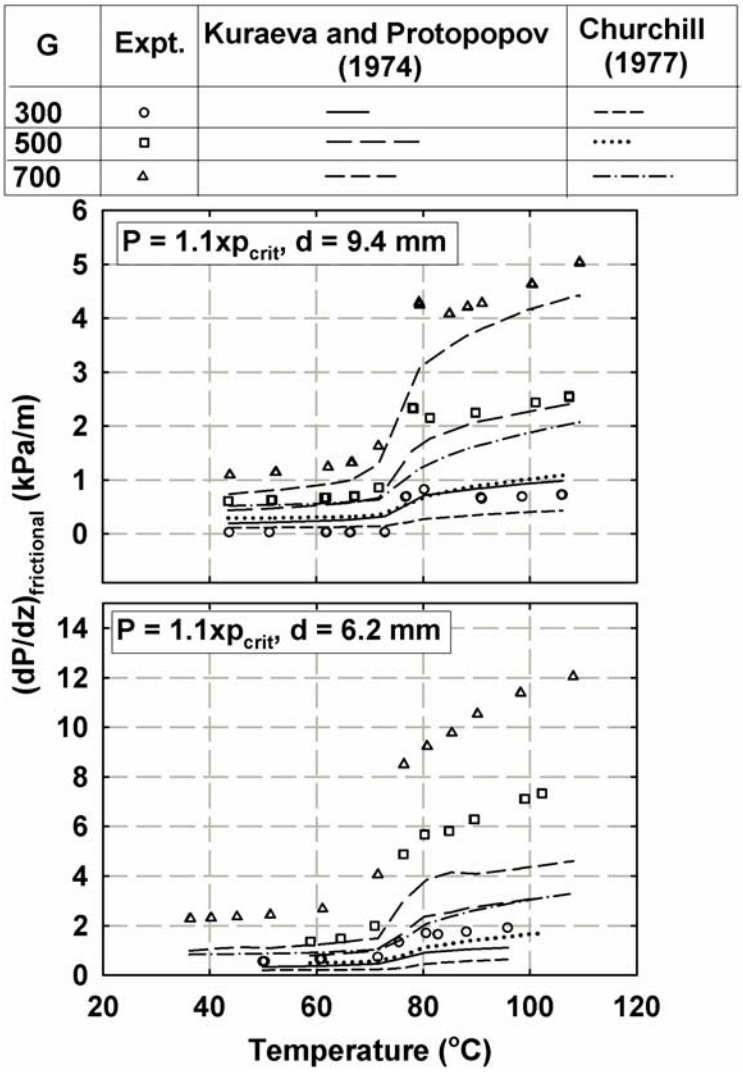

Figure 6.16 Representative Trends Predicted by Kuraeva and Protopopov (1974) and Churchill (1977) Correlations

decreases gradually. In the pseudo-critical transition regime, the density and viscosity of the refrigerant decrease sharply with an increase in temperature, while specific heat, volume expansion coefficient and Prandtl number pass through a maximum. In the gas-like regime, the refrigerant properties gradually approach the properties of an ideal gas as the temperature increases. These flow regime transition criteria are defined quantitatively based on the specific work of thermal expansion (contraction), E_o,by Kurganov (1998a; 1998b), as follows:

$$E_o = \left(p \cdot \partial V / \partial h\right)_p = p \cdot \beta / \left(\rho \cdot C_p\right) \tag{6. 12}$$

E_o (dimensionless) is the ratio of the work done by the refrigerant during cooling to the heat convected out of it during the flow. Plots of E_o with respect to enthalpy and temperature for R410A are shown in Figure 6.17. The plot of E_o versus enthalpy shows a gradual increase to a point where $E_o = 0.04$, followed by an abrupt change in the slope until $E_o \approx 0.1826$ where the curve reaches a maximum and then decreases with a further increase in enthalpy. Based on this, three regimes are defined: (a) a liquid-like (low

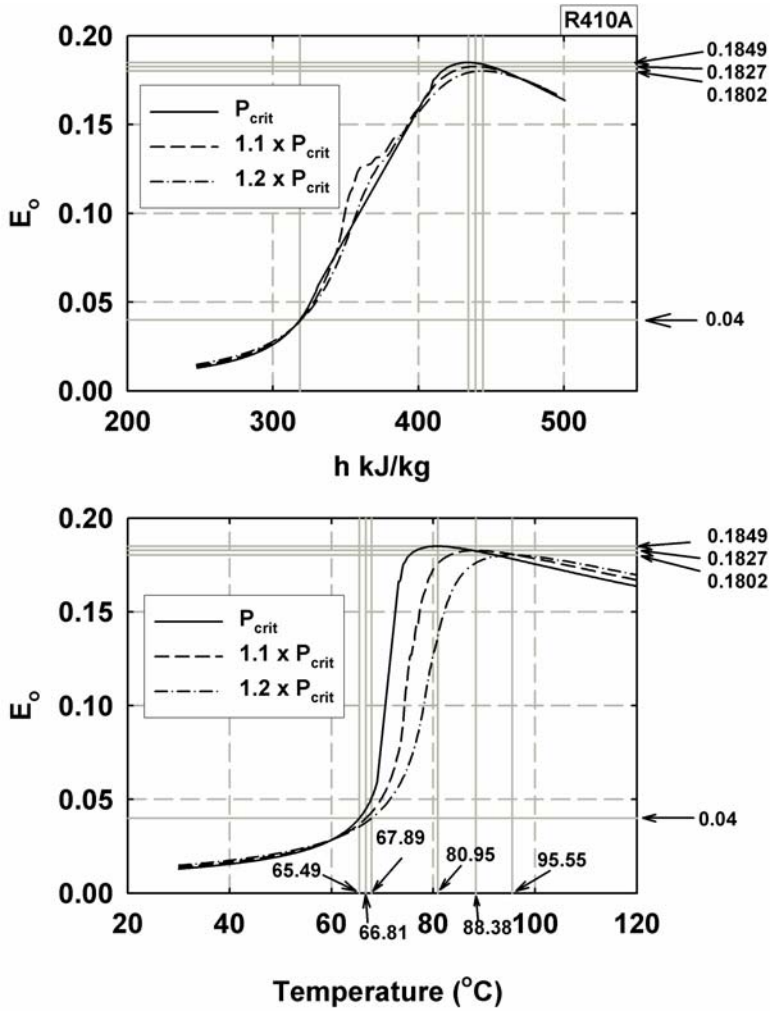

Figure 6.17 E_o versus Enthalpy and Temperature

temperature) regime where the change in E_o with temperature (or enthalpy) is gradual, mostly due to small property variations; (b) pseudo-critical transition regime where the change in E_o is rapid with temperature (or enthalpy) (although not two-phase flow, this regime has some characteristics of phase-change flow): the work done by contraction increases significantly due to an abrupt decrease in density, thereby increasing E_o; and (c) the gas-like regime where the E_o starts to decline as temperature (or enthalpy) increases. In the gas-like regime, property changes are small and hence, from equation (6.12), E_o is proportional to β. In this regime, β tends to ideal gas behavior and is proportional to 1/T. Thus E_o is found to be inversely proportional to temperature in this regime.

The transition temperatures from the pseudo-critical transition regime to the gas-like regime were found when $dE_o/dh = 0$. For the transition between the liquid-like regime and the pseudo-critical transition regime, since dE_o/dh does not change sign, the transition temperatures were located at the temperature where the slope change occurs. Upon examination of the data, it was found that for a given enthalpy h, E_o was largely independent of pressure. Hence, the corresponding temperatures were used as the basis for dividing the data into liquid-like, pseudo-critical transition and gas-like regimes. The E_o versus temperature plots in Figure 6.17 show the temperature boundaries of the flow regimes. These transition temperatures are tabulated in Table 6.1.

Table 6.1 Boundaries of the Flow Regimes

P_r	Liquid-Like Regime	Pseudo-Critical Transition Regime	Gas-Like Regime
1.0	T < 65.49°C	65.49°C ≤ T ≤ 80.95°C	T > 80.95°C
1.1	T < 66.81°C	66.81°C ≤ T ≤ 88.38°C	T > 88.38°C
1.2	T < 67.89°C	67.89°C ≤ T ≤ 95.55°C	T > 95.55°C

6.2.2 Pressure Drop Model

The frictional pressure drops obtained above from the data were used to compute the Darcy friction factors as follows:

$$\left(\frac{dP}{dz}\right)_{Frictional} = -\frac{1}{2}\cdot f \cdot \rho \cdot v^2 \cdot \frac{1}{d_{test}} \tag{6. 13}$$

The resulting friction factors are plotted in Figure 6.18, where the flow-regime definitions described above are used to distinguish the data in the three regimes. This figure shows that the liquid-like and gas-like regime data appear grouped together, whereas the transition regime shows a wide scatter.

In the literature, to account for variable-property effects in internal flows, the use of a ratio of fluid properties or the ratio of bulk temperature-to-wall temperature as multipliers to a constant-property heat transfer or friction factor correlation is often recommended. For liquids, a viscosity or Prandtl number ratio is used as they vary more significantly, while for gases, a temperature ratio is used since ρ, μ, and k are well-behaved functions of absolute temperature (Mills, 1995). In the present study, supercritical heat transfer coefficients and pressure drops were modeled using single-phase correlations with bulk and wall fluid property ratio multipliers to account for the large property variations, based on the specific flow regime, i.e., liquid-like, pseudo-critical transition, and gas-like regimes. However, in the present supercritical case, the behavior of the fluid properties, i.e., ρ, μ, Cp and k, is much different from that of a liquid or a gas. Among these properties, viscosity generally leads to a velocity gradient across the flow, with its magnitude and variation affecting the profile, for all fluids. The velocity gradient is also significantly affected due to the sharp density variation across the cross-section of flow. The other thermophysical properties such as specific heat and

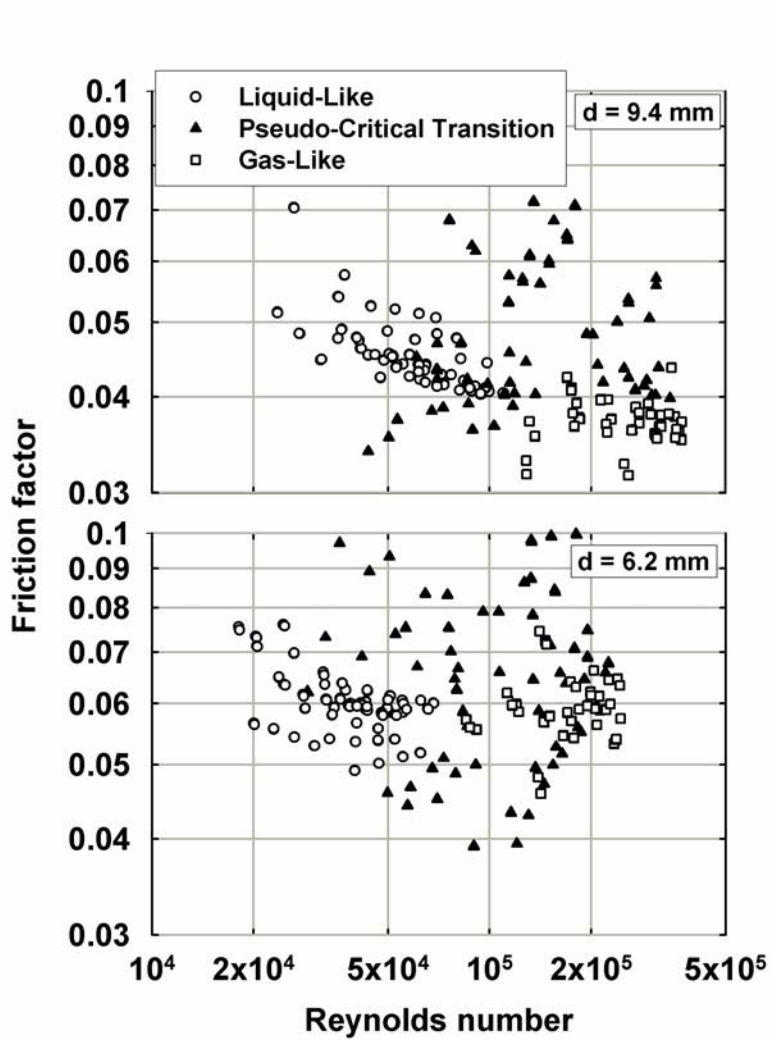

Figure 6.18 Supercritical Friction Factor versus Reynolds Number, All Cases

conductivity lead to temperature gradients across the flow and along the axis of the heat exchanger, in turn affecting the pressure drop. Therefore, these property ratios could have much stronger effects on heat transfer and pressure drop under supercritical conditions than in conventional single-phase flow. Furthermore, these influences could be different in the gas-like, liquid-like and pseudo-phase transition regions.

Thus in the present study, supercritical pressure drops were modeled using the Darcy form of the single-phase Churchill (1977b) friction factor correlation with bulk and wall density ratio multipliers to account for the large property variations, based on the

specific flow regime, i.e., liquid-like, pseudo-critical transition, and gas-like regimes. The following form of the friction factor was found to yield the best results:

$$f = a \cdot f_{Churchill} \left(\frac{\rho_w}{\rho_b} \right)^b \left(\frac{d_{actual}}{d_{baseline}} \right)^c \tag{6. 14}$$

It should be noted that 9.4 mm was chosen as the baseline diameter in the above equation, with the diameter ratio accounting for the variation in friction factors with diameter. The constants and exponents for the above equation are shown in Table 6.2 for each supercritical region. Referring to Table 6.2, the exponent of the density ratio (b) is almost halved from the liquid-like regime to the pseudo-critical transition regime, and vanishes in the gas-like regime. However, for the conditions tested, the wall-to-bulk density ratio increases from ~1-1.2 in liquid-like region to ~1.2-4 in pseudo-critical transition regime, and further to ~3-5 for a majority of the data in the gas-like regime. The combined influence of this varying magnitude of the density ratio and the exponent accounts for the varying effects of density ratio in determining the friction factor. From Table 6.2, it can also be seen that the exponent of the diameter ratio multiplier increases in magnitude from -0.184 in liquid-like regime to -0.531 in the pseudo-critical transition regime and then marginally increases to -0.587 in the gas-like regime. Thus, the friction factor increases with a decrease in diameter, with this influence being greater at the higher temperatures. The increasing influence of the diameter ratio might indicate the varying importance of the velocity gradients in the different regimes of supercritical flow.

Table 6.2 Constants and Exponents in Friction Factor Correlation

	Liquid-Like Regime	Pseudo-Critical Transition Regime	Gas-Like Regime
a	2.415	2.622	2.872
b	0.507	0.230	0.000
c	-0.184	-0.531	-0.587

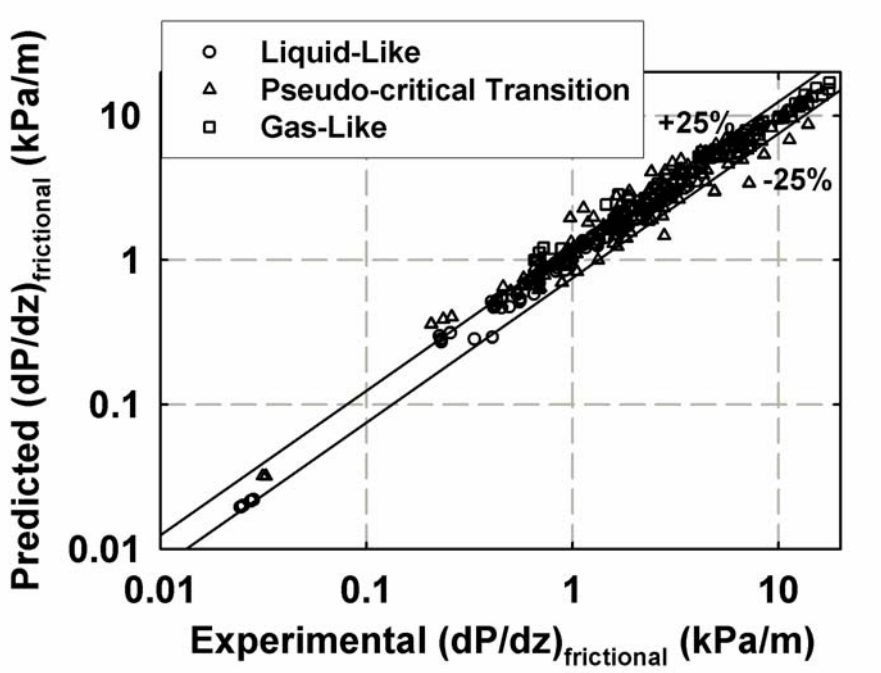

Figure 6.19 Overall Predictions, Supercritical Pressure Drop Model

Figure 6.19 shows a comparison of the measured frictional pressure gradients and those predicted using the friction factor correlation developed here. The overall statistics of the model predictions are shown in Table 6.3, and demonstrate an excellent agreement between the measured and predicted values over the range of fluids and tube diameters used in this study, with somewhat larger average deviations in the pseudo-critical transition regime, as expected in this region with abrupt transitions. Representative predictions as a function of temperature for all the mass fluxes for R410A for the two tubes are shown in Figures 6.20-6.25. It can be seen clearly that the pressure drop models are able to capture the experimentally observed trends within each regime and in the transitions across the regimes very well.

Table 6.3 Overall Prediction Statistics for Pressure Drop Model

Flow Regime	Average Deviation	% points within ±25%
Liquid-like	10.7%	97%
Pseudo-Critical Transition	23.7%	69%
Gas-Like	15.5%	86%

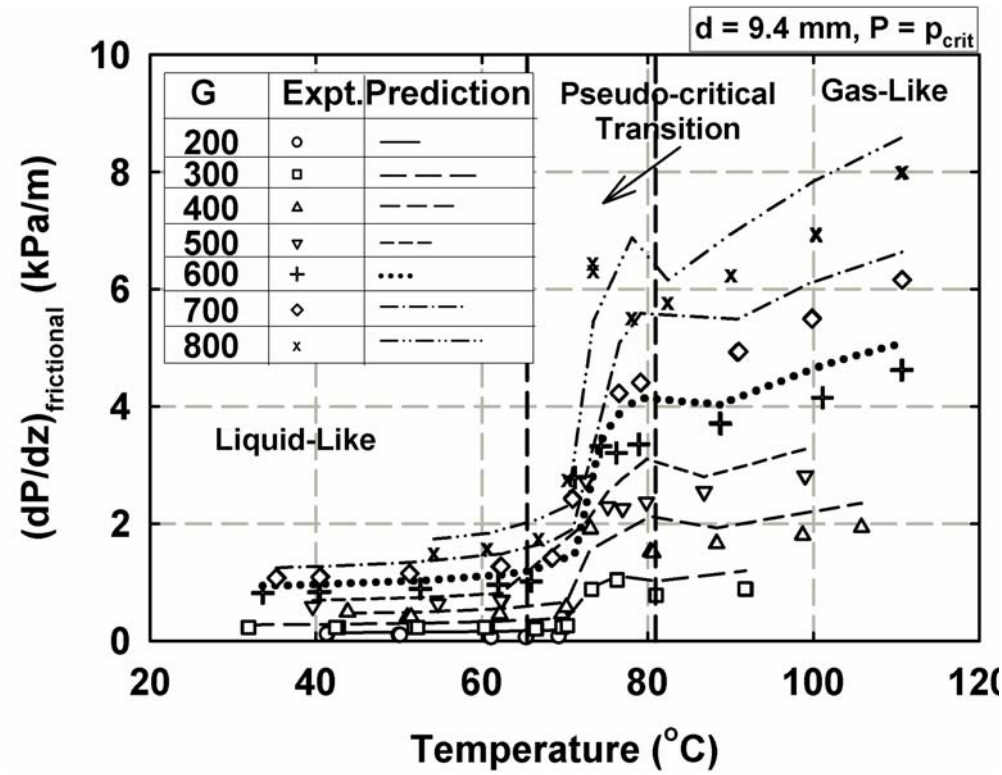

Figure 6.20 Supercritical Frictional Pressure Drop Predictions (9.4 mm Tube, P = p_{crit})

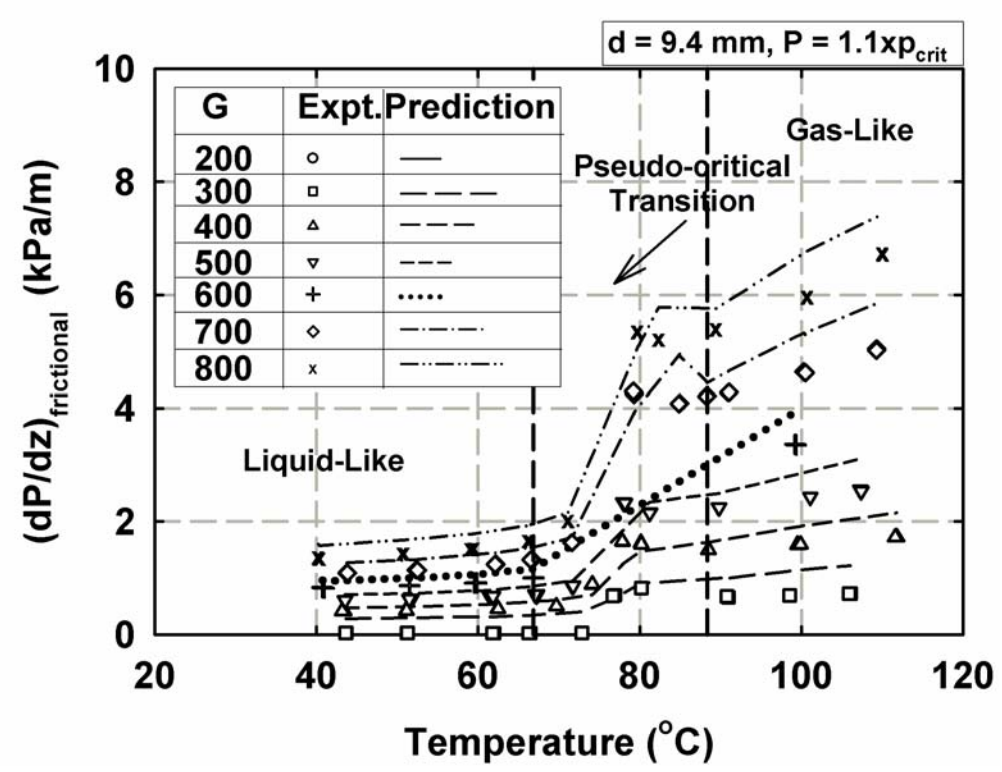

Figure 6.21 Supercritical Frictional Pressure Drop Predictions (9.4 mm Tube, P = 1.1×p_{crit})

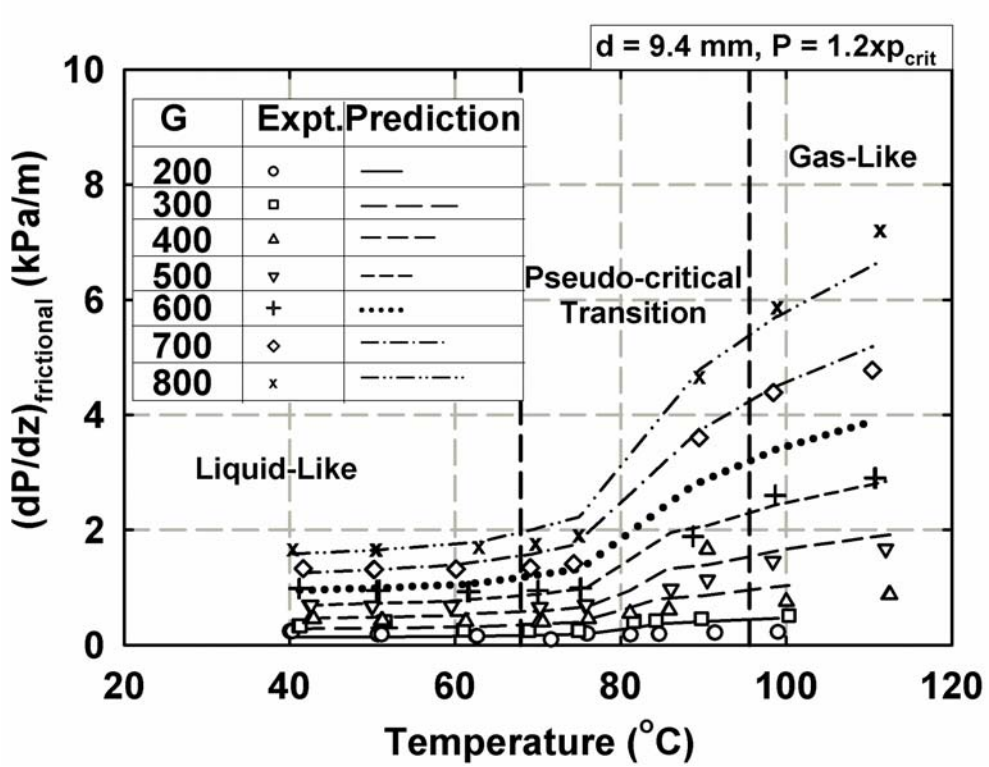

Figure 6.22 Supercritical Frictional Pressure Drop Predictions (9.4 mm Tube, P = 1.2×p$_{crit}$)

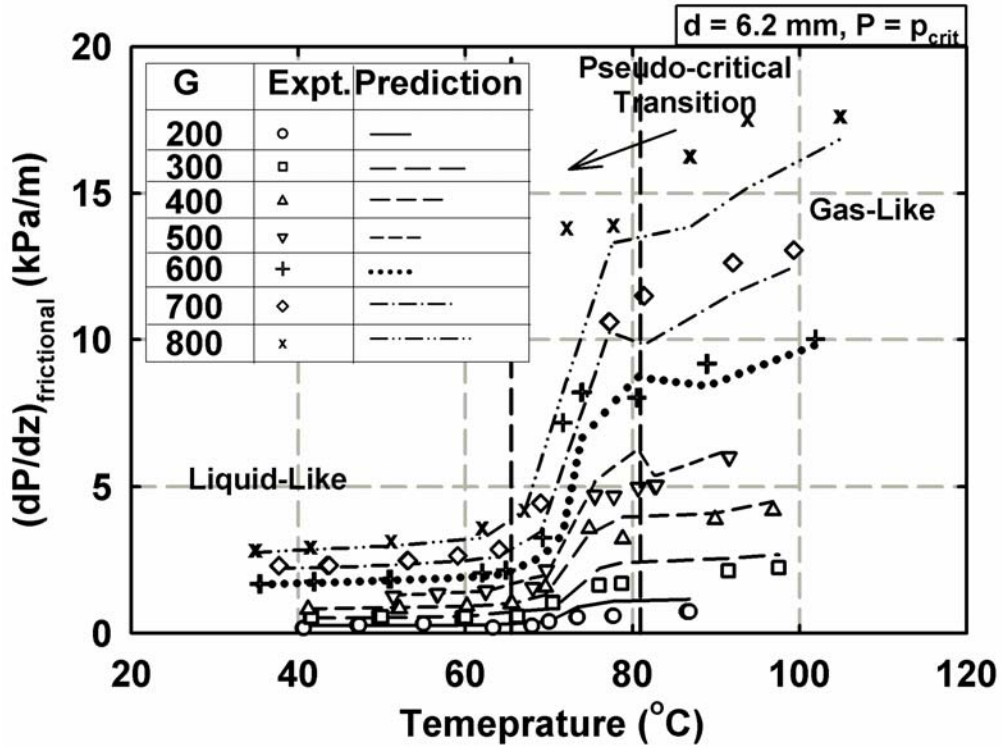

Figure 6.23 Supercritical Frictional Pressure Drop Predictions (6.2 mm Tube, P = p$_{crit}$)

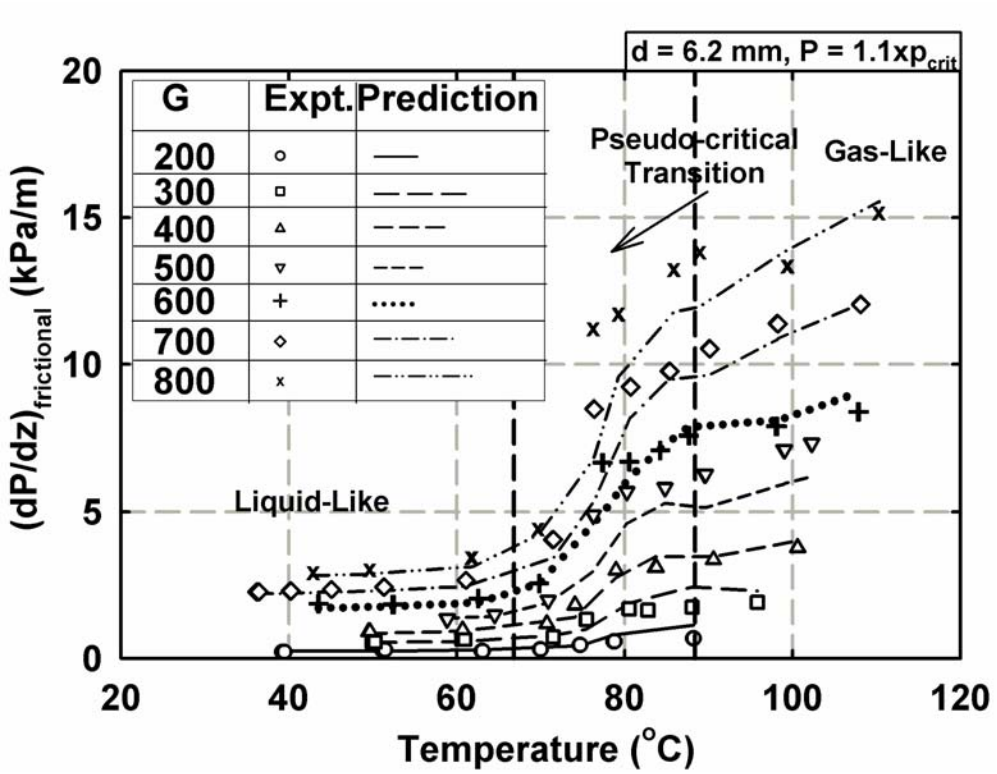

Figure 6.24 Supercritical Frictional Pressure Drop Predictions (6.2 mm Tube, P = 1.1×p_{crit})

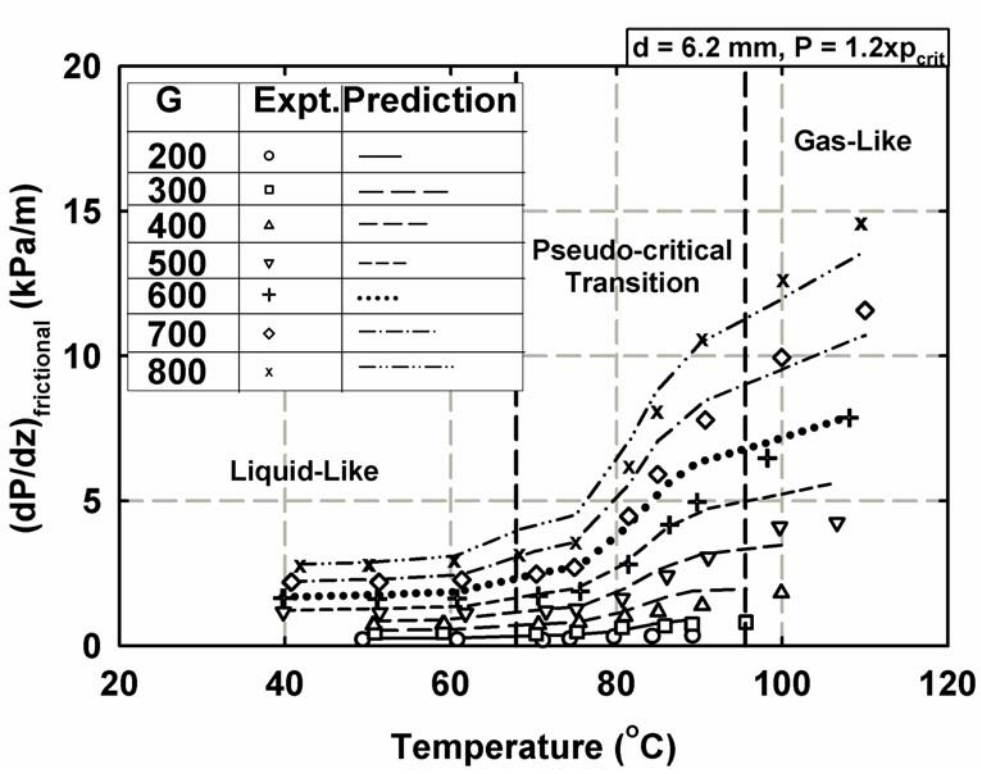

Figure 6.25 Supercritical Frictional Pressure Drop Predictions (6.2 mm Tube, P = 1.2×p_{crit})

6.2.3 Heat Transfer Coefficient Model

Experimentally obtained Nusselt numbers from this study are plotted in Figure 6.26, where the flow-regime definitions described above are used to distinguish the data in the three regimes. The liquid-like regime (at lower temperatures) is characterized by low Reynolds numbers and corresponding low Nusselt numbers. The Reynolds number and Nusselt number for the pseudo-critical transition regime span a wide range, while the gas-like regime points are clustered together at the higher Re range with the Nu being slightly less than the corresponding Nu values for the pseudo-critical transition regime for the same Re.

These Nusselt numbers were modeled using the single-phase Nusselt number correlation by Churchill (1977a) with property and diameter ratio multipliers based on the specific flow regime, i.e., liquid-like, pseudo-critical transition, and gas-like regimes as follows.

$$Nu = a \cdot Nu_{Churchill-modified} \cdot \left(\frac{c_{p,w}}{c_{p,b}} \right)^{b} \cdot \left(\frac{d_{actual}}{d_{baseline}} \right)^{c} \qquad (6.\ 15)$$

In the above equation, $Nu_{Churchill\text{-}modified}$ is the Churchill (1977a) equation for Nusselt number using the friction factor expression (equation 6.14) developed in the present study. As stated above, the baseline diameter in the above equation is 9.4 mm. The constants and exponents for the above equation are shown in Table 6.4 for each

Table 6.4 Constants and Exponents in Nusselt Number Correlation

Constants	Liquid-Like Regime	Pseudo-Critical Transition Regime	Gas-Like Regime
a	1.004	0.928	1.093
b	0.455	0.236	-0.212
c	-0.283	-0.119	-0.353

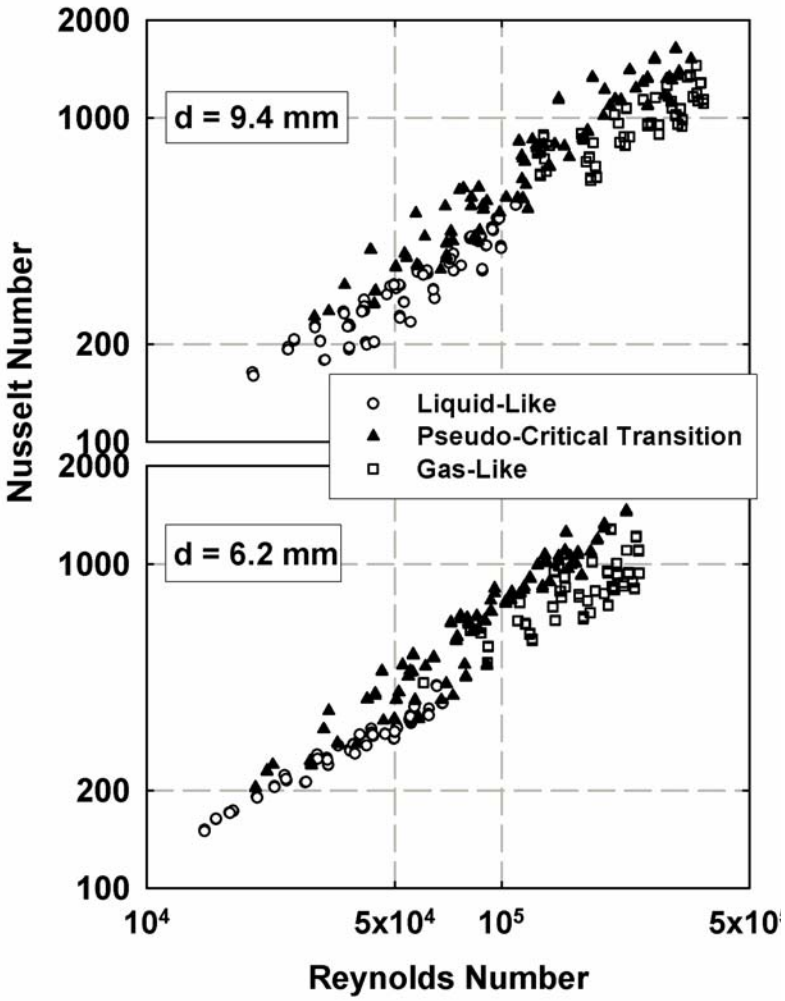

Figure 6.26 Nusselt Number versus Reynolds Number for all Supercritical Cases

supercritical region.

Similar to the density ratio multiplier in the pressure drop model, the exponent of the specific heat ratio decreases from 0.46 in the liquid-like regime to 0.24 in the pseudo-critical transition regime and to -0.21 in the gas-like regime. The wall-to-bulk specific heat ratio in the liquid-like regime ranges from 0.96 to 0.58, decreasing with an increase in temperature. In the pseudo-critical transition regime, the ratio ranges from 0.1 to 3.14 with the values decreasing from 0.58 to 0.1 as $T_{Pseudo\text{-}critical}$ is approached and the bulk

specific heat reaches a maximum, increasing to 3.14 beyond this temperature. This latter increase is because in this region, the wall temperature is closer to $T_{Pseudo\text{-}critical}$ than the bulk temperature. The change in the sign of the exponent in the gas-like regime is therefore expected, because the wall-to-bulk specific heat ratio is greater than 1 in this regime, whereas it is < 1 for the data in the first two regimes.

Figure 6.27 shows a comparison of the measured Nusselt numbers and those predicted using the correlation developed here. The overall statistics of the model predictions are shown in Table 6.5, and demonstrate an excellent agreement between the measured and predicted values over the range of fluids and tube diameters used in this study. Representative predictions as a function of temperature for all the mass fluxes for

Table 6. 5 Overall Prediction Statistics for the Heat Transfer Model

Flow Regime	Average Deviation	% points within ±25%
Liquid-like	12.0%	91.6%
Pseudo-Critical Transition	14.0%	86.0%
Gas-Like	13.7%	88.4%

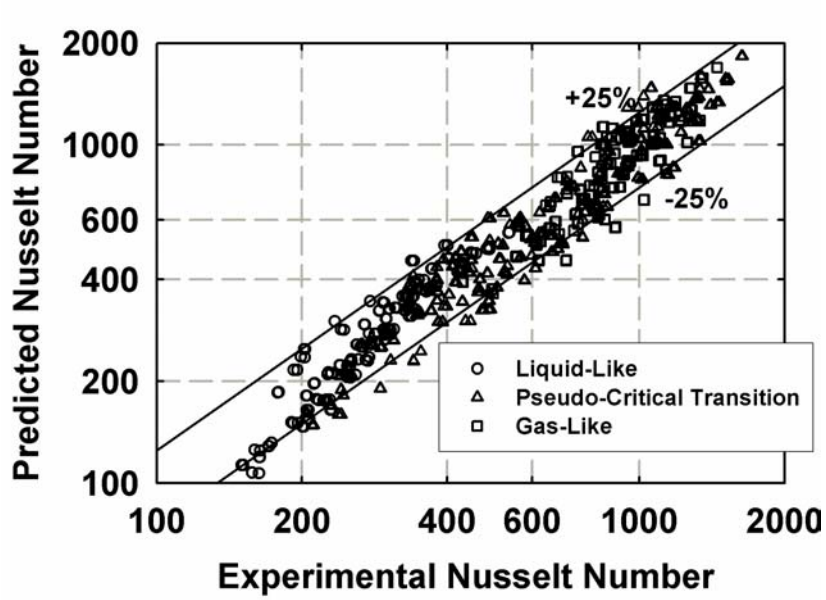

Figure 6.27 Overall Predictions, Supercritical Heat Transfer Model

R410A for the two tubes are shown in Figures 6.28-6.33. It can be seen clearly that the heat transfer models are able to capture the experimentally observed trends within each regime and in the transitions across the regimes very well.

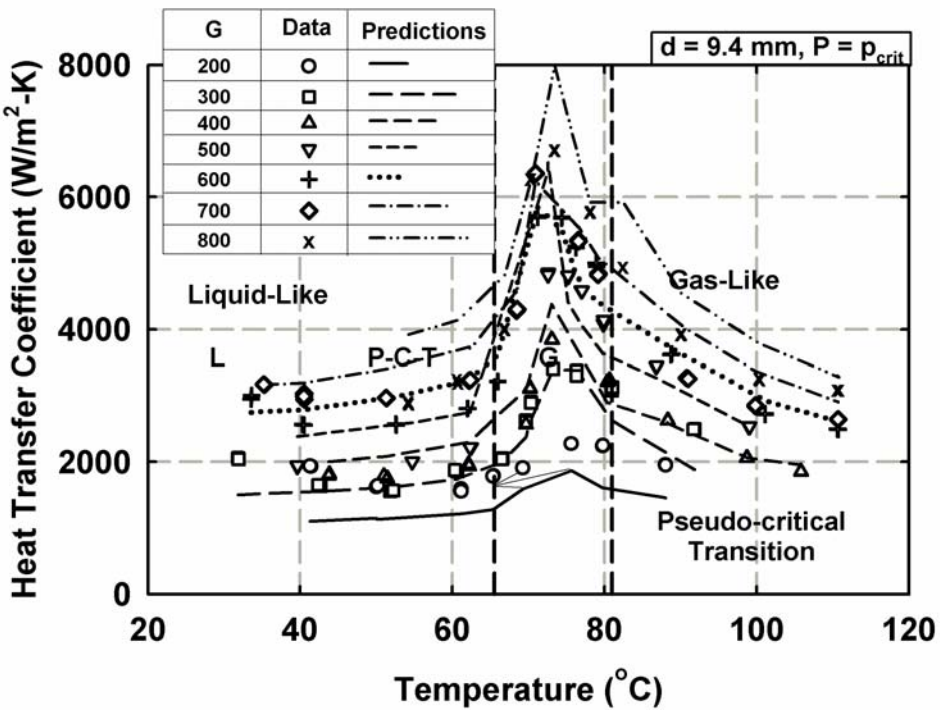

Figure 6.28 Supercritical Heat Transfer Model Predictions (9.4 mm Tube, P = p_{crit})

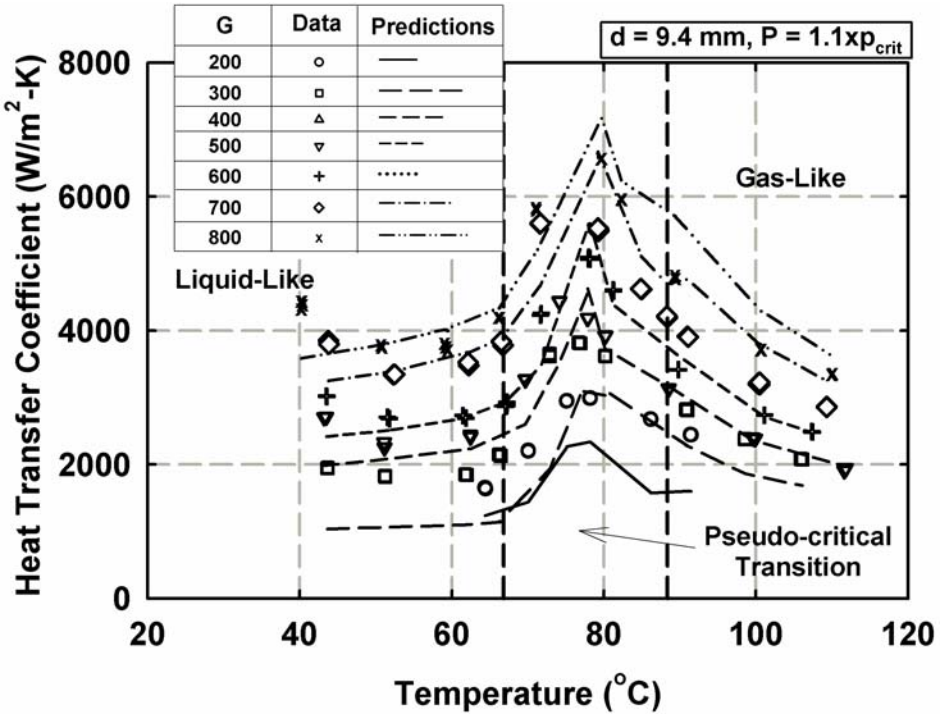

Figure 6.29 Supercritical Heat Transfer Model Predictions (9.4 mm Tube, P = 1.1×p_{crit})

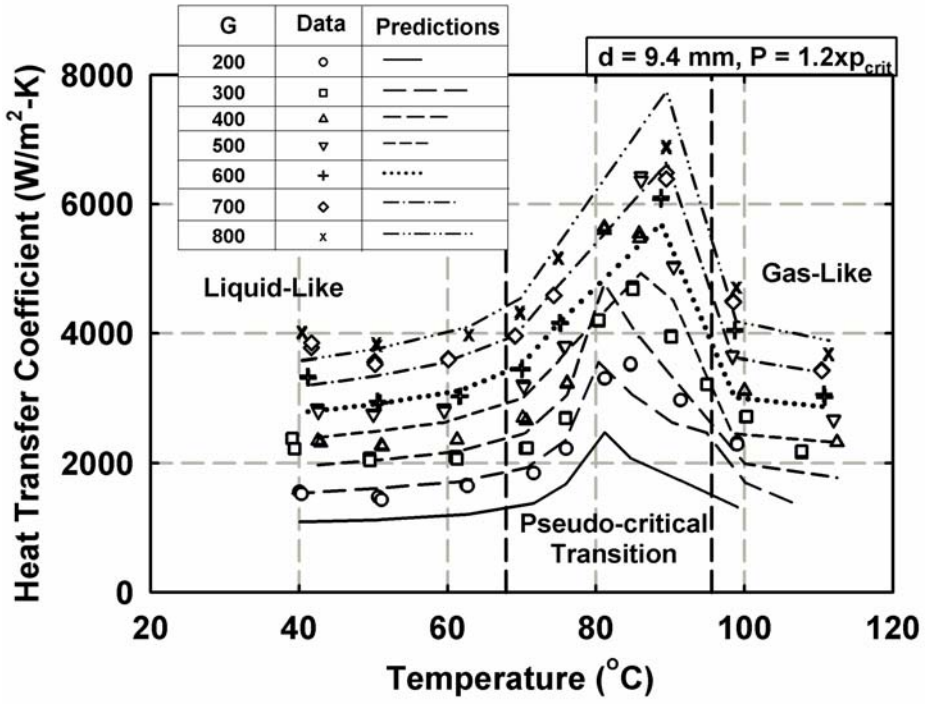

Figure 6.30 Supercritical Heat Transfer Model Predictions (9.4 mm Tube, P = 1.2×p_{crit})

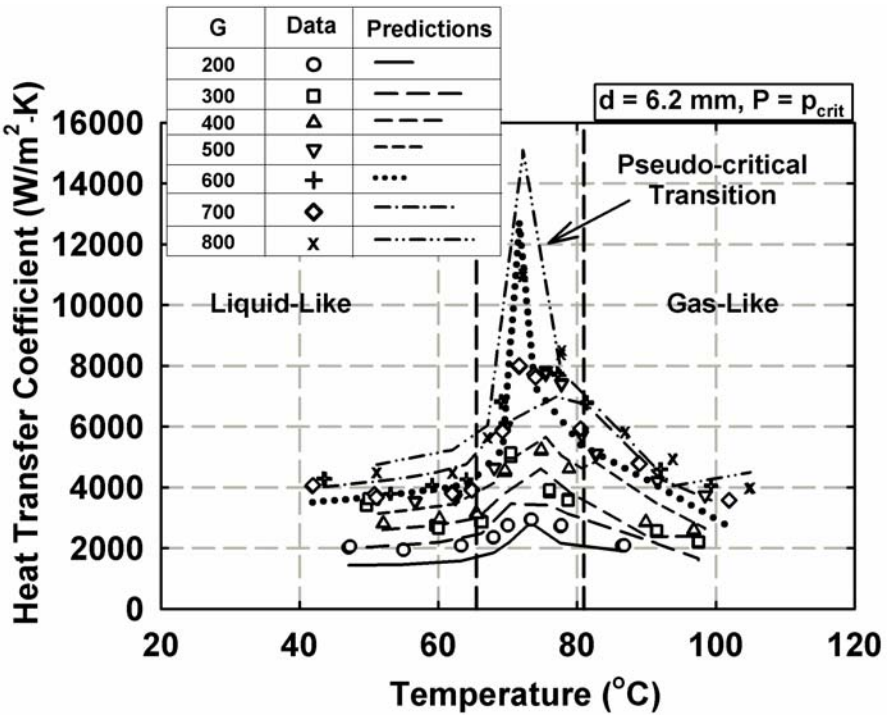

Figure 6.31 Supercritical Heat Transfer Model Predictions (6.2 mm Tube, P = p_{crit})

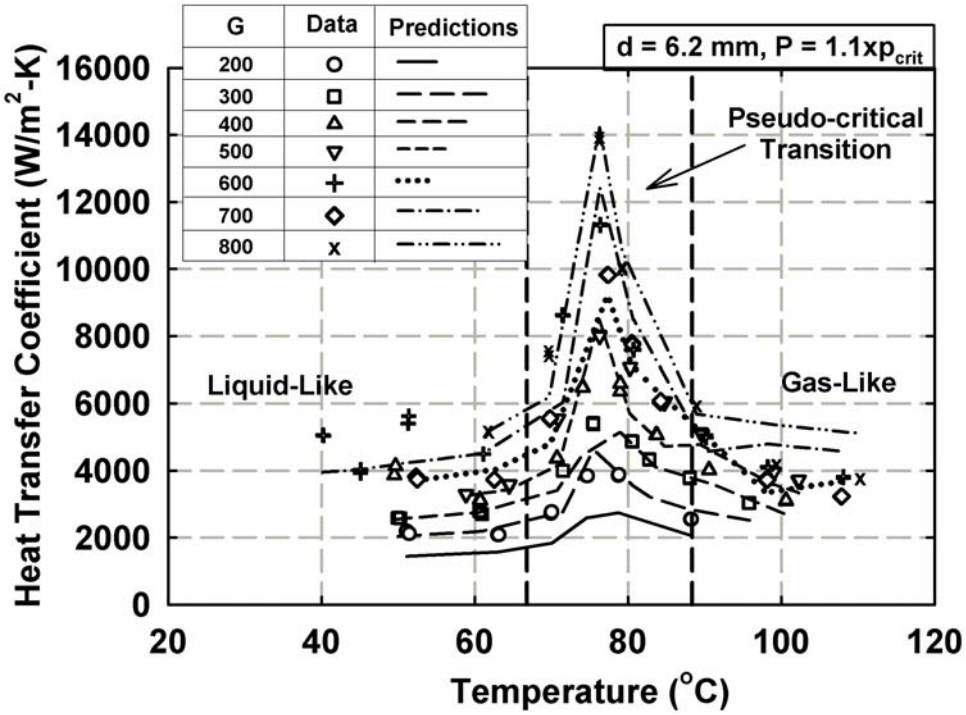

Figure 6.32 Supercritical Heat Transfer Model Predictions (6.2 mm Tube, P = 1.1×p_{crit})

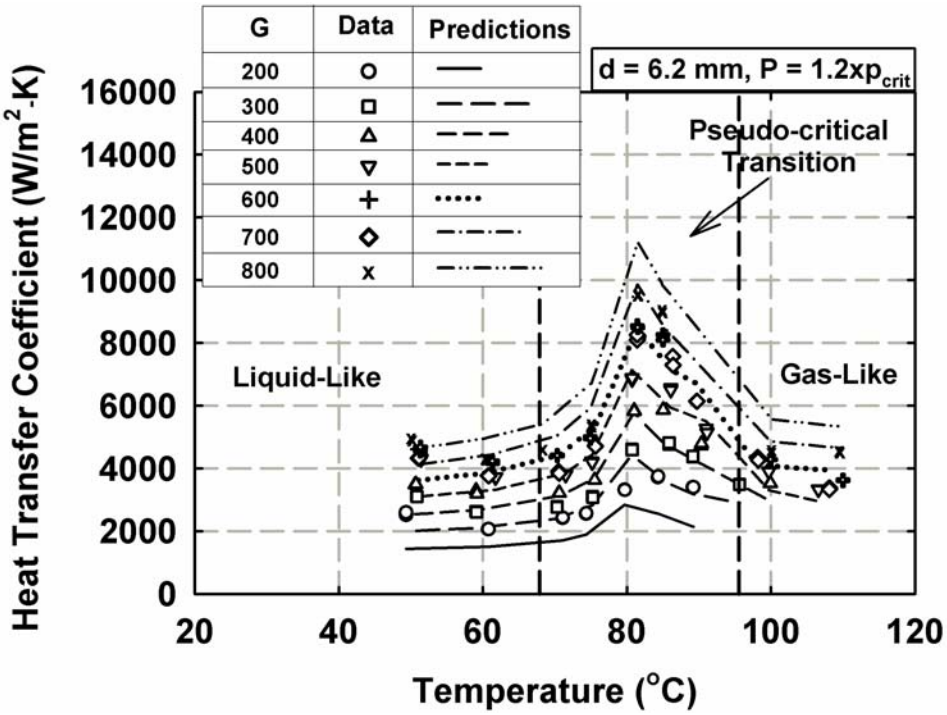

Figure 6.33 Supercritical Heat Transfer Model Predictions (6.2 mm Tube, P = 1.2×p_{crit})

CHAPTER 7 CONCLUSIONS

Heat transfer and pressure drop during condensation and supercritical cooling of R410A inside a 9.4 and 6.2 mm tubes were investigated. The experiments were conducted at five nominal pressures: $0.8\times P_{crit}$, $0.9\times P_{crit}$, P_{crit}, $1.1\times P_{crit}$, and $1.2\times P_{crit}$ (P_{crit} = 4903 kPa for R410A). Heat transfer coefficients were measured using a thermal amplification technique that measures heat duty accurately while also providing refrigerant heat transfer coefficients with low uncertainties. For condensation tests, local heat transfer coefficients and pressure drops were measured for the mass flux range $200 < G < 800$ kg/m^2-s in small quality increments over the entire vapor-liquid region. An uncertainty analysis showed that the average uncertainties in the heat transfer coefficients were ±9.61% and 13.8% for 9.4 mm and 6.2 mm tubes, respectively. For supercritical tests, local heat transfer coefficients and pressure drops were measured for the same mass flux range as in the condensation tests for temperatures ranging from 30 – 110^{o}C. The average uncertainties in these heat transfer coefficients were around ±7.72% and ±13% for 9.4 mm and 6.2 mm tubes, respectively. For the mass flux range $300 < G < 800$ kg/m^2-s, the average uncertainty in pressure drops for the supercritical conditions was ±2.36%. Accurate pressure drop measurements could not be conducted at G = 200 kg/m^2-s due to the relatively small pressure drops compared to the measurement uncertainties of the differential pressure transducer.

For both phase-change condensation and supercritical cooling, frictional pressure gradients were calculated by separating the deceleration component from the measured pressure gradients. The deceleration component was determined from an estimation of

the change in fluid velocities (and momentum) due to the change in quality for phase-change condensation, and the change in density for supercritical cooling, respectively.

It is found that, due to the compensating variations in properties at near-critical pressures, a change in reduced pressure from 0.8 to 0.9 is not significant enough to cause an appreciable change in heat transfer coefficients. However, the effect of reduced pressure on the pressure gradient is more pronounced for the two pressures under consideration. The pressure drop is lower at higher reduced pressures because as the reduced pressure increases, the difference between the properties of the two phases decreases, resulting in a reduction in the shear between the phases, and therefore the pressure drop.

It is found that the flow regime maps (or transition criteria) developed by Coleman and Garimella (2003), Breber *et al.* (1980) and Dobson and Chato (1998) result in similar categorization of the condensation data into the applicable flow regimes. Therefore, flow regime transition criteria developed by Coleman and Garimella (2003) were first used to designate the prevailing flow regimes for a given combination of mass flux and quality. For the implementation of the heat transfer and pressure drop models, the following flow regime classifications were used:

- For Soliman modified Froude number (Soliman, 1982) $Fr_{so} < 1.75$, the flow is considered to be intermittent flow.
- For $1.75 < Fr_{so} < 18$, the flow is considered to be in the wavy-stratified regime.
- For $18 < Fr_{so} < 65$, the flow is considered to be in the annular flow regime.
- For $Fr_{so} > 65$, the flow is considered to be in the mist flow regime.

Using these criteria, the data from the present study primarily fell into two flow regimes: wavy-stratified and annular flow. There were extremely few points in the intermittent and mist flow regimes.

The condensation heat transfer coefficients and pressure gradients obtained from the present study were compared with several newly developed correlations found in the literature. It was shown that many commonly used correlations were not able to predict the heat transfer and pressure drop for condensation of the refrigerant blend R410A at such high reduced pressures. The wavy flow model of Dobson and Chato (1998) under-predicts the data, whereas their annular flow model over-predicted the data. Furthermore, they assumed an abrupt transition between the annular and wavy flow regimes, resulting in abrupt changes in heat transfer coefficient predictions from wavy to annular flow. The heat transfer coefficient predictions of Cavallini *et al.* (2002a; 2002b) are better than those of the other correlations mentioned above. However, their pressure drop model underpredicts the data. This, in turn, affects the heat transfer results when pressure gradients are used as an intermediate step for heat transfer calculation. The El Hajal *et al.* (2003) and Thome *et al.* (2003) models were the best predictors of the heat transfer data among the models found in literature. However these models showed some unexpected trends with an increase in reduced pressure and at qualities approaching one.

Condensation heat transfer and pressure drop models were developed for annular and wavy flow (Table 7.1 and 7.2). The annular flow model was based on a two-phase multiplier approach, recognizing that the liquid film in the flow almost always exhibited fully turbulent behavior. In the wavy flow model, it was assumed that the local heat transfer was the sum of film condensation on the top portion of the tube and forced

convection in the liquid pool at the bottom. In computing the liquid-phase Reynolds number for the model, proper account was taken of the volume and surface area of the liquid pool, rather than basing it on the tube diameter. The pressure drop models for both annular and wavy flow were modifications of Chisholm (1973) two-phase multiplier approach based on recent work by Tran *et al.* (2000). An appropriate interpolation technique for conditions in the transition region between annular and wavy flow was also defined, which eliminated the abrupt transition in heat transfer coefficients and pressure gradients. The overall heat transfer model (annular, wavy and transition) predicted 98% (503 out of 513) of the data within ±15%, with an average absolute deviation between the data and predictions of 5.91%. The overall pressure drop model (annular, wavy and transition) predicted 87% (393 out of 452) of the data within ±15% with an average absolute deviation between the data and predictions of 7.75%. The range of validity for these models is $200 < G < 800$ kg/m^2-s, $0.8 < P_r < 0.9$ and $6.2 <$ I.D. < 9.4 mm.

In supercritical cooling, the sharp variations in thermophysical properties in the vicinity of the critical temperature were found to have a substantial effect on heat transfer coefficients and led to peaks in the heat transfer coefficients. It was found that temperature variations above the vapor-liquid dome have a much more significant effect on heat transfer than the independent variation of mass flux, because they affect thermal properties as well as the flow-related Reynolds number substantially. Also, as the pressure increases, the peaks in heat transfer shift to higher temperatures. It was also found that, as the pressure increases, the variation in heat transfer coefficients decreases due to a decrease in property variations. The pressure drop during supercritical cooling drops abruptly at the transition temperature due to the sudden change in refrigerant

properties from gas-like to liquid-like properties. At temperatures below the transition temperature, pressure does not vary significantly due to the small property variation in the liquid-like region. Flow regime designations at the supercritical conditions were based on the characteristics of the specific work of thermal contraction (expansion) E_o as suggested by Kurganov (1998a). Thus, the data from the supercritical tests were grouped into three regimes: liquid-like regime where the change in E_o with temperature (or enthalpy) is not significant, pseudo-critical transition regime where the change in E_o with temperature (or enthalpy) is significant, and gas-like regime where the E_o starts to decline as temperature (or enthalpy) increases. The corresponding temperatures were used as the basis for dividing the data into liquid-like, pseudo-critical transition and gas-like regimes.

The supercritical cooling heat transfer coefficients and pressure gradients obtained from the present study were compared with several correlations available in the literature, including Churchill (1977b; 1977a), Gnielinski (1976), Krasnoshchekov *et al.* (1970), Kuraeva and Protopopov (1974) and Pitla *et al.*(2002). It was found that the correlations developed for CO_2 could not be extrapolated to the refrigerant blend R410A with an acceptable level of accuracy. Most of the models underpredicted the data with the predictions being severe at higher mass fluxes. All the models except Pitla *et al.* (2002) followed the heat transfer or pressure drop trends reasonably well. In supercritical heat transfer, the bulk and wall temperatures approach critical temperature at different locations and therefore the Pitla *et al.* (2002) method of arithmetically averaging the bulk and wall Nusselt numbers leads to unrealistic variations in heat transfer coefficients above the critical temperature.

Heat transfer and pressure drop (friction factor) models for supercritical cooling were developed for each flow regime (Table 6.3). For pressure drop models, only the data in the mass flux range of $300 < G < 800$ kg/m^2-s were used to develop the model due to the relatively large uncertainties associated with the $G = 200$ kg/m^2-s pressure drop data. These models were based on single-phase turbulent flow with property ratio multipliers to account for the large property variations between the bulk fluid and wall temperatures. The overall heat transfer model (liquid-like, pseudo-critical transition and gas-like) predicted 88%, i.e., 588 out of 667 data points, within ±25%. The applicability range of these models is $200 < G < 800$ kg/m^2-s, $1.0 < P_r < 1.2$ and $6.2 < \text{I.D.} < 9.4$ mm. For the overall pressure gradient model (liquid-like, pseudo-critical transition and gas-like), 84% of the data points were predicted within ±25%. The applicability range of these models is $300 < G < 800$ kg/m^2-s, $1.0 < P_r < 1.2$ and $6.2 < \text{I.D.} < 9.4$ mm.

The above discussion shows that the present study has characterized heat transfer and pressure drop of refrigerant R410A for phase-change condensation at near-critical pressure and supercritical cooling through careful measurements and flow regime based models. These results yield insights into the effect of reduced pressure, quality, mass flux, temperature, and property variations at near-critical conditions. It is expected that these experimentally validated models will enable more accurate design of refrigerant condensers and gas-coolers. It is believed that the present study represents one of the first attempts at obtaining these measurements for refrigerants close to and above the critical region. The results from this study will also provide a basis for the validation of further studies on high reduced pressure condensation and supercritical cooling of refrigerant blends, such as numerical simulation of such flows.

The research conducted in this study may be viewed as the beginning of an overall attempt to develop more environmentally benign space-conditioning systems. A comprehensive experimental research project for the visualization of flow patterns at near-critical pressures over ranges of mass fluxes, qualities (phase-change condition) and temperatures (supercritical condition) will complement the results of the present study. This will help establish any potential fundamental differences in the flow patterns when the pressure is close to the critical pressure. Void fraction measurements at these conditions would also substantially advance the understanding of these flows and improve the heat transfer and pressure drop predictions. Similar studies are also recommended for tube diameters much smaller than were investigated in the present study to establish the effect of decreasing diameter at such high reduced pressures. System-level design simulation and optimization and testing would be of further help in the determination of the appropriate trade-offs between capital and operating cost for such space-conditioning systems. This is particularly useful for the development of more thermally efficient and cost effective heat exchangers in view the large heat transfer coefficient variations in the gas-cooler.

Table 7. 1 Summary of Condensation Heat Transfer Coefficient Model

Wavy Flow

$$h_{wavy} = \frac{\theta_l}{\pi} h_{film} + \left(1 - \frac{\theta_l}{\pi}\right) h_{forced}$$

$$Nu_{film} = \frac{1.1212}{\theta_l}\left[\frac{Ga\,\mathrm{Pr}_l}{Ja_l}\right]^{1/4}\left[\int_0^{\theta_l} \sin^{1/3}\theta d\theta\right]^{3/4},\quad h_{film} = \frac{Nu_{film}\cdot k}{d_{actual}}$$

$$Nu_{forced} = 0.005\,\mathrm{Re}_{liquid}^{0.97}\,\mathrm{Pr}_l^{0.3}\left[1 + \left(\frac{x}{1-x}\right)\left(\frac{\rho_l}{\rho_v}\right)\right]\left(\frac{d_{actual}}{d_{basline}}\right)^{-0.56}$$

$$\mathrm{Re}_{liquid} = \frac{G\cdot(1-x)\cdot D_{h,liquid\ pool}}{\mu_l},\quad D_{h,liquid\ pool} = \frac{\left[\sin\theta_l\cos\theta_l + (\pi - \theta_l)\right]}{\left[\sin\theta_l + (\pi - \theta_l)\right]}\times d_{actual}$$

θ_l is evaluated by Baroczy (1965) void fraction model

$$\left(1 - \frac{\theta_l}{\pi}\right) \cong \frac{\arccos(2\alpha - 1)}{\pi},\quad \alpha = \left(1 + \left(\frac{1-x}{x}\right)^{0.74}\left(\frac{\rho_v}{\rho_l}\right)^{0.65}\left(\frac{\mu_l}{\mu_v}\right)^{0.13}\right)^{-1}$$

$$d_{baseline} = 9.4\,mm$$

Annular Flow

$$Nu_{annular} = 0.0134\,\mathrm{Re}_l^{0.84}\,\mathrm{Pr}_l^{0.3}\left[1 + \left(\left(\frac{x}{1-x}\right)\left(\frac{\rho_l}{\rho_v}\right)\right)^{0.8}\right]\left(\frac{d_{actual}}{d_{baseline}}\right)^{-0.32}$$

$$\mathrm{Re}_l = \frac{G(1-x)d_{actual}}{\mu_l},\quad h_{annular} = \frac{Nu_{annular}\cdot k}{d_{actual}},\quad d_{baseline} = 9.4\,mm$$

Wavy-Annular Transition

$$Nu = \left(\frac{Fr_{so} - Fr_{so,wavy}}{Fr_{so,annular} - Fr_{wavy}}\right)Nu_{annular} + \left(\frac{Fr_{so,annular} - Fr_{so}}{Fr_{so,annular} - Fr_{so,wavy}}\right)Nu_{wavy}$$

$$Nu_{wavy} = \frac{h_{wavy}\cdot d_{actual}}{k}$$

Table 7. 2 Summary of Condensation Pressure Drop Model

Wavy and Annular Flow

$$\left(\frac{dP}{dz}\right)_f = \phi_{LO}^{\ 2}\left(\frac{dP}{dz}\right)_{f,LO}$$

$$\phi_{LO}^{\ 2} = 1+[CY^2-1][N_{conf}x^{\frac{2-n}{2}}(1-x)^{\frac{2-n}{2}}+x^{2-n}]$$

$$N_{conf} = \frac{1}{d_{actua}l}\left[\frac{\sigma}{g(\rho_l-\rho_v)}\right]^{0.5} \quad n = \begin{cases} 1 & \mathrm{Re}_{LO} < 2300 \\ 0.25 & 2300 < \mathrm{Re}_{LO} < 20000 \\ 0.2 & \mathrm{Re}_{LO} > 20000 \end{cases}, \; Y^2 = \frac{(dP/dz)_{f,GO}}{(dP/dz)_{f,LO}}$$

$$\mathrm{Re}_{GO} = \frac{Gd_{actual}}{\mu_v}, \; \mathrm{Re}_{LO} = \frac{Gd_{actual}}{\mu_l}$$

$$f_{GO} = \begin{cases} 16/\mathrm{Re}_{GO} & \mathrm{Re}_{GO} < 2300 \\ 0.079\,\mathrm{Re}_{GO}^{-0.25} & 2300 < \mathrm{Re}_{GO} < 20000 \\ 0.046\,\mathrm{Re}_{GO}^{-0.2} & \mathrm{Re}_{GO} > 20000 \end{cases}, \; f_{LO} = \begin{cases} 16/\mathrm{Re}_{LO} & \mathrm{Re}_{LO} < 2300 \\ 0.079\,\mathrm{Re}_{LO}^{-0.25} & 2300 < \mathrm{Re}_{LO} < 20000 \\ 0.046\,\mathrm{Re}_{LO}^{-0.2} & \mathrm{Re}_{LO} > 20000 \end{cases}$$

$$(dP/dz)_{f,GO} = 2f_{GO}G^2/(d_{actual}\rho_v), \; (dP/dz)_{f,LO} = 2f_{LO}G^2/(d_{actual}\rho_l)$$

$$C(x) = \begin{cases} \left(18.22-31.97x+17.21x^2\right)\left(\frac{d_{actual}}{d_{baseline}}\right)^{-0.34} & \text{For Annular Flow} \\ \left(\frac{0.12}{x^2}+\frac{2.9}{x}-0.76\right)\left(\frac{d_{actual}}{d_{baseline}}\right)^{-0.77} & \text{For Wavy Flow} \end{cases}$$

$$d_{baseline} = 9.4\,mm$$

Wavy-Annular Transition

$$\left(\frac{dP}{dz}\right)_f = \left(\frac{Fr_{so\,f}-Fr_{so,wavy}}{Fr_{so,annular}-Fr_{wavy}}\right)\left(\frac{dP}{dz}\right)_{f,annular} + \left(\frac{Fr_{so,annular}-Fr_{so}}{Fr_{so,annular}-Fr_{so,wavy}}\right)\left(\frac{dP}{dz}\right)_{f,wavy}$$

Table 7. 3 Summary of Supercritical Heat Transfer and Pressure Drop Models

Heat Transfer Models	
Liquid-Like Region	$$Nu_{liquid-like} = 1.004 Nu_{Churchill-corrected} \left(\frac{c_{p,w}}{c_{p,b}}\right)^{0.455} \left(\frac{d_{actual}}{d_{baseline}}\right)^{-0.283}$$ $$d_{baseline} = 9.4\,mm$$ $$Nu_{Churchill}^{10} = 4.364^{10} + \left[\frac{\exp\left(\frac{2200-\mathrm{Re}}{365}\right)}{4.364^2} + \frac{1}{\left(6.3 + \frac{0.079(f/8)^{1/2}\,\mathrm{Re}\,\mathrm{Pr}_t}{\left(1+\mathrm{Pr}_t^{4/5}\right)^{5/6}}\right)^2}\right]^{-5}$$
Pseudo-Critical Transition	$$Nu_{pseudo-critical} = 0.928 Nu_{Churchill-corrected} \left(\frac{c_{p,w}}{c_{p,b}}\right)^{0.236} \left(\frac{d_{actual}}{d_{baseline}}\right)^{-0.119}$$
Gas-Like Region	$$Nu_{gas-like} = 1.093 Nu_{Churchill-corrected} \left(\frac{c_{p,w}}{c_{p,b}}\right)^{-0.212} \left(\frac{d_{actual}}{d_{baseline}}\right)^{-0.353}$$
Pressure Drop Models	
Liquid-Like Region	$$f_{liquid-like} = 2.415 f_{Churchill} \left(\frac{\rho_w}{\rho_b}\right)^{0.507} \left(\frac{d_{actual}}{d_{baseline}}\right)^{-0.184}$$ $$d_{baseline} = 9.4\,mm$$ $$f_{Churchill} = 8\left[\left(\frac{8}{\mathrm{Re}}\right)^{12} + \frac{1}{\left(\left[2.457\ln\left(\frac{1}{(7/\mathrm{Re})^{0.9} + 0.27\varepsilon}\right)\right]^{16} + \left[\frac{37530}{\mathrm{Re}}\right]^{16}\right)^{1.5}}\right]^{1/12}$$
Pseudo-Critical Transition	$$f_{pseudo-crtical} = 2.622 f_{Churchill} \left(\frac{\rho_w}{\rho_b}\right)^{0.230} \left(\frac{d_{actual}}{d_{baseline}}\right)^{-0.531}$$
Gas-Like Region	$$f_{gas-like} = 2.872 f_{Churchill} \left(\frac{d_{actual}}{d_{baseline}}\right)^{-0.587}$$

APPENDIX A PHASE-CHANGE HEAT TRANSFER COEFFICIENT DERIVATION

(Representative Data Point: G = 302 kg/m^2-s, p_r = 0.78, x = 0.66)

Geometry

Pre-Condenser (Shell-and-Tube Heat Exchanger)		
	British Units	***SI Units***
Length	8.13”	0.207 m
Outside diameter of the shell	1.5”	38.1 mm
Thickness of the shell	0.065”	1.65 mm
Inside diameter of the shell	1.37”	34.8 mm
Insulation Thickness	0.875”	22.2 mm
Post-Condenser (Tube-in-Tube Heat Exchanger)		
Length	51”	1.295 m
Outside diameter of the outer tube	0.5”	12.7 mm
Thickness of the outer tube	0.035”	0.89 mm
Inside diameter of the outer tube	0.43	10.9 mm
Outside diameter of the inner tube	0.375”	9.53 mm
Thickness of the inner tube	0.035”	0.89 mm
Inside diameter of the inner tube	0.305”	7.75 mm
Insulation Thickness	1”	25.4 mm
Test Section (Tube-in-Tube Heat Exchanger)		
Length	11.5”	0.292 m
Outside diameter of the outer tube	0.75”	19.05 mm
Thickness of the outer tube	0.065”	1.65 mm
Inside diameter of the outer tube	0.62”	15.75 mm
Outside diameter of the inner tube	0.5”	12.7 mm
Thickness of the inner tube	0.065”	1.65 mm
Inside diameter of the inner tube	0.37”	9.4 mm
Insulation Thickness	1.05”	26.7 mm

Secondary Heat Exchanger (Shell-and-Tube Heat Exchanger)		
Length	6.81”	0.173 m
Outside diameter of the shell	1”	25.4 mm
Thickness of the shell	0.049”	1.25 mm
Inside diameter of the shell	0.902	22.9 mm
Insulation Thickness	1.11”	28.2 mm
Tubing Dimensions:		
Tube Length	100”	2.54 m
Flow Meter Equivalent Length	21.4”	0.543 m
Pump Equivalent Length	44.6”	1.133 m
Equivalent Length	165.6”	4.21 m
Outside diameter	0.5”	12.7 mm
Thickness	0.035”	0.89 mm
Inside diameter	0.43”	10.92 mm
Insulation Thickness	0.729”	18.5 mm

Input Parameters:

Critical Pressure : 4902.6 kPa (711.1 psia)		
Pre-Condenser:		
Inlet water temperature	58.53°F	14.74°C
Inlet water pressure (assumption)	60 psia	413.7 kPa
Outlet water temperature	136.80°F	58.22°C
Outlet water pressure (assumption)	20 psia	137.9 kPa
Water flow rate	0.194 gpm	1.223×10^{-5} m^3/s

Inlet refrigerant temperature	222.39°F	105.77°C
Inlet refrigerant pressure (T_{sat} = 60.00°C, $\Delta T_{Super\ Heat}$ = 45.77°C)	554.5 psia	3822.8 kPa
Outlet refrigerant temperature	139.35°F	59.64°C
Outlet refrigerant pressure	554.2 psia	3820.9 kPa
Post-Condenser:		
Inlet water temperature	57.00°F	13.89°C
Inlet water pressure (assumption)	60 psia	413.7 kPa
Outlet water temperature	68.56°F	20.31°C
Outlet water pressure (assumption)	20 psia	137.9 kPa
Water flow rate	1.14 gpm	7.17×10^{-5} m^3/s
Inlet refrigerant temperature	138.43°F	59.13°C
Inlet refrigerant pressure	554.31	3821.8 kPa
Outlet refrigerant temperature	115.05°F	46.14°C
Outlet refrigerant pressure (T_{sat} = 59.75°C, $\Delta T_{Sub\ Cool}$ = 13.61°C)	552.38 psia	3808.5 kPa
Test Section:		
Inlet refrigerant temperature	139.60°F	59.78°C
Inlet refrigerant pressure (T_{sat} = 60°C, Err T_{sat} = - 0.22°C)	554.18 psia	3820.9 kPa
Inlet reduced pressure (p_r)		0.78
Outlet refrigerant temperature	139.35°F	59.64°C
Outlet refrigerant pressure (T_{sat} = 59.96°C, Err T_{sat} = - 0.32°C)	554.30 psia	3821.8 kPa
Outlet reduced pressure (p_r)		0.78
Refrigerant flow rate	2.77 lbm/min	2.097×10^{-2} kg/s

Secondary Heat Exchanger:		
Inlet tube water temperature (primary)	94.95°F	34.97°C
Outlet tube water temperature (primary)	93.78°F	34.32°C
Inlet shell water temperature (secondary)	57.40°F	14.11°C
Outlet shell water temperature (secondary)	77.85°F	25.47°C
Shell water flow rate (secondary)	1.5 lbm/min	1.181×10^{-2} kg/s
Average water pressure (assumption)	40 psia	275.8 kPa
Primary Loop:		
Inlet test section water temperature	93.78°F	34.32°C
Outlet test section water temperature	94.95°F	34.97°C
Volumetric water flow rate	1.816 gpm	1.146×10^{-4} m^3/s
Average water pressure (assumption)	60 psia	413.7 kPa
Ambient Temperature: 23°C = 73.4°F (assumption)		

Mass Flux

Eq. No	***Equation***	***Inputs***	***Outputs***	***Reference***
(1)	$d_{i,i} = d_{i,o} - 2 \times t_{test}$	$d_{i,o}$ = 12.7 mm, t_{test} = 1.65 mm	$d_{i,i}$ = 9.4 mm	
(2)	$A_{test} = \frac{\pi \cdot d_{i,i}^{\ 2}}{4}$	$d_{i,i}$ = 9.4 mm	$A_{test} = 6.94 \times 10^{-5}$ m^2	
(3)	$G = \frac{m_{test,r}}{A_{test}}$	$\dot{m}_{test,r} = 2.097 \times 10^{-2}$ kg/s	G = 302 kg/m^2-s	

Pre-Condenser Outlet/Test Section Inlet Quality Calculation

Eq. No	Equation	Inputs	Outputs	Reference
(4)	$P_{pre,w,avg} = \frac{P_{pre,w,in} + P_{pre,w,out}}{2}$	$P_{pre,w,in}$ = 413.7 kPa, $P_{pre,w,out}$ = 137.9 kPa	$P_{pre,w,avg}$ = 275.8 kPa	
(5)	$T_{pre,w,avg} = \frac{T_{pre,w,in} + T_{pre,w,out}}{2}$	$T_{pre,w,in}$ = 14.74°C, $T_{pre,w,out}$ = 58.22°C	$T_{pre,w,avg}$ = 36.48°C	
(6)	$\rho_{pre,w} = f(T_{pre,w,avg}, P_{pre,w,avg})$ $Cp_{pre,w} = f(T_{pre,w,avg}, P_{pre,w,avg})$ $h_{pre,r,in} = f(T_{pre,r,in}, P_{pre,r,in})$	$P_{pre,w,avg}$ = 275.8 kPa $T_{pre,w,avg}$ = 36.48°C $P_{pre,r,in}$ = 3822.8 kPa $T_{pre,r,in}$ = 105.77°C	$\rho_{pre,w}$ = 993.6 kg/m^3 $Cp_{pre,w}$ = 4.18 kJ/kg-K $h_{pre,r,in}$ = 494.3 kJ/kg	
(7)	$\dot{m}_{pre,w} = \rho_{pre,w} \cdot VolFlo_{pre,w}$	$\rho_{pre,w}$ = 993.6 kg/m^3, $VolFlo_{pre,w}$ = 1.223×10^{-5} m^3/s	$\dot{m}_{pre,w}$ = 1.215×10^{-2} kg/s	
(8)	$\dot{Q}_{pre,w} = \left(T_{pre,w,out} - T_{pre,w,in}\right) \cdot \dot{m}_{pre,w} \cdot Cp_{pre,w}$	$\dot{m}_{pre,w}$ = 1.215×10^{-2} kg/s, $Cp_{pre,w}$ = 4.18 kJ/kg-K, $T_{pre,w,out}$ = 58.22°C, $T_{pre,w,in}$ = 14.74°C,	$\dot{Q}_{pre,w}$ = 2.21 kW	
(9)	$h_{pre,r,out} = h_{pre,r,in} - \dot{Q}_{pre,w} / \dot{m}_{pre,r}$	$\dot{Q}_{pre,w}$ = 2.21 kW $h_{pre\_r\_in}$ = 494.3 kJ/kg $\dot{m}_{pre,r}$ = 2.097×10^{-2} kg/s	$h_{pre,r,out}$ = 388.9 kJ/kg	
(10)	REFPROP, $x_{pre,r,out} = x(P_{pre,r,out}, h_{pre,r,out})$ $T_{pre,sat,out} = T(P_{pre,r,out}, h_{pre,r,out})$	$P_{pre,r,out}$ = 3820.9 kPa, $h_{pre,r,out}$ = 388.9 kJ/kg,	$x_{pre,r,out}$ = 0.7544 $T_{pre,sat,out}$ = 60.00°C	
(11)	$T_{pre,sat,err} = T_{pre,r,out} - T_{pre,sat,out}$	$T_{pre,sat,out}$ = 60.00°C $T_{pre,r,out}$ = 59.64°C	$T_{pre,sat,err}$ = - 0.36°C	

Post Condenser Inlet/Test Section Outlet Quality Calculation

Eq. No	Equation	Inputs	Outputs	Reference
(12)	$P_{post,w,avg} = \frac{P_{post,w,in} + P_{post,w,out}}{2}$	$P_{post,w,in}$ = 413.7 kPa, $P_{post,w,out}$ = 137.9 kPa	$P_{post,w,avg}$ = 275.8 kPa	
(13)	$T_{post,w,avg} = \frac{T_{post,w,in} + T_{post,w,out}}{2}$	$T_{post,w,in}$ = 13.89°C, $T_{post,w,out}$ = 20.31°C	$T_{post,w,avg}$ = 17.10°C	
(14)	$\rho_{post,w} = f(T_{post,w,avg}, P_{post,w,avg})$ $Cp_{post,w} = f(T_{post,w,avg}, P_{post,w,avg})$ $h_{post,r,out} = f(T_{post,r,out}, P_{post,r,out})$	$P_{post,w,avg}$ = 275.8 kPa $T_{post,w,avg}$ = 17.10°C $P_{post,r,out}$ = 3808.5 kPa $T_{post,r,out}$ = 46.14°C	$\rho_{post,w}$ = 998.9 kg/m^3 $Cp_{post,w}$ = 4.18 kJ/kg-K $h_{post,r,out}$ = 277.2 kJ/kg	
(15)	$\dot{m}_{post,w} = \rho_{post,w} \cdot VolFlo_{post,w}$	$\rho_{post,w}$ = 998.9 kg/m^3, $VolFlo_{post,w}$ = 7.17×10^{-5} m^3/s	$\dot{m}_{post,w}$ = 7.16×10^{-2} kg/s	
(16)	$\dot{Q}_{post,w} = \left(T_{post,w,out} - T_{post,w,in}\right) \cdot \dot{m}_{post,w} \cdot Cp_{post,w}$	$\dot{m}_{post,w}$ = 7.16×10^{-2} kg/s, $Cp_{post,w}$ = 4.18 kJ/kg-K, $T_{post,w,out}$ = 20.31°C, $T_{post,w,in}$ = 13.89°C,	$\dot{Q}_{post,w}$ = 1.92 kW	
(17)	$h_{post,r,in} = h_{post,r,out} + \dot{Q}_{post,w} / \dot{m}_{post,r}$	$\dot{Q}_{post,w}$ = 1.92 kW $h_{post\_r\_out}$ = 277.2 kJ/Kg $\dot{m}_{post,r}$ = 2.097×10^{-2} kg/s	$h_{post,r,in}$ = 368.9 kJ/Kg	
(18)	REFPROP, $x_{post,r,in} = x(P_{post,r,in}, h_{post,r,in})$ $T_{post,sat,in} = T(P_{post,r,in}, h_{post,r,in})$	$h_{post,r,in}$ = 368.9 kJ/kg, $P_{post,r,in}$ = 3821.8 kPa	$x_{post,r,in}$ = 0.5639 $T_{post,sat,in}$ = 59.96°C	
(19)	$T_{post,sat,err} = T_{post,r,in} - T_{post,sat,in}$	$T_{post,sat,in}$ = 59.96°C $T_{post,r,in}$ = 59.13°C	$T_{post,sat,err}$ = - 0.83°C	

(20)	$x_{test} = \frac{x_{pre,r,out} + x_{post,r,in}}{2}$	$x_{pre,r,out}$ = 0.7544 $x_{post,r,in}$ = 0.5639	x_{test} = 0.6592	

Heat Duty of the Secondary Heat Exchanger

Eq. No	Equation	Inputs	Outputs	Reference
(21)	$T_{sec,w,avg} = \frac{T_{sec,w,in} + T_{sec,w,out}}{2}$	$T_{sec,w,in}$ = 14.11°C $T_{sec,w,out}$ = 25.47°C	$T_{sec,w,avg}$ = 19.79°C	
(22)	$\rho_{sec,w} = f(T_{sec,w,avg}, P_{sec,w})$ $Cp_{sec,w} = f(T_{sec,w,avg}, P_{sec,w})$	$P_{sec,w}$ = 275.8 kPa $T_{sec,w,avg}$ = 19.79°C	$\rho_{sec,w}$ = 998.4 kg/m^3 $Cp_{sec,w}$ = 4.18 kJ/kg-K	
(23)	$VolFlo_{sec,w} = \dot{m}_{sec,w} / \rho_{sec,w}$.	$\rho_{sec,w}$ = 998.4 kg/m^3, $\dot{m}_{sec,w}$ = 1.181×10^{-2} kg/s	$VolFlo_{sec,w}$ = 1.184 × 10^{-5} m^3/s	
(24)	$\dot{Q}_{sec,w} = \dot{m}_{sec,w} \cdot Cp_{sec,w} \cdot (T_{sec,w,out} - T_{sec,w,in})$	$\dot{m}_{sec,w}$ = 1.181×10^{-2} kg/s $Cp_{sec,w}$ = 4.18 kJ/kg-K $T_{sec,w,out}$ = 25.47°C, $T_{sec,w,in}$ = 14.11°C	$\dot{Q}_{sec,w}$ = 561.1 W	

Pump Heat Addition:

Eq. No	Equation	Inputs	Outputs	Reference
(25)	$\dot{Q}_{pump} = 10.66 \cdot VolFlo_{prim,w,gpm}^{1.2474}$	$VolFlo_{prim,w,gpm}$ = 1.816 gpm	$\dot{Q}_{pump}$ = 22.44 W	From pressure drop analysis and pump curve (Appendix B)

Test Section Ambient Heat Loss

Eq. No	Equation	Inputs	Outputs	Reference
(26)	$\rho_w = f(T_{test,w}, P_{test,w})$ $\mu_w = f(T_{test,w}, P_{test,w})$ $\mathrm{Pr}_w = f(T_{test,w}, P_{test,w})$ $k_w = f(T_{test,w}, P_{test,w})$	$T_{test,w}$ = 34.65°C $P_{sec,w}$ = 413.7 kPa	ρ_w = 994.3 kg/m^3 μ_w = 7.269×10^{-4} kg/s-m Pr_w = 4.98 k_w = 0.61 W/m-K	
(27)	$d_{o,i} = d_{o,o} - 2 \times t_{test}$	$d_{o,o}$ = 19.05 mm t_{test} = 1.65 mm	$d_{o,i}$ = 15.75 mm	
(28)	$A_{annulus} = \frac{\pi}{4}\left[{d_{o,i}}^2 - {d_{i,o}}^2 \right]$	$d_{o,i}$ = 15.75 mm, $d_{i,o}$ = 12.7 mm	$A_{annulus}$ = 6.82×10^{-5} m^2	
(29)	$V_{annulus} = \frac{VolFlo_w}{A_{annulus}}$	$VolFlo_w$ = 1.146×10^{-4} m^3/s, $A_{annulus}$ = 6.82×10^{-5} m^2	$V_{annulus}$ = 1.68 m/s	
(30)	$d_h = d_{o,i} - d_{i,o}$	$d_{o,i}$ = 15.75 mm, $d_{i,o}$ = 12.7 mm	d_h = 3.05 mm	
(31)	$\mathrm{Re}_{annulus} = \frac{\rho_w \cdot V_{annulus} \cdot d_h}{\mu_w}$	ρ_w = 994.3 kg/m^3 $V_{annulus}$ = 1.68 m/s, d_h = 3.05 mm, μ_w = 7.269 ×10^{-4} kg/s-m	$Re_{annulus}$ = 7014	
(32)	$r_{ratio} = d_{i,o} / d_{o,i}$	$d_{i,o}$ = 12.7 mm, $d_{o,i}$ = 15.75 mm	r_{ratio} = 0.8065	
(33)	$Re_{cl} = 2089.26 + 686.15 \cdot r_{ratio}$	r_{ratio} = 0.8065	Re_{cl} = 2643	(Kays and Leung 1963) Garimella and
(34)	$Re_{cu} = 2963.02 + 334.16 \cdot r_{ratio}$	r_{ratio} = 0.8065	Re_{cu} = 3233	

(35)	$Nu_{lam} = \frac{1}{0.186 + 0.029 \cdot ln\left(r_{ratio}\right) - 0.008 \cdot \left(ln\left(r_{ratio}\right)\right)^2}$	r_{ratio} = 0.8065 $Re_{annulus} <= Re_{cl}$	Nu_{lam} = 5.574	Christensen (1995)
(36)	$Nu_{turb} = 0.025 \cdot Re^{0.78} \cdot Pr_w^{0.48} \cdot r_{ratio}^{-0.14}$	r_{ratio} = 0.8065, Pr_w = 4.98, $Re_{annulus}$ = 7014	Nu_{turb} = 55.68 $Re_{annulus} >= Re_{cu}$ ∴Flow Turbulent ∴Nu = 55.68	
(37)	$h_{annulus} = \frac{Nu \cdot k_w}{d_h}$	Nu = 55.68, k_w = 0.61 W/m-K, d_h = 3.05 mm	$h_{annulus}$ = 11143 W/m^2-K	
(38)	$A_{eff} = \pi d_{o,i} L_{test}$	$d_{o,i}$ = 15.75 mm L_{test} = 0.292 m	A_{eff} = 1.445×10^{-2} m^2	Effective area is the area of the inside surface of the outer tube
(39)	$R_{conv} = \frac{1}{h_{annulus} \cdot A_{eff}}$	$h_{annulus}$ = 11143 W/m^2-K, A_{eff} = 1.445×10^{-2} m^2	R_{conv} = 6.21×10^{-3} K/W	
(40)	$k_{tube} = f(T_{test,w})$	$T_{test,w}$ = 34.65°C	k_{tube} = 15.02 W/m-K	
(41)	$R_{tube} = \frac{\ln\left[\frac{d_{o,o}}{d_{o,i}}\right]}{2 \cdot \pi \cdot Length \cdot k_{tube}}$	$d_{o,o}$ = 19.05 mm, $d_{o,i}$ = 15.75 mm, Length = 0.292 m, k_{tube} = 15.02 W/m-K	R_{tube} = 6.90×10^{-3} K/W	
(42)	$R_{insulation} = \frac{\ln\left[\frac{d_{o,o} + 2 \cdot t_{ins}}{d_{o,o}}\right]}{2 \cdot \pi \cdot Length \cdot k_{insulation}}$	$d_{o,o}$ = 19.05 mm, t_{ins} = 26.67 mm, Length = 0.292 m, $k_{insulation}$ = 0.043 W/m-K,	$R_{insulation}$ = 16.92 K/W	

(43)	$\rho_{air} = f(T_\infty, P_\infty)$ $\mu_{air} = f(T_\infty, P_\infty)$ $\mathrm{Pr}_{air} = f(T_\infty, P_\infty)$ $\beta_{air} = f(T_\infty, P_\infty)$ $k_{air} = f(T_\infty, P_\infty)$	T_∞ = 23°C (assumption) P_∞ = 101.3 kPa (assumption)	ρ_{air} = 1.193 kg/m^3, β_{air} = 3.378×10^{-3} 1/K, Pr_{air} = 0.73, μ_{air} = 1.839×10^{-5} kg/s-m k_{air} = 2.54×10^{-2} W/m-K	
(44)	$d_{ins} = d_{o,o} + 2\times t_{ins}$	$d_{o,o}$ = 19.05 mm t_{ins} = 26.67 mm	d_{ins} = 72.4 mm	
(45)	$Ra = \frac{g \cdot \beta_{air} \cdot \lvert (T_s - T_\infty) \rvert \cdot d_{ins}^3 \cdot \rho_{air}^2 Pr_{air}}{\mu_{air}^2}$	g = 9.81 m^2/s β_{air} = 3.378×10^{-3} 1/K, d_{ins} = 72.4 mm ρ_{air} = 1.193 kg/m^3, Pr_{air} = 0.73, μ_{air} = 1.839×10^{-5} kg/s-m T_s = 24.26°C T_∞ = 23°C	Ra = 48809	T_s is assumed here and verified later in equation (51)
(46)	$Nu_{nc} = \left[0.6 + 0.387 \frac{Ra^{(1/6)}}{\left(1 + \left[\frac{0.559}{\mathrm{Pr}_{air}}\right]^{\left[\frac{9}{16}\right]}\right)^{\left[\frac{8}{27}\right]}} \right]^2$	Ra = 48809, Pr_{air} = 0.73	Nu_{nc} = 6.484	(Churchill and Chu 1975) Applicability: Ra ≤ 10^{12}
(47)	$h_{nc} = Nu_{nc} \frac{k_{air}}{d_{ins}}$	Nu_{nc} = 6.484, k_{air} = 2.54×10^{-2} W/m-K d_{ins} = 72.4 mm	h_{nc} = 2.271 W/m^2-K	
(48)	$h_r = \varepsilon \cdot \sigma \cdot (T_s^2 + T_\infty^2) \cdot (T_s + T_\infty)$ (T_s, T_∞ in K)	T_s = 24.26°C, T_∞ = 23°C, ε = 0.85, σ = 5.67×10^{-8} W/m^2-K^4	h_r = 5.031 W/m^2-K	

(49)	$\dot{Q}_{loss,test\,section} = \left(\frac{1}{R_{insulation} + R_{tube} + R_{conv}}\right) \cdot \left(T_{water} - T_s\right)$	$R_{insulation}$ = 16.92 K/W, R_{tube} = 6.90×10^{-3} K/W R_{conv} = 6.21×10^{-3} K/W T_{water} = 34.65°C T_s = 24.26°C,	$\dot{Q}_{loss,test\,section}$ = 0.61 W	
(50)	$A_{ins} = \pi d_{ins} L_{test}$	d_{ins} = 72.4 mm L_{test} = 0.292 m	A_{ins} = 6.64×10^{-2} m^2	
(51)	$\dot{Q}_{loss,test\,section} = (h_r + h_{nc}) \cdot A_{ins} \cdot \left(T_s - T_\infty\right)$	T_∞ = 23°C, $\dot{Q}_{loss,test\,section}$ = 0.61 W, h_r = 5.031 W/m^2-K, h_{nc} = 2.271 W/m^2-K, A_{ins} = 6.64×10^{-2} m^2	T_s = 24.26°C	T_s and $\dot{Q}_{loss,test\,section}$ evaluated iteratively using equation (45) to (51)

Secondary Heat Exchanger Ambient Heat Loss[1]

Eq. No	Equation	Inputs	Outputs	Reference
(52)	$k_{tube} = f(T_{sec,w,avg})$	$T_{sec,w,avg}$ = 19.79°C	k_{tube} = 14.6 W/m-K	
	$d_{i,t} = d_{o,t} - 2 \times t_{shell}$	$d_{o,t}$ = 25.4 mm, t_{shell} = 1.25 mm	$d_{i,t}$ = 22.9 mm	
(53)	$R_{tube} = \frac{\ln(d_{o,t} / d_{i,t})}{2 \cdot \pi \cdot k_{tube} \cdot L}$	$d_{o,t}$ = 25.4 mm, $d_{i,t}$ = 22.9 mm, k_{tube} = 14.6 W/m-K, L = 0.173 m	R_{tube} = 64.98×10^{-4} K/W	
(54)	$d_{ins,sec} = d_{o,t} + 2 \times t_{ins,sec}$	$d_{o,t}$ = 25.4 mm $t_{ins,sec}$ = 28.2 mm	$d_{ins,sec}$ = 81.8 mm	
(55)	$R_{ins} = \frac{\ln(d_{ins,sec} / d_{o,t})}{2 \cdot \pi \cdot k_{ins} \cdot L}$	d_{ins} = 81.8 mm, $d_{o,t}$ = 25.4 mm, k_{ins} = 0.043 W/m-K, L = 0.173 m	R_{ins} = 25.02 K/W	

(56)	$\rho_{air} = f(T_\infty, P_\infty)$ $\mu_{air} = f(T_\infty, P_\infty)$ $\mathrm{Pr}_{air} = f(T_\infty, P_\infty)$ $\beta_{air} = f(T_\infty, P_\infty)$ $k_{air} = f(T_\infty, P_\infty)$	T_∞ = 23°C (assumption) P_∞ = 101.3 kPa (assumption)	ρ_{air} = 1.193 kg/m^3, β_{air} = 3.378×10^{-3} 1/K, Pr_{air} = 0.73, μ_{air} = 1.839×10^{-5} kg/s-m k_{air} = 2.54×10^{-2} W/m-K	
(57)	$Ra = \frac{g \cdot \beta_{air} \cdot \lvert (T_s - T_\infty) \rvert \cdot d_{ins,\mathrm{sec}}^3 \cdot \rho_{air}^2 Pr_{air}}{\mu_{air}^2}$	g = 9.81 m^2/s, ρ_{air} = 1.193 kg/m^3, β_{air} = 3.378×10^{-3} 1/K, Pr_{air} = 0.73, μ_{air} = 1.839×10^{-5} kg/s-m $d_{ins,sec}$ = 81.8 mm T_s = 295.6 K =22.62°C, T_∞ = 296 K=23°C	Ra = 21417	
(58)	$Nu = \left[0.6 + 0.387 \frac{Ra^{(1/6)}}{\left(1 + \left[\frac{0.559}{\mathrm{Pr}} \right]^{\left[\frac{9}{16}\right]} \right)^{\left[\frac{8}{27}\right]}} \right]^2$	Ra = 21417, Pr = 0.73	Nu = 5.275	(Churchill and Chu 1975)
(59)	$h_c = Nu \frac{k_{air}}{d_{ins,\mathrm{sec}}}$	k_{air} = 2.54×10^{-2} W/m-K $d_{ins,sec}$ = 81.8 mm, Nu = 5.275	h_c = 1.634 W/m^2-K	
(60)	$h_r = \varepsilon \cdot \sigma \cdot \left(T_s^2 + T_a^2\right) \cdot \left(T_s + T_a\right)$ (T_s, T_∞ in K)	ε = 0.85, σ = 5.67×10^{-8} W/m^2-K^4, T_s = 22.62°C, T_∞ = 23°C	h_r = 4.99 W/m^2-K	
(61)	$A_{ins,\mathrm{sec}} = \pi d_{ins,\mathrm{sec}} L_{\mathrm{sec}}$	$d_{ins,sec}$ = 81.8 mm L_{sec} = 0.173 m	$A_{ins,sec}$ = 4.44×10^{-2} m^2	

(62)	$\dot{Q}_{loss,secondary} = \left(\frac{1}{R_{ins}+R_{tube}}\right)\cdot\left(T_{sec,w}-T_s\right)$ $= (h_r+h_c)\cdot A_{ins,sec}\cdot\left(T_s-T_\infty\right)$	R_{tube} = 64.98×10^{-4} K/W R_{ins} = 25.02 K/W $T_{sec,w}$ = 19.79°C, h_r = 4.99 W/m^2-K, h_c = 1.634 W/m^2-K, $A_{ins,sec}$ = 4.44×10^{-2} m^2 T_∞ = 23°C	$\dot{Q}_{loss,secondary}$ = -0.11 W T_s = 22.62°C	T_s and $\dot{Q}_{loss,secondary}$ evaluated iteratively using equation (57) to (62)

Primary Loop Tubing Ambient Heat Loss

Eq. No	Equation	Inputs	Outputs	Reference
(63)	$d_{i,t} = d_{o,t} - 2\times t_{tube}$	$d_{o,t}$ = 12.7 mm t_{tube} = 0.89 mm	$d_{i,t}$ = 10.92 mm	
(64)	$v_{refrigerant} = \frac{VolFlo_{prim,w}}{0.25\cdot\pi\cdot d_{i,t}^2}$	$VolFlo_{prim,w}$ = 1.146×10^{-4} m^3/s , $d_{i,t}$ = 10.92 mm	$v_{refrigerant}$ = 1.22 m/s	
(65)	$\rho_{prim,w} = f(T_{prim,w}, P_{prim,w})$ $\mu_{prim,w} = f(T_{prim,w}, P_{prim,w})$ $\mathrm{Pr}_{prim,w} = f(T_{prim,w}, P_{prim,w})$ $k_{prim,w} = f(T_{prim,w}, P_{prim,w})$	$T_{prim,w}$ = 34.65°C $P_{prim,w}$ = 413.7 kPa	ρ_w = 994.3 kg/m^3 μ_w = 7.269×10^{-4} kg/s-m Pr_w = 4.98 k_w = 0.61 W/m-K	
(66)	$\mathrm{Re} = \frac{\rho_w\cdot v_{refrigerant}\cdot d_{i,t}}{\mu_w}$	$v_{refrigerant}$ = 1.22 m/s, $d_{i,t}$ = 10.92 mm ρ_w = 994.3 kg/m^3, μ_w = 7.269×10^{-4} kg/s-m	Re = 18269	
(67)	$Nu_w = 0.023\cdot\mathrm{Re}^{0.8}\cdot\mathrm{Pr}^{0.3}$	Re = 18269, Pr = 4.98	Nu_w = 95.58	(Dittus and Boelter 1930)

(68)	$h_{\text{single}} = \frac{Nu_w \cdot k_{water}}{d_{i,t}}$	Nu_w = 95.58, k_{water} = 0.61 W/m-K, $d_{i,t}$ = 10.92 mm	h_{single} = 5339 W/m^2-K	
(69)	$k_{tube} = f(T_{prim,w,avg})$	$T_{prim,w,avg}$ = 34.65°C	k_{tube} = 15.27 W/m-K	
(70)	$R_{water} = \frac{1}{h_{\text{sin}gle} \cdot \pi \cdot d_{i,t} \cdot L_{tube}}$	h_{single} = 5339 W/m^2-K, $d_{i,t}$ = 10.92 mm L_{tube} = 4.22 m	R_{water} = 1.29×10^{-3} K/W	
(71)	$R_{tube} = \frac{\ln\left(d_{o,t}/d_{i,t}\right)}{2 \cdot \pi \cdot k_{tube} \cdot L_{tube}}$	$d_{o,t}$ = 12.7 mm, $d_{i,t}$ = 10.92 mm, k_{tube} = 15.27 W/m-K, L_{tube} = 4.22 m	R_{tube} = 3.70×10^{-4} K/W	
(72)	$d_{ins} = d_{o,t} + 2 \times t_{ins}$	$d_{o,t}$ = 12.7 mm, t_{ins} = 18.5 mm	d_{ins} = 49.7 m	
(73)	$R_{ins} = \frac{\ln\left(d_{ins}/d_{o,t}\right)}{2 \cdot \pi \cdot k_{ins} \cdot L_{tube}}$	d_{ins} = 49.7 mm, $d_{o,t}$ = 12.7 mm, k_{ins} = 0.043 W/m-K, L_{tube} = 4.22 m	R_{ins} = 1.197 K/W	
(74)	$\rho_{air} = f(T_\infty, P_\infty)$ $\mu_{air} = f(T_\infty, P_\infty)$ $\text{Pr}_{air} = f(T_\infty, P_\infty)$ $\beta_{air} = f(T_\infty, P_\infty)$ $k_{air} = f(T_\infty, P_\infty)$	T_∞ = 23°C (assumption) P_∞ = 101.3 kPa (assumption)	ρ_{air} = 1.193 kg/m^3, β_{air} = 3.378×10^{-3} 1/K, Pr_{air} = 0.73, μ_{air} = 1.839×10^{-5} kg/s-m k_{air} = 2.54×10^{-2} W/m-K	
(75)	$Ra = \frac{g \cdot \beta_{air} \cdot \lvert\left(T_s - T_\infty\right)\rvert \cdot d_{ins}^3 \cdot \rho_{air}^2 Pr_{air}}{\mu_{air}^2}$	g = 9.81 m^2/s, β_{air} = 3.378×10^{-3} 1/K, d_{ins} = 49.7 m Pr_{air} = 0.73, ρ_{air} = 1.193 kg/m^3, μ_{air} = 1.839×10^{-5} kg/s-m T_s = 24.64°C, T_a = 23°C	Ra = 20566	

(76)	$Nu_{nc} = \left[0.6 + 0.387 \frac{Ra^{(1/6)}}{\left(1 + \left[\frac{0.559}{Pr_{air}} \right]^{\left[\frac{9}{16}\right]} \right)^{\left[\frac{8}{27}\right]}} \right]^2$	$Ra = 20566$, $Pr_{air} = 0.73$	$Nu_{nc} = 5.22$	(Churchill and Chu 1975)
(77)	$h_{nc} = Nu_{nc} \frac{k_{air}}{d_{ins}}$	$Nu_{nc} = 5.22$, $k_{air} = 2.54\times10^{-2}$ W/m-K , $d_{ins} = 49.7$ mm	$h_{nc} = 2.66$ W/m^2-K	
(78)	$h_r = \varepsilon \cdot \sigma \cdot \left(T_s^2 + T_\infty^2\right) \cdot \left(T_s + T_\infty\right)$ (T_s, T_∞ in K)	$\varepsilon = 0.85$, $\sigma = 5.67\times10^{-8}$ W/m^2-K^4, $T_s = 24.64$°C, $T_\infty = 23$°C	$h_r = 5.04$ W/m^2-K	
(79)	$\dot{Q}_{loss,tubing} = \left(\frac{1}{R_{ins} + R_{tube} + R_{water}} \right) \cdot \left(T_{prim,w,avg} - T_s \right)$	$R_{water} = 1.29\times10^{-3}$ K/W, $R_{tube} = 3.70\times10^{-4}$ K/W, $R_{ins} = 1.197$ K/W, $T_{prim,w} = 34.65$°C $T_s = 24.64$°C	$\dot{Q}_{loss,tubing} = 8.35$ W	
(80)	$A_{ins,prim} = \pi d_{ins} L_{prim}$	$d_{ins} = 49.7$ mm $L_{prim} = 4.22$ m	$A_{ins,prim} = 6.59\times10^{-1}$ m^2	
(81)	$\dot{Q}_{loss,tubing} = (h_r + h_{nc}) \cdot A_{ins,prim} \cdot \left(T_s - T_\infty \right)$	$h_{nc} = 2.66$ W/m^2-K, $h_r = 5.04$ W/m^2-K, $A_{ins,prim} = 6.59\times10^{-1}$ m^2 $\dot{Q}_{loss,tubing} = 8.35$ W, $T_\infty = 23$°C	$T_s = 24.64$°C	T_s and $\dot{Q}_{loss,tubing}$ evaluated iteratively using equation (75) to (81)

Heat Transfer Coefficient Calculation

Eq. No	Equation	Inputs	Outputs	Reference
(82)	$\dot{Q}_{ambient} = \dot{Q}_{loss,secondary} + \dot{Q}_{loss,testsection} + \dot{Q}_{loss,tubing}$	$\dot{Q}_{loss,secondary}$ = -0.11 W, $\dot{Q}_{loss,testsection}$ = 0.61 W, $\dot{Q}_{tubing}$ = 8.35 W	$\dot{Q}_{ambient}$ = 8.85 W	
(83)	$\dot{Q}_{test} = \dot{Q}_{sec,w} + \dot{Q}_{ambient} - \dot{Q}_{pump}$	$\dot{Q}_{ambient}$ = 8.85 W, $\dot{Q}_{sec,w}$ = 561.1 W, $\dot{Q}_{pump}$ = 22.44 W	$\dot{Q}_{test}$ = 547.5 W	
(84)	$k_{wall} = f(T_{wall})$	T_{wall} = 36.49°C	k_{wall} = 398.4 W/m-K	
(85)	$d_{i,i} = d_{i,o} - 2 \times t_{test}$	$d_{i,o}$ = 12.7 mm, t_{test} = 1.65 mm	$d_{i,i}$ = 9.4 mm	
(86)	$R_{innertube} = \frac{Ln\left[\frac{d_{i,o}}{d_{i,i}}\right]}{2 \cdot \pi \cdot k_{wall} \cdot L_{test}}$	$d_{i,o}$ = 12.7 mm, $d_{i,i}$ = 9.4 mm, k_{wall} = 398.4 W/m-K, L_{test} = 0.292 m	$R_{innertube}$ = 4.12×10^{-4} K/W	
(87)	$R_{annulus} = \frac{1}{h_{annulus} \cdot \pi \cdot d_{i,o} \cdot L_{test}}$	$d_{i,o}$ = 12.7 mm, L_{test} = 0.292 m, $h_{annulus}$ = 11143 W/m^2-K	$R_{annulus}$ = 7.7×10^{-3} K/W	
(88)	$LMTD = \frac{\left(T_{r,in} - T_{w,out}\right) - \left(T_{r,out} - T_{w,in}\right)}{Ln\left(\frac{T_{r,in} - T_{w,out}}{T_{r,out} - T_{w,in}}\right)}$	$T_{r,in}$ = 59.78°C, $T_{r,out}$ = 59.64°C, $T_{w,in}$ = 34.32°C, $T_{w,out}$ = 34.97°C	LMTD = 25.06°C	

(89)	$UA = \frac{\dot{Q}_{test}}{LMTD}$	$\dot{Q}_{test}$ = 547.5 W, LMTD = 25.06°C	UA = 21.85 W/K	
(90)	$R_{total} = \frac{1}{UA}$	UA = 21.85 W/K	$R_{total} = 4.58\times10^{-2}$ K/W	
(91)	$R_{refrigerant} = R_{total} - R_{annulus} - R_{innertube}$	$R_{total} = 4.58\times10^{-2}$ K/W $R_{annulus} = 7.7\times10^{-3}$ K/W $R_{innertube} = 4.12\times10^{-4}$ K/W	$R_{refrigerant} = 3.77\times10^{-2}$ K/W	
(92)	$h_{refrigerant} = \frac{1}{R_{refrigerant} \cdot \pi \cdot d_{i,i} \cdot L_{test}}$	$R_{refrigerant} = 3.77\times10^{-2}$ K/W, $d_{i,i}$ = 9.4 mm, L_{test} = 0.292 m	$h_{refrigerant}$ = 3079 W/m^2-K	
(93)	$R_{ratio} = \frac{R_{refrigerant}}{R_{annulus}}$	$R_{refrigerant} = 3.77\times10^{-2}$ K/W $R_{annulus} = 7.7\times10^{-3}$ K/W	R_{ratio} = 4.9	

1. The shell inner wall temperature of the secondary shell-and-tube heat exchanger is assumed to be same as the average water temperature inside the shell

APPENDIX B PUMP HEAT ADDITION

(Representative Data Point: G = 302.4 kg/m^2-s, p_r = 0.78, x = 0.66)

Test Section Pressure Drop

Eq. No	Equation	Inputs	Outputs	Reference
(1)	$\rho_w = f(T_{test,w}, P_{test,w})$ $\mu_w = f(T_{test,w}, P_{test,w})$ $\mathrm{Pr}_w = f(T_{test,w}, P_{test,w})$ $k_w = f(T_{test,w}, P_{test,w})$	$T_{test,w}$ = 34.65°C $P_{sec,w}$ = 413.7 kPa	ρ_w = 994.3 kg/m^3 μ_w = 7.269×10^{-4} kg/s-m Pr_w = 4.98 k_w = 0.61 W/m-K	
(2)	$d_{o,i} = d_{o,o} - 2t_{outer}$	$d_{o,o}$ = 19.05 mm t_{outer} = 1.65 mm	$d_{o,i}$ = 15.75 mm	
(3)	$D_{h,annulus} = \frac{4A_{f,annulus}}{P} = d_{o,i} - d_{i,o}$	$d_{i,o}$ = 12.70 mm $d_{o,i}$ = 15.75 mm	$D_{h,annulus}$ = 3.05 mm	
(4)	$A_{f,annulus} = \frac{\pi}{4}\left[d_{o,i}{}^2 - d_{i,o}{}^2\right]$	$d_{i,o}$ = 12.70 mm $d_{o,i}$ = 15.75 mm	$A_{f,annulus}$ = 6.82×10^{-5} m^2	
(5)	$V_{annulus} = Vol_{primary} / A_{f,annulus}$	$Vol_{primary}$ = 1.146×10^{-4} m^3/s $A_{f,annulus}$ = 6.82×10^{-5} m^2	$V_{annulus}$ = 1.68 m/s,	
(6)	$\mathrm{Re}_{annulus} = \frac{\rho_w V_{annulus} D_{h,annulus}}{\mu_w}$	ρ_w = 994.3 kg/m^3, $V_{annulus}$ = 1.68 m/s, $D_{h,annulus}$ = 3.05 mm μ_w = 7.269×10^{-4} kg/m-s	$Re_{annulus}$ = 7,014	

(7)	$r^* = d_{i,o} / d_{o,i}$	$d_{i,o}$ = 12.70 mm $d_{o,i}$ = 15.75 mm	r^* = 0.8065	
(8)	$\mathrm{Re}_{CL} = 2089.26 + 686.15 r^*$	r^* = 0.8065	Re_{CL} = 2,643	
(9)	$\mathrm{Re}_{CU} = 2963.02 + 334.16 r^*$	r^* = 0.8065	Re_{CU} = 3,233	
(10)	If $\mathrm{Re}_{annulus} < \mathrm{Re}_{CL}$ $f_{annulus} = \frac{96}{\mathrm{Re}_{annulus}} \left(r^*\right)^{0.035}$ If $\mathrm{Re}_{annulus} > \mathrm{Re}_{CU}$ $f_{annulus} = 4\left[1.737 \ln\left(\frac{\mathrm{Re}_{annulus}}{1.964 \ln(\mathrm{Re}_{annulus}) - 3.8215}\right)\right]^{-2} \cdot \left(1 + 0.0925 r^*\right)$ If $\mathrm{Re}_{CL} \le \mathrm{Re}_{annulus} \le \mathrm{Re}_{CU}$ $\frac{\ln[f_{annulus}] - \ln[f_{lam}(\mathrm{Re}_{CL})]}{\ln[f_{turb}(\mathrm{Re}_{CU})] - \ln[f_{lam}(\mathrm{Re}_{CL})]} = \frac{\ln[\mathrm{Re}_{annulus}] - \ln[\mathrm{Re}_{CL}]}{\ln[\mathrm{Re}_{CU}] - \ln[\mathrm{Re}_{CL}]}$	r^* = 0.8065 Re_{CL} = 2,643 Re_{CU} = 3,233 $\mathrm{Re}_{annulus}$ = 7014	$f_{annulus}$= 0.0365	Garimella and Christensen (1995), Kays and Leung (1963), Walker *et al.* (1957)
(11)	$\Delta P_{test} = \frac{1}{2} f_{annulus} \rho_w V_{annulus}^2 \frac{L_{test}}{D_{h,annulus}} \cdot \frac{1}{1000}$	$f_{annulus}$= 0.0365 ρ_w = 994.3 kg/m^3 L_{test} = 0.292 $D_{h,annulus}$ = 3.05 mm $V_{annulus}$ = 1.68 m/s	ΔP_{test} = 4.9 kPa	

Secondary Heat Exchanger Pressure Drop

Eq. No	Equation	Inputs	Outputs	Reference
(12)	$\Delta P_{shell}(\text{in psi}) = 0.49157(\text{VolFlo}_{\text{prim,w,gpm}})^{1.9}$	$\text{VolFlo}_{\text{prim,w,gpm}}$ = 1.816 gpm	ΔP_{shell} = 1.527 psi = 10.5 kPa	(Exergy Model 00540-4). Equation by manufacturer

Primary Loop Tubing Pressure Drop

Eq. No	Equation	Inputs	Outputs	Reference
(13)	$L_{equiv} = L_{prim} + L_{eq,flowmeter}$	L_{prim} = 2.54 m $L_{\text{eq,flowmeter}}$ = 0.54 m	L_{equiv} = 3.08 m	
(14)	$d_{i,tube} = d_{o,tube} - 2t_{tube}$	$d_{\text{o,tube}}$ = 12.70 mm t_{tube} = 0.89 mm	$d_{\text{i,tube}}$ = 10.92 mm	
(15)	$A_{f,tube} = \pi d_{i,tube}^2 / 4$	$d_{\text{i,tube}}$ = 10.92 mm	$A_{\text{f,tube}} = 9.37\times10^{-5}$ m^2	
(16)	$V_{w,tubing} = Vol_{primary} / A_{f,tube}$	$\text{Vol}_{\text{primary}} = 1.146\times10^{-4}$ m^3/s $A_{\text{f,tube}} = 9.37\times10^{-5}$ m^2	$V_{\text{w,tube}}$ = 1.22 m/s	
(17)	$\text{Re}_{w,tube} = \frac{\rho_w V_{w,tube} d_{i,tube}}{\mu_w}$	$V_{\text{w,tube}}$ = 1.22 m/s ρ_w = 994.3 kg/m^3 $d_{\text{i,tube}}$ = 10.92 mm $\mu_w = 7.269\times10^{-4}$ kg/m-s	$\text{Re}_{\text{w,tube}}$ = 18,269	

(18)	$f_{w,tube} = 8\left[\left(\frac{8}{\mathrm{Re}_{w,tube}}\right)^{12} + \left(\left[2.457\ln\left(\left[\frac{7}{\mathrm{Re}_{w,tube}}\right]^{0.9} + 0.27\varepsilon_d\right)\right]^{16} + \left[\frac{37350}{\mathrm{Re}_{w,tube}}\right]^{16}\right)^{-1.5}\right]^{1/12}$	$\mathrm{Re}_{w,tube}$ = 18,269 ε_d = 0.0015	$f_{w,tube}$ = 0.0296	Churchill (1977a)
(19)	$K_{\mathrm{minor}} = N_{\mathrm{elbow}}K_{\mathrm{elbow}} + N_{\mathrm{Tee,branch}}K_{\mathrm{Tee,branch}} + N_{\mathrm{Ball,valve}}K_{\mathrm{Ball,valve}} + N_{180,\mathrm{return}}K_{180,\mathrm{return}}$	K_{elbow} = 1.5 N_{elbow} = 5 $K_{Tee,branch}$ = 2 $N_{Tee,branch}$ = 6 $K_{Ball,valve}$ = 0.05 $N_{Ball,valve}$ = 1 $K_{180,return}$ = 1.5 $N_{180,return}$ = 1	K_{minor} = 21.05	Munson *et al.* (1998)
(20)	$\Delta P_{fric,tube} = \frac{1}{2} f_{w,tube}\rho_w V_{w,tube}{}^2 \frac{L_{equiv}}{D_{i,tube}} \cdot \frac{1}{1000}$	L_{equiv} = 3.08 m $d_{i,tube}$ = 10.92 mm $V_{w,tube}$ = 1.22 m/s $f_{w,tube}$ = 0.0296 ρ_w = 994.3 kg/m^3	$\Delta P_{fric,tube}$ = 6.2 kPa	
(21)	$\Delta P_{\mathrm{minor},tube} = \frac{1}{2}\rho_w V_{w,tube}{}^2 K_{\mathrm{minor}} \cdot \frac{1}{1000}$	K_{minor} = 21.05 $V_{w,tube}$ = 1.22 m/s ρ_w = 994.3 kg/m^3	$\Delta P_{minor,tube}$ = 15.7 kPa	
(22)	$\Delta P_{tube} = \Delta P_{fric,tube} + \Delta P_{\mathrm{minor},tube}$	$\Delta P_{minor,tube}$ = 15.7 kPa $\Delta P_{fric,tube}$ = 6.2 kPa	ΔP_{tube} = 21.9 kPa	

Total Primary Loop Pressure Drop

Eq. No	Equation	Inputs	Outputs	Reference
(23)	$\Delta P = \Delta P_{test} + \Delta P_{shell} + \Delta P_{tube}$	ΔP_{tube} = 21.9 kPa ΔP_{shell} = 10.5 kPa ΔP_{test} = 4.9 kPa	ΔP = 37.3 kPa	

Ideal Pump Work

Eq. No	Equation	Inputs	Outputs	Reference
(24)	$W_{ideal} = Vol_{primary} \cdot \Delta P$	$Vol_{primary} = 1.146 \times 10^{-4}$ m^3/s $\Delta P = 37.3$ kPa	$W_{ideal} = 4.27$ W	

Pump Shaft Work

Eq. No	Equation	Inputs	Outputs	Reference
(25)	$W_{shaft} = \text{Torque} \cdot \frac{\text{RPM} \cdot 2\pi}{60}$	Torque = 0.15 N-m RPM = 1700 rpm	$W_{shaft} = 26.69$ W	

Pump Efficiency

Eq. No	Equation	Inputs	Outputs	Reference
(26)	$\eta = \frac{W_{ideal}}{W_{shaft}}$	$W_{ideal} = 4.27$ W $W_{shaft} = 26.69$ W	$\eta = 0.16$	

Pump Heat Addition

Eq. No	Equation	Inputs	Outputs	Reference
(27)	$Q_{pump} = (1-\eta)W_{shaft}$	$W_{shaft} = 26.69$ W $\eta = 0.16$	$Q_{pump} = 22.42$ W	

Note:

1. By applying the above method to flowrates ranging from 1.5 to 4 gpm, a power series curvefit (shown below) was developed to calculate the pump heat addition as a function of the volumetric flow rate. For a flow of 1.816 gpm, Q_{pump} = 22.44 W.

   $$\dot{Q}_{pump} = 10.66 \cdot VolFlo_{prim,w,gpm}^{1.2474}$$

2. It is assumed that all the pump losses are rejected into the coolant as heat

APPENDIX C CALCULATION OF SUPERCRITICAL HEAT TRANSFER COEFFICIENT

(Representative Point: G = 400, P_r = 1.0, T_{test} = 62.1°C)

Geometry:

Pre-Cooler (Shell-and-Tube Heat Exchanger)		
	British Units	***SI Units***
Length	18.13”	0.461 m
Outside diameter of the shell	1.5”	38.1 mm
Thickness of the shell	0.065”	1.65 mm
Inside diameter of the shell	1.37”	34.8 mm
Insulation Thickness	0.71”	18.0 mm
Post-Cooler (Shell-and-Tube Heat Exchanger)		
Length	8.13”	0.207 m
Outside diameter of the outer tube	1.5”	38.1 mm
Thickness of the outer tube	0.065”	1.65 mm
Inside diameter of the shell	1.37”	34.8 mm
Insulation Thickness	0.875”	22.2 mm
Test Section (Tube-in-Tube Heat Exchanger)		
Length	11.5”	0.292 m
Outside diameter of the outer tube	0.75”	19.05 mm
Thickness of the outer tube	0.065”	1.65 mm
Inside diameter of the outer tube	0.62”	15.75 mm
Outside diameter of the inner tube	0.5”	12.7 mm
Thickness of the inner tube	0.065”	1.65 mm
Inside diameter of the inner tube	0.37”	9.4 mm
Insulation Thickness	1.05”	26.7 mm
Secondary Heat Exchanger (Shell-and-Tube Heat Exchanger)		
Length	6.81”	0.173 m
Outside diameter of the shell	1”	25.4 mm

Thickness of the shell	0.049”	1.24 mm
Inside diameter of the shell	0.902	22.9 mm
Insulation Thickness	1.11”	28.2 mm
Tubing Dimensions:		
Tube Length	100”	2.54 m
Flow Meter Equivalent Length	21.4”	0.543 m
Pump Equivalent Length	44.6”	1.133 m
Equivalent Length	165.6”	4.21 m
Outside diameter	0.5”	12.7 mm
Thickness	0.035”	0.89 mm
Inside diameter	0.43”	10.92 mm
Insulation Thickness	0.729”	18.5 mm

Input Parameters:

Critical Pressure : 4902.6 kPa (711.1 psia)		
Critical Temperature : 71.36℃ (169.45℉)		
Pre-Cooler:		
Inlet water temperature	65.57°F	18.65°C
Inlet water pressure (assumption)	60 psia	413.7 kPa
Outlet water temperature	158.04°F	70.02°C
Outlet water pressure (assumption)	20 psia	137.9 kPa
Water flow rate	0.380 gpm	2.399×10^{-5} m^3/s
Inlet refrigerant temperature	237.25°F	114.03°C

Inlet refrigerant pressure	715.9 psia	4936.4 kPa
Outlet refrigerant temperature	146.62°F	63.68°C
Outlet refrigerant pressure	716.19 psia	4937.7 kPa
Post-Cooler:		
Inlet water temperature	64.60°F	18.11°C
Inlet water pressure (assumption)	60 psia	413.7 kPa
Outlet water temperature	73.18°F	22.88°C
Outlet water pressure (assumption)	20 psia	137.9 kPa
Water flow rate	1.064 gpm	6.71×10^{-5} m^3/s
Inlet refrigerant temperature	138.60°F	59.22°C
Inlet refrigerant pressure	715.9 psia	4936.2 kPa
Outlet refrigerant temperature	98.33°F	36.85°C
Outlet refrigerant pressure	712.5 psia	4912.2 kPa
Test Section:		
Inlet refrigerant temperature	147.20°F	64.00°C
Inlet refrigerant pressure	716.2 psia	4937.7 kPa
Outlet refrigerant temperature	140.41°F	60.23°C
Outlet refrigerant pressure	715.9 psia	4936.2 kPa
Refrigerant flow rate	3.67 lb_m/min	2.777×10^{-2} kg/s
Secondary Heat Exchanger:		
Inlet tube water temperature (primary)	109.58°F	43.10°C
Outlet tube water temperature (primary)	109.15°F	42.86°C
Inlet shell water temperature (secondary)	68.52°F	20.29°C
Outlet shell water temperature (secondary)	108.75°F	42.64°C
Shell water flow rate (secondary)	0.432 lb_m/min	3.27×10^{-3} kg/s

Average water pressure (assumption)	40 psia	275.8 kPa
Primary Loop:		
Inlet test section water temperature	109.15°F	42.86°C
Outlet test section water temperature	109.58°F	43.10°C
Volumetric water flow rate	2.286 gpm	1.442×10^{-4} m^3/s
Average water pressure(assumption)	60 psia	413.7 kPa
Ambient Temperature: 23°C (73.4°F) (assumption)		

Mass Flux

Eq. No	Equation	Inputs	Outputs	Reference
(1)	$d_{i,i} = d_{i,o} - 2 \times t_{test}$	$d_{i,o}$ = 12.7 mm, t_{test} = 1.65 mm	$d_{i,i}$ = 9.4 mm	
(2)	$A_{test} = \frac{\pi \cdot d_{i,i}^{\,2}}{4}$	$d_{i,i}$ = 9.4 mm	$A_{test} = 6.94\times10^{-5}$ m^2	
(3)	$G = \frac{m_{test,r}}{A_{test}}$	$\dot{m}_{test,r}$ = 2.777×10^{-2} kg/s	G = 400 kg/m^2-s	

Pre-Cooler Heat Duty Calculation

Eq. No	Equation	Inputs	Outputs	Reference
(4)	$P_{pre,w,avg} = \frac{P_{pre,w,in} + P_{pre,w,out}}{2}$	$P_{pre,w,in}$ = 413.7 kPa, $P_{pre,w,out}$ = 137.9 kPa	$P_{pre,w,avg}$ = 275.8 kPa	

(5)	$T_{pre,w,avg} = \frac{T_{pre,w,in} + T_{pre,w,out}}{2}$	$T_{pre,w,in}$ = 18.65°C, $T_{pre,w,out}$ = 70.02°C	$T_{pre,w,avg}$ = 44.34°C	
(6)	$\rho_{pre,w} = f(T_{pre,w,avg}, P_{pre,w,avg})$ $Cp_{pre,w} = f(T_{pre,w,avg}, P_{pre,w,avg})$ $h_{pre,r,in} = f(T_{pre,r,in}, P_{pre,r,in})$	$P_{pre,w,avg}$ = 275.8 kPa $T_{pre,w,avg}$ = 44.34°C $P_{pre,r,in}$ = 4936.4 kPa $T_{pre,r,out}$ = 114.03°C	$\rho_{pre,w}$ = 990.6 kg/m^3 $Cp_{pre,w}$ = 4.18 kJ/kg-K $h_{pre,r,in}$ = 492.0 kJ/kg	
(7)	$\dot{m}_{pre,w} = \rho_{pre,w} \cdot VolFlo_{pre,w}$	$\rho_{pre,w}$ = 990.6 kg/m^3, $VolFlo_{pre,w}$ = 2.399×10^{-5} m^3/s	$\dot{m}_{pre,w}$ = 2.38×10^{-2} kg/s	
(8)	$\dot{Q}_{pre,w} = \left(T_{pre,w,out} - T_{pre,w,in}\right) \cdot \dot{m}_{pre,w} \cdot Cp_{pre,w}$	$\dot{m}_{pre,w}$ = 2.38×10^{-2} kg/s, $Cp_{pre,w}$ = 4.18 kJ/kg-K, $T_{pre,w,in}$ = 18.65°C, $T_{pre,w,out}$ = 70.02°C	$\dot{Q}_{pre,w}$ = 5.11 kW	
(9)	$h_{pre,r,out} = h_{pre,r,in} - \dot{Q}_{pre,w} / \dot{m}_{pre,r}$	$\dot{Q}_{pre,w}$ = 5.11 kW $h_{pre,r,in}$ = 492.0 kJ/kg $\dot{m}_{pre,r}$ = 2.777×10^{-2} kg/s	$h_{pre,r,out}$ = 308 kJ/kg	
(10)	REFPROP, $T_{Enthalpy\ Based} = T(P_{pre,r,out}, h_{pre,r,out})$	$P_{pre,r,out}$ = 4937.7 kPa, $h_{pre,r,out}$ = 308 kJ/kg,	$T_{Enthalpy\ Based}$ = 61.7°C	
(11)	$T_{pre,err} = T_{Enthalpy\ Based} - T_{pre,r,out}$	$T_{Enthalpy\ Based}$ = 61.67°C $T_{pre,r,out}$ = 63.68°C	$T_{pre,err}$ = -2.01°C	

Post-Cooler Heat Duty Calculation

Eq. No	Equation	Inputs	Outputs	Reference
(12)	$P_{post,w,avg} = \frac{P_{post,w,in} + P_{post,w,out}}{2}$	$P_{post,w,in}$ = 413.7 kPa, $P_{post,w,out}$ = 137.9 kPa	$P_{post,w,avg}$ = 275.8 kPa	

(13)	$T_{post,w,avg} = \frac{T_{post,w,in} + T_{post,w,out}}{2}$	$T_{post,w,in}$ = 18.11°C, $T_{post,w,out}$ = 22.88°C	$T_{post,w,avg}$ = 20.50°C	
(14)	$\rho_{post,w} = f(T_{post,w,avg}, P_{post,w,avg})$ $Cp_{post,w} = f(T_{post,w,avg}, P_{post,w,avg})$ $h_{post,r,out} = f(T_{post,r,out}, P_{post,r,out})$	$P_{post,w,avg}$ = 275.8 kPa $T_{post,w,avg}$ = 20.50°C $P_{post,r,out}$ = 4912.2 kPa $T_{post,r,out}$ = 36.85°C	$\rho_{post,w}$ = 998.2 kg/m^3 $Cp_{post,w}$ = 4.18 kJ/kg-K $h_{post,r,out}$ = 259.3 kJ/kg	
(15)	$\dot{m}_{post,w} = \rho_{post,w} \cdot VolFlo_{post,w}$	$\rho_{post,w}$ = 998.2 kg/m^3, $VolFlo_{post,w}$ = 6.71×10^{-5} m^3/s	$\dot{m}_{post,w}$ = 6.698×10^{-2} kg/s	
(16)	$\dot{Q}_{post,w} = \left(T_{post,w,out} - T_{post,w,in}\right) \cdot \dot{m}_{post,w} \cdot Cp_{post,w}$	$\dot{m}_{post,w}$ = 6.698×10^{-2} kg/s $Cp_{post,w}$ = 4.18 kJ/kg-K, $T_{post,w,out}$ = 22.88°C, $T_{post,w,in}$ = 18.11°C	$\dot{Q}_{post,w}$ = 1.34 kW	
(17)	$h_{post,r,in} = h_{post,r,out} + \dot{Q}_{post,w} / \dot{m}_{post,r}$	$\dot{Q}_{post,w}$ = 1.34 kW $h_{post,r,out}$ = 259.3 kJ/kg $\dot{m}_{post,r}$ = 2.777×10^{-2} kg/s	$h_{post,r,in}$ = 307.6 kJ/kg	
(18)	REFPROP, $T_{Enthalpy\ Based} = T(P_{post,r,in}, h_{post,r,in})$	$P_{post,r,in}$ = 4936.2 kPa, $h_{post,r,in}$ = 307.6 kJ/kg	$T_{Enthalpy\ Based}$ = 61.43°C	
(19)	$T_{pre,err} = T_{Enthalpy\ Based} - T_{post,r,in}$	$T_{Enthalpy\ Based}$ = 61.43°C $T_{post,r,in}$ = 59.22°C	$T_{pre,err}$ = 2.21°C	

Heat Duty of the Secondary Heat Exchanger

Eq. No	Equation	Inputs	Outputs	Reference
(20)	$T_{\text{sec},w,avg} = \frac{T_{\text{sec},w,in} + T_{\text{sec},w,out}}{2}$	$T_{sec,w,in}$ = 20.29°C $T_{sec,w,out}$ = 42.64°C	$T_{sec,w,avg}$ = 31.47°C	
(21)	$Cp_{\text{sec},w} = f(T_{\text{sec},w,avg}, P_{\text{sec},w,avg})$	$P_{sec,w}$ = 275.8 kPa $T_{sec,w,avg}$ = 31.47°C	$Cp_{sec,w}$ = 4.18 kJ/kg-K	
(22)	$\dot{Q}_{\text{sec},w} = \dot{m}_{\text{sec},w} \cdot Cp_{\text{sec},w} \cdot \left(T_{\text{sec},w,out} - T_{\text{sec},w,in}\right)$	$\dot{m}_{\text{sec},w}$ = 3.27×10^{-3} kg/s $Cp_{sec,w}$ = 4.18 kJ/kg-K, $T_{sec,w,out}$ = 42.64°C, $T_{sec,w,in}$ = 20.29°C	$\dot{Q}_{\text{sec,w}}$ = 305.5 W	

Pump Heat Addition:

Eq. No	Equation	Inputs	Outputs	Reference
(23)	$\dot{Q}_{pump} = 10.66 \cdot VolFlo_{prim,w,gpm}^{1.2474}$	$VolFlo_{prim,w,gpm}$ = 2.286 gpm	$\dot{Q}_{\text{pump}}$ = 29.9 W	From pressure drop analysis and pump curve. See Appendix B

Heat Transfer Coefficient Calculation

Eq. No	Equation	Inputs	Outputs	Reference
(24)	$\dot{Q}_{ambient} = \dot{Q}_{loss,secondary} + \dot{Q}_{loss,test\,section} + \dot{Q}_{tubing}$	$\dot{Q}_{\text{loss,secondary}}$ = 0.3 W,	$\dot{Q}_{\text{ambient}}$ = 15.9 W	From Appendix A $\dot{Q}_{\text{loss,secondary}}$ is

		$\dot{Q}_{loss,test,section}$ = 1.1 W, $\dot{Q}_{tubing}$ = 14.5 W		obtained using eq (52)-(62) $\dot{Q}_{loss,test,section}$ is obtained using eq (26)-(51) $\dot{Q}_{tubing}$ = 14.5 W is obtained using eq (63)-(81)
(25)	$\dot{Q}_{test} = \dot{Q}_{sec,w} + \dot{Q}_{ambient} - \dot{Q}_{pump}$	$\dot{Q}_{ambient}$ = 15.9 W, $\dot{Q}_{sec,w}$ = 305.5 W, $\dot{Q}_{pump}$ = 29.9 W	$\dot{Q}_{test}$ = 291.5 W	
(26)	$k_{wall} = f(T_{wall})$	$T_{,w}$ = 43.8°C	k_{wall} = 398 W/m-K	
(27)	$d_{i,i} = d_{i,o} - 2 \times t_{test}$	$d_{i,o}$ = 12.7 mm, t_{test} = 1.65 mm	$d_{i,i}$ = 9.4 mm	
(28)	$R_{innertube} = \frac{Ln\left[\frac{d_{i,o}}{d_{i,i}}\right]}{2 \cdot \pi \cdot k_{wall} \cdot L_{test}}$	$d_{i,o}$ = 12.7 mm, $d_{i,i}$ = 9.4 mm, k_{wall} = 398 W/m-K, L_{test} = 0.292 m	$R_{innertube} = 4.12\times10^{-4}$ K/W	
(29)	$R_{annulus} = \frac{1}{h_{annulus} \cdot \pi \cdot d_{i,o} \cdot L_{test}}$	$d_{i,o}$ = 12.7 mm, L_{test} = 0.292 m, $h_{annulus}$ = 14088 W/m^2-K	$R_{annulus} = 6.09\times10^{-3}$ K/W	$h_{annulus}$ calculated using eq. (26) to (37) in Appendix A
(30)	$LMTD = \frac{\left(T_{r,in} - T_{w,out}\right) - \left(T_{r,out} - T_{w,in}\right)}{Ln\left(\frac{T_{r,in} - T_{w,out}}{T_{r,out} - T_{w,in}}\right)}$	$T_{r,in}$ = 64.00°C, $T_{r,out}$ = 60.23°C, $T_{w,in}$ = 42.86°C, $T_{w,out}$ = 43.10°C	LMTD = 19.08°C	
(31)	$UA = \frac{\dot{Q}_{test}}{LMTD}$	$\dot{Q}_{test}$ = 291.5 W, LMTD = 19.08°C	UA = 15.28 W/K	
(32)	$R_{total} = \frac{1}{UA}$	UA = 15.28 W/K	$R_{total} = 6.54\times10^{-2}$ K/W	

(33)	$R_{refrigerant} = R_{total} - R_{annulus} - R_{innertube}$	$R_{total} = 6.54\times10^{-2}$ K/W $R_{annulus} = 6.09\times10^{-3}$ K/W $R_{innertube} = 4.12\times10^{-4}$K/W	$R_{refrigerant} = 5.89\times10^{-2}$ K/W	
(34)	$h_{refrigerant} = \frac{1}{R_{refrigerant} \cdot \pi \cdot d_{i,i} \cdot L_{test}}$	$R_{refrigerant} = 5.89\times10^{-2}$ K/W, $d_{i,i} = 9.4$ mm $L_{test} = 0.292$ m	$h_{refrigerant} = 1969$ W/m^2-K	

APPENDIX D COMPARISON WITH PHASE-CHANGE LITERATURE

(Representative Data Point: G = 302 kg/m^2-s, p_r = 0.78, x = 0.66, T_{ref} = 59.71°C, T_w = 36.5)

Refrigerant Properties

Eq. No	Equation	Inputs	Outputs	Reference
(1)	$\rho_l, \rho_v, \mu_l, \mu_v, k_l, k_v, c_{p,l}, c_{p,v}, \mathrm{Pr}_l, \mathrm{Pr}_v, h_{fg} = f(T_{sat})$	T_{sat} = 59.71°C P_{test} = 3821.4 kPa	ρ_l = 820.4 kg/m^3 ρ_v = 197.4 kg/m^3 $\mu_l = 6.95 \times 10^{-5}$ kg/m-s $\mu_v = 1.956 \times 10^{-5}$ kg/m-s $k_l = 7.466 \times 10^{-2}$ W/m-K $k_v = 3.222 \times 10^{-2}$ W/m-K Cp_l = 3.08 kJ/kg-K Cp_v = 3.81 kJ/kg-K Pr_l = 2.867 Pr_v = 2.313 h_{fg} = 106.75 kJ/kg $\sigma = 0.808 \times 10^{-3}$ N/m	REFPROP (Lemmon *et al.* 2002)

Dobson and Chato (1998) Model

Eq. No	Equation	Inputs	Outputs	Reference
(2)	$Ja_l = Cp_l \cdot \left[\frac{T_{ref} - T_w}{h_{fg}} \right]$	Cp_l = 3.08 kJ/kg-K T_{ref} = 59.71°C T_w = 36.5°C h_{fg} = 106.75 kW/kg	Ja_l = 0.6699	

(3)	$\alpha = \left(1 + \frac{1-x}{x}\left(\frac{\rho_v}{\rho_l}\right)^{2/3}\right)^{-1}$	x = 0.66 ρ_v = 197.4 kg/m^3 ρ_l = 820.4 kg/m^3	α = 0.8329	Zivi (1964)
(4)	$X_{tt} = \left[\frac{1-x}{x}\right]^{0.9} \cdot \left[\frac{\rho_v}{\rho_l}\right]^{0.5} \cdot \left[\frac{\mu_l}{\mu_v}\right]^{0.1}$	$\mu_l = 6.95 \times 10^{-5}$ kg/m-s $\mu_v = 1.956 \times 10^{-5}$ kg/m-s ρ_v = 197.4 kg/m^3 ρ_l = 820.4 kg/m^3 x = 0.66	X_{tt} = 0.3084	
(5)	$\mathrm{Re}_l = \frac{G \cdot (1-x) \cdot D}{\mu_l}$	x = 0.66 D = 9.4 mm G = 302 kg/m^2-s $\mu_l = 6.95 \times 10^{-5}$ kg/m-s	Re_l = 13965	
(6)	$\mathrm{Re}_{vo} = \frac{G \cdot D}{\mu_v}$	D = 9.4 mm G = 302 kg/m^2-s $\mu_v = 1.956 \times 10^{-5}$ kg/m-s	Re_l = 145253	
(7)	$Ga = \frac{D^3 \cdot \rho_l \cdot (\rho_l - \rho_v) \cdot g}{\mu_l^2}$	ρ_l = 820.4 kg/m^3 ρ_v = 197.4 kg/m^3 D = 9.4 mm $\mu_l = 6.95 \times 10^{-5}$ kg/m-s g = 9.807 m^2/s	Ga = 8.615×10^8	
(8)	$Fr_l = \frac{G^2}{\rho_l^2 \cdot g \cdot D}$	ρ_l = 820.4 kg/m^3 g = 9.807 m/s D = 9.4 mm G = 302 kg/m^2-s	Fr_l = 1.474	
(9)	$c_1 = 4.172 + 5.48 \cdot Fr_l - 1.564 \cdot Fr_l^2$ for $Fr_l \le 0.7$ $c_1 = 7.242$ for $Fr_l > 0.7$	Fr_l = 1.474	c_1 = 7.242	
(10)	$c_2 = 1.773 - 0.169 \cdot Fr_l$ for $Fr_l \le 0.7$ $c_2 = 1.655$ for $Fr_l > 0.7$	Fr_l = 1.474	c_2 = 1.655	
(11)	$\theta_l = \pi - \arccos(2 \cdot \alpha - 1)$	α = 0.8329	θ_l = 2.299	

(12)	$Fr_{so} = 0.025 \cdot \mathrm{Re}_l^{1.58} \cdot \left[\frac{1 + 1.09 \cdot X_{tt}^{0.039}}{X_{tt}} \right]^{1.5} \cdot \frac{1}{Ga^{0.5}}$ for, $Re_l \le 1250$ $Fr_{so} = 1.26 \cdot \mathrm{Re}_l^{1.04} \cdot \left[\frac{1 + 1.09 \cdot X_{tt}^{0.039}}{X_{tt}} \right]^{1.5} \cdot \frac{1}{Ga^{0.5}}$ for, $Re_l > 1250$	$\mathrm{Re}_l = 13965$ $Ga = 8.615 \times 10^8$ $X_{tt} = 0.3084$	$Fr_{so} = 14.95$	
(13)	$\phi_{L,X_{tt}} = \left[1.376 + \frac{c_1}{X_{tt}^{c2}} \right]^{0.5}$	$X_{tt} = 0.3084$ $c_1 = 7.242$ $c_2 = 1.655$	$\phi_{L,Xtt} = 7.219$	
(14)	$Nu_{forced} = 0.0195 \cdot \mathrm{Re}_l^{0.8} \cdot \mathrm{Pr}_l^{0.4} \, \phi_{L,X_{tt}}$	$\phi_{L,Xtt} = 7.219$ $\mathrm{Re}_l = 13965$ $\mathrm{Pr}_l = 2.867$	$Nu_{forced} = 444$	
(15)	IF $G \ge 500 kg/m^2 - s$ OR $Fr_{so} > 20$ $Nu = 0.023 \cdot \mathrm{Re}_l^{0.8} \cdot \mathrm{Pr}_l^{0.4} \cdot \left[1 + \frac{2.22}{X_{tt}^{0.58}} \right]$ IF $Fr_{so} < 20$ AND $G < 500 \ kg/m^2 - s$ $Nu = 0.23 \left[\frac{\mathrm{Re}_{vo}^{0.12}}{1 + 1.11 \cdot X_{tt}^{0.58}} \right] \cdot \left[\frac{Ga \cdot \mathrm{Pr}_l}{Ja_l} \right]^{0.25} + \left[1 - \frac{\theta_l}{\pi} \right] \cdot Nu_{forced}$	$Fr_{so} = 14.95$ $\mathrm{Pr}_l = 2.867$ $G = 302$ kg/m^2-s $Ga = 8.615 \times 10^8$ $Ja_l = 0.6699$ $Nu_{forced} = 444$ $\mathrm{Re}_l = 13965$ $\mathrm{Re}_{vo} = 145253$ $X_{tt} = 0.3084$ $\theta_l = 2.299$ (Wavy Model Applies)	$Nu = 270.2$	
(16)	$h_{Dobson} = \frac{Nu \cdot k_l}{D}$	$Nu = 270.3$ $k_l = 0.07466$ W/m-K $D = 9.4$ mm	$h_{Dobson} = 2147$ W/m^2-K	
(17)	$Deviation = \frac{\left\| \left(h_{Dobson} - h_{Experimental} \right) \right\|}{h_{Experimental}} \times 100$	$h_{Dobson} = 2147$ W/m^2-K $h_{Experimental} = 3079$ W/m^2-K	Deviation = 30.27% (under-prediction)	

Cavallini (2002 a,b) Heat Transfer Coefficient Model

Eq. No	Equation	Inputs	Outputs	Reference
(18)	$J_G = \frac{x \cdot G}{\left(gD_{i,i}\rho_v(\rho_l - \rho_v)\right)^{0.5}}$	G = 302 kg/m^2-s x = 0.66 $d_{i,i}$ = 9.4 mm ρ_l = 820 kg/m^3 ρ_v = 197.4 kg/m^3 g = 9.81 m/s^2	J_G = 1.87	
(19)	$X_{tt} = \left(\frac{1-x}{x}\right)^{0.9}\left(\frac{\rho_v}{\rho_l}\right)^{0.5}\left(\frac{\mu_l}{\mu_v}\right)^{0.1}$	ρ_l = 820.4 kg/m^3 ρ_v = 197.4 kg/m^3 $\mu_l = 6.95\times10^{-5}$ kg/m-s $\mu_v = 1.956\times10^{-5}$ kg/m-s x = 0.66	X_{tt} = 0.3084	
(20)	If $J_G \geq 2.5$ and $X_{tt} < 1.6$, annular model If $J_G < 2.5$ and $X_{tt} < 1.6$, stratified model If $J_G < 2.5$ and $X_{tt} > 1.6$, slug model	J_G = 1.87 X_{tt} = 0.3084	Stratified Model will be applied for this data point	
(21)	$h_{LO} = 0.023\,\mathrm{Re}_{LO}^{0.8}\,\mathrm{Pr}_l^{0.4}\,k_l / d_{i,i}$ $= 0.023[Gd_{i,i}/\mu_l]^{0.8}(c_{p,l}\mu_l/k_l)^{0.4}k_l/d_{i,i}$	$k_l = 7.466\times10^{-2}$ W/m-K $c_{p,l}$ = 3.08 kJ/kg-K Pr_l = 2.867 $d_{i,i}$ = 9.4 mm Re_{LO} = 40,887 $\mu_l = 6.95\times10^{-5}$ kg/m-s G = 302 kg/m^2-s	h_{LO} = 1362 W/m^2-K	
(22)	$h_L = h_{LO}(1-x)^{0.8}$	h_{LO} = 1362 W/m^2-K x = 0.66	h_L = 576.5 W/m^2-K	

(23)	$\alpha = \left(1 + \frac{1-x}{x}\left(\frac{\rho_v}{\rho_l}\right)^{2/3}\right)^{-1}$	ρ_l = 820.4 kg/m^3 ρ_v = 197.4 kg/m^3 x = 0.66	α = 0.8329	Zivi (1964)
(24)	$\left(1-\frac{\theta_L}{\pi}\right) \cong \frac{\arccos(2\alpha\text{-}1)}{\pi}$ $h_{strat} = 0.725\{1+0.82[(1-x)/x]^{0.268}\}^{-1}$ $[k_l^3 \rho_l(\rho_l-\rho_G)g h_{fg}/(\mu_l d_{i,i}\Delta T)]^{0.25} + h_L(1-\theta_L/\pi)$	α = 0.8329 h_{fg} = 106.75 kJ/kg ρ_l = 820.4 kg/m^3 ρ_v = 197.4 kg/m^3 x = 0.66 μ_l = 6.95×10^{-5} kg/m-s h_L = 576.5 W/m^2-K ΔT = 23.2°C k_l = 7.466×10^{-2} W/m-K $d_{i,i}$ = 9.4 mm	h_{strat} = 996.1 W/m^2-K	
(25)	$h_{trans} = (h_{an,J_G=2.5} - h_{strat})(J_G/2.5) + h_{strat}$	h_{strat} = 996.1 W/m^2-K J_G = 1.87 $h_{an,J_G=2.5}$ = 2729 W/m^2-K	h_{trans} = 2293 W/m^2-K	$h_{an,J_G=2.5}$ is calculated using eq (26) to (39)
(26)	$G_{J_G=2.5} = \frac{J_G \cdot \left(9.8 D_{i,i}\rho_v(\rho_l-\rho_v)\right)^{0.5}}{x}$	x = 0.66 J_G = 2.5 $d_{i,i}$ = 9.4 mm ρ_l = 820.4 kg/m^3 ρ_v = 197.4 kg/m^3	$G_{J_G=2.5}$=404.2 kg/m^2-s	
(27)	$\mathrm{Re}_l = \frac{G(1-x)d_{i,i}}{\mu_l}$	$G_{J_G=2.5}$ = 404.2 kg/m^2-s $d_{i,i}$ = 9.4 mm μ_l = 6.95 × 10^{-5} kg/m-s x = 0.66	Re_l = 18,670	

(28)	$\delta^+ = \left(\frac{\mathrm{Re}_L}{2}\right)^{0.5}$ For Re_L<=1145 $\delta^+ = 0.0504 \cdot \mathrm{Re}_L^{7/8}$ For Re_L>1145	Re_L = 18,670	δ^+ = 275.2	
(29)	$T^+ = \delta^+ \cdot \mathrm{Pr}_l$ For $\delta^+ \le 5$ $T^+ = 5 \cdot \left[\mathrm{Pr}_l + \ln\left(1 + \mathrm{Pr}_l\left[\frac{\delta^+}{5} - 1\right]\right)\right]$ For $5 < \delta^+ < 30$ $T^+ = 5 \cdot \left[\mathrm{Pr}_l + \ln(1 + 5 \cdot \mathrm{Pr}_l) + 0.495 \cdot \ln\left(\frac{\delta^+}{30}\right)\right]$ For $\delta^+ \ge 30$	δ^+ = 275.2 Pr_l = 2.867	T^+ = 33.47	
	$\mathrm{Re}_{vo} = \frac{G \cdot D}{\mu_v}$	D = 9.4 mm G = 404.2 kg/m^2-s $\mu_v = 1.956 \times 10^{-5}$ kg/m-s	Re_l = 194,185	
(30)	$f_{LO} = 0.046 \cdot \left[\frac{G \cdot D}{\mu_L}\right]^{-0.2}$ Re_{vo} > 2000 $f_{LO} = 16 \Big/ \frac{G \cdot D}{\mu_L}$ $\mathrm{Re}_{vo} \le 2000$	G = 404.2 kg/m^2-s D = 9.4 mm $\mu_l = 6.95 \times 10^{-5}$ kg/m-s Re_{vo} = 194,185	f_{LO} = 0.005191	
(31)	$f_{GO} = 0.046 \cdot [G \cdot D/\mu_G]^{-0.2}$ Re_{vo} > 2000 $f_{GO} = 16 \Big/ \left[\frac{G \cdot D}{\mu_g}\right]$ $\mathrm{Re}_{vo} \le 2000$	G = 404.2 kg/m^2-s D = 9.4 mm $\mu_g = 1.956 \times 10^{-5}$ kg/m-s Re_{vo} = 194,185	f_{GO} = 0.004028	

(32)	$We = \frac{G^2 \cdot D}{\rho_v \cdot \sigma}$	G = 404.2 kg/m^2-s D = 9.4 mm ρ_v = 197.4 kg/m^3 $\sigma = 0.808 \times 10^{-3}$ N/m	We = 9626	
(33)	$H = \left[\frac{\rho_l}{\rho_v}\right]^{0.3278} \cdot \left[\frac{\mu_v}{\mu_l}\right]^{-1.181} \cdot \left[1 - \frac{\mu_v}{\mu_l}\right]^{3.477}$	$\mu_v = 1.956 \times 10^{-5}$ kg/m-s $\mu_l = 6.95 \times 10^{-5}$ kg/m-s ρ_l = 820.4 kg/m^3 ρ_v = 197.4 kg/m^3	H = 2.259	
(34)	$F = x^{0.6978}$	x = 0.66	F = 0.7471	
(35)	$E = (1-x)^2 + x^2 \cdot \frac{(\rho_L \cdot f_{GO})}{(\rho_G \cdot f_{LO})}$	f_{GO} = 0.004028 f_{LO} = 0.005191 ρ_L = 820.4 kg/m^3 ρ_G = 197.4 kg/m^3	E = 1.515	
(36)	$\phi_{lo} = \left[E + \frac{1.262 \cdot F \cdot H}{We^{0.1458}}\right]^{0.5}$	F = 0.7471 H = 2.259 E = 1.515 We = 9626	ϕ_{lo} = 1.44	
(37)	$\left(\frac{dp}{dz}\right)_f = \frac{\phi_{LO}^2 \cdot 2 \cdot f_{LO} \cdot G^2}{D \cdot \rho_L}$	ϕ_{lo} = 1.44 f_{LO} = 0.005191 G = 404.2 kg/m^2-s D = 9.4 mm ρ_l = 820.4 kg/m^3	$\left(\frac{dp}{dz}\right)_f$ = 456.4 Pa/m	
(38)	$\tau = \left(\frac{dp}{dz}\right)_f \cdot \frac{D}{4}$	$\left(\frac{dp}{dz}\right)_f$ = 456.4 Pa/m D = 9.4 mm	τ = 1.072 Pa	
(39)	$h_{an,J_G=2.5} = \frac{\rho_l \cdot Cp_l \cdot \left[\frac{\tau}{\rho_l}\right]^{0.5}}{T^+}$	τ = 1.072 Pa ρ_l = 820.4 kg/m^3 Cp_l = 3.08 kJ/kg-K T^+ = 33.47	$h_{an,J_G=2.5}$ = 2729 W/m^2-K	

(40)	$Deviation = \frac{\left\lvert \left(h_{Cavallini} - h_{Experimental} \right) \right\rvert}{h_{Experimental}} \times 100$	$h_{Cavallini} = h_{trans} = 2293$ W/m^2-K $h_{Experimental} = 3079$ W/m^2-K	Deviation = 25.53% (under-prediction)	

Cavallini (2002 a,b) Pressure Drop Model

Eq. No	Equation	Inputs	Outputs	Reference
(41)	$J_G = \frac{x \cdot G}{\left(9.8 D_{i,i} \rho_v (\rho_l - \rho_v)\right)^{0.5}}$	G = 302 kg/m^2-s x = 0.66 $d_{i,i}$ = 9.4 mm ρ_l = 820.4 kg/m^3 ρ_v = 197.4 kg/m^3	J_G = 1.87	
(42)	If $J_G \geq 2.5$ Cavallini Friction factor model (equation 26 to 37 above) If $J_G < 2.5$ Friedel (1979) pressure drop model	J_G = 1.87	Friedel (1979) pressure drop model will be used	
(43)	$\mathrm{Re}_{vo} = \frac{G \cdot D}{\mu_v}$	D = 9.4 mm G = 302 kg/m^2-s $\mu_v = 1.956 \times 10^{-5}$ kg/m-s	Re_{vo} = 145253	
(44)	$f_{LO} = 0.046 \cdot \left[\frac{G \cdot D}{\mu_L} \right]^{-0.2}$ $\mathrm{Re}_{vo} > 2000$ $f_{LO} = 16 \Big/ \frac{G \cdot D}{\mu_L}$ $\mathrm{Re}_{vo} \leq 2000$	G = 302 kg/m^2-s D = 9.4 mm $\mu_l = 6.95 \times 10^{-5}$ kg/m-s Re_{vo} = 145253	f_{LO} = 0.005501	
(45)	$f_{GO} = 0.046 \cdot \left[G \cdot D / \mu_G \right]^{-0.2}$ $\mathrm{Re}_{vo} > 2000$ $f_{GO} = 16 \Big/ \left[\frac{G \cdot D}{\mu_g} \right]$ $\mathrm{Re}_{vo} \leq 2000$	G = 302 kg/m^2-s D = 9.4 mm $\mu_g = 1.956 \times 10^{-5}$ kg/m-s Re_{vo} = 145253	f_{GO} = 0.004269	

(46)	$E = (1-x)^2 + x^2 \frac{\rho_l f_{GO}}{\rho_v f_{LO}}$	$f_{GO} = 0.004269$ $f_{LO} = 0.005501$ $\rho_L = 820.4$ kg/m^3 $\rho_G = 197.4$ kg/m^3 x = 0.66	E = 1.515	
(47)	$F = x^{0.78}(1-x)^{0.24}$	x = 0.66	F = 0.5578	
(48)	$H = \left(\frac{\rho_l}{\rho_v}\right)^{0.91} \left(\frac{\mu_v}{\mu_l}\right)^{0.19} \left(1 - \frac{\mu_v}{\mu_l}\right)^{0.7}$	$\mu_v = 1.956 \times 10^{-5}$ kg/m-s $\mu_l = 6.95 \times 10^{-5}$ kg/m-s $\rho_l = 820.4$ kg/m^3 $\rho_v = 197.4$ kg/m^3	H = 2.26	
(49)	$\rho_{tp} = \left(\frac{x}{\rho_v} + \frac{1-x}{\rho_l}\right)^{-1}$	x = 0.66 $\rho_l = 820.4$ kg/m^3 $\rho_v = 197.4$ kg/m^3	$\rho_{tp} = 266.5$ kg/m^3	
(50)	$Fr = \frac{G^2}{gd\rho_{tp}^2}$	G = 302 kg/m^2-s d = 9.4 mm $\rho_{tp} = 266.5$ kg/m^3 g = 9.81 m/s^2	Fr = 13.97	
(51)	$We = \frac{G^2 d}{\rho_{tp}\sigma}$	G = 302 kg/m^2-s d = 9.4 mm $\rho_{tp} = 266.5$ kg/m^3 $\sigma = 0.808 \times 10^{-3}$ N/m	We = 3969	
(52)	$\Phi_{LO}^2 = E + \frac{3.24F \cdot H}{Fr^{0.045} We^{0.035}}$	F = 0.5578 H = 2.26 E = 1.515 We = 3969	$\phi_{lo} = 2.062$	
(53)	$(dP/dz)_f = \Phi_{LO}^2 \cdot 2f_{Lo} \frac{G^2}{d\rho_l}$	$\phi_{lo} = 2.062$ $f_{LO} = 0.005501$ G = 302 kg/m^2-s D = 9.4 mm $\rho_l = 820.4$ kg/m^3	$\left(\frac{dp}{dz}\right)_f = 554.9$ Pa/m	

Acceleration/Deceleration Term

Eq. No	Equation	Inputs	Outputs	Reference
(54)	Equation (41) to (53) are evaluated with test section inlet quality, temperature and G to calculate $(dP/dz)_{f,in}$	$x_{in} = 0.75$ $T_{in} = 59.75°C$ $G = 302$	$(dP/dz)_{f,in} =$ 603.2 Pa/m $\delta^+_i = 161.6$	
(55)	Equation (41) to (53) are evaluated with test section outlet quality, temperature and G to calculate $(dP/dz)_{f,in}$	$x_{out} = 0.56$ $T_{in} = 59.64°C$ $G = 302$	$(dP/dz)_{f,out} =$ 494.2 Pa/m $\delta^+_o = 265.7$	
(56)	$\tau_{in} = (dP/dz)_{f,in} \frac{d}{4}$	$(dp/dz)_{f,in} = 603.2$ Pa/m $d = 9.4$ mm	$\tau_{in} = 1.418$ Pa	
(57)	$u_{\tau,in} = (\tau_{in}/\rho_{l,in})^{0.5}$	$\tau_{in} = 1.418$ Pa $\rho_{l,in} = 817.6$ kg/m^3	$u_{\tau,in} = 0.04165$ m/s	
(58)	$\delta_{in} = \delta^+_{in} \frac{\mu_{l,in}}{\rho_{l,in} u_{\tau,in}}$	$u_{\tau,in} = 0.04165$ m/s $\rho_{l,in} = 817.6$ kg/m^3 $\mu_{l,in} = 6.909\times10^{-5}$ kg/m-s $\delta^+_i = 161.6$	$\delta_{in} = 3.279\times10^{-4}$ m	
(59)	$\varepsilon_{in} = [1 - 2\delta_{in}/d]^2$	$\delta_{in} = 3.279\times10^{-4}$ m $d = 9.4$ mm	$\varepsilon_{in} = 0.8653$	
(60)	Equation 46 to 49 are evaluated with outlet quality, temperature and G	$x_{out} = 0.56$ $T_{in} = 59.75°C$ $G = 302$	$\tau_{out} = 1.161$ Pa $u_{\tau,out} = 0.0377$ m/s $\delta_{out} = 5.959\times10^{-4}$ m $\varepsilon_{out} = 0.76$	

(61)	$(dp/dz)_a = G^2\left(\frac{\left[\frac{x^2}{\rho_v\varepsilon}+\frac{(1-x)^2}{\rho_l(1-\varepsilon)}\right]_{out}-\left[\frac{x^2}{\rho_v\varepsilon}+\frac{(1-x)^2}{\rho_l(1-\varepsilon)}\right]_{in}}{L_{test}}\right)$	$\varepsilon_{in} = 0.8653$ $\varepsilon_{out} = 0.76$ $x_{in} = 0.75$ $x_{out} = 0.56$ $L_{test} = 0.292$ m $\rho_{l,in} = 817.6$ kg/m^3 $\rho_{v,in} = 199.4$ kg/m^3 $\rho_{l,out} = 817.7$ kg/m^3 $\rho_{v,out} = 199.3$ kg/m^3	$(dP/dz)_a = -240.8$ Pa/m	
(62)	$(dp/dz)_{cavallini} = (dp/dz)_f + (dp/dz)_a$	$(dp/dz)_f = 554.9$ Pa/m $(dP/dz)_a = -240.8$ Pa/m	$dp/dz_{Cavallini} = 314.1$ Pa/m	
(63)	$Deviation = \frac{\left\lvert\left((dp/dz)_{cavallini} - (dp/dz)_{experiment}\right)\right\rvert}{(dp/dz)_{experiment}} \times 100$	$dp/dz_{Cavallini} = 314.1$ Pa/m $dp/dz_{Experiment} = 683.6$ Pa/m	Deviation = 54.05% (under-prediction)	

El. Hajal *et al.* (2003) and Thome *et al.* (2003) Heat Transfer Coefficient Model

Eq. No	*Equation*	*Inputs*	*Outputs*	*Reference*
(64)	$\alpha_h = \left[1+\frac{1-x}{x}\left(\frac{\rho_v}{\rho_l}\right)\right]^{-1}$	$\rho_l = 820.4$ kg/m^3 $\rho_v = 197.4$ kg/m^3 $x = 0.66$	$\alpha_h = 0.8891$	Homogeneous void fraction model
(65)	$\alpha_{ra} = \frac{x}{\rho_v}\left(\left[1+0.12(1-x)\right]\left[\frac{x}{\rho_v}+\frac{1-x}{\rho_l}\right]+\frac{1.18(1-x)\left[g\cdot\sigma(\rho_l-\rho_v)\right]^{0.25}}{G\cdot\rho_l^{0.5}}\right)^{-1}$	$\rho_l = 820.4$ kg/m^3 $\rho_v = 197.4$ kg/m^3 $x = 0.66$ $G = 302$ kg/m^2-s $g = 9.81$ m/s^2 $\sigma = 0.808\times10^{-3}$ N/m	$\alpha_{ra} = 0.8391$	Modified Rouhani-Axelsson void fraction model from Steiner (1993)

(66)	$\alpha = \frac{\alpha_h - \alpha_{ra}}{\ln\left(\frac{\alpha_h}{\alpha_{ra}}\right)}$	$\alpha_h = 0.8891$ $\alpha_{ra} = 0.8391$	$\alpha = 0.8639$	
(67)	$A = \pi\left(D^2/4\right)$	$D = 9.4$ mm	$A = 6.937\times10^{-5}$ m^2	
(68)	$A_L = A\left(1-\alpha\right)$	$A = 6.937\times10^{-5}$ m^2 $\alpha = 0.8639$	$A_L = 9.444\times10^{-6}$ m^2	
(69)	$A_V = A\alpha$	$\alpha = 0.8639$ $A = 6.937\times10^{-5}$ m^2	$A_V = 5.992\times10^{-5}$ m^2	
(70)	$A_{Ld} = \left(A_L/D^2\right)$	$A_L = 9.444\times10^{-6}$ m^2 $D = 9.4$ mm	$A_{Ld} = 0.1069$ m^2	
(71)	$A_{vd} = \left(A_v/D^2\right)$	$A_V = 5.992\times10^{-5}$ m^2 $D = 9.4$ mm	$A_{Vd} = 0.6785$ m^2	
(72)	$A_{Ld} = \frac{1}{8}\left[\left(2\pi-\theta_{strat}\right)-\sin\left(2\pi-\theta_{strat}\right)\right]$	$A_{Ld} = 0.1069$ m^2	$\theta_{strat} = 4.46$ rad	Obtained iteratively
(73)	$h_{Ld} = 0.5\left(1-\cos\left(\frac{2\pi-\theta_{strat}}{2}\right)\right)$	$\theta_{strat} = 4.46$ rad	$h_{Ld} = 0.1938$	
(74)	$P_{id} = \sin\left(\frac{2\pi-\theta_{strat}}{2}\right)$	$\theta_{strat} = 4.46$ rad	$P_{id} = 0.7906$	
(75)	$\left(\frac{We}{Fr}\right)_L = \frac{gD^2\rho_l}{\sigma}$	$\rho_l = 820.4$ kg/m^3 $\sigma = 0.808\times10^{-3}$ N/m $D = 9.4$ mm $g = 9.81$ m/s^2	$\left(\frac{We}{Fr}\right)_L = 879.3$	
(76)	$\xi = \left[1.138 + 2\log\left(\frac{\pi}{1.5A_{Ld}}\right)\right]^{-2}$	$A_{Ld} = 0.1069$ m^2	$\xi = 0.0722$	

(77)	$G_{wavy} = \left\{ \frac{16A_{Vd}^3 g D \rho_l \rho_v}{x^2 \pi^2 \left(1-\left(2h_{Ld}-1\right)^2\right)^{0.5}} \left[\frac{\pi^2}{25 h_{Ld}^2} \left(\frac{We}{Fr} \right)_L^{-1.023} + 1 \right] \right\}^{0.5} + 50 - 75 e^{-\left(x^2-0.97\right)^2 / x(1-x)}$	$\left(\frac{We}{Fr} \right)_L = 879.3$ $\rho_l = 820.4$ kg/m^3 $\rho_v = 197.4$ kg/m^3 x = 0.66 D = 9.4 mm $h_{Ld} = 0.1938$ $A_{Vd} = 0.6785$ m^2 g = 9.81 m/s^2	$G_{wavy} = 178.4$ kg/m^2-s	
(78)	$G_{strat} = \left\{ \frac{\left(226.3\right)^2 A_{Ld} A_{Vd}^2 \rho_v \left(\rho_l - \rho_v\right) \mu_l g}{x^2 \left(1-x\right) \pi^3} \right\}^{1/3} + 20x$	$\rho_l = 820.4$ kg/m^3 $\rho_v = 197.4$ kg/m^3 x = 0.66 $\mu_l = 6.95 \times 10^{-5}$ kg/m-s g = 9.81 m/s^2 $A_{Ld} = 0.1069$ m^2 $A_{Vd} = 0.6785$ m^2	$G_{strat} = 49$ kg/m^2-s	
(79)	$x_{1A} = \left\{ \left[0.2914 \left(\frac{\rho_v}{\rho_l} \right)^{-1/1.75} \left(\frac{\mu_l}{\mu_v} \right)^{-1/7} \right] + 1 \right\}^{-1}$	$\rho_l = 820.4$ kg/m^3 $\rho_v = 197.4$ kg/m^3 $\mu_l = 6.95 \times 10^{-5}$ kg/m-s $\mu_v = 1.956 \times 10^{-5}$ kg/m-s	$x_{1A} = 0.6465$	
(80)	$G_{mist} = \left\{ \frac{7680 A_{Vd}^2 g D \rho_l \rho_v}{x^2 \pi^2 \xi} \left(\frac{Fr}{We} \right)_L \right\}^{0.5}$	$\left(\frac{Fr}{We} \right)_L = 1.137 \times 10^{-3}$ $\rho_l = 820.4$ kg/m^3 $\rho_v = 197.4$ kg/m^3 D = 9.4 mm x = 0.66 $\xi = 0.0722$ $A_{Vd} = 0.6785$ m^2 g = 9.81 m-s^2	$G_{mist} = 440.8$ kg/m^2-s	
(81)	$G_{bubbly} = \left\{ \frac{256 A_{Vd} A_{Ld}^2 D^{1.25} \rho_l \left(\rho_l - \rho_v\right) g}{0.3164 \left(1-x\right)^{1.75} \pi^2 P_{id} \mu_l^{0.25}} \right\}^{\frac{1}{1.75}}$	$\rho_l = 820.4$ kg/m^3 $\rho_v = 197.4$ kg/m^3 $\mu_l = 6.95 \times 10^{-5}$ kg/m-s D = 9.4 mm x = 0.66	$G_{bubly} = 2440$ kg/m^2-s	

		$A_{Ld} = 0.1069\ m^2$ $A_{Vd} = 0.6785\ m^2$ $P_{id} = 0.7906$		
(82)	IF $G > G_{wavy,}$ $G < G_{mist}$ & $x > x_{1A}$ Flow regime : Annular flow IF $G > G_{wavy}$, $G < G_{mist}$ or $G < G_{bubbly}$ & $x < x_{1A}$ Flow regime : Intermittent flow IF $G_{strat} < G < G_{wavy}$ Flow regime : Stratified Flow IF $G < G_{strat}$ Flow regime : Fully stratified IF $G > G_{mist}$ Flow regime : Mist Flow	$G = 302\ kg/m^2\text{-}s$ $G_{wavy} = 178.4\ kg/m^2\text{-}s$ $G_{strat} = 49\ kg/m^2\text{-}s$ $G_{mist} = 440.8\ kg/m^2\text{-}s$ $G_{bubly} = 2440\ kg/m^2\text{-}s$ $x = 0.66$ $x_{1A} = 0.6465$	Flow regime = Annular flow	
(83)	$A_L = \frac{(2\pi-\theta)}{8}\left[D^2-(D-2\delta)^2\right]$	$A_L = 9.444\times10^{-6}\ m^2$ $D = 9.4\ mm$ $\theta = 0\ rad$	$\delta = 0.3316\ mm$	Obtained iteratively ($\theta = 0$ rad) Assumption for Annular flow model
(84)	$Re_l = \frac{4G(1-x)\delta}{(1-\alpha)\mu_l}$	$\delta = 0.3316\ mm$ $G = 302\ kg/m^2\text{-}s$ $\mu_l = 6.95\times10^{-5}\ kg/m\text{-}s$ $x = 0.66$ $\alpha = 0.8639$	$Re_l = 14{,}476$	
(85)	$u_L = \frac{G(1-x)}{\rho_l(1-\alpha)}$	$G = 302\ kg/m^2\text{-}s$ $x = 0.66$ $\rho_l = 820.4\ kg/m^3$ $\alpha = 0.8639$	$u_L = 0.92\ m/s$	

(86)	$u_V = \frac{Gx}{\rho_v \alpha}$	G = 302 kg/m^2-s x = 0.66 ρ_v = 197.4 kg/m^3 α = 0.8639	u_v = 1.17 m/s	
(87)	$f_i = 1 + \left(\frac{u_V}{u_L}\right)^{1/2} \left(\frac{(\rho_l - \rho_v) g \delta^2}{\sigma}\right)^{1/4}$	u_L = 0.92 m/s u_v = 1.17 m/s ρ_l = 820.4 kg/m^3 ρ_v = 197.4 kg/m^3 δ = 0.3316 mm σ = 0.808×10^{-3} N/m g = 9.81 m/s^2	f_i = 2.073	
(88)	$h_{Thome} = 0.003 Re_l^{0.74} Pr_l^{0.5} \frac{k_l}{\delta} f_i$	f_i = 2.073 k_l = 7.466×10^{-2} W/m-K Re_l = 14,476 Pr_l = 2.867 δ = 0.3316 mm	h_{Thome} = 2843 W/m^2-K	
(89)	$Deviation = \frac{\left\lvert \left(h_{Thome} - h_{Experimental}\right) \right\rvert}{h_{Experimental}} \times 100$	h_{Thome} = 2843 W/m^2-K $h_{Experimental}$ = 3079 W/m^2-K	Deviation = 7.66% (under-prediction)	

APPENDIX E COMPARISON WITH SUPERCRITICAL LITERATURE

(Representative Data Point: G = 400.3, P_r = 1.0, T_{test} = 62.1°C, $h_{expt.}$ = 1968 W/m^2-K, $(dP/dz)_f$ = 0.456 kPa/m)

Refrigerant Properties

Eq. No	Equation	Inputs	Outputs	Reference
(2)	$\rho_{bulk}, \mu_{bulk}, c_{p,bulk}, k_{bulk}, \mathrm{Pr}_{bulk}, h_{bulk} = f(T_{test}, P_{test})$	T_{test} = 62.1°C P_{test} = 4937 kPa	ρ_{bulk} = 845.7 m^3/s, μ_{bulk} = 7.28×10^{-5} kg/m-s Cp_{bulk} = 2.49 kJ/kg-K k_{bulk} = 0.0756 W/m-K Pr_{bulk} = 2.402 h_{bulk} = 309.1 kJ/kg	
(3)	$\rho_{wall}, \mu_{wall}, c_{p,wall}, k_{wall}, \mathrm{Pr}_{wall}, h_{wall} = f(T_{wall}, P_{test})$	T_{wall} = 43.8°C P_{test} = 4937 kPa	ρ_{wall} = 989.9 m^3/s μ_{wall} = 1.008×10^{-4} kg/m-s $C_{p,wall}$ = 1.81 kJ/kg-K k_{wall} = 0.0874 W/m-K Pr_{wall} = 2.088 h_{wall} = 271.5 kJ/kg	

Gnielinski (1976) Heat Transfer Coefficient Model

Eq. No	Equation	Inputs	Outputs	Reference
(3)	$V = G / \rho_{bulk}$	G = 400.3 kg/m^2-s ρ_{bulk} = 845.7 m^3/s,	V = 0.4733 m/s	

(4)	$\mathrm{Re}_D = \frac{\rho_{bulk} \cdot d \cdot V}{\mu_{bulk}}$	ρ_{bulk} = 845.7 kg/m^3 μ_{bulk} = 7.28×10^{-5} kg/m-s V = 0.4733 m/s d = 9.4 mm	Re_D = 51,667	
(5)	$f = (0.790\ln(\mathrm{Re}_D) - 1.64)^{-2}$	Re_D = 51,667	f = 2.08×10^{-2}	Incropera and Dewitt (2002)
(6)	$Nu_D = \frac{(f/8)(\mathrm{Re}_D - 1000)\,\mathrm{Pr}_{bulk}}{1 + 12.7(f/8)^{1/2}(\mathrm{Pr}_{bulk}^{2/3} - 1)}$	Pr_{bulk} = 2.402 Re_D = 51,667 f = 2.08×10^{-2}	Nu_D = 209	Gnielinski (1976)
(7)	$h_{Gnielinski} = \frac{Nu \cdot k_{bulk}}{d}$	k_{bulk} = 0.0756 W/m-K Nu_D = 209 d = 9.4 mm	$h_{Gnielinski}$ = 1681 W/m^2-K	
(8)	$Deviation = \frac{\left\lvert \left(h_{Gnielinski} - h_{Experimental} \right) \right\rvert}{h_{Experimental}} \times 100$	$h_{Gnielinski}$ = 1681 W/m^2-K $h_{Experimental}$ = 1968 W/m^2-K	Deviation = 14.58% (under-prediction)	

Krasnoshchekov *et al.* (1970) Heat Transfer Coefficient Model

Eq. No	Equation	Inputs	Outputs	Reference
(9)	$V = G / \rho_{wall}$	G = 400.3 kg/m^2-s, ρ_{wall} = 989.9 kg/m^3	V_{wall} = 0.4044 m/s	
(10)	$\mathrm{Re}_{wall} = \frac{\rho_{wall} \cdot d \cdot V_{wall}}{\mu_{wall}}$	ρ_{wall} = 989.9 kg/m^3, μ_{wall} = 1.008×10^{-4} kg/m-s d = 9.4 mm V_{wall} = 0.4044 m/s	Re_{wall} = 37,328	
(11)	$c_{p,bar} = \frac{(h_{bulk} - h_{wall})}{(T_{test,avg} - T_{wall,avg})}$	$T_{test,avg}$ = 62.1°C $T_{wall,avg}$ = 43.8°C h_{bulk} = 309.1 kJ/kg h_{wall} = 271.5 kJ/kg	$C_{p,bar}$ = 2.053 kJ/kg-K	
(12)	$f = (0.790 \ln(\mathrm{Re}_{wall}) - 1.64)^{-2}$	Re_{wall} = 37,328	f = 0.0224	Incropera and Dewitt (2002)
(13)	$m = B\left(\frac{c_{p,bar}}{c_{p,wall}}\right)^{k}$	$C_{p,wall}$ = 1.81 kJ/kg-K $C_{p,bar}$ = 2.053 kW/kg-K B = 0.6 k = 0.4	m = 0.631	B, k from Pitla *et al.* (1998): Figure 6
(14)	$Nu_D = \frac{(f/8)\mathrm{Re}_{wall}\,\mathrm{Pr}_{wall}}{1.07 + 12.7(f/8)^{1/2}(\mathrm{Pr}_{wall}^{2/3} - 1)}$	f = 0.0224 Re_{wall} = 37,328 Pr_{wall} = 2.088	Nu = 145.9	

(15)	$Nu = Nu_D \left(\frac{\rho_{wall}}{\rho_{bulk}} \right)^n \left(\frac{c_{p,bar}}{c_{p,wall}} \right)^m$	ρ_{wall} = 989.9 kg/m^3 ρ_{bulk} = 845.7 kg/m^3 $c_{p,wall}$ = 1.81 kJ/kg-K $C_{p,bar}$ = 2.053 kW/kg-K n = 0.2 m = 0.631 Nu_D = 145.9	Nu = 163	n from Pitla *et al.* (1998): Figure 6
(16)	$h_{Krasnoshchekov} = \frac{Nu \cdot k_{bulk}}{d}$	k_{bulk} = 0.0756 W/m-K d = 9.4 mm Nu = 163	$h_{Krasnoshchekov}$ = 1311 W/m^2-K	
(17)	$Deviation = \frac{\left\lvert \left(h_{Krasnoshchekov} - h_{Experimental} \right) \right\rvert}{h_{Experimental}} \times 100$	$h_{Krasnoshchekov}$ = 1311 W/m^2-K $h_{Experimental}$ = 1968 W/m^2-K	Deviation = 33.38% (under-prediction)	

Pitla *et al.* (2002) Heat Transfer Coefficient Model

Eq. No	Equation	Inputs	Outputs	Reference
(18)	***Find Nusselt Number at wall temperature*** Use velocity at test section inlet to compute the Reynolds number regardless of the actual location.			
(19)	$V_{in} = G / \rho_{in}$	G = 400.3 kg/m^2-s ρ_{in} = 823 kg/m^3	V = 0.4864 m/s	
(20)	$\mathrm{Re}_{D,wall} = \frac{\rho_{wall} \cdot d \cdot V_{in}}{\mu_{wall}}$	ρ_{wall} = 989.9 kg/m^3 μ_{wall} = 1.008×10^{-4} kg/m-s d = 9.4 mm	$\mathrm{Re}_{D,wall}$ = 44,895	
(21)	$f_{wall} = (0.790 \ln(\mathrm{Re}_{D,wall}) - 1.64)^{-2}$	$\mathrm{Re}_{D,wall}$ = 44,895	f_{wall} = 2.146×10^{-2}	Incropera and Dewitt (2002)

(22)	$Nu_{D,wall} = \frac{(f_{wall}/8)(\mathrm{Re}_{D,wall} - 1000)\,\mathrm{Pr}_{wall}}{1 + 12.7(f_{wall}/8)^{1/2}(\mathrm{Pr}_{wall}^{2/3} - 1)}$	Pr_{wall} = 2.088 f_{wall} = 2.146×10^{-2} $Re_{D,wall}$ = 44,895	$Nu_{D,wall}$ = 173.5	Gnielinski (1976)
(23)	$V_{bulk} = G / \rho_{bulk}$	G = 400.3 kg/m^2-s ρ_{bulk} = 845.7 kg/m^3	V = 0.4733 m/s	
(24)	$\mathrm{Re}_{D,bulk} = \frac{\rho_{bulk} \cdot d \cdot V_{bulk}}{\mu_{bulk}}$	ρ_{bulk} = 845.7 kg/m^3 μ_{bulk} = 7.281×10^{-5} kg/m-s d = 9.4 mm V = 0.4733 m/s	Re_D = 51,667	
(25)	$f_{bulk} = (0.790 \ln(\mathrm{Re}_{D,bulk}) - 1.64)^{-2}$	$Re_{D,bulk}$ = 51,667	f = 2.08×10^{-2}	
(26)	$Nu_{D,bulk} = \frac{(f_{bulk}/8)(\mathrm{Re}_{D,bulk} - 1000)\,\mathrm{Pr}_{bulk}}{1 + 12.7(f_{bulk}/8)^{1/2}(\mathrm{Pr}_{bulk}^{2/3} - 1)}$	Pr_{bulk} = 2.402 $Re_{D,bulk}$ = 51,667 f = 2.08×10^{-2}	$Nu_{D,bulk}$ = 208.8	
(27)	$Nu_D = \frac{\left(Nu_{D,wall} + Nu_{D,bulk}\right)}{2}\left(\frac{k_{wall}}{k_{bulk}}\right)$	$Nu_{D,bulk}$ = 208.8 $Nu_{D,wall}$ = 173.5 k_{wall} = 0.087 W/m-K k_{bulk} = 0.0756 W/m-K	Nu_D = 220.9	
(28)	$h_{Pitla} = \frac{Nu_D \cdot k_{bulk}}{d}$	Nu_D = 220.9 d = 9.4 mm k_{bulk} = 0.0756 W/m-K	h_{Pitla} = 1777 W/m^2-K	
(29)	$Deviation = \frac{\left\lvert\left(h_{Pitla} - h_{Experimental}\right)\right\rvert}{h_{Experimental}} \times 100$	h_{Pitla} = 1777 W/m^2-K $h_{Experimental}$ = 1968 W/m^2-K	Deviation = 9.71% (under-prediction)	

Kuraeva and Protopopov (1974) Pressure Drop Model

Eq. No	Equation	Inputs	Outputs	Reference
(30)	$V = G / \rho_{bulk}$	G = 400.3 kg/m^2-s ρ_{bulk} = 845.7 kg/m^3	V = 0.4733 m/s	
(31)	$\mathrm{Re}_D = \frac{\rho_{bulk} \cdot d \cdot V}{\mu_{bulk}}$	ρ_{bulk} = 845.7 kg/m^3 μ_{bulk} = 7.281×10^{-5} kg/m-s d = 9.4 mm	Re_D = 51,667	
(32)	$f_{Filonenko} = (0.790 \ln(\mathrm{Re}_D) - 1.64)^{-2}$	Re_D = 51,667	$f_{filonenko}$ = 2.08×10^{-2}	
(33)	$Gr = \frac{g \cdot \beta \cdot \lvert (T_b - T_w) \rvert \cdot d^3 \cdot \rho_b^2}{\mu_b^2}$	ρ_{bulk} = 845.7 kg/m^3 μ_{bulk} = 7.281×10^{-5} kg/m-s T_b = 62.1°C T_w = 43.8°C d = 9.4 mm β = 1.373×10^{-2} 1/K	Gr = 2.76×10^8	
(34)	$r = \frac{Gr}{\mathrm{Re}_D^2}$	Gr = 2.76×10^8 Re_D = 51,667	r = 0.1034	
(35)	f_o = 0.02 $\quad Re_D > 100{,}000$ $f_o = f_{filonenko} \quad Re_D < 100{,}000$	Re_D = 51,667 $f_{filonenko}$ = 2.08×10^{-2}	f_o = 2.08×10^{-2}	
(36)	$f = f_o (\mu_w / \mu_b)^{0.22} \quad r < 0.0005$ $f = f_o (\mu_w / \mu_b)^{0.22} \cdot (2.15 \cdot r^{0.1}) \quad r > 0.0005$	f_o = 2.08×10^{-2} r = 0.1034 μ_b = 7.281×10^{-5} kg/m-s μ_w = 1.008×10^{-4} kg/m-s	f = 0.03829	
(37)	$(\Delta P / \Delta z) = \frac{1}{2} f \cdot \rho_b \cdot V^2 \frac{1}{d} \cdot \frac{1}{1000}$	V = 0.4733 m/s f = 0.03829 ρ_b = 845.7 kg/m^3 d = 9.4 mm	$(\Delta P/dz)_f$ = 0.3859 kPa/m	

(38)	$Deviation = \frac{\left\lvert \left(\left(\Delta P / \Delta z \right)_{pred} - \left(\Delta P / \Delta z \right)_{Expt} \right) \right\rvert}{\left(\Delta P / \Delta z \right)_{Expt}} \times 100$	$(\Delta P/dz)_{f,pred}$ = 0.3859 kPa/m $(\Delta P/dz)_{f,Expt}$ = 0.456 kPa/m	Deviation = 15.37% (under-prediction)	

APPENDIX F PHASE-CHANGE HEAT TRANSFER AND PRESSURE DROP MODELS

Representative Data Points:

Wavy Flow Regime	
	Values
G (kg/m^2-s)	302.2
d_i (mm)	9.4
P_{test} (kPa)	3815
T_b , T_w (°C)	59.6, 37.7
x	0.53
h (W/m^2-K), $(dP/dz)_f$ (kPa/m) (experimental values)	2710, 0.779
Annular Flow Regime	
	Values
G (kg/m^2-s)	700.6
d_i (mm)	6.22
P_{test} (kPa)	3932
T_b , T_w (°C)	59.8, 50.5
x	0.83
h (W/m^2-K), $(dP/dz)_f$ (kPa/m) (experimental values)	7404, 9.27
Transition Regime	
	Values
G (kg/m^2-s)	499.4
d_i (mm)	9.4
P_{test} (kPa)	4305
T_b , T_w (°C)	65.05, 44.7
x	0.57
h (W/m^2-K), $(dP/dz)_f$ (kPa/m) (experimental values)	4151, 1.81

Wavy Flow Regime (Heat Transfer Coefficient)

Eq. No	Equation	Inputs	Outputs	Reference
(4)	$\rho_l, \rho_v, \mu_l, \mu_v, k_l, c_{p,l}, \mathrm{Pr}_l, h_{fg} = f(T_b)$	T_b = 59.6°C	ρ_l = 821.6 kg/m^3 ρ_v = 196.6 kg/m^3 μ_l = 6.967×10^{-5} kg/m-s μ_v = 1.953×10^{-5} kg/m-s $c_{p,l}$ = 3.082 kJ/kg-K Pr_l = 2.588 k_l = 7.47×10^{-2} W/m-k h_{fg} = 107.2 kJ/kg	
(2)	$\mathrm{Re}_l = \frac{G(1-x)d}{\mu_l}$	G = 302.2 kg/m^2-s d = 9.4 mm μ_l = 6.97×10^{-5} kg/m-s x = 0.53	Re_l = 19,040	
(3)	$X_{tt} = \left(\frac{1-x}{x}\right)^{0.9}\left(\frac{\rho_v}{\rho_l}\right)^{0.5}\left(\frac{\mu_l}{\mu_v}\right)^{0.1}$	ρ_l = 821.6 kg/m^3 ρ_v = 196.6 kg/m^3 μ_l = 6.967×10^{-5} kg/m-s μ_v = 1.953×10^{-5} kg/m-s x = 0.53	X_{tt} = 0.493	
(4)	$\mathrm{Ga} = \frac{9.8\rho_l(\rho_l-\rho_v)\cdot d^3}{\mu_l^{\,2}}$	ρ_l = 821.6 kg/m^3 ρ_v = 196.6 kg/m^3 μ_l = 6.967×10^{-5} kg/m-s d = 9.4 mm	Ga = 8.613×10^8	

(5)	$\mathrm{Fr}_{so} = 0.025\mathrm{Re}_l^{1.59}\left[\frac{1+1.09X_{tt}^{0.039}}{X_{tt}}\right]^{1.5}\frac{1}{\mathrm{Ga}^{0.5}}$ If $\mathrm{Re}_l \le 1250$ $\mathrm{Fr}_{so} = 1.26\mathrm{Re}_l^{1.04}\left[\frac{1+1.09X_{tt}^{0.039}}{X_{tt}}\right]^{1.5}\frac{1}{\mathrm{Ga}^{0.5}}$ If $\mathrm{Re}_l > 1250$	$\mathrm{Ga} = 8.613\times10^8$ $\mathrm{Re_l} = 19{,}040$ $X_{tt} = 0.493$	$\mathrm{Fr_{so}} = 10.35$	
(6)	If $1.75 < \mathrm{Fr_{so}} < 14$, wavy flow model If $14 < \mathrm{Fr_{so}} < 24$, wavy-to-annular transition model If $24 < \mathrm{Fr_{so}} < 65$, annular flow model	$\mathrm{Fr_{so}} = 10.35$	Implies Wavy Regime	
(7)	$\alpha = \left(1+\left(\frac{1-x}{x}\right)^{0.74}\left(\frac{\rho_v}{\rho_l}\right)^{0.65}\left(\frac{\mu_l}{\mu_v}\right)^{0.13}\right)^{-1}$	$\rho_l = 821.6$ kg/m^3 $\rho_v = 196.6$ kg/m^3 $\mu_l = 6.967\times10^{-5}$ kg/m-s $\mu_v = 1.953\times10^{-5}$ kg/m-s $x = 0.53$	$\alpha = 0.703$	Baroczy (1965)
(8)	$\left(1-\frac{\theta_l}{\pi}\right) \cong \frac{\arccos(2\alpha - 1)}{\pi}$	$\alpha = 0.703$	$\theta_l = 1.989$ rad	
(9)	$\mathrm{Ja}_l = \frac{c_{p,l}(T_{sat}-T_{wall})}{h_{fg}}$	$c_{p,l} = 3.082$ kJ/kg-K $T_{sat} = 59.6$°C $T_{wall} = 37.7$°C $h_{fg} = 107.2$ kJ/kg	$\mathrm{Ja_l} = 0.6268$	
(10)	$Nu_{film} = \frac{1.1212}{\theta_l}\left[\frac{Ga\,\mathrm{Pr}_l}{Ja_l}\right]^{1/4}\left[\int_0^{\theta_l}\sin^{1/3}\theta d\theta\right]^{3/4}$	$\mathrm{Ga} = 8.613\times10^8$ $\mathrm{Ja_l} = 0.6268$ $\mathrm{Pr} = 2.588$ $\theta_l = 1.989$ rad	$\mathrm{Nu_{film}} = 205.6$	
(11)	$D_{h,liquid\ pool} = \frac{\left[\sin\theta_l\cos\theta_l + (\pi-\theta_l)\right]}{\left[\sin\theta_l + (\pi-\theta_l)\right]}\times d$	$\theta_l = 1.989$ rad $d = 9.4$ mm	$\mathrm{D_{h,liquid\ pool}} = 3.55$ mm	

(12)	$\mathrm{Re}_{liquid} = \frac{G \cdot (1-x) \cdot D_{h,liquid\ pool}}{\mu_l}$	$D_{h,liquid\ pool}$ = 3.55 mm $\mu_l = 6.967\times10^{-5}$ kg/m-s x = 0.53 G = 302.2 kg/m^2-s	Re_{liquid} = 7191	
(13)	$Nu_{forced} = 0.005\,\mathrm{Re}_{liquid}^{0.97}\,\mathrm{Pr}_l^{0.3}\left[1+\left(\frac{x}{1-x}\right)\left(\frac{\rho_l}{\rho_v}\right)\right] \cdot\left(\frac{d}{d_{basline}}\right)^{-0.56}$	Re_{liquid} = 7191 x = 0.533 ρ_l = 821.6 kg/m^3 ρ_v = 196.6 kg/m^3 Pr_l = 2.588 d = 9.4 mm $d_{baseline}$ = 9.4 mm	Nu_{forced} = 211.4	
(14)	$Nu_{wavy} = \frac{\theta_l}{\pi} Nu_{film} + \left(1-\frac{\theta_l}{\pi}\right) \cdot \frac{Nu_{forced}}{d_h/d}$	$D_{h,liquid\ pool}$ = 3.55 m d = 9.4 mm Nu_{forced} = 211.4 Nu_{film} = 205.6 θ_l = 1.989 rad	Nu_{wavy} = 335.5	
(15)	$h_{wavy} = \frac{Nu_{wavy} \cdot k_l}{d}$	$k_l = 7.47\times10^{-2}$ W/m-k Nu_{wavy} = 335.5 d = 9.4 mm	h_{wavy} = 2667 W/m^2-k	
(16)	$Deviation = \frac{\lvert h_{expt.} - h_{pred.} \rvert}{h_{expt.}}$	h_{pred} = 2667 W/m^2-k h_{expt} = 2710 W/m^2-k	Deviation = 1.59% (under-prediction)	

Annular Flow Regime (Heat Transfer Coefficient)

Eq. No	Equation	Inputs	Outputs	Reference
(17)	$\rho_l, \rho_v, \mu_l, k_l, \mathrm{Pr}_l = f(T_b)$	T_b = 59.8°C	ρ_l = 820 kg/m^3 ρ_v = 197.7 kg/m^3 $\mu_l = 6.944\times10^{-5}$ kg/m-s	

			$Pr_l = 2.871$ $k_l = 7.46\times10^{-2}$ W/m-k	
(18)	$\mathrm{Re}_l = \frac{G(1-x)d}{\mu_l}$	G = 700.6 kg/m^2-s, x = 0.83 d = 6.2 mm $\mu_l = 6.944\times10^{-5}$ kg/m-s	Re_l = 10,822	
(19)	$Nu_{annular} = 0.0134\,\mathrm{Re}_l^{0.84}\,\mathrm{Pr}_l^{0.3}\left[1+\left(\left(\frac{x}{1-x}\right)\left(\frac{\rho_l}{\rho_v}\right)\right)^{0.8}\right] \cdot\left(\frac{d}{d_{baseline}}\right)^{-0.32}$	Re_l = 10,822 Pr_l = 2.871 x = 0.83 ρ_l = 820 kg/m^3 ρ_v = 197.7 kg/m^3 d = 6.2 mm $d_{baseline}$ = 9.4 mm	$Nu_{annular}$ = 622	
(20)	$h_{annular} = \frac{Nu_{annular}\cdot k_l}{d}$	$Nu_{annular}$ = 622 d = 6.2 mm $k_l = 7.46\times10^{-2}$ W/m-k	$h_{annular}$ = 7484 W/m^2-k	
(21)	$Deviation = \frac{\lvert h_{expt.} - h_{pred.}\rvert}{h_{expt.}}$	h_{pred} = 7484 W/m^2-k h_{expt} = 7404 W/m^2-k	Deviation = 1.08% (over-prediction)	

Transition Regime (Heat Transfer Coefficient)

Eq. No	Equation	Inputs	Outputs	Reference
(22)	$k_l = f(T_b)$	T_b = 65.05°C	$k_l = 7.26\times10^{-2}$ W/m-k	
(23)	Nu_{wavy} = Nu calculated using wavy flow model $Nu_{annular}$ = Nu calculated using annular flow model		Nu_{wavy} = 485 $Nu_{annular}$ = 526	

(24)	$Nu_{transition} = \left(\frac{Fr_{so} - Fr_{so,wavy}}{Fr_{so,annular} - Fr_{so,wavy}} \right) Nu_{annular} + \left(\frac{Fr_{so,annular} - Fr_{so}}{Fr_{so,annular} - Fr_{so,wavy}} \right) Nu_{wavy}$	$Fr_{so} = 18.77$ $Fr_{so,annular} = 24$ $Fr_{so,wavy} = 14$ $Nu_{wavy} = 485$ $Nu_{annular} = 526$	$Nu_{transition} = 504.55$	
(25)	$h_{transition} = \frac{Nu_{transition} \cdot k_l}{d}$	$Nu_{transition} = 504.55$ $k_l = 7.26\times10^{-2}$ W/m-k d = 9.4 mm	$h_{transition} = 3897$ W/m^2-k	
(26)	$Deviation = \frac{\lvert h_{expt.} - h_{pred.} \rvert}{h_{expt.}}$	$h_{pred} = 3897$ W/m^2-k $h_{expt} = 4151$ W/m^2-k	Deviation = 6.12% (under-prediction)	

Wavy Flow Regime (Frictional Pressure Drop)

Eq. No	Equation	Inputs	Outputs	Reference
(27)	$\rho_l, \rho_v, \mu_l, \mu_v, k_l, c_{p,l}, \mathrm{Pr}_l, h_{fg} = f(T_b)$	$T_b = 59.6°C$	$\rho_l = 821.6$kg/m^3 $\rho_v = 196.6$ kg/m^3 $\mu_l = 6.967\times10^{-5}$ kg/m-s $\mu_v = 1.953\times10^{-5}$ kg/m-s $c_{p,l} = 3.082$ kJ/kg-K $Pr_l = 2.588$ $k_l = 7.47\times10^{-2}$ W/m-k $h_{fg} = 107.2$ kJ/kg	
(28)	$\mathrm{Re}_{GO} = \frac{Gd}{\mu_v}$, $\mathrm{Re}_{LO} = \frac{Gd}{\mu_l}$	G = 302.2 kg/m^2-s, d = 9.4 mm $\mu_v = 1.953\times10^{-5}$ kg/m-s $\mu_l = 6.967\times10^{-5}$ kg/m-s	$Re_{GO} = 145{,}438$ $Re_{LO} = 40{,}768$	

(29)	$f_{GO} = \begin{cases} 16/\mathrm{Re}_{GO} & \mathrm{Re}_{GO} < 2300 \\ 0.079\,\mathrm{Re}_{GO}^{-0.25} & 2300 < \mathrm{Re}_{GO} < 20000 \\ 0.046\,\mathrm{Re}_{GO}^{-0.2} & \mathrm{Re}_{GO} > 20000 \end{cases}$ $f_{LO} = \begin{cases} 16/\mathrm{Re}_{LO} & \mathrm{Re}_{LO} < 2300 \\ 0.079\,\mathrm{Re}_{LO}^{-0.25} & 2300 < \mathrm{Re}_{LO} < 20000 \\ 0.046\,\mathrm{Re}_{LO}^{-0.2} & \mathrm{Re}_{LO} > 20000 \end{cases}$	Re_{GO} = 145,438 Re_{LO} = 40,768	$f_{GO} = 4.268\times10^{-3}$ $f_{LO} = 5.504\times10^{-3}$	
(30)	$(dP/dz)_{f,GO} = 2f_{GO}G^2/(d_{actual}\rho_v \cdot 1000)$ $(dP/dz)_{f,LO} = 2f_{LO}G^2/(d_{actual}\rho_l \cdot 1000)$	$f_{GO} = 4.268\times10^{-3}$ $f_{LO} = 5.504\times10^{-3}$ d = 9.4 mm G = 302.2 kg/m^2-s, ρ_l = 821.6 kg/m^3 ρ_v = 196.6 kg/m^3	$(dP/dz)_{f,GO}$ = 0.422 kPa/m $(dP/dz)_{f,LO}$ = 0.130 kPa/m	
(31)	$Y^2 = \dfrac{(dP/dz)_{f,GO}}{(dP/dz)_{f,LO}}$	$(dP/dz)_{f,GO}$ = 0.4221 kPa/m $(dP/dz)_{f,LO}$ = 0.1302 kPa/m	Y = 1.8	
(32)	$n = \begin{cases} 1 & \mathrm{Re}_{LO} < 2300 \\ 0.25 & 2300 < \mathrm{Re}_{LO} < 20000 \\ 0.2 & \mathrm{Re}_{LO} > 20000 \end{cases}$	Re_{LO} = 40,768	n = 0.2	
(33)	$N_{conf} = \dfrac{1}{d}\left[\dfrac{\sigma}{g(\rho_l - \rho_v)}\right]^{0.5}$	$\sigma = 0.8114\times10^{-3}$ N/m ρ_l = 821.6 kg/m^3 ρ_v = 196.6 kg/m^3 d = 9.4 mm	N_{conf} = 0.03871	

(34)	$C(x) = \left(\frac{0.12}{x^2} + \frac{2.9}{x} - 0.76\right)\left(\frac{d}{d_{baseline}}\right)^{-0.77}$	x = 0.53 d = 9.4 mm $d_{baseline}$ = 9.4 mm	C(x) = 5.1	
(35)	$\phi_{LO}{}^2 = 1 + [CY^2 - 1][N_{conf} x^{\frac{2-n}{2}}(1-x)^{\frac{2-n}{2}} + x^{2-n}]$	C = 5.1 N_{conf} = 0.03871 Y = 1.8 n = 0.2 x = 0.53	$\phi_{LO}{}^2$ = 6.17	
(36)	$\left(\frac{dP}{dz}\right)_f = \phi_{LO}{}^2 \left(\frac{dP}{dz}\right)_{f,LO}$	$\phi_{LO}{}^2$ = 6.17 $(dP/dz)_{f,LO}$ = 0.130 kpa/m	$(dP/dz)_f$ = 0.80 kPa/m	
(37)	$Deviation = \frac{\left\|(dP/dz)_{f,Expt.} - (dP/dz)_{f,\Pr ed.}\right\|}{(dP/dz)_{f,Expt}} \cdot 100\%$	$(dP/dz)_{f\,\text{pred}}$ = 0.80 kPa/m $(dP/dz)_{f\,\text{expt}}$ = 0.78 kPa/m	Deviation = 2.56% (over-prediction)	

Annular Flow Regime (Frictional Pressure Drop)

Eq. No	Equation	Inputs	Outputs	Reference
(38)	f_{GO} , $f_{LO,}$ $(dP/dz)_{f,GO}$, $(dP/dz)_{f,LO}$, Y, n, N_{conf} for annular flow are calculated using equation 28 to 33		$f_{GO} = 3.919\times10^{-3}$ $f_{LO} = 5.049\times10^{-3}$ $(dP/dz)_{f,GO}$ =	

	above		3.14 kPa/m $(dP/dz)_{f,LO}$ = 0.971 kPa/m Y = 1.8 n = 0.2 N_{conf} = 0.05832	
(39)	$C(x) = \left(18.22 - 31.97x + 17.21x^2\right)\left(\frac{d}{d_{baseline}}\right)^{-0.34}$	x = 0.83 d = 6.2 mm $d_{baseline}$ = 9.4 mm	C (x) = 4.09	
(40)	$\phi_{LO}{}^2 = 1 + [CY^2 - 1][N_{conf} x^{\frac{2-n}{2}}(1-x)^{\frac{2-n}{2}} + x^{2-n}]$	C = 4.09 N_{conf} = 0.05832 Y = 1.8 n = 0.2 x = 0.83	$\phi_{LO}{}^2$ = 9.78	
(41)	$\left(\frac{dP}{dz}\right)_f = \phi_{LO}{}^2 \left(\frac{dP}{dz}\right)_{f,LO}$	$\phi_{LO}{}^2$ = 9.78 $(dP/dz)_{f,LO}$ = 0.971 kPa/m	$(dP/dz)_f$ = 9.52 kPa/m	
(42)	$Deviation = \frac{\left\lvert (dP/dz)_{f,Expt.} - (dP/dz)_{f,\Pr ed.} \right\rvert}{(dP/dz)_{f,Expt}} \cdot 100\%$	$(dP/dz)_{f\,\text{pred}}$ = 9.52 kPa/m $(dP/dz)_{f\,\text{expt}}$ = 9.27 kPa/m	Deviation = 2.70% (over-prediction)	

Transition Regime (Frictional Pressure Drop)

Eq. No	Equation	Inputs	Outputs	Reference
(43)	$(dP/dz)_{f,wavy}$ = calculated using wavy flow model $(dP/dz)_{f,annular}$ = calculated using annular flow model		$(dP/dz)_{f,wavy}$ = 1.68 kPa/m $(dP/dz)_{f,annular}$ = 1.96 kPa/m	
(44)	$\left(\frac{dP}{dz}\right)_{f,transition} = \left(\frac{Fr_{so} - Fr_{so,wavy}}{Fr_{so,annular} - Fr_{so,wavy}}\right)\left(\frac{dP}{dz}\right)_{f,annular} + \left(\frac{Fr_{so,annular} - Fr_{so}}{Fr_{so,annular} - Fr_{so,wavy}}\right)\left(\frac{dP}{dz}\right)_{f,wavy}$	Fr_{so} = 18.77 $Fr_{so,annular}$ = 24 $Fr_{so,wavy}$ = 14 $(dP/dz)_{f,wavy}$ = 1.68 kPa/m $(dP/dz)_{f,annular}$ = 1.96 kPa/m	$(dP/dz)_{f}$ = 1.814 kPa/m	
(45)	$Deviation = \frac{\left\lvert (dP/dz)_{f,Expt.} - (dP/dz)_{f,\mathrm{Pred.}} \right\rvert}{(dP/dz)_{f,Expt}} \cdot 100\%$	$(dP/dz)_{f\,\mathrm{pred}}$ = 1.814 kPa/m $(dP/dz)_{f\,\mathrm{expt}}$ = 1.81 kPa/m	Deviation = 0.24% (over-prediction)	

APPENDIX G SUPERCRITICAL HEAT TRANSFER AND PRESSURE DROP MODELS

Representative Data Points:

Liquid-Like Regime	
	Values
G (kg/m^2-s)	502.2
d_i (mm)	6.2
P_{test} (kPa)	4935
p_r	1.01
T_b , T_w (°C)	56.69, 44.17
ρ_b, ρ_w (kg/m^3)	898.4, 987.6
Cp_b,Cp_w (kJ/kg-K)	2.147, 1.817
Pr_b	2.21
k (W/m-K)	0.067
Re	38322
h (W/m^2-K), $(dP/dz)_f$ (kPa/m) (Experimental)	2988, 1.34
Pseudo-Critical Transition Regime	
	Values
G (kg/m^2-s)	698
d_i (mm)	6.2
P_{test} (kPa)	4941
p_r	1.01
T_b , T_w (°C)	77.15, 64.97
ρ_b, ρ_w (kg/m^3)	254.8, 809.8
Cp_b,Cp_w (kJ/kg-K)	3.564, 2.856
Pr_b	2.127
k (W/m-K)	0.032
Re	194,664
h (W/m^2-K), $(dP/dz)_f$ (kPa/m) (Experimental)	6657, 10.61

Gas-Like Regime	
	Values
G (kg/m^2-s)	800
d_i (mm)	9.4
P_{test} (kPa)	4932
p_r	1.01
T_b , T_w (°C)	82.42, 57.71
ρ_b, ρ_w (kg/m^3)	221, 890
Cp_b,Cp_w (kJ/kg-K)	2.45, 2.19
Pr_b	1.62
k (W/m-K)	0.027
Re	354,037
h (W/m^2-K), $(dP/dz)_f$ (kPa/m) (Experimental)	4204, 5.80

Liquid-Like Regime Correlation

Eq. No	***Equation***	***Inputs***	***Outputs***	***Reference***
(5)	$f_{Churchill} = 8\left[\left(\frac{8}{\mathrm{Re}_{w,tube}}\right)^{12} + \left(\left[2.457\ln\left(\left[\frac{7}{\mathrm{Re}_{w,tube}}\right]^{0.9} + 0.27\varepsilon_D\right)\right]^{16} + \left[\frac{37350}{\mathrm{Re}_{w,tube}}\right]^{16}\right)^{-1.5}\right]^{1/12}$	Re = 38,322 $\varepsilon_D = 0$	$f_{churchill} = 0.0221$	
(6)	$f_{liquid-like} = 2.415 f_{Churchill}\left(\frac{\rho_w}{\rho_b}\right)^{0.507}\left(\frac{d_{actual}}{d_{baseline}}\right)^{-0.184}$	$f_{churchill} = 0.0221$ $\rho_b = 898.4$ kg/m^3 $\rho_w = 987.6$ kg/m^3 $d_{actual} = 6.2$ mm $d_{baseline} = 9.4$ mm	$f_{liquid\text{-}like} = 0.0603$	

(3)	$V = G / \rho_b$	G = 502.2 kg/m^2-s ρ_b = 898.4 kg/m^3	V = 0.559 m/s	
(4)	$\left(\frac{dP}{dz}\right)_{f,liquid-like} = \frac{1}{2} f_{liquid-like} \rho_b V^2 \frac{L_{test}}{d}$	$f_{liquid-like}$ = 0.0603 ρ_b = 898.4 kg/m^3 d = 6.2 mm L_{test} = 1 V = 0.559 m/s	$(dP/dz)_{f,liquid-like}$ = 1.36 kPa/m	
(5)	$Deviation = \frac{\left\|(dp/dz)_{f,Expt.} - (dp/dz)_{f,Pred.}\right\|}{(dp/dz)_{f,Expt.}}$	$(dp/dz)_{f,Expt.}$ = 1.34 kPa/m $(dp/dz)_{f,Pred.}$ = 1.36 kPa/m	Deviation = 1.49% (over-prediction)	
(6)	$Nu_{Churchill-modified} = \left[4.364^{10} + \left(\frac{\exp\left[\frac{2200-\mathrm{Re}}{365}\right]}{4.364^2} + \frac{1}{\left[6.3 + \frac{0.079 \cdot \left(f_{liquid-like}/8\right)^{0.5} \cdot Re \cdot \mathrm{Pr}}{\left(1+\mathrm{Pr}^{0.8}\right)^{(5/6)}}\right]^2}\right)^{-5}\right]^{\frac{1}{10}}$	Re = 38,322 $f_{liquid-like}$ = 0.0603 Pr = 2.21	$Nu_{Churchill-Modified}$ = 246.5	
(7)	$Nu_{liquid-like} = 1.004 Nu_{Churchill-modified} \left(\frac{c_{p,w}}{c_{p,b}}\right)^{0.455} \cdot \left(\frac{d_{actual}}{d_{baseline}}\right)^{-0.283}$	$Nu_{Churchill-Modified}$ = 246.5 Cp_b = 2.147 (kJ/kg-K) Cp_w = 1.817 (kJ/kg-K) d_{actual} = 6.2 mm $d_{baseline}$ = 9.4 mm	$Nu_{Liquid-Like}$ = 257.79	
(8)	$h_{liquid-like} = \frac{Nu_{liquid-like} k_b}{d}$	$Nu_{Liquid-Like}$ = 257.79 k_b = 0.0671 W/m-K d = 6.2 mm	$h_{Liquid-Like}$ = 2783 W/m^2-k	
(9)	$Deviation = \frac{\left\|h_{Expt.} - h_{Pred.}\right\|}{h_{Expt.}}$	$h_{Expt.}$ = 2988 W/m^2-k $h_{Pred.}$ = 2783 W/m^2-k	Deviation = 6.86% (under-prediction)	

Pseudo-Critical Transition Regime Correlation

Eq. No	Equation	Inputs	Outputs	Reference
(10)	$f_{Churchill} = 8\left[\left(\frac{8}{\mathrm{Re}_{w,tube}}\right)^{12} + \left(\left[2.457\ln\left(\left[\frac{7}{\mathrm{Re}_{w,tube}}\right]^{0.9} + 0.27\varepsilon_D\right)\right]^{16} + \left[\frac{37350}{\mathrm{Re}_{w,tube}}\right]^{16}\right)^{-1.5}\right]^{1/12}$	Re = 194,664 $\varepsilon_D = 0$	$f_{churchill} = 0.0156$	
(11)	$f_{pseudo-crtical} = 2.622 f_{Churchill}\left(\frac{\rho_w}{\rho_b}\right)^{0.230}\left(\frac{d_{actual}}{d_{baseline}}\right)^{-0.531}$	$f_{churchill} = 0.0156$ $\rho_b = 254.8$ kg/m^3 $\rho_w = 809.8$ kg/m^3 $d_{actual} = 6.2$ mm $d_{baseline} = 9.4$ mm	$f_{Pseudo\text{-}Critical} = 0.0665$	
(12)	$V = G/\rho_b$	G = 698 kg/m^2-s $\rho_b = 254.8$ kg/m^3	V = 2.74 m/s	
(13)	$\left(\frac{dP}{dz}\right)_{f,Pseudo-Critical} = \frac{1}{2} f_{Pseudo-Critical}\rho_b V^2 \frac{L_{test}}{d}$	$f_{Pseudo\text{-}Critical} = 0.0665$ $\rho_b = 254.8$ kg/m^3 d = 6.2 mm $L_{test} = 1$ V = 2.74 m/s	$(dP/dz)_{f,\ Pseudo\text{-}Critical}$ = 10.21 kPa/m	
(14)	$Deviation = \frac{\left\lvert (dp/dz)_{f,Expt.} - (dp/dz)_{f,Pred.}\right\rvert}{(dp/dz)_{f,Expt.}}$	$(dp/dz)_{f,Expt.}$ = 10.61 kPa/m $(dp/dz)_{f,Pred.}$ = 10.21 kPa/m	Deviation = 3.8% (under-prediction)	

(15)	$Nu_{Churchill-modified} = \left[4.364^{10} + \left(\frac{\exp\left[\frac{2200-\mathrm{Re}}{365}\right]}{4.364^2} + \frac{1}{\left[6.3 + \frac{0.079 \cdot \left(f_{liquid-like}/8\right)^{0.5} \cdot Re \cdot \mathrm{Pr}}{\left(1+\mathrm{Pr}^{0.8}\right)^{(5/6)}}\right]^2} \right)^{-5} \right]^{\frac{1}{10}}$	Re = 194,664 $f_{Pseudo-Critical}$ = 0.0665 Pr = 2.127	$Nu_{Churchill-Modified}$ = 1260	
(16)	$Nu_{pseudo-critical} = 0.928 Nu_{Churchill-modified} \left(\frac{c_{p,w}}{c_{p,b}}\right)^{0.236} \cdot \left(\frac{d_{actual}}{d_{baseline}}\right)^{-0.119}$	$Nu_{Churchill-Modified}$ = 1260 Cp_b = 3.564 (kJ/kg-K) Cp_w = 2.856 (kJ/kg-K) d_{actual} = 6.2 mm $d_{baseline}$ = 9.4 mm	$Nu_{Pseudo-Critical}$= 1166	
(17)	$h_{Pseudo-Critical} = \frac{Nu_{Pseudo-Critical} k_b}{d}$	$Nu_{Pseudo-Critical}$ = 1166 k_b = 0.0321 W/m-K d = 6.2 mm	$h_{Liquid-Like}$ = 6011 W/m^2-k	
(18)	$Deviation = \frac{\left\lvert h_{Expt.} - h_{Pred.} \right\rvert}{h_{Expt.}}$	$h_{Expt.}$ = 6657 W/m^2-k $h_{Pred.}$ = 6011 W/m^2-k	Deviation = 9.7% (under-prediction)	

Gas-Like Regime Correlation

Eq. No	Equation	Inputs	Outputs	Reference
(19)	$f_{Churchill} = 8 \left[\left(\frac{8}{\mathrm{Re}_{w,tube}}\right)^{12} + \left(\left[2.457 \ln\left(\left[\frac{7}{\mathrm{Re}_{w,tube}}\right]^{0.9} + 0.27\varepsilon_D \right) \right]^{16} + \left[\frac{37350}{\mathrm{Re}_{w,tube}}\right]^{16} \right)^{-1.5} \right]^{1/12}$	Re = 354,037 ε_D = 0	$f_{churchill}$ = 0.01395	

(20)	$f_{gas-like} = 2.872 f_{Churchill} \left(\frac{d_{actual}}{d_{baseline}} \right)^{-0.587}$	$f_{churchill}$ = 0.01395 ρ_b = 221 kg/m^3 ρ_w = 890 kg/m^3 d_{actual} = 9.4 mm $d_{baseline}$ = 9.4 mm	$f_{gas-like}$ = 0.04	
(21)	$V = G / \rho_b$	G = 800 kg/m^2-s ρ_b = 221 kg/m^3	V = 3.62 m/s	
(22)	$\left(\frac{dP}{dz} \right)_{f,gas-like} = \frac{1}{2} f_{liquid-like} \rho_b V^2 \frac{L_{test}}{d}$	$f_{gas-like}$ = 0.04 ρ_b = 221 kg/m^3 d = 9.4 mm L_{test} = 1 V = 3.62 m/s	$(dP/dz)_{f, gas-like}$ = 6.16 kPa/m	
(23)	$Deviation = \frac{\left\| (dp/dz)_{f,Expt.} - (dp/dz)_{f,Pred.} \right\|}{(dp/dz)_{f,Expt.}}$	$(dp/dz)_{f,Expt.}$ = 5.80 kPa/m $(dp/dz)_{f,Pred.}$ = 6.16 kPa/m	Deviation = 6.2% (over-prediction)	
(24)	$Nu_{Churchill-modified} = \left[4.364^{10} + \left(\frac{\exp\left[\frac{2200 - \mathrm{Re}}{365} \right]}{4.364^2} + \frac{1}{\left[6.3 + \frac{0.079 \cdot \left(f_{liquid-like}/8 \right)^{0.5} \cdot Re \cdot \mathrm{Pr}}{\left(1 + \mathrm{Pr}^{0.8} \right)^{(5/6)}} \right]^2} \right)^{-5} \right]^{\frac{1}{10}}$	Re = 354037 $f_{gas-like}$ = 0.04 Pr = 1.62	$Nu_{Churchill- Modified}$ = 1514	
(25)	$Nu_{gas-like} = 1.093 Nu_{Churchill-modified} \left(\frac{c_{p,w}}{c_{p,b}} \right)^{-0.212} \cdot \left(\frac{d_{actual}}{d_{baseline}} \right)^{-0.353}$	$Nu_{Churchill- Modified}$ = 1514 Cp_b = 2.45 (kJ/kg-K) Cp_w = 2.19 (kJ/kg-K) d_{actual} = 9.4 mm $d_{baseline}$ = 9.4 mm	$Nu_{gas-Like}$ = 1695	

(26)	$h_{gas-like} = \frac{Nu_{gas-like} k_b}{d}$	$Nu_{gas\text{-}Like} = 1695$ $k_b = 0.027$ W/m-K d = 9.4 mm	$h_{gas\text{-}Like} = 4869$ W/m^2-k	
(27)	$Deviation = \frac{\left\|h_{Expt.} - h_{Pred.}\right\|}{h_{Expt.}}$	$h_{Expt.} = 4204$ W/m^2-k $h_{Pred.} = 4869$ W/m^2-k	Deviation = 15.8% (over-prediction)	

REFERENCES

Akers, W. W., Deans, H. A. and Crosser, O. K. (1959), "Condensation Heat Transfer within Horizontal Tubes," *Chemical Engineering Progress Symposium Series* Vol. 55(29) pp. 171-176.

Akers, W. W. and Rosson, H. F. (1960), "Condensation inside a Horizontal Tube," *Chem. eng. Prog. Symp. Series* Vol. 56 pp. 145-149.

Baroczy, C. J. (1965), "Correlation of Liquid Fraction in Two-Phase Flow with Applications to Liquid Metals," *Chemical Engineering Progress Symposium Series* Vol. 61(57) pp. 179-191.

Beattie, D. R. H. and Whalley, P. B. (1982), "A Simple Two-Phase Frictional Pressure Drop Calculation Method," *International Journal of Multiphase Flow* Vol. 8(1) pp. 83-87.

Boissieux, X., Heikal, M. R. and Johns, R. A. (2000), "Two-Phase Heat Transfer Coefficients of Three Hfc Refrigerants inside a Horizontal Smooth Tube, Part Ii: Condensation," *International Journal of Refrigeration* Vol. 23(5) pp. 345-352.

Boyko, L. D. and Kruzhilin, G. N. (1967), "Heat Transfer and Hydraulic Resistance During Condensation of Steam in a Horizontal Tube and in a Bundle of Tubes," *International Journal of Heat and Mass Transfer* Vol. 10(3) pp. 361-373.

Breber, G., Palen, J. W. and Taborek, J. (1980), "Prediction of Horizontal Tubeside Condensation of Pure Components Using Flow Regime Criteria," *Journal of Heat Transfer, Transactions ASME* Vol. 102(3) pp. 471-476.

Cavallini, A., Censi, G., Del Col, D., Doretti, L., Longo, G. A. and Rossetto, L. (2001), "Experimental Investigation on Condensation Heat Transfer and Pressure Drop of New Hfc Refrigerants (R134a, R125, R32, R410a, R236ea) in a Horizontal Smooth Tube: Etude Experimentale Sur Le Transfert De Chaleur Lors De La Condensation Et Sur La Chute De Pression Des Nouveaux Frigorigenes Hfc (R134a, R125, R32, R410a, Et R236ea) Dans Un Tube Lisse Horizontal," *International Journal of Refrigeration* Vol. 24(1) pp. 73-87.

Cavallini, A., Censi, G., Del Col, D., Doretti, L., Longo, G. A. and Rossetto, L. (2002a), "Condensation of Halogenated Refrigerants inside Smooth Tubes," *HVAC and R Research* Vol. 8(4) pp. 429-451.

Cavallini, A., Censi, G., Del Col, D., Doretti, L., Longo, G. A., Rossetto, L. and Mathur, G. D. (2002b), "In-Tube Condensation of Halogenated Refrigerants," *2002 ASHRAE Winter Meeting, Jan 13-16 2002*, Atlantic City, NJ, Amer. Soc. Heating, Ref. Air-Conditoning Eng. Inc., pp. 146-161.

Cavallini, A., Censi, G., Del Col, D., Doretti, L., Longo, G. A., Rossetto, L. and Zilio, C. (2003), "Condensation inside and Outside Smooth and Enhanced Tubes -- a Review of Recent Research," *International Journal of Refrigeration* Vol. 26(4) pp. 373-392.

Cavallini, A. and Zecchin, R. (1971), "High Velocity Condensation of Organic Refrigerants inside Tubes," *Proceedings of 8th International Congress of Refrigeration*, Washington D.C., pp. 193-200.

Cavallini, A. and Zecchin, R. (1974), "Dimensionless Correlation for Heat Transfer in Forced Convection Condensation," *Int Heat Transfer Conf, 5th, Proc* pp. 309-313.

Chato, J. C. (1962), "Laminar Condensation inside Horizontal and Inclined Tubes," *ASHRAE Journal* Vol. 4(2) pp. 52-60.

Chisholm, D. (1973), "Pressure Gradients Due to Friction During the Flow of Evaporating Two-Phase Mixtures in Smooth Tubes and Channels," *International Journal of Heat and Mass Transfer* Vol. 16(2) pp. 347-358.

Chisholm, D. (1983). *Two-Phase Flow in Pipelines and Heat Exchangers*. London, New York, G. Godwin in association with the Institution of Chemical Engineers.

Churchill, S. W. (1977a), "Comprehensive Correlating Equations for Heat, Mass and Momentum Transfer in Fully Developed Flow in Smooth Tubes," *Industrial & Engineering Chemistry, Fundamentals* Vol. 16(1) pp. 109-116.

Churchill, S. W. (1977b), "Friction-Factor Equation Spans All Fluid-Flow Regimes," *Chemical Engineering Progress* Vol. 84(24) pp. 91-92.

Churchill, S. W. and Chu, H. H. S. (1975), "Correlating Equations for Laminar and Turbulent Free Convection from a Vertical Plate," *International Journal of Heat and Mass Transfer* Vol. 18(11) pp. 1323-1329.

Cicchitti, A., Lombardi, C., Silvestri, M., Soldaini, G. and Zavattarelli, R. (1960), "Two-Phase Cooling Experiments: Pressure Drop, Heat Transfer and Burnout Measurements," *Energia Nucleare* Vol. 7(6) pp. 407-425.

Coleman, J. W. (2000). *Flow Visualization and Pressure Drop for Refrigerant Phase Change and Air-Water Flow in Small Hydraulic Diameter Geometries*. Department of Mechanical Engineering. Ames, Iowa, Iowa State University.

Coleman, J. W. and Garimella, S. (2000a), "Two-Phase Flow Regime Transitions in Microchannel Tubes: The Effect of Hydraulic Diameter," *American Society of Mechanical Engineers, Heat Transfer Division*, Orlando, FL, American Society of Mechanical Engineers, pp. 71-83.

Coleman, J. W. and Garimella, S. (2000b), "Visualization of Two-Phase Refrigerant Flow During Phase Change," *Proceedings of the 34th National Heat Transfer Conference*, Pittsburgh, PA, ASME

Coleman, J. W. and Garimella, S. (2003), "Two-Phase Flow Regimes in Round, Square and Rectangular Tubes During Condensation of Refrigerant R134a," *International Journal of Refrigeration* Vol. 26(1) pp. 117-128.

Dobson, M. K. and Chato, J. C. (1998), "Condensation in Smooth Horizontal Tubes," *Journal of Heat Transfer, Transactions ASME* Vol. 120(1) pp. 193-213.

Dobson, M. K., Chato, J. C., Wattelet, J. P., Gaibel, J. A., Ponchner, M., Kenney, P. J., Shimon, R. L., Villaneuva, T. C., Rhines, N. L., Sweeney, K. A., Allen, D. G. and Hershberger, T. T. (1994). *Heat Transfer and Flow Regimes During Condensation in Horizontal Tubes*. ACRC Technical Report 57. Urbana-Champaign, University of Illinois at Urbana-Champaign.

Dukler, A. E., Wicks III, M. and Cleveland, R. G. (1964), "Frictional Pressure Drop in Two-Phase Flow," *A.I.Ch.E. Journal* Vol. 10(1) pp. 38-51.

Ebisu, T. and Torikoshi, K. (1998), "Heat Transfer Characteristics and Correlations for R-410a Flowing inside a Horizontal Smooth Tube," *ASHRAE Transactions* Vol. 104(2) pp. 556-561.

Eckels, S. J. and Pate, M. B. (1991), "Experimental Comparison of Evaporation and Condensation Heat Transfer Coefficients for Hfc-134a and Cfc-12," *International Journal of Refrigeration* Vol. 14(2) pp. 70-77.

El Hajal, J., Thome, J. R. and Cavallini, A. (2003), "Condensation in Horizontal Tubes, Part 1: Two-Phase Flow Pattern Map," *International Journal of Heat and Mass Transfer* Vol. 46(18) pp. 3349-3363.

Ewing, M. E., Weinandy, J. J. and Christensen, R. N. (1999), "Observations of Two-Phase Flow Patterns in a Horizontal Circular Channel," *Heat Transfer Engineering* Vol. 20(1) pp. 9-14.

Filonenko, G. K. (1954), "Hydraulic Resistance in Pipes," *Teploenergetika (In Russian)* Vol. 1 pp. 10-44.

Friedel, L. (1979), "Improved Friction Pressure Drop Correlations for Horizontal and Vertical Two Phase Pipe Flow," *European Two Phase Flow Group Meeting, Ispra, Italy, paper E2*

Friedel, L. (1980), "Pressure Drop During Gas/Vapor-Liquid Flow in Pipes," *International Chemical Engineering* Vol. 20(3) pp. 352-367.

Garimella, S. and Bandhauer, T. M. (2001), "Measurement of Condensation Heat Transfer Coefficients in Microchannel Tubes," *2001 ASME International Mechanical Engineering Congress and Exposition*, New York, NY, United States, American Society of Mechanical Engineers, pp. 243-249.

Garimella, S. and Christensen, R. N. (1995), "Heat Transfer and Pressure Drop Characteristics of Spirally Fluted Annuli, Part Ii: Heat Transfer," *ASME Journal of Heat Transfer* Vol. 117 pp. 61-68.

Ghajar, A. J. and Asadi, A. (1986), "Improved Forced Convective Heat Transfer Correlations for Liquids in the near-Critical Region," *AIAA Journal* Vol. 24(12) pp. 2030-2037.

Ghorbani-Tari, S. and Ghajar, A. J. (1985), "Improved Free Convective Heat-Transfer Correlations in the near-Critical Region," *AIAA Journal* Vol. 23(10) pp. 1647-1649.

Gnielinski, V. (1976), "New Equations for Heat and Mass Transfer in Turbulent Pipe and Channel Flow," *International Chemical Engineering.* Vol. 16(2) pp. 359-368.

Han, D.-H. and Lee, K.-J. (2001), "Experiments on Condensation Heat Transfer Characteristics inside a 7 Mm Outside Diameter Microfin Tube with R410a," *35th National Heat Transfer Conference, Anaheim, California*.

Haraguchi, H., Koyama, S. and Haraguchi, T. (1994), "Condensation of Refigerants Hcfc22, Hfc134a and Hcfc123 in a Horizontal Smooth Tube.," *Transactions of the Japan Society of Mechanical Engineers (In Japanese)* Vol. 60(574) pp. 245-252.

Hewitt, G. F., Shires, G. L. and Bott, T. R. (1994). *Process Heat Transfer*. Boca Raton, CRC Press; Begell House.

Incropera, F. P. and DeWitt, D. P. (2002). *Fundamentals of Heat and Mass Transfer*. 5th Ed Ed. New York, J. Wiley.

Jackson, J. D. and Fewster, J. (1975). Aere-R8158. Harwell.

Jaster, H. and Kosky, P. G. (1976), "Condensation Heat Transfer in a Mixed Flow Regime," *International Journal of Heat and Mass Transfer* Vol. 19(1) pp. 95-99.

Jiang, Y. (2004). *Quasi Single-Phase and Condensation Heat Transfer and Pressure Drop of Refrigerant R404a at Supercritical and near Critical Pressures*. Mechanical Engineering Department. Ames, Iowa State University.

Kattan, N., Thome, J. R. and Favrat, D. (1998a), "Flow Boiling in Horizontal Tubes: Part 1 - Development of a Diabatic Two-Phase Flow Pattern Map," *Journal of Heat Transfer, Transactions ASME* Vol. 120(1) pp. 140-147.

Kattan, N., Thome, J. R. and Favrat, D. (1998b), "Flow Boiling in Horizontal Tubes: Part 2 - New Heat Transfer Data for Five Refrigerants," *Journal of Heat Transfer, Transactions ASME* Vol. 120(1) pp. 148-155.

Kattan, N., Thome, J. R. and Favrat, D. (1998c), "Flow Boiling in Horizontal Tubes: Part 3 - Development of a New Heat Transfer Model Based on Flow Pattern," *Journal of Heat Transfer, Transactions ASME* Vol. 120(1) pp. 156-165.

Kawahara, A., Chung, P. M.-Y. and Kawaji, M. (2002), "Investigation of Two-Phase Flow Pattern, Void Fraction and Pressure Drop in a Microchannel," *International Journal of Multiphase Flow* Vol. 28(9) pp. 1411-1435.

Kays, W. M. and Leung, E. Y. (1963), "Heat Transfer in Annular Passages: Hydrodynamically Developed Flow with Arbitrarily Prescribed Heat Flux," *Int. J. Heat Mass Transfer* Vol. 6 pp. 537-557.

Klein, S. A. (2003). *Engineering Equation Solver*. 6.840-3D, F-Chart Software.

Kosky, P. G. and Staub, F. W. (1971), "Local Condensing Heat Transfer Coefficients in the Annular Flow Regime," *AIChe Journal* Vol. 17(5) pp. 1037-1043.

Krasnoshchekov, E. A., Kuraeva, I. V. and Protopopov, V. S. (1970), "Local Heat Transfer of Carbon Dioxide at Supercritical Pressure under Cooling Conditions.," *Teplofizika Vysokikh Temperatur* Vol. 7(5) pp. 922-930.

Kuraeva, I. V. and Protopopov, V. S. (1974), "Mean Friction Coefficients for Turbulent Flow of a Liquid at a Supercritical Pressure in Horizontal Circular Tubes," *Teplofizika Vysokikh Temperatur* Vol. 12(1) pp. 218-220.

Kurganov, V. A. (1998a), "Heat Transfer and Pressure Drop in Tubes under Supercritical Pressure of the Coolant. Part 1: Specifics of the Thermophysical Properties, Hydrodynamics, and Heat Transfer of the Liquid. Regimes of Normal Heat Transfer," *Thermal Engineering (English translation of Teploenergetika)* Vol. 45(3) pp. 177-185.

Kurganov, V. A. (1998b), "Heat Transfer and Pressure Drop in Tubes under Supercritical Pressure. Part 2. Heat Transfer and Friction at High Heat Fluxes. The Influence of Additional Factors. Enhancement of Deteriorated Heat Transfer," *Thermal Engineering (English translation of Teploenergetika)* Vol. 45(4) pp. 301-310.

Kwon, J. T., Ahn, Y. C. and Kim, M. H. (2001), "A Modeling of in-Tube Condensation Heat Transfer for a Turbulent Annular Film Flow with Liquid Entrainment," *International Journal of Multiphase Flow* Vol. 27(5) pp. 911-928.

Kwon, J. T. and Kim, M. H. (2000), "Modeling and Experiments of in-Tube Condensation Heat Transfer for R22 and Its Alternative Refrigerant," *JSME International Journal, Series B* Vol. 43(4) pp. 596-601.

Lee, H. J. and Lee, S. Y. (2001), "Pressure Drop Correlations for Two-Phase Flow within Horizontal Rectangular Channels with Small Heights," *International Journal of Multiphase Flow* Vol. 27(5) pp. 783-796.

Lemmon, E. W., McLinden, M. O. and Huber, M. L. (2002). *Refprop Version, 7.0 Beta Version*. NIST Standard Reference Database 23, NIST.

Lin, S., Kwok, C. C. K., Li, R.-Y., Chen, Z.-H. and Chen, Z.-Y. (1991), "Local Frictional Pressure Drop During Vaporization of R-12 through Capillary Tubes," *International Journal of Multiphase Flow* Vol. 17(1) pp. 95-102.

Lockhart, R. W. and Martinelli, R. C. (1949), "Proposed Correlation of Data for Isothermal Two-Phase, Two-Component Flow in Pipes," *Chemical Engineering Progress* Vol. 45(1) pp. 39-45.

Mandhane, J. M., Gregory, G. A. and Aziz, K. (1974), "A Flow Pattern Map for Gas-Liquid Flow in Horizontal Pipes," *International Journal of Multiphase Flow* Vol. 1(4) pp. 537-553.

Martinelli, R. C. (1947), *Transactions of ASME* Vol. 69 p. 947.

McAdams, W. H. (1954). *Heat Transmission*. 3 Ed. New York, McGraw-Hill.

Mills, A. F. (1995). *Heat and Mass Transfer*, Concord, MA, Richard D. Irwin, Inc.

Mishima, K. and Hibiki, T. (1996), "Some Characteristics of Air-Water Two-Phase Flow in Small Diameter Vertical Tubes," *International Journal of Multiphase Flow* Vol. 22(4) pp. 703-712.

Mishima, K., Hibiki, T. and Nishihara, H. (1993), "Some Characteristics of Gas-Liquid Flow in Narrow Rectangular Ducts," *International Journal of Multiphase Flow International Conference on Multiphase Flows '91 - Tsukuba (ICM'91), Sep 23-27 1991* Vol. 19(1) pp. 115-124.

Mishima, K. and Ishii, M. (1984), "Flow Regime Transition Criteria for Upward Two-Phase Flow in Vertical Tubes," *International Journal of Heat and Mass Transfer* Vol. 27(5) pp. 723-737.

Munson, B. R., Young, D. F. and Okiishi, T. H. (1998). *Fundamentals of Fluid Mechanics*. 3nd. Ed.

Nusselt, W. (1916), "Die Oberflachenkondensation Des Wasser-Dampfes," *Z. Ver. Dt. Ing.* Vol. 60 pp. 541-546, 569-575.

Owens, W. L. (1961). Two-Phase Pressure Gradient. *Int. Dev. In Heat Transfer, Pt Ii*. New York, ASME.

Petukhov, B. S. (1970), "Heat Transfer and Friction in Turbulent Pipe Flow with Variable Physical Properties," *Advances in Heat Transfer* Vol. 6 pp. 503-564.

Pilavachi, P. A., Ed. (1993). *Energy Efficiency in Process Technology*. Boiling in Small Parallel Channels. New York, Elsevier.

Pitla, S. S., Groll, E. A. and Ramadhyani, S. (2001a), "Convective Heat Transfer from in-Tube Cooling of Turbulent Supercritical Carbon Dioxide: Part 2 - Experimental Data and Numerical Predictions," *HVAC&R Research* Vol. 7(4) pp. 367-382.

Pitla, S. S., Groll, E. A. and Ramadhyani, S. (2001b), "Convective Heat Transfer from in-Tube Flow of Turbulent Supercritical Carbon Dioxide: Part 1 - Numerical Analysis," *HVAC&R Research* Vol. 7(4) pp. 345-366.

Pitla, S. S., Groll, E. A. and Ramadhyani, S. (2002), "New Correlation to Predict the Heat Transfer Coefficient During in-Tube Cooling of Turbulent Supercritical Co_2," *International Journal of Refrigeration* Vol. 25(7) pp. 887-895.

Pitla, S. S., Robinson, D. M., Groll, E. A. and Ramadhyani, S. (1998), "Heat Transfer from Supercritical Carbon Dioxide in Tube Flow : A Critical Review," *HVAC&R Research* Vol. 4(3).

Rouhani, S. Z. and Axelsson, E. (1970), "Calculation of Void Volume Fraction in the Subcooled and Quality Boiling Regions," *International Journal of Heat and Mass Transfer* Vol. 13(2) pp. 383-393.

Rufer, C. E. and Kezios, S. P. (1966), "Analysis of Two-Phase One Component Stratified Flow with Condensation," *Journal of heat Transfer* Vol. 88(c) p. 265.

Shah, M. M. (1976), "New Correlation for Heat Transfer During Boiling Flow through Pipes.," *Proc of Annu Meet, Jun 27-Jul 1 1976* Vol. 82 pat 2 pp. 66-86.

Shah, M. M. (1979), "A General Correlation for Heat Transfer During Film Condensation inside Pipes," *International Journal of Heat and Mass Transfer* Vol. 22(4) pp. 547-556.

Shitsman, M. E. (1963), "Impairment of the Heat Transmission at Supercritical Pressures," *Teplofizika Vysokikh Temperatur* Vol. 1(2) pp. 267-275.

Shitsman, M. E. (1974), "Heat Transfer to Supercritical Helium, Carbon Dioxide, Water: Analysis of Thermodynamic and Transport Properties and Experimental Data," *Cryogenics* pp. 77-83.

Singh, A., Ohadi, M. M. and Dessiatoun, S. V. (1996), "Empirical Modeling of Stratified-Wavy Flow Condensation Heat Transfer in Smooth Horizontal Tubes," *ASHRAE Transactions* Vol. 102(2) pp. 596-603.

Soliman, H. M. (1982), "On the Annular-to-Wavy Flow Pattern Transition During Condensation inside Horizontal Tubes," *Canadian Journal of Chemical Engineering* Vol. 60(4) pp. 475-481.

Soliman, H. M. (1986), "Mist-Annular Transition During Condensation and Its Influence on the Heat Transfer Mechanism," *International Journal of Multiphase Flow* Vol. 12(2) pp. 277-288.

Sugawara, S., Katsuta, K., lshihara, I. and Muto, T. (1967), "Consideration on the Pressure Loss of Two-Phase Flow in Small-Diameter Tubes," *Proc. 4th National Heat Transfer Symp. of Japan (in Japanese)*, pp. 169-172.

Sweeney, K. A. (1996). *The Heat Transfer and Pressure Drop Behavior of a Zeotropic Refrigerant Mixture in a Micro-Finned Tube*. Dept. Mechanical

and Industrial Engineering. Urbana, IL, University of Illionis at Urbana-Champaign.

Taitel, Y. and Dukler, A. E. (1976), "A Model for Predicting Flow Regime Transitions in Horizontal and near Horizontal Gas-Liquid Flow," *AIChE Journal* Vol. 22(1) pp. 47-55.

Tanaka, H., Nishiwaki, N., Hirate, M. and Tsage, A. (1971), "Forced Convection Heat Transfer to a Fluid near Critical Point Flowing in Circular Tube," *International Journal of Heat and Mass Transfer* Vol. 14 pp. 739-750.

Tandon, T. N., Varma, H. K. and Gupta, C. P. (1985), "Prediction of Flow Patterns During Condensation of Binary Mixtures in a Horizontal Tube," *Journal of Heat Transfer, Transactions ASME* Vol. 107(2) pp. 424-430.

Tang, L. (1997). *Empirical Study of New Refrigerant Flow Condensation inside Horizontal Smooth and Micro-Fin Tubes*, University of Maryland at College Park p. 251.

Taylor, B. N. and Kuyatt, C. E. (1994). *Guidelines for Evaluating and Expressing the Uncertainty of Nist Measurement Results*, National Institute of Standards and Technology.

Thome, J. R., El Hajal, J. and Cavallini, A. (2003), "Condensation in Horizontal Tubes, Part 2: New Heat Transfer Model Based on Flow Regimes," *International Journal of Heat and Mass Transfer* Vol. 46(18) pp. 3365-3387.

Tran, T. N., Chyu, M.-C., Wambsganss, M. W. and France, D. M. (2000), "Two-Phase Pressure Drop of Refrigerants During Flow Boiling in Small Channels: An Experimental Investigation and Correlation Development," *International Journal of Multiphase Flow* Vol. 26(11) pp. 1739-1754.

Traviss, D. P., Rohsenow, W. M. and Baron, A. B. (1973), "Forced-Convection Condensation inside Tubes: A Heat Transfer Equation for Condenser Design," *ASHRAE Transactions* Vol. 79(1) pp. 157-165.

Walker, J. E., Whan, G. A. and Rothfus, R. R. (1957), "Fluid Friction in Noncircular Ducts," *AIChE Journal* Vol. 3(4) pp. 484-489.

Zivi, S. M. (1964), "Estimation of Steady-State Steam Void-Fraction by Means of the Principle of Minimum Entropy Production," *Journal of Heat Transfer* Vol. 86 pp. 247-252.